

INM - ROSKILDE UNIVERSITY

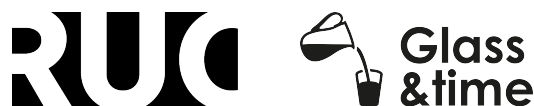
PHD IN PHYSICS

**Investigation of Simplicity in Room
Temperature Ionic Liquids**

Author:
Kira L. ELIASSEN

Supervisors:
Kristine NISS
& Tage CHRISTENSEN

April 2023



This thesis has been submitted to the PhD School of Science and Environment

Abstract

This thesis investigates dynamic properties of supercooled room temperature ionic liquids (RTIL) with shear mechanical and dielectric spectroscopy as well as quasi-elastic neutron scattering (QENS). The aim is to investigate if the dynamic signal of RTILs resembles that of non-associated molecular liquids and to look for simplicity in this class of liquids, where the structure factor reveals a complex microscopic structure. This increased knowledge of glass-forming liquids can help drive theory development of the viscous slowing down of supercooled liquids and the glass transition.

For Pyr1*n*-TFSI with $n = 4, 6$ and 8 as well as Pyr18-TFSI mixed with $x = 0.2$ and $x = 0.4$ molar fraction of Li-TFSI, the shear mechanical and dielectric alpha relaxation time and inverse steady state conductivity exhibited a temperature dependence close to independent of alkyl chain length and Li-salt concentration. An Arrhenius plot showed that the beta relaxation present in all liquids was of much weaker temperature dependence than the alpha relaxation, and this beta relaxation appeared to be constant across alkyl chain length and Li-salt concentration. This suggests a common origin, possibly the anion. This conclusion was also supported by QENS results on Pyr14-TFSI which confirmed the existence of two additional fast relaxations connected to the methyl groups on the cation.

The neat pyrrolidinium based ionic liquids showed dynamics resembling those of non-associated molecular liquids, whereas for Pyr18-TFSI mixed with Li-salt this was true except for the presence of a slow mode in the shear mechanical signal. This slow mode was also detected in the RTILs Omim-BF₄ and Pmim-BF₄, where the latter has no pre-peak in the x-ray structure factor. Furthermore, the temperature dependence of the alpha relaxation time in Pyr14-TFSI and Pmim-BF₄ followed the shoving model prediction well, as has also been observed in molecular liquids. It was also observed that the charges in the ionic liquids contribute significantly to their viscosity. As a consequence of the above mentioned, RTILs can be said to exhibit dynamics resembling those of non-associated liquids only to some extent, but there are clear deviations.

None of the RTILs studied exhibited completely simple behavior in the sense of time-temperature superposition of the relaxation spectra, constant timescale index and identical spectral shape across response functions. However, there was a high degree of simplicity for the alpha relaxation seen as TTS in the shear mechanical spectrum, as well as a conductivity and fluidity spectrum which followed the random barrier model prediction around the alpha relaxation. This indicates that deviation from simplicity is due to the beta relaxation and it supports the idea of a "zeroth-order approximation" theory for all classes of liquids. This simple theory should describe the alpha relaxation as the fundamental phenomenology in viscous liquids and the glass transition.

Resumé

Denne afhandling undersøger dynamiske egenskaber i superkølede stuetemperatur-ionvæsker ved hjælp af shear mekanisk og dielektrisk spektroskopi samt quasi-elastisk neutron spredning. Målet er at undersøge om det dynamiske signal fra ionvæskerne ligner det man ser i ikke-associerede molekylvæsker og at se efter simplicitet i denne klasse af væsker, hvor røntgen-strukturfaktoren afslører en kompleks mikroskopisk struktur. Denne øgning af viden om glass-formende væsker kan hjælpe med at drive teoriudviklingen omkring superkølede væsker fremad.

For Pyr1 n -TFSI med $n = 4, 6$ og 8 samt Pyr18-TFSI blandet med $x = 0.2$ og $x = 0.4$ molær fraktion af Li-TFSI viser den shear mekaniske og dielektriske alfa-relaksation samt den inverse ledningsevne en temperaturafhængighed tæt på værende uafhængig af alkylkædelængde samt Li-salt koncentration. Et Arrhenius-plot viste at beta-relaksationen, som er til stede i alle ionvæskerne, er meget svagere i sin temperaturafhængighed end alfa-relaksationen og at denne beta-relaksation så ud til at være konstant på tværs af alkylkædelængde og Li-salt koncentration. Dette tyder på en fælles oprindelse som muligvis er anionen. Denne konklusion blev også støttet af neutronspretnings resultater på Pyr14-TFSI som bekræftede eksistensen af to yderligere, hurtigere relaksationer som var forbundet med methylgrupperne på kationen.

De rene pyrrolidiniumbaserede ionvæsker udviste dynamik der ligner det set fra ikke-associerede molekylære væsker, hvorimod for Pyr18-TFSI blandet med Li-salt var dette sandt undtagen ved tilstedeværelsen af et langsomt, dynamisk mode i det shear mekaniske signal. Dette langsomme mode blev også detekteret i ionvæskerne Omim-BF₄ og Pmim-BF₄ hvor i den sidste er der ikke noget pre-peak i strukturfaktoren. Ud over det, blev det også observeret at ladningerne i ionvæskerne bidrager signifikant til deres viskositet. En konsekvens af det ovenstående er, at ionvæsker kan til en vis grad har dynamik der ligner det set fra ikke-associerede molekylære væsker.

Ingen af de studerede ionvæsker viste fuld simpel opførsel i form af tid-temperatur-superposition (TTS) af relaksationsspektret, konstant tidsskala-index samt en identisk form af spektret på tværs af responsfunktioner. Men, der var en høj grad af simpel opførsel for alfa-relaksationen set som TTS i det shear mekaniske spektrum omkring alfa-relaksationen samt et ledningsevne- og fluiditetsspektrum der fulgte forudsigelsen fra random barrier modellen omkring alfa-relaksationen. Dette indikerer at afvigelsen fra simpel opførsel skyldes beta relaksationen og det støtter idéen med en "nulte-ordens-approksimation" teori for alle klasser af væsker. Denne simple teori skal så kunne beskrive alfa-relaksationen som den fundamentale fænomenologi i viskøse væsker og glasovergangen.

Acknowledgement

I would like to thank my supervisor Kristine Niss for making this opportunity come true for me. I have always wanted a PhD degree in physics since researching the world around us is my great passion and something I would very much like to continue doing on a professional basis. It felt like it was meant to be when I saw the job opening back in late 2018 and decided to apply for the position with the philosophy, that we only regret the chances we didn't take. So, thank you Kristine, for believing in me and for always pushing me to strive for improvement. These four years have helped me to grow tremendously both as a person and professionally and I am truly thankful to have been a part of the project.

A thank you as well to my other supervisor Tage Christensen, who has always been ready to help me whenever I knocked on his door and to provide invaluable feedback. He has especially been there to, with great patience, explain the more complicated mathematical details and to help me understand things in depth.

A big thank you to the rest of the Glass and Time group at INM. You have all with your positive attitude, friendliness and great dedication to physics and glass-forming liquids created the perfect working environment for a young physicist like myself. I have always felt welcome and respected both as a person and as a researcher and your support has been invaluable.

Thank you to Bo Jakobsen for both being a key part in the creation of this project of investigating simplicity and slow modes in room temperature ionic liquids and for always being there when I needed technical assistance. My technical skills and flair have improved greatly during these years thanks to your help and guidance. The latter also applies to Ib Høst Pedersen, Bjarne Christensen and the rest of the extremely talented INM workshop, who was always there to help me with equipment, fixing broken transducers and making creative ways to solve detailed problems like how to seal a 0.5 mm thin glass tube inside a glove box. So, thank you to all of you for your patience and for always lifting my spirit.

I would also like to thank Aleksandar Matic and Catalin Gainaru for being generous hosts on my two exchange tours. I am grateful for your friendliness, hospitality and extended knowledge in the world of viscous liquids which has helped make my project even better.

Last, but in no means least, I would like to thank my husband Glenn for always being there for me and always believing that I could do this. Even when I doubted it myself. He is truly my greatest support, and I could not have done this without him.

This project called RiDILiq was supported by the Independent Research Fund Denmark.

List of Abbreviations

Abbreviations for liquids

Cations

Pyr14	1-butyl-1-methylpyrrolidinium
Pyr15	1-pentyl-1-methylpyrrolidinium
Pyr16	1-hexyl-1-methylpyrrolidinium
Pyr18	1-octyl-1-methylpyrrolidinium
Emim	1-ethyl-3-methylimidazolium
Pmim	1-propyl-3-methylimidazolium
Bmim	1-butyl-3-methylimidazolium
Hmim	1-hexyl-3-methylimidazolium
Omim	1-methyl-3-octylimidazolium
N8881	methyltrioctylammonium
N2228	octyltriethylammonium
P2228	octyltriethylphosphonium
TEOP	triethyl-octyl-phosphonium
TEDP	triethyl-dodecyl-phosphonium
TBOP	tributyl-octyl-phosphonium
TBDP	tributyl-dodecyl-phosphonium
TMP	tri-isobutyl-methyl-phosphonium

Anions

Li	lithium
TFSI	bis(trifluoromethanesulfonyl)imide
BF ₄	tetrafluoroborate
Tos	tosylate
DCA	dicyanamide
TCM	tricyanomethanide
Al ₂ Cl ₇	heptachlorodialuminate
Cl	chloride

Molecular liquids

DC704	tetramethyl-tetraphenyl-trisiloxane
5PPE	5-polyphenyl ether
PC	propylene carbonate

Contents

1	Introduction	3
2	Viscous liquids and the glass transition	5
2.1	The glass transition	5
2.2	Simplicity in glass forming liquids	10
3	Experimental techniques	15
3.1	Dynamic mechanical spectroscopy	15
3.1.1	Shear stress and strain	15
3.1.2	Shear viscosity	16
3.1.3	Linear viscoelasticity	17
3.1.4	Piezoelectric shear modulus gauge (PSG)	21
3.1.5	Parallel plate rheology	31
3.2	Dielectric spectroscopy	39
3.2.1	Theory of dielectric relaxation	39
3.2.2	Broadband dielectric spectroscopy	42
3.2.3	Finding the conductivity	43
3.3	Neutron scattering	43
3.3.1	Basic principles	44
3.3.2	Basic scattering theory	45
3.3.3	Cross section and the structure factor	46
3.3.4	Separation of motion	47
3.3.5	QENS	48
3.3.6	Backscattering	50
4	Room Temperature Ionic Liquids	51
4.1	General properties	52
4.2	Structure	53
4.3	RTILs in this work	54
5	Molecular mimic	59
5.1	Pressure-volume measurements	60
5.1.1	Method	60
5.1.2	Results	60
5.1.3	Discussion and conclusion	63

6	Calorimetric measurements	65
6.1	Differential Scanning Calorimetry	65
6.2	Thermalization Calorimetry	66
6.3	Results	68
6.4	Discussion	71
7	Comparative analysis, Pyr1n-TFSI	75
7.1	Dynamic Mechanical Spectroscopy	76
7.1.1	Method	76
7.1.2	Pyr14-TFSI	77
7.1.3	Pyr16-TFSI	78
7.1.4	Pyr18-TFSI	79
7.1.5	Alpha relaxation	81
7.1.6	Beta relaxation	82
7.1.7	TTS	85
7.2	Broadband Dielectric Spectroscopy	86
7.2.1	Method	86
7.2.2	Alpha relaxation	87
7.2.3	Beta relaxation	88
7.2.4	Conductivity	92
7.3	Coupling between shear and conductivity	94
7.4	Overview	97
7.5	Discussion	97
7.6	Conclusion	100
8	Comparative analysis, Pyr18-TFSI with Li-TFSI	103
8.1	Dynamic Mechanical Spectroscopy	104
8.1.1	Method	104
8.1.2	Pyr18-TFSI with $x = 0.2$ Li-TFSI	104
8.1.3	Pyr18-TFSI with $x = 0.4$ Li-TFSI	106
8.1.4	Alpha relaxation	106
8.1.5	Beta relaxation	108
8.1.6	TTS	109
8.2	Broadband Dielectric Spectroscopy	111
8.2.1	Method	111
8.2.2	Alpha relaxation	112
8.2.3	Beta relaxation	113
8.2.4	Conductivity	116
8.3	Coupling between shear and conductivity	119
8.4	Overview	122
8.5	Discussion	122
8.6	Conclusion	126

9	Looking for the slow mode	129
9.1	Introduction	129
9.1.1	The pre-peak and mesoscopic structure	129
9.1.2	Literature overview	130
9.1.3	Opposing views	133
9.2	Results	134
9.2.1	Dynamic Mechanical Spectroscopy	134
9.2.2	Broadband Dielectric spectroscopy	137
9.3	Discussion	139
9.4	Conclusion	142
10	Simplicity of spectral shapes	147
10.1	Random Barrier model	147
10.2	Fluidity and spectral shapes	149
10.3	Conclusion	156
11	Quasi-elastic neutron scattering	159
11.1	Pyr14-TFSI	159
11.1.1	Inelastic fixed window scans	160
11.1.2	Elastic fixed window scans	165
11.1.3	Time scales in Pyr14-TFSI	170
11.2	Pmim-BF ₄	173
11.2.1	Inelastic fixed window scans	174
11.2.2	Elastic fixed window scans	176
12	Testing the shoving model	179
12.1	The energy landscape picture	179
12.2	Elastic models	181
12.2.1	The shoving model	182
12.2.2	The landscape equivalent of the shoving model	183
12.3	Pyr14-TFSI	185
12.4	Pmim-BF ₄	186
12.5	Discussion and conclusion	188
13	Summary and concluding discussion	191
	Bibliography	195
	Appendices	
A	Calorimetric measurements	213
A.1	Extra results	213
B	Water contamination	215
B.0.1	Water contamination	215
C	Fit to model	219

D	X-ray structure factor on RTIL	221
E	Reprint of publications	223
E.1	High frequency dynamics and test of the shoving model for the glass-forming ionic liquid Pyr14-TFSI	223
E.2	Pressing matter: why are ionic liquids so viscous?	236
E.3	Piezoelectric shear rheometry: Further developments in experimental implementation and data extraction	246

"I have a friend who's an artist and has sometimes taken a view which I don't agree with very well. He'll hold up a flower and say 'look how beautiful it is', and I'll agree. Then he says 'I as an artist can see how beautiful this is but you as a scientist take this all apart and it becomes a dull thing,' and I think that he's kind of nutty. First of all, the beauty that he sees is available to other people and to me too, I believe. Although I may not be quite as refined aesthetically as he is... I can appreciate the beauty of a flower. At the same time, I see much more about the flower than he sees. I could imagine the cells in there, the complicated actions inside, which also have a beauty. I mean it's not just beauty at this dimension, at one centimeter; there's also beauty at smaller dimensions, the inner structure, also the processes. The fact that the colors in the flower evolved in order to attract insects to pollinate it is interesting; it means that insects can see the color. It adds the question: does this aesthetic sense also exist in the lower forms? Why is it aesthetic? All kinds of interesting questions which the science knowledge only adds to the excitement, the mystery and the awe of a flower. It only adds. I don't understand how it subtracts."

- Richard P. Feynman in "The Pleasure of Finding Things Out: The Best Short Works of Richard Feynman"

Chapter 1

Introduction

The field of condensed matter physics studies the structure and behavior of matter and therefore plays a significant role in society. This was seen with the development of semiconductors, a central part of the transistor which is the basic building block and workhorse of all modern electronics such as computers and smartphones. It is difficult to imagine a modern world without these devices, and it is safe to say that condensed matter physics and material science are central to developing new technology.

Another important, but maybe less recognized, material in our everyday lives is glass. Glass of course plays a more classic part in the construction of buildings, just try to imagine a house without windows, and in construction of containers such as bottles, glasses, and beakers. However, glass has many other uses, such as in optic fibers used to carry light, and thus information, across great distances, in the making of glass-ceramics used in e.g the display on our smartphones and in pharmaceuticals where pills in the glassy state are more easily dissolved [1]. In addition to this, most everyday plastic materials consist of glassy polymers.

All these applications clearly show how important the glassy state is in our society and how important it is on a fundamental level to understand these kinds of materials, both from a practical viewpoint but also a theoretical one. This is where the field of glass-forming liquids and the glass transition enters. Despite the central role of the glassy state, it was not until relatively recently, in the 1990s, that the study of viscous liquids and the glass transition became an accepted field of research in condensed matter physics [2].

A glass is fundamentally created when a liquid is cooled fast enough to avoid crystallization since the atoms or molecules need time to settle into the ordered crystal structure. Instead, the fast cooling slows the atoms or molecules down until they become frozen in place and in every way behaves like a solid but with the disorder of a liquid. It is, in other words, an amorphous solid. While this happens the viscosity of the liquid increases drastically, which is a feature exploited in the well-known phenomenon of blowing glass. Here the liquid silicon dioxide is so viscous that it can literally be held with a stick and manipulated to form intricate works of art.

There is no question that glass is a fundamental part of our society and the

glassy state with its isotropic structure and lack of long-range order can even be regarded as the fourth state of conventional matter. Additionally, any liquid can form a glass if cooled fast enough [2]. Despite this universality and decades of dedicated research in viscous liquids and the glass transition, fundamental questions remain open for discussion, like what mechanisms drive the glass transition itself?

Thus, the research in viscous liquids and the glass transition is still very relevant, and this thesis will be a small contribution to the giant puzzle that is the solution to what 1977 Nobel laureate P. W. Anderson famously called "*the deepest and most interesting unsolved problem in solid state theory*" [3].

Reading guide The thesis will begin with an introduction to the field of studying glass-forming liquids and the glass transition, followed by a background chapter containing the basic knowledge behind the three main experimental techniques used in the study of ionic liquids in this study; dynamic mechanical spectroscopy, neutron scattering and dielectric spectroscopy. The final background chapter is about room temperature ionic liquids (RTIL) in general and will very briefly introduce the reader to this diverse and interesting class of glass-forming liquids.

The rest of the thesis will contain the research performed during the four years that this thesis was underway. It starts with a small chapter about the work done on molecular mimics in collaboration with Frederik Philippi from Imperial College London. In this, I played a role in the density measurements on a molecular mimic designed to mimic an ionic liquid but without any charge. The following chapter about calorimetric measurements serves to characterize the ionic liquids further studied in this work and thus also to introduce the reader to these liquids.

The following three chapters share a common theme; they are all comparative analyses between five RTILs forming two series with small variations to the chemical composition. The first two of these chapters are for each series, where the dynamic properties measured with shear mechanical and dielectric methods are compared across the different liquids in order to investigate systematic changes to these properties. The third chapter compares the low frequency signal of both series and compares these results to literature.

The next two chapters changes the theme in that they are mainly about quasi-elastic neutron scattering and shear mechanical measurements. The first chapter of these two study both the dynamic modes as well as the mean square displacement in the two liquids. The latter is used in the second chapter of the two, where the relation between fast and slow dynamics is tested.

The final chapter with experimental results will investigate the simplicity of spectral shapes, and the thesis ends with a chapter summarizing the results and discussing these in relation to further research and literature. With these chapters it is attempted to answer the question if room temperature ionic liquids have dynamic properties resembling those of non-associated molecular liquids, and if "simple" behavior can be seen in this chemically complex class of liquids.

Chapter 2

Viscous liquids and the glass transition

This chapter will introduce the field of viscous liquids and the glass transition in order to frame the research questions posed in this study. It will begin with a general description of glass forming liquids and how supercooled liquids can form a glassy state, and subsequently move on to the more specific topics investigated in the following chapters.

2.1 The glass transition

When cooling a liquid sufficiently fast it can avoid crystallizing at the melting temperature, T_m , and instead continue down in temperature as a supercooled liquid. Upon further cooling the now supercooled liquid will reach a point where the time it takes for the atoms or molecules to rearrange will be so long that they in practice are stuck in place, and the liquid has become an amorphous solid [2]. This amorphous solid is what we call the glassy state and the temperature where this happens is the glass transition temperature, T_g . The glassy state has the same structure as the liquid, but the dynamics change significantly.

The process is illustrated in figure 2.1 which shows the volume change as a function of temperature. The liquid follows the light blue line down in temperature past the melting point and down into the supercooled region. At T_g there is a kink in the volume change which corresponds to a jump in its derivative and a jump in the expansion coefficient. The green line shows the volume change with temperature of the crystal.

The glass transition temperature is dependent on cooling rate which is illustrated in figure 2.1 as two dark blue lines in the glass denoted a and b with corresponding glass transition temperature of $T_{g,a}$ and $T_{g,b}$. The difference between a and b is the cooling rate in the supercooled region. A fast cooling rate will give a higher glass transition temperature than a slow cooling rate [2].

This dependence of the cooling rate clearly tells that the glass transition itself is not an intrinsic thermodynamic property such as crystallization, but rather a phenomenon which is governed by the dynamics of the system. Another

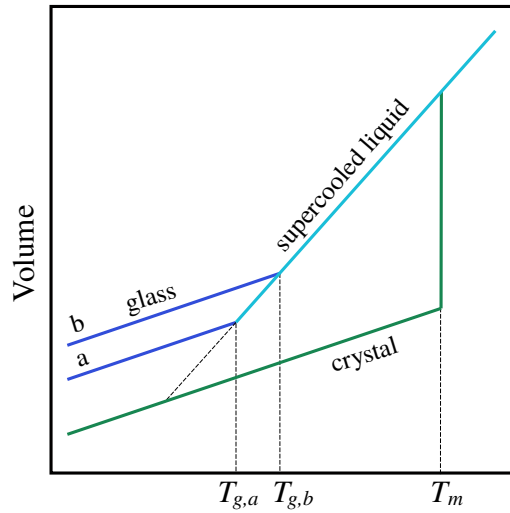


Figure 2.1: A sketch of volume change as a function of temperature. The light blue line represents volume change upon cooling past the melting point and into the supercooled region. At the glass transition temperature, T_g , there is a kink in the volume change as the liquid enters the glassy state. T_g depends on cooling rate which is illustrated with the two dark blue lines in the glassy state. A fast cooling rate gives a higher glass transition temperature, $T_{g,b}$ than a slow cooling rate, $T_{g,a}$.

consequence is that the glass transition temperature is not strictly defined, and it can even vary with several degrees depending on the method used to find T_g . However, a practical definition is that the liquid has entered the glassy state when the viscosity reaches 10^{12} Pa s.

As the liquid is cooled down the change in volume occur for two reasons, the first is the on a phonon time scale isostructural change which is simply due to the distance between atoms or molecules getting shorter, the second is more complex and is a structural volume change driven by a change in the packing of atoms or molecules. When the liquid is cooled the system goes out of equilibrium and the atoms/molecules start to rearrange in order to get to the new equilibrium point. This rearranging to reach equilibrium is called relaxation and the time it takes to do so is called the structural or alpha relaxation time, τ_α [4].

The structural relaxation time changes with temperature and if it was to follow a simple Arrhenius behavior, i.e.

$$\tau_\alpha = \tau_0 e^{E_\alpha/k_B T} \quad (2.1.1)$$

where τ_0 is a microscopic time, k_b Boltzmann's constant and E_α is the activation energy of the structural relaxation, then plotting the logarithm of τ_α as a function of inverse temperature would form a straight line beginning in τ_0 and having E_α/k_B as the slope.

In reality however, the structural relaxation time in most glass forming liquids do not have Arrhenius behavior and are instead much more temperature

dependent [2, 5, 6]. This can be seen in a classic plot from 1985 in figure 2.2 showing viscosity as a function of inverse temperature for a range of different liquids. Viscosity is roughly proportional to τ_α through the high-frequency limiting shear modulus, G_∞ . This relation is the Maxwell relation, $\eta = G_\infty \tau_\alpha$.

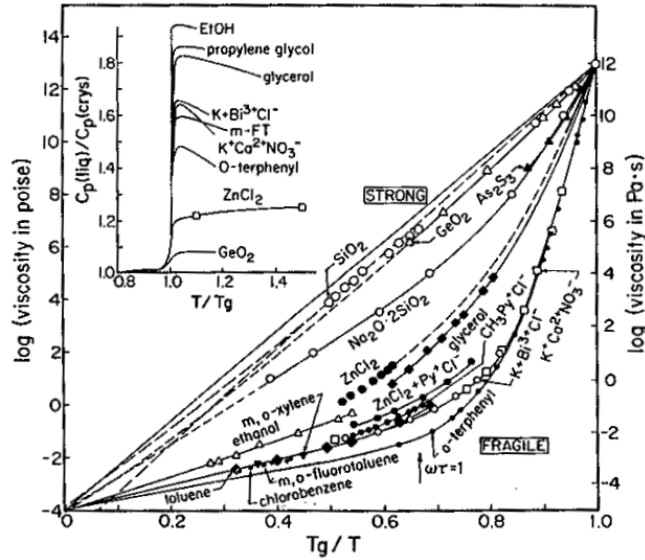


Figure 2.2: A T_g scaled Arrhenius plot showing viscosity as a function of inverse temperature for various glass forming liquids. "Strong" liquids lie close to a straight line were as "Fragile" liquids deviates significantly from this. The insert shows the expansion coefficient. From [7].

The plot clearly shows how many liquids deviate from Arrhenius behavior. A way to classify this deviation is a parameter called the fragility index, m , which was introduced in 1992 by R. Böhmer and A. C. Angell [8, 9]. This parameter is defined as the slope of the logarithm of the alpha relaxation time or viscosity at the glass transition and will thus inform about the "steepness" of the viscous slowing down or in other words how far from Arrhenius behavior the liquid is.

This translates into the mathematical definition as

$$m = \left. \frac{d \log_{10}(\tau_\alpha)}{d T_g/T} \right|_{T=T_g} \quad (2.1.2)$$

For Arrhenius behavior the fragility index is equal to 16 and liquids close to this value are called strong liquids. The opposite end of the scale are liquids with a high fragility index of 80 or more and these are called fragile liquids.

Another puzzling feature of the structural relaxation is related to the spectral shape. In the simplest model of molecular motion, the relaxation in the time domain would follow an exponential function, $R(t) = \exp(-t)$, which gives a symmetric Lorentzian relaxation loss peak in the imaginary part of the frequency domain through a Fourier-Laplace transformation. This is illustrated in figure 2.3 as the dashed, blue line in both the time (left) and frequency (right) domain.

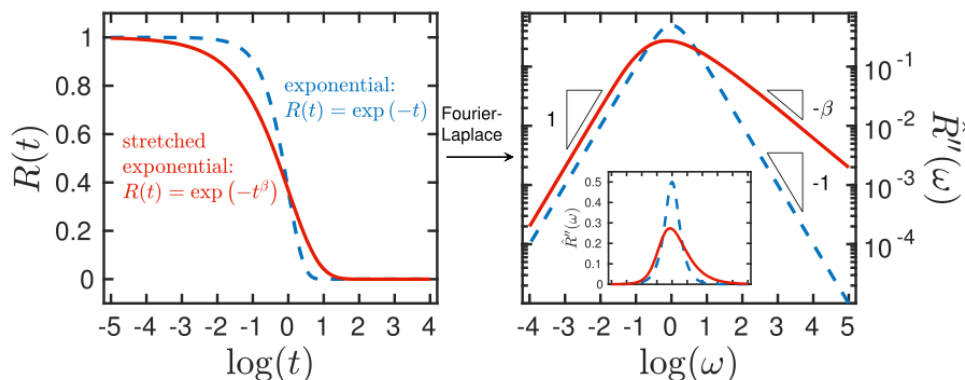


Figure 2.3: An illustration of the difference between an exponential (blue dotted line) and a stretched exponential (red solid line) response function. To the left shown in the time domain and to the right in the frequency domain (obtained by Fourier-Laplace transformation). To the right, the main figure is a log-log plot whereas the insert is a log-lin plot. The triangles in the main figure show the slopes of the graphs. From [4].

Here the symmetric loss peak has a slope of 1 in the double logarithmic plot to both sides of the peak.

But in reality, the relaxation in supercooled liquids is a highly stretched exponential given as $R(t) = \exp(-t^\beta)$ in the time domain with β as the stretching factor [2, 5]. This translates in the imaginary part of the frequency domain as a loss peak where the high-frequency part is stretched out over many decades in frequency with a slope in the double logarithmic plot of β . This stretched exponential is illustrated in figure 2.3 as the solid, red line.

The explanation for this non-exponential relaxation is still not found and so it remains, together with the non-Arrhenius nature, one of the fundamental, unanswered questions in the study of glass-forming liquids.

The shoving model A way to investigate the temperature dependence of the alpha relaxation and thus the viscous slowing down of glass-formers is to test the shoving model. This model was developed here at Roskilde University, and it connects the instantaneous shear modulus with the structural relaxation time [10]. Details will be given in chapter 12.

It has been tested with success in our group on several van der Waals liquids such as cumene, 5PPE and propylene carbonate [11, 12]. In keeping with this tradition of testing the shoving model, it will also be used to investigate the temperature dependence of the alpha relaxation time of RTILs in this thesis. This way it will also be possible to study how much the viscous slowing down in RTILs differ from non-associated molecular liquids.

The beta relaxation In glass-forming liquids several secondary relaxations are often observed at higher frequencies than the primary alpha relaxation and

they usually have a weaker amplitude [13, 14]. There are however some general phenomenological features to the beta relaxation such as a weaker temperature dependence than the alpha relaxation where this is often of an Arrhenius nature. Furthermore, this secondary dynamic mode often persists far into the glassy state and the spectral shape is wider than the alpha relaxation with a Cole-Cole-type shape in the dielectric susceptibility [14].

The origin of this beta relaxation is a complex matter and is still up to much debate, but it is reported in literature that beta relaxations can originate in intramolecular motions such as rotations of molecular side groups or other forms of intramolecular degrees of freedom. These kinds of relaxations are considered to be independent of the structural alpha relaxation. But it was discovered that even rigid molecules also give rise to a beta relaxation, the so-called Johari-Goldstein (JG) relaxations [15]. The origin of these JG modes is thus intermolecular, and it is suggested that they are intimately linked to the alpha relaxation and can merge with the alpha relaxation at higher temperatures. In contrast to this, the intramolecular beta relaxation can cross the alpha relaxation and have relaxations time higher than this, i.e. $\tau_\beta > \tau_\alpha$ [14].

Due to instrument limitations, it is usually not possible to measure the shear modulus of liquids at a high enough frequency to see the beta relaxation and as a consequence this secondary relaxation is primarily studied using dielectric spectroscopy. But with the development of the piezoelectric shear modulus gauge (PSG) at Roskilde University it is possible to measure the shear modulus at frequencies as high as 30 kHz and thus measure the beta relaxation. This is however still a quite unique technique and so the study of the beta relaxation in the shear modulus of glass-forming liquids is limited [16]. Furthermore, it cannot be assumed that the properties of the beta relaxation are the same in the shear mechanical spectra and so it is of interest to study these high-frequency relaxations with shear mechanical methods as well [16].

This study will investigate the beta relaxation of RTILs since the PSG method makes it possible to measure shear mechanical behavior in this high-frequency region. Dielectric spectroscopy measurements in the same frequency region then makes it possible to further expand the analysis on the beta relaxation, by comparing this dynamic mode across response functions.

Slow relaxations Some liquids display a relaxation mode at lower frequencies than the alpha relaxation, the so-called slow mode. This is a well established feature in polymeric melts where the origin of the slow mode is covalently bonded structures [17]. A slow mode has furthermore recently been shown to be present in systems with supra-molecular structures formed from hydrogen-bonding [18–21].

2.2 Simplicity in glass forming liquids

There is to this day no consensus in the scientific community about what mechanisms govern the viscous slowing down of supercooled liquids and the glass transition itself, despite decades of hard effort. It is a gap in the condensed matter physics knowledge and so the search for an explanation continues. The problem is not to understand that there is a viscous slowing down of liquids and a glass transition, but rather to explain the microscopic mechanisms that drive this process.

One of the ultimate goals in the glass science community would be to obtain a universal theory which can describe and predict the glass transition in all classes of liquids from the van der Waals-bonding liquids to hydrogen-bonding liquids, metallic melts, liquid polymers and ionic liquids. A problem is, however, that to this day there is not even agreement on what the key phenomenology of such a universal theory would be [4].

More recently another approach to tackle this problem has begun to gain increasing attention; the investigation of simplicity instead of universality. This approach shifts the focus from finding and predicting universal behavior in liquids to instead search for features which can be described as "simple". Simple in this regard refers to features in the relaxation spectra which can be described with very few parameters, a sort of "zeroth-order approximation" of the dynamics. Or in other words, a model which is for liquids what the ideal gas law is for gases or the Ising model is for ferromagnetism.

This idea of simplicity was concretized with the formulation of isomorph theory. This theoretical framework predicts that structure, dynamics, and excess entropy are invariant for some liquids and solids along specific curves in the thermodynamic phase diagram. This implies that the phase diagram is essentially one-dimensional with respect to several properties when these are expressed in reduced units [22].

The isomorph theory only predicts this simple behavior for certain liquids where there is a strong correlation between the potential energy and the virial [23]. It is therefore not a universal theory but one that describes simplicity. It has been shown to work in model liquids with van der Waals-like interactions but not in hydrogen-bonding and ionic liquids [4]. Isomorph theory, however, do not predict spectral shapes in relaxation spectra and it does not contain any details on the non-exponential relaxation and non-Arrhenius behavior of glass-forming liquids.

The formulation of isomorph theory then later on inspired another discussion of simplicity in a paper from 2018 by K. Niss and T. Hecksher [4] where, as opposed to isomorph theory, the spectral shape of relaxation in liquids was also taken into account. In this paper it was concluded that glass-forming liquids can be defined as "simple" if they uphold these four requirements for simple behavior:

1. Time-temperature-pressure superposition (TTPS). TTPS is an expansion of the more used time-temperature superposition (TTS) principle. TTS is present

in a liquid if the shape of the relaxation spectrum is constant throughout change in temperature and time/frequency. This is a remarkable feature since the time scale of the alpha relaxation can change many orders of magnitude while the spectral shape stays the same. This feature then becomes even more remarkable if it also applies to change in pressure, thus giving TTPS.

Typically, secondary relaxations have a much weaker temperature dependence than the alpha relaxation and so TTPS will generally only apply to the latter. This means that a truly simple liquid cannot have any discernible secondary relaxations which do not have the same temperature dependence as the alpha relaxation.

2. The spectral shape is identical for different response functions. This criterion refers to the observation that the alpha relaxation in some liquids has the same shape across different response functions. This applies to for example DC704 where the relaxation loss peak is indistinguishable when measured with dielectric and shear mechanical methods.

This constant in spectral shape across different response functions was also shown in two studies from 2017 and 2019 [24, 25] where the random barrier model [26–28] was shown to fall on top of the shear fluidity of the alpha relaxation measured for several different glass-formers. The random barrier model has previously been shown to fit conductivity spectra to a very high degree in several different studies [29–31]. The model only contains two fitting parameters which are not related to the shape but only to shifts in frequency and response function, fluidity or conductivity in this case, and so a fit of data to the random barrier model across measuring methods clearly shows simplicity in the spectral shape.

3. Constant time-scale index is the third criterion for simplicity. A time-scale index is a way to quantify the decoupling between different response functions and it is the logarithm ratio of the alpha relaxation time of two different experimental observables at a given temperature. A constant time-scale index is when there is no temperature dependence, i.e. no decoupling between the alpha relaxation time of different response functions. The time scales can be different, but this difference must be constant with temperature. Such a constant time-scale index is present in for example DC704, 5PPE and hexanetriol [32, 33]. In squalane a decoupling was found as a temperature dependent time-scale index but this could be explained by the influence of a secondary relaxation contribution and not the dynamics of the structural relaxation itself [33].

4. Density scaling is the final criterion for simplicity. Density scaling is when the relaxation time can be expressed as a function of a single scaling variable, $\Gamma(\rho, T) = \rho^\gamma/T$, rather than being an independent function of pressure and temperature [13]. With this scaling variable the alpha relaxation times across different densities will collapse and can thus be described with just this single scaling variable.

Density scaling works well for van der Waals-bonding liquids with the exponent, γ , having values of 3-8 [13, 34] and for some hydrogen-bonding liquids [34] and ionic liquids [34].

These four criteria may not specifically be the correct ones, but it does not change the idea that a model or theory describing and predicting the glass-transition should include the simplest phenomenology found among glass-forming liquids. A phenomenology that is not universal, since the four listed criteria do not apply to all glass-formers, but nonetheless a phenomenology that is so striking it should be a fundamental part of the glass-transition [4]. Deviations from simplicity could then be due to system-specific complications adding to the basic, simple behavior in the glass-transition. This is fundamentally what is meant by a "zeroth-order approximation".

As the paper by K. Niss and T. Hecksher states: *"It may not be realistic to understand all aspects of the dynamics of all glass-forming systems in one universal framework. The first step in understanding the phenomenon could therefore be to understand viscous slowing down and the glass transition in the simplest case."* [4].

This idea of simplicity in glass-forming liquids is frequently used as framework when studying supercooled liquids in the research group Glass and Time at Roskilde University that I am a part of. It was thus natural to expand this specific way of investigating the glass transition to other and more complex classes of liquids than the van der Waals liquids, which has previously been the main focus [4].

Ionic liquids were a natural choice in that this class of liquids is interesting both from a fundamental research point of view and in relation to application in the industry. Furthermore, measuring supercooled ionic liquids is feasible with our current in-house methods.

Simplicity in this study Ionic liquids are molten salts and therefore liquids consisting solely of ions, i.e. positively charged cations and negatively charged anions in order to obtain charge neutrality. The introduction of charges adds a degree of complexity in the structure of these liquids due to competing interactions such as van der Waals forces and Coulomb interactions. This complexity is clearly shown in the x-ray structure factor of this class of liquids, but it remains an open question if the complexity is reflected in the dynamics and therefore if the simplicity criteria listed above apply to ionic liquids.

This study will aim to further fill the gap in the understanding of simplicity by testing some of the above listed criteria on a number of ionic liquids. Specifically, this study will investigate the spectral shape across different response functions, constant time-scale index and test of the shoving model. Hopefully, this increase of knowledge about simplicity can help drive theory development.

Furthermore, the study will also expand the idea of simplicity in the sense that it will investigate if the criteria for simplicity hold across different degrees of structural complexity. This can be viewed as a sort of TTPS principle but

where instead of varying pressure and temperature, the chemical composition is varied. This change in chemical composition has in literature been shown to induce dramatic changes in the structure and so it is interesting to see if this also changes the degree of simplicity in ionic liquids.

The ionic liquids are not expected to display completely simple behavior like DC704, but the main question is how significant the deviation from simple behavior is.

Chapter 3

Experimental techniques

This chapter will go through the different experimental techniques used in this thesis in order to provide the reader with the basic knowledge of the different systems and methods used to investigate the room temperature ionic liquids.

Linear response Linear response theory (LRT) is a way to describe the time dependent response of a system that has been affected by an outer disturbance. The outer disturbance is denoted $x(t)$ and the output of the system is $y(t)$. The connection between the two is linear if the response of the system on two disturbances is equal to the reaction on the sum of the two disturbances, which can happen if the external perturbation of the system is sufficiently small. LRT is very general and can be applied to several different physical systems [35].

Examples of inputs and outputs in experiments are dielectrics with electric field as input and polarization as output with a corresponding compliance and modulus being dielectric susceptibility and electric modulus respectively. For mechanical shear the input is shear stress, output is shear angle and the corresponding compliance and modulus is called shear compliance, $J^*(\omega)$, and shear modulus, $G^*(\omega)$, respectively.

It is in all experimental work in this thesis assumed that the response of the system is linear.

3.1 Dynamic mechanical spectroscopy

This chapter will go through the basic theory of the mechanical properties of liquids used in this thesis before moving on to the experimental techniques used in the following chapter. It will start with the concept behind properties of condensed matter such as stress, strain and viscosity and then move on to more specific theoretical ideas behind viscous liquids used in the analysis of data.

3.1.1 Shear stress and strain

When a solid body is exposed to an outside force it will exhibit a deformation, i.e. a change in the volume and the shape of the body. In the case of pure shear

deformation there is conservation of volume and only the shape changes.

This can be imagined as a solid box of height h where the bottom is stationary and the top is exposed to a force, F , parallel to the upper surface with an area of A . The box will then be deformed a distance of Δx in the direction of the force with an angle of θ . This is illustrated in figure 3.1.

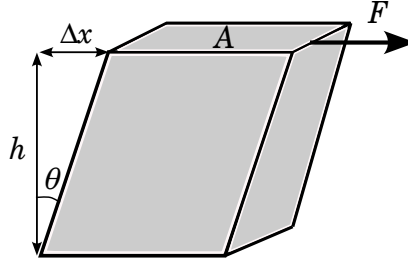


Figure 3.1: An illustration of a shear deformation of a solid box. See text for a further explanation.

The force per area of the surface is called the shear stress, $\sigma = F/A$, and the deformation per height is called the shear strain, $\epsilon = \Delta x/h$. The constant of proportionality between the shear stress and shear strain is called the shear modulus and is denoted as G giving

$$G = \frac{F/A}{\Delta x/h} \quad (3.1.1)$$

The shear modulus is thus a measure of how much a material resists deformation and has the SI unit of pascal (Pa). The shear compliance is given as the inverse of the shear modulus, so that

$$J = 1/G \quad (3.1.2)$$

In a more general case, the stress-strain relation is a generalized Hooke's law

$$\sigma_{ij} = c_{ijkl}\epsilon_{ij} \quad (3.1.3)$$

where σ and ϵ are now tensors and the c is the complete elastic tensor which describes the relation between stress and strain in all directions. In the case of pure shear deformation in an isotropic material the elastic tensor is drastically reduced and equation (3.1.3) becomes [36]

$$\sigma_{ij} = 2G(\epsilon_{ij} - \frac{1}{3}\delta_{ij}\epsilon_{kk}) \quad (3.1.4)$$

3.1.2 Shear viscosity

Shear viscosity can be defined by imagining a system as shown in figure 3.2 where a viscous liquid is placed between two plates of area A separated by y . The lower plate is stationary and the upper plate moves under the action of a force, F , with the relative velocity of v_x . If the liquid is viscous, which almost every liquid is,

then the upper plate will drag the horizontal layer of atoms or molecules just below with it. The friction force of this particle layer will then drag the layer just below it and so on down through the liquid layer. This will create a positive velocity gradient given as $\frac{dv_x(y)}{dy}$.

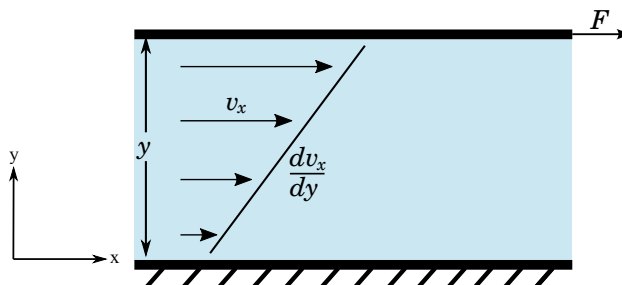


Figure 3.2: A figure illustrating how the velocity gradient in a plane laminar flow is derived. The horizontal arrows show how the velocity is different through the height of the liquid.

The liquid planes will exert a positive shear stress as the force per area on each other and in Newton's law of viscosity this shear stress is simply proportional to the velocity gradient, so that [36]

$$\sigma_{xy} = \eta \frac{dv_x(y)}{dy} \quad (3.1.5)$$

where the constant of proportionality, η , is the shear viscosity.

The strain rate is given as $\dot{\epsilon} = dv_x(y)/dy$ and equation (3.1.5) can then be written as (without subscript)

$$\sigma = \eta \dot{\epsilon} \quad (3.1.6)$$

The unit of viscosity is thus Pa s and liquids which obey this relation between shear stress and shear rate are called Newtonian liquids [37].

3.1.3 Linear viscoelasticity

Some liquids are impossible to characterize with viscosity alone, since the materials also exhibits solid-like properties. These liquids are called viscoelastic and are both able to store energy through elastic deformation and to dissipate energy as heat [37]. The properties of the viscoelastic material, such as a response to a shear deformation, thus becomes complex and frequency dependent.

The Maxwell model

In order to work further with viscoelastic liquids, it is convenient to derive properties based on a basic, mechanical model. The two elements in this model are a spring that represents a Hookean elastic deformation and a dashpot representing a Newtonian viscous flow. The two elements can be placed in series, as seen

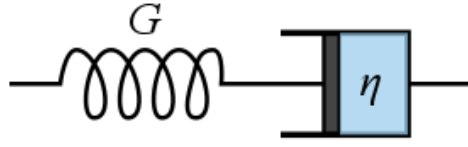


Figure 3.3: An illustration showing the Maxwell element used in the Maxwell model. The spring corresponds to the shear modulus, G , and is connected to a dashpot that corresponds to viscosity, η , thus combining both elastic and viscous behavior.

in figure 3.3, which is called a Maxwell element and simulates a combination of both elastic and viscous behavior.

As a force (or stress) is pulling on the spring, the spring will start to deform thus store energy. At the same time, the piston is also being pulled to the left, causing energy to dissipate through the liquid. If this process happens very fast where the force is rapidly applied and removed again, no dissipation will have time to happen, and the system only has elastic behavior from the spring. The opposite situation, where there is a negligible extension of the spring and a small extension rate, the system only has viscous behavior. Between these two situations the behavior of the system will be a combination of both elastic and viscous.

Newtons law of viscosity will describe the dashpot

$$\sigma = \eta \dot{\epsilon}_N \quad (3.1.7)$$

and the spring is described by Hooke's law of solids;

$$\sigma = G_\infty \epsilon_H \quad (3.1.8)$$

where $\dot{\epsilon}_N$ is the rate of extension of the dashpot and ϵ_H is the extension of the spring. The total rate of extension is

$$\begin{aligned} \dot{\epsilon} &= \dot{\epsilon}_N + \dot{\epsilon}_H \\ \Rightarrow \dot{\epsilon} &= \frac{\sigma}{\eta} + \frac{\dot{\sigma}}{G_\infty} \end{aligned} \quad (3.1.9)$$

This can be rewritten to

$$\begin{aligned} \eta \dot{\epsilon} &= \sigma + \frac{\eta}{G_\infty} \dot{\sigma} \\ \eta \dot{\epsilon} &= \sigma + \tau \dot{\sigma} \end{aligned} \quad (3.1.10)$$

$\tau = \eta/G$ is called the Maxwell relaxation time and has a dimension of time. This differential equation can be solved, e.g. assuming a complex sinusoidal strain on

the form $\epsilon = \epsilon_0 \exp(i\omega t)$

$$\begin{aligned}
 i\omega\eta\epsilon &= \sigma + i\omega\tau\sigma \\
 \Rightarrow i\omega\eta\epsilon &= \sigma(1 + i\omega\tau) \\
 \Rightarrow \frac{\sigma}{\epsilon} &= \frac{i\omega\eta}{1 + i\omega\tau} \\
 \Rightarrow G^*(\omega) &= \frac{i\omega\eta}{1 + i\omega\tau}
 \end{aligned} \tag{3.1.11}$$

where $G^*(\omega) = G(\omega) + iG''(\omega)$. Rationalizing and rewrite gives the real and imaginary parts of $G^*(\omega)$ as

$$G'(\omega) = G_\infty \frac{(\omega\tau)^2}{1 + (\omega\tau)^2} \tag{3.1.12}$$

and

$$G''(\omega) = G_\infty \frac{\omega\tau}{1 + (\omega\tau)^2} \tag{3.1.13}$$

where G_∞ is the shear modulus in the limit as $\omega \rightarrow \infty$. Finally, one have for the real part of the viscosity

$$\eta'(\omega) = \frac{G''(\omega)}{\omega} = \frac{1}{1 + \omega^2\tau^2} \tag{3.1.14}$$

These three equations are plotted in figure 3.4.

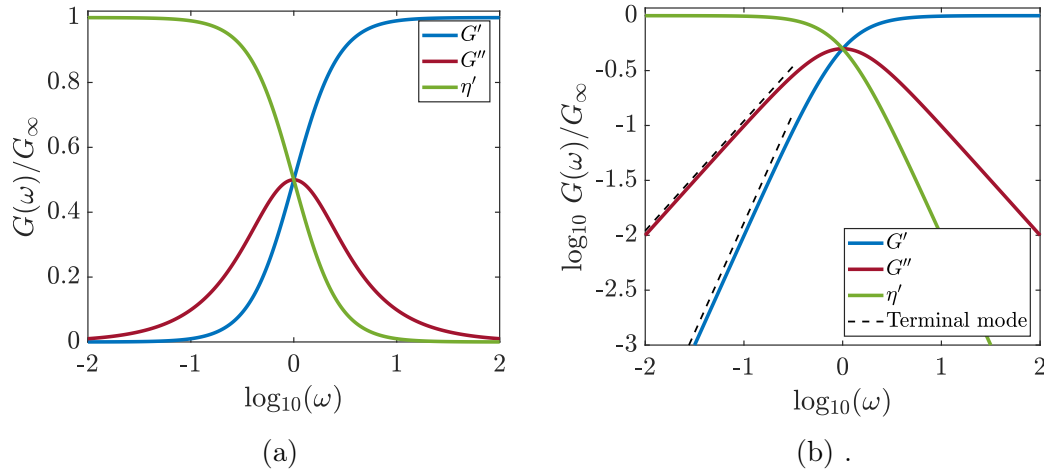


Figure 3.4: A plot showing the solution of an oscillatory response of the Maxwell element normalized to G_∞ . The blue and red line are the real and imaginary part of the elastic modulus, G^* , respectively. The green line is the real part of the viscosity. b) shows the same but in a double logarithmic plot in order to show the power law behavior of the liquid.

$G'(\omega)$ is called the storage modulus and is the ratio of the stress in phase with the strain to the strain. $G''(\omega)$ is called the loss modulus and is the ratio of

stress 90° out of phase with the strain. As seen in figure 3.4, at high frequencies, $G'(\omega)$ is at its maximum ($G'(\omega) = G_\infty$) and $G''(\omega)$ is zero. Here, the liquid has purely elastic behavior and acts as a solid/glass, even though the temperature can be far above T_g . This corresponds to the case where the spring is rapidly extended and relaxed giving the liquid in the dashpot no time to dissipate.

In the low frequency region, the case is the opposite. Here $G'(\omega)$ is equal to zero and $G''(\omega) = \omega\eta$ and the liquid has purely viscous behavior, also called the terminal mode. Here the low frequency region of the real and imaginary part of the shear modulus will have a slope of 2 and 1 respectively. It corresponds to the case where there is a negligible extension of the spring in the Maxwell element.

The Maxwell model of a viscous liquid will give a Debye-like alpha relaxation of the shear modulus which, as was discussed in chapter 2, is not the case for real viscoelastic liquids.

Other models

In real viscoelastic liquids the low-frequency side of the alpha relaxation peak is Debye-like with a slope in the real and imaginary part of 2 and 1 respectively, but the high-frequency side will be stretched. This is due to the relaxation process being described in the time domain with a stretched exponential as was explained in chapter 2.

Instead of describing the relaxation spectrum with a simple Maxwell model, a more realistic function can be used instead. This could be the empirical model called the Cole-Cole function, which is variations of the original Debye model. It is given as

$$G^*(\omega) = G_\infty - \frac{G_\infty}{1 + (i\omega\tau_{CC})^\beta} \quad (3.1.15)$$

where β is the stretching parameter with $0 < \beta < 1$ which leads to a symmetrical broadening of the relaxation function and τ_{CC} is the Cole-Cole relaxation time. The Cole-Cole model is illustrated in figure 3.5a and 3.5b with different stretching parameters. This model does not preserve the low frequency Debye-like behavior with a slope in the real and imaginary part of 2 and 1 respectively.

Instead, another empirical model can be used, namely the Cole-Davidson [38] function which for the shear modulus reads [39]

$$G^*(\omega) = G_\infty - \frac{G_\infty}{(1 + i\omega\tau_{CD})^\gamma} \quad (3.1.16)$$

where γ is the stretching parameter with $0 < \gamma < 1$ which importantly leads to an asymmetric broadening of the relaxation function. See figures 3.5c and 3.5d for an illustration of the Cole-Davidson model. Here the dashed and dashed-dotted line is with a γ of 0.8 and 0.6 respectively. It clearly shows how the stretching parameter smoothens out the edges of G' and the loss peak of G'' . Note that with $\gamma = 1$ the original Debye function is retrieved and that the low-frequency side of the relaxation follow a Debye-like behavior.

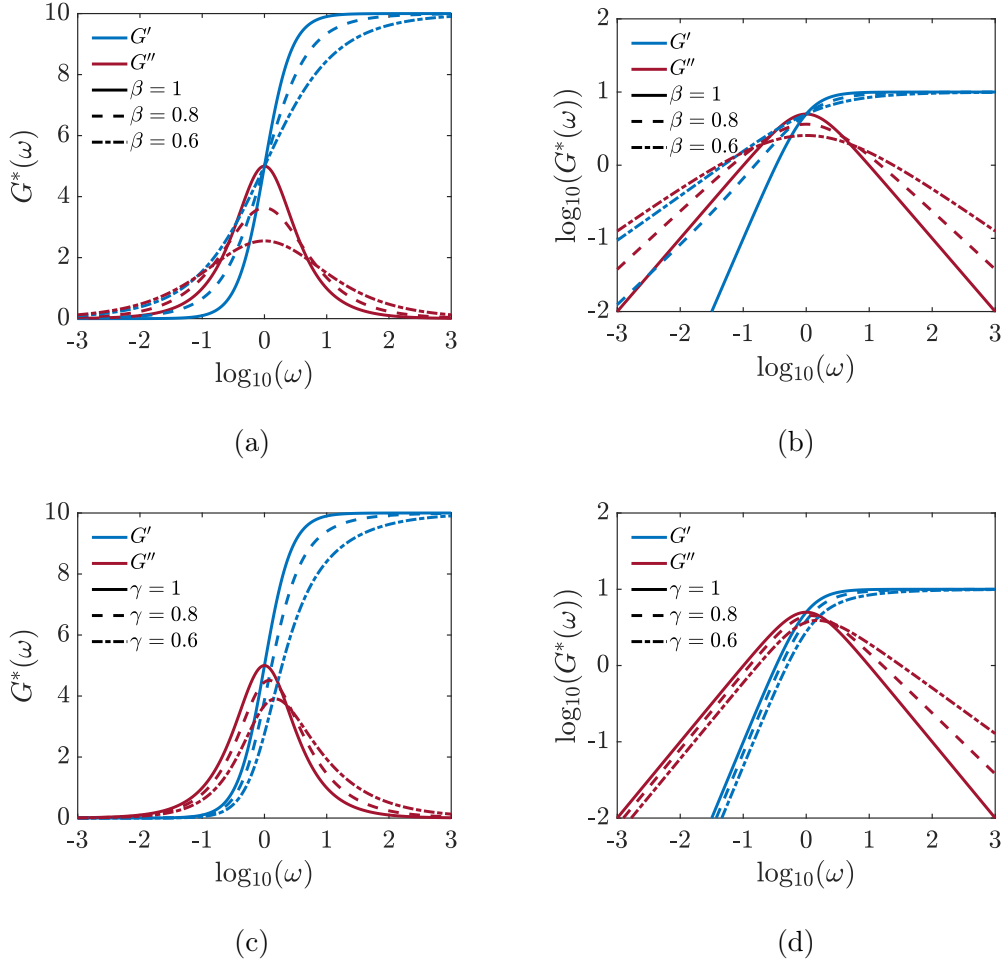


Figure 3.5: An illustration of the Cole-Cole model plotted in a) lin-log and b) log-log plot with stretching parameter, β , given as 1 (solid), 0.8 (dashed) and 0.6 (dashed-dotted). The Cole-Davidson model plotted in a c) lin-log and d) log-log plot with stretching parameter, γ , given as 1 (solid), 0.8 (dashed) and 0.6 (dashed-dotted).

3.1.4 Piezoelectric shear modulus gauge (PSG)

The piezo-electric shear modulus gauge, commonly referred to as the PSG, was developed and refined by T. Christensen and N. B. Olsen at Roskilde University and is thus an in-house developed instrument. This section will be based mainly on the original paper published in Review of Scientific Instruments in 1995 [40].

It was at the time of development a new kind of rheometer designed specifically to measure the shear modulus of very stiff liquids (shear modulus > 1 MPa), e.g. supercooled liquids at the glass transition. With the PSG, it is possible to measure the shear modulus on viscoelastic liquids in the frequency range 1 mHz-50 kHz and in the modulus range of 0.1 MPa-10 GPa, making it a powerful tool when studying dynamic mechanical properties of supercooled liquids.

A schematic of the PSG can be seen in figure 3.6. It consists of three piezo-

electric ceramic disks (PZ-disks) covered with electrodes on the top and the bottom, which let them work as a capacitor. The disks are stacked on top of each other with a separation of 0.5 mm and with an electric connection such that the two outer disks are in series while they are in parallel with the middle disk. This configuration ensures that there is no field in the gap between the disks where the liquid is loaded. The consequence of this is that the liquid will only be affected by a pure mechanical perturbation.

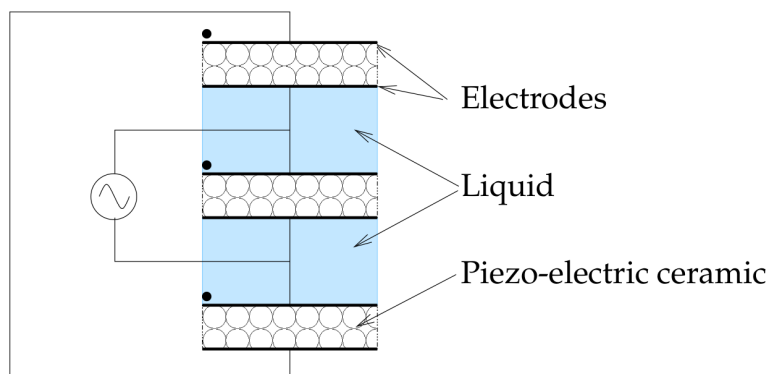


Figure 3.6: A schematic showing the filled PSG transducer from the side. It consists of three parts, 1) the three PZ-disks, 2) the electrodes covering the disks and 3) the liquid (blue) in between. The disks are electrically connected such that the upper and lower disks are in series and the middle disk is in parallel with the two other disks. This way of connecting the three disks ensures that the liquid is field free and will only be affected by a pure mechanical perturbation. The black dots show the direction of polarity of the PZ-disks. From [41].

This perturbation, or strain field, is created by applying a voltage across the PZ-disks. Due to the piezo-electric nature of the disks, the electric signal will be transformed to a radial expansion or contraction depending on the direction of the electric field between the electrodes and the polarity of the piezo-electric ceramic. Since all three disks have polarity in the same direction while the electric field is in the opposite direction for the middle disk the two outer disks will expand/contract opposite to the middle disk. Furthermore, the middle disk will move twice the radial distance compared to the outer disks.

The main principle behind the PSG is that a capacitor that is clamped due to its surface being in contact with a stiff liquid will have a capacitance different from the free capacitor. This difference in capacitance is directly related to the stiffness of the liquid, i.e. the shear modulus. This is clearly illustrated by an example seen in figure 3.7, where the measured capacitance is shown for the empty and filled transducer at both 300 K and 226 K. At 226 K there is a difference in capacitance between the filled and the empty transducer above ~ 100 Hz due to the increased stiffness of the liquid, causing partial clamping of the capacitor.

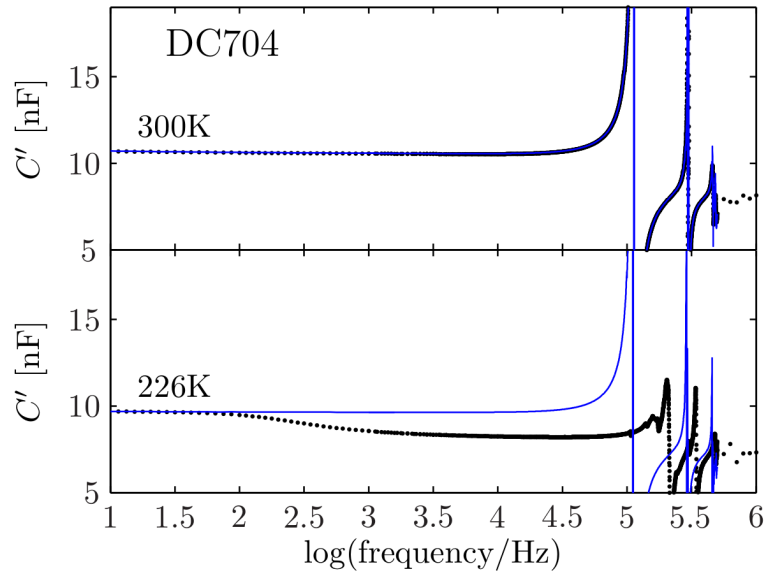


Figure 3.7: A spectrum showing the real part of the capacitance for the empty (blue) and filled (black) PSG at 300 K (top) and 226 K (bottom). At the 226 K there is a clear difference between the empty and full measurements shown as a suppression of capacitance above ~ 100 Hz. This is due to partial clamping of the capacitor caused by the increasingly stiff liquid in between the PZ-disks. From [41].

Mathematical modeling

This section will give an overview of the theory behind the PSG which will show how the measured capacitance is connected to the shear modulus of the liquid. It will mainly be based on the newly published paper on further developments on the PSG [42] and the reader is referred to this paper as well as the original PSG paper [40] for further details.

In order to translate the capacitance, C , of the PSG to shear modulus, G , of the liquid, it is necessary to model the device and find a theoretical expression for the capacitance. Instead of modeling the whole three-disk device, the problem can be significantly simplified by realizing that the radial displacement of the disks creates a plane in the liquid between two disks where all points are motionless when the disks move, i.e. there is no radial displacement of any point belonging to this plane.

As a consequence of this fact the mathematical modeling of the device can be reduced to modeling a virtual one-disk device consisting of a liquid layer in between a PZ-disk at the top and an infinitely rigid support below. This one-disk device will have a liquid layer of $d/3$.

The main relation in this problem is the ratio between the capacitance of the filled and thus clamped PSG, C_{cl} (is the black curve in the bottom panel of figure 3.7) and that of the empty and thus free to move PSG, C_f (the blue curve in the bottom panel of figure 3.7). This ratio can be expressed using the planar

coupling constant, k_p , as

$$\frac{C_{cl}}{C_f} = 1 - k_p^2 \quad (3.1.17)$$

The coupling constant is a material property and for the PZ-disks used here it is equal to 0.56 giving the relation $C_{cl}/C_f = 0.69$.

The special feature of a piezoelectric material is that the stress, σ_{ij} , and strain, ϵ_{ij} tensors besides coupling to each other also couples to the applied electric field, E_i , and the electric displacement field, D_i . If the strain is chosen as input, then these couplings can be reduced to

$$\begin{pmatrix} \sigma_{rr} \\ \sigma_{\phi\phi} \\ D_z \end{pmatrix} = \begin{pmatrix} c_{11} & c_{12} & -e_{13} \\ c_{12} & c_{11} & -e_{13} \\ e_{13} & e_{13} & \epsilon_{33}^s \end{pmatrix} \begin{pmatrix} \epsilon_{rr} \\ \epsilon_{\phi\phi} \\ E_z \end{pmatrix} \quad (3.1.18)$$

where c_{11} and c_{12} are elastic constants, ϵ_{33}^s is a dielectric constant and e_{13} is a piezoelectric constant. r is the radial component, z the component in the axial direction, and ϕ the azimuthal component.

Since the problem to be solved is finding the capacitance of the PZ-disk with a filled PSG transducer, the focus for the following will be on the charge, Q , the potential difference of the electrodes of the PZ-disk, U . This will give a measured capacitance of

$$C_m = \frac{Q}{U} = \frac{\int_0^{R_0} 2\pi r D_z(r) dr}{h E_z} \quad (3.1.19)$$

where R_0 and h is the radius and thickness of the PZ-disk respectively.

This leads to

$$C_m = \frac{2\pi e_{13} R}{h E_z} u_r(R_0) + C_{cl} \quad (3.1.20)$$

where the measured capacitance is now proportional to the radial displacement at the edge of the PZ-disk, $u_r(R_0)$.

To simplify the problem to be solved, the dimensionless capacitance is introduced and defined as

$$F \equiv \frac{C_m - C_{cl}}{C_f - C_{cl}} = \left(\frac{C_m}{C_{cl}} - 1 \right) \frac{1 - k_p^2}{k_p^2} \quad (3.1.21)$$

this will give that

$$F = \frac{1}{E_z R_0 d_{31}} u_r(R_0) \quad (3.1.22)$$

which shows that F is directly given by the measurable quantity C_m . The next step is to find how the radial displacement relates to the shear modulus, G , of the liquid.

This can be done by considering a differential volume element of the PZ-disk and then solving the equations of motions. Due to the shape of the disk it is

convenient to work with cylindrical coordinates and this will, when working in displacement of the volume element, give an equation of motion as

$$c_{11}(r^2 u_r'' + u_r' - u_r) - \frac{\sigma_l}{h} r^2 = -\omega^2 r^2 \rho u_r \quad (3.1.23)$$

where it is assumed that the the time dependence of the fields is proportional to $e^{-i\omega t}$ and that u_r is then the complex amplitude. The prime denotes a derivative to r and ρ is the density of the PZ-disk.

What is now interesting is the parameter σ_l . This is the tangential stress on the PZ-disk created by the liquid layer which will be proportional to the complex shear modulus, G^* , through

$$\sigma_l = \frac{G^* u_r(r)}{d_{ef}} \quad (3.1.24)$$

where d_{ef} is the effective liquid layer in the virtual one-one device which in this case is $d/3$.

Solving the differential equations This can be viewed in a dimensionless picture, which drastically simplifies the problem. Here $x \equiv r/R_0$ and

$$e(x) = \frac{1}{(1+p)d_{13}E_z R_0} u_r(R_0 x) \quad (3.1.25)$$

where p is Poissons' cross-contraction ratio.

This will now give an equation of motion through rewriting equal to

$$x^2 e(x)'' + x e(x)' + \left(\left[\frac{\omega^2 \rho R_0^2}{c_{11}} - \frac{G^* R_0^2}{c_{11} d_{ef} h} \right] x^2 - 1 \right) e(x) = 0 \quad (3.1.26)$$

Furthermore, two characteristic parameters are introduced: The characteristic shear modulus

$$G_c \equiv \frac{c_{11} d_{ef} h}{R_0^2} \quad (3.1.27)$$

and the characteristic frequency

$$\omega_c^2 \equiv \frac{c_{11}}{\rho R_0^2} \quad (3.1.28)$$

then

$$x^2 e(x)'' + x e(x)' + \left(\left[\frac{\omega^2}{\omega_c^2} - \frac{G^*}{G_c} \right] x^2 - 1 \right) e(x) = 0 \quad (3.1.29)$$

then it is clear that the frequency and the complex shear modulus is connected through the wave vector k as

$$k^2 = \left(\frac{\omega}{\omega_c} \right)^2 - \frac{G^*}{G_c} \quad (3.1.30)$$

If then

$$S \equiv \left(\frac{\omega}{\omega_c} \right)^2, \quad V \equiv \frac{G(\omega)}{G_c} \quad \text{and} \quad k^2 \equiv S - V \quad (3.1.31)$$

equation 3.1.29 can be rewritten to

$$x^2 e''(x) + x e(x) + (k^2 x^2 - 1)e(x) = 0 \quad (3.1.32)$$

which is recognized as a Bessel differential equation [43] on the form

$$x^2 y'' + x y' + (x^2 - \nu^2)y = 0 \quad (3.1.33)$$

with $\nu = 1$ and the general solution as a first order Bessel function, with $y = e(x)$, as

$$e(x) = A J_1(kx) + B Y_1(kx) \quad (3.1.34)$$

The coefficients A and B can be determined from the boundary conditions, but this will not be shown here. Remember that equation (3.1.22) tells that the dimensionless capacitance, F , is related to $e(x)$ as $F = (1 + p)e(1)$ and that the dimensionless capacitance, F , is again directly linked to the measured capacitance.

The solution to Bessel equation (3.1.32) is

$$e(x) = \frac{J_1(kx)}{kJ_0(kx) + (p - 1)J_1(kx)} \quad (3.1.35)$$

so that

$$F(k) = (1 + p) \frac{J_1(k)}{kJ_0(k) + (p - 1)J_1(k)} \quad (3.1.36)$$

giving a full expression for the measured capacitance as

$$C_m(\omega) = C_{cl} \left(F(S, V) \frac{k_p^2}{1 - k_p^2} + 1 \right) \quad (3.1.37)$$

Here it is now seen how the measured capacitance is related to the shear modulus $G(\omega)$ through the wave vector k . This means that finding $G(\omega)$ can be done by inverting $F(k)$. It should be noted that $F(k)$ has singularities and therefore resonances when the denominator in equation (3.1.36) is equal to zero, i.e. when

$$0 = k_n J_0(k_n) + (p - 1)J_1(k_n) \quad (3.1.38)$$

for $k = k_n$, $n = 1, 2, \dots$. This is a particularly important property since it can determine the characteristic frequency needed for the inversion of the capacitance.

Further considerations The resulting equations for the three disk PSG device is the simplest case where it is assumed that the capacitor is completely and perfectly filled. In reality this will not be the case both because it can be technically difficult to fill the capacitor perfectly, but also since cooling of the liquid will cause it to contract due to the thermal expansion coefficient and move away from the edges. In the original paper this was considered among other things as a change in the boundary conditions of the differential equations.

Another consideration is that there is a hub in the center of the device which will introduce a new boundary condition as the relative radius $x_h = r_h/R$ where r_h and R are the radius of the hub and the PZ disk respectively. This will again alter the boundary conditions and thus the solution to the differential equations. A further complication is that the elasticity of this hub also needs to be considered.

A further explanation of these extra considerations and how it effects the solution to the differential equations is out of scope with this thesis, but they were implemented in the inversion of the capacitance.

Frequency dependence of the piezoceramics An especially important property of the piezoceramic disk to consider is that they have a weak frequency dependence in the dielectric constant meaning that $C_f = C_f(\omega)$ and $C_{cl} = C_{cl}(\omega)$. This problem can be worked around by assuming that their ratio and thus the coupling constant, k_p , is frequency independent since it is known that $\frac{C_{cl}}{C_f} = 1 - k_p$. This means that the effect of the frequency dependence can be scaled out by taking the ratio of the empty or reference spectra with the liquid spectra.

Thermal relaxation Another property to consider is the inevitable temperature dispersion of the PZ-disks. As the temperature is changed the piezoceramic disks will relax in order to reach the new equilibrium state. This relaxation can however take days and so it is not practically possible to wait until equilibrium is reached. Instead, one must wait just long enough after each temperature shift to be able to assume that the capacitance is constant during the frequency scan at that temperature.

That this assumption is being met can be ensured by performing two subsequent measurements at the given temperature. If the spectra of the two repeating measurements are constant, then the waiting time after the temperature shift was sufficient.

Inversion of capacitance

There are four unknown parameters in order to have a complete expression for $F(k)$ and thus $G(\omega)$ which are ω_c , G_c , p and k_p . ω_c can be found by measuring the first resonance frequency, since $\omega_c = \omega_1/k_1$, where k_1 is found from a numerical solution to equation (3.1.38). This will yield the characteristic modulus, since $G_c = \omega_c^2 M_c$, where M_c is a constant consisting of material and geometrical constants.

$p = 0.31$ and is found from numerical calculations of the resonance frequencies and k_p is found from fitting the capacitance of the empty transducer, which will be explained further in the following.

To get the exact value for the resonance frequency, ω_1 , the capacitance spectrum measured linearly around the resonance frequency on an empty transducer needs to be fitted to the expression for measured capacitance, equation (3.1.36), since the resonance frequency itself cannot be measured.

See figure 3.7 for an example of such a spectrum around the first resonance. In practice, the region just around the resonance frequency is then cut out of the data set before the fitting routine, after being normalized to the low frequency limit of the spectrum.

In the fitting routine there are six parameters: 1) Constant capacitance to the left of the resonance, 2) k_p from the relation $C_{cl}/C_f = 1 - k_p^2$, 3) characteristic frequency, $f_c = \omega_c/2\pi$, 4) the radius of the hub, r_h , 5) a quality factor, Q_{pz} compensating for the dissipation of the PZ disk and 6) the radius of the liquid layer, r_c , respectively. In the linear fit, the first three are free and the rest are fixed, since they are constants.

The Newton-Raphson method With these by fitting found parameters the capacitance spectrum is ready to be inverted to shear modulus and this can be done using the Newton-Raphson algorithm [44]. This specific method works by finding the shear modulus, G_0 , that fits the measured capacitance, F_m , in order to reach $F_m = F(G_0)$ where G_0 is the limit of the iterations of trial functions $G_{t,n}$.

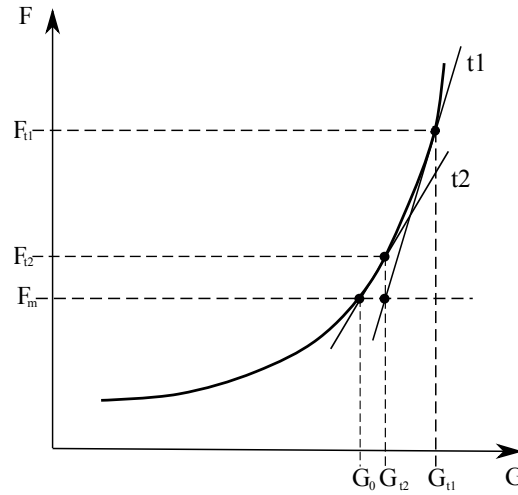


Figure 3.8: A graph illustrating an example of finding the true value, G_0 , by the method of the Newton-Raphson algorithm. Here with two iterations, t_1 and t_2 .

Based on figure 3.8 an expression for this iterative method can be deduced. A function, F of G , has a measured value F_m but an unknown corresponding G_0 . A Taylor expansion of the function to first order around the starting guess, G_{t1} , will yield

$$F_m - F_{t1} = F'(G_{t1})(G_{t2} - G_{t1}) \quad (3.1.39)$$

This defines the value of G_{t2} with the corresponding point $F(G_{t2})$, as is also illustrated in figure 3.8. The knowns of equation 3.1.39 are now F_m , G_{t1} and F_{t1} . With numerical differentiation it is possible to find the expression for $F'(G_{t1})$ as

$$F'(G_{t1}) = \frac{F((1 + \delta)G_{t1}) - F(G_{t1})}{(1 + \delta)G_{t1} - G_{t1}} \quad (3.1.40)$$

This leaves the unknown of equation (3.1.39) to be

$$G_{t2} = \frac{1}{F'(G_{t1})}(F_m - F_{t1}) + G_{t1} \quad (3.1.41)$$

Rearranging this and rewrite it to a general, iterative form will give

$$G_{t,n+1} = G_{t,n} \left(1 + \delta \frac{F_m - F(G_{t,n})}{F((1 + \delta)G_{t,n}) - F(G_{t,n})} \right) \quad (3.1.42)$$

Through iteration, the algorithm then makes small steps of δ in order to differentiate F and change $G_{t,n}$ until it finally fits F_m . δ is a small number, around 0.01, which sets the step size of the numerical differentiation of F .

In eq. (3.1.42) there are three different functions: 1) $G_{t,n}$ is the trial function, 2) is F_m which is the measured capacitance and 3) $F(G_{t,n})$ is the theoretical capacitance as a function of G which, in this case, is the trial function to be changed through iterations. The algorithm is fulfilled when the guess for G ensures that $F(G)$ matches F_m , i.e. $F_m = F(G_0)$.

The final piece of this inversion method is then to find an initial fitting trial function for the Newton-Raphson algorithm. This function needs to be sufficiently close to the real G_0 since otherwise, the iteration algorithm will diverge. In this case the expression

$$G_{t1} = G_c \left[\left(\frac{f}{f_c} \right)^2 + k_1^2 \frac{1 - F_1}{F_1} \right] \quad (3.1.43)$$

is a good choice, see M. Mikkelsen et al. for more details [42] and here $F_1 = F_m$. The inversion algorithm was tested on the Maxwell model showing excellent agreement below the first resonance frequency and so it is the chosen method of inversion for all PSG data in this work.

The 1-disk PSG

A new version of the classic three-disk PSG was used in the shear mechanical measurements of the RTILs in this work. This is the so-called 1-disk since the two outer PZ-disks have been replaced by rigid supports in the form of sapphire disks and so only the middle PZ-disk remains. The two sample liquid layers of thickness d is thus sandwiched in between the sapphire disks and the PZ-disk.

This section will be an overview of how the 1-disk differs from the original 3-disk and will be based on a paper by M. Mikkelsen et al. published in Journal of Rheology, 66, 2022 with me as a co-author [42].

A schematic overview of the 1-disk PSG can be seen in figure 3.9. An AC voltage source is connecting the two electrode surfaces of the PZ-disk. Here the field outside the capacitor is zero everywhere except for a small field at the edge which will be negligible due to the high dielectric permittivity of the PZ ceramic material. A consequence of this is that, just as with the 3-disk PSG, the dielectric properties of the sample do not contribute to the signal.

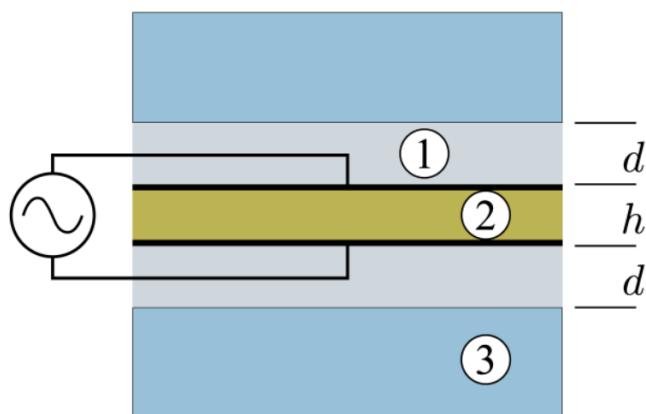


Figure 3.9: A schematic of the 1-disk PSG with the two layers of sample liquid (1) of thickness d in between two sapphire disks (3) and a PZ-disk (2) of thickness h . The PZ-disk has silver on the surface which forms the electrodes of the capacitor. There is an AC voltage source connecting the two electrode surfaces. From [42].

An advantage of using the 1-disk PSG instead of the 3-disk version is that it reduces the risk of getting excess liquid in the edge of a PZ-disk since there is only one of them. In the case of conducting liquids, e.g. the ionic liquids used in this work, excess liquid on the edge of the PZ-disk can short circuit the whole device and the resulting measurements will be disrupted by a huge conductivity contribution.

An key point from the paper is that even though the 1-disk PSG should give the exact same results as that of the 3-disk PSG, there is a small shift of the spectra to higher frequencies which increases slightly with decreasing temperature. This can be explained by the fact that upon cooling the liquid contracts radially towards the center of the disks. This flow will however be gradually hindered by the increase in viscosity until the liquid can no longer flow in that direction. When this happens, the liquid will start to contract in the z -direction, i.e. downwards. This contraction will bend the upper PZ-disk allowing the liquid to continuously adjusting the volume with the increasing in contraction creating isobaric conditions.

This cannot happen in the 1-disk PSG since the upper disk is made of stiff sapphire that cannot be bent by the liquid. The pressure in the liquid will thus change creating isochoric conditions which gives a relaxation time faster than under isobaric conditions. The isobaric conditions of the 3-disk PSG and thus the time scales of the relaxation can be recreated by introducing a small and soft kapton spacers between the hub and the sapphire disks in the 1-disk PSG which will then allow for axial contraction.

Unfortunately, this was discovered at a time when several liquids had already been measured for this thesis. Thus, consideration to the comparability between repeated measurements and measurements on different liquids meant that kapton spacers were not introduced in the setup. Therefore, all conclusions made from results measured with the 1-disk PSG in this thesis must be made within the

uncertainty created by the shift in frequency. Fortunately, this shift is tiny in relation to the overall change in the alpha relaxation time.

Mapping onto the virtual 1-disk device The basis of the theoretical modeling of the 3-disk device was that a virtual 1-disk device, called the one-one device, with a liquid layer of $(1/3)d$ and an infinitely rigid support could be constructed. For the theory to apply for the 1-disk device as well, it needs to be mapped onto this mathematical model.

The argument that it can be mapped to the mathematical one-one device is simple. The 1-disk has an actual rigid support in the form of the sapphire disks and so, the one-one device can be used in the modeling of the 1-disk PSG if these disks are assumed to be infinitely rigid. This holds if they are much more rigid than the liquid layer which is assumed to be the case in this study. Thus the theory from subsection 3.1.4 and 3.1.4 still applies with the exception that the effective sample layer is $d/2$ instead of $d/3$.

3.1.5 Parallel plate rheology

Parallel plate rheology was one of the techniques used to determine the shear modulus of some of the liquids in this study. Two instruments related to this technique was used; TA instruments DHR2 and an Anton Paar MCR 502 with EVU 20. The first is located at RUC and the second is located at Dortmund Technical University.

The basic idea behind is quite simple; a lower and an upper vertical rod of a given diameter (also known as plate size) can contain the liquid to be studied in a small gap between them so that the rods are only connected through this liquid. The upper or the lower shaft will then be rotated at small angles with a given angle while the instrument simultaneously measures the torque required to rotate the rod this angle. The relationship between the torque and displacement is then enough to calculate the shear mechanical properties needed to further analyze the sample; e.g. shear modulus.

The two parallel plate rheometers used also have temperature control enabling one to measure the temperature dependence of the shear rheology properties, which is crucial in the study of glass forming liquids.

Calculating shear modulus

The only non-zero component of the stress tensor is $\sigma_{z\theta}$ which gives the stress-strain response as seen in figure 3.10a. Here Ω is the motor angular velocity giving a velocity of Ωr at radius r on the upper disk, where at the lower plate, the velocity equals to zero. In the case of the parallel plate geometry the shear, ϵ , and shear rate, $\dot{\epsilon}$, vary linearly with the radial coordinate, r , as

$$\epsilon = \frac{\theta r}{h} \text{ and } \dot{\epsilon} = \frac{\Omega r}{h} \quad (3.1.44)$$

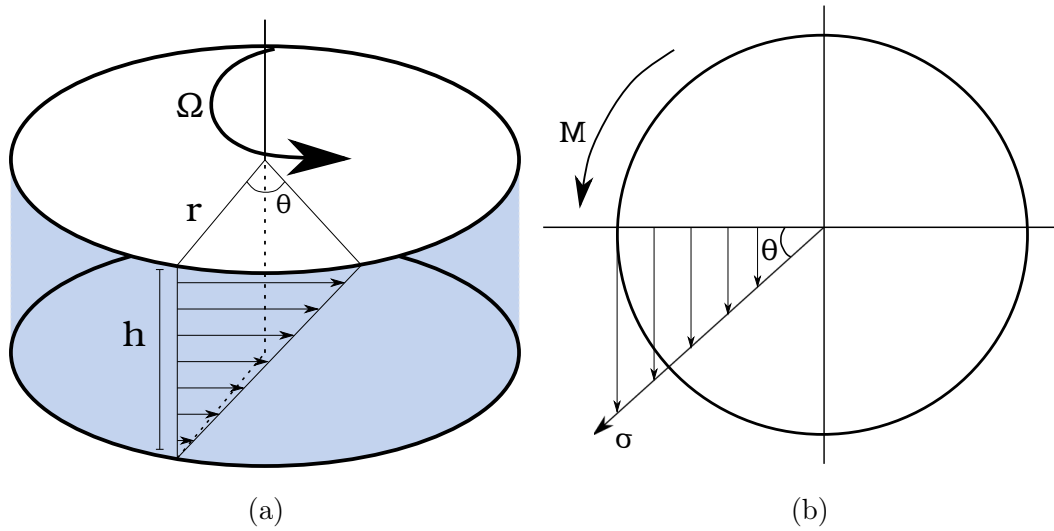


Figure 3.10: a) A schematic showing the filled parallel plate rheometer viewed from the side, when the upper plate has moved with an angle of θ counter clockwise. The arrows depict the difference in displacement and thus shear stress over the radius of the disk. b) The top plate viewed from the top. The large arrow is the direction of the torque, M , moving the plate to a displacement, θ . The arrow, σ , shows the shear stress through a cross section of the cylinder.

where θ is the angular displacement of the upper plate. This and the following applies only when it is assumed that there is a non-slip boundary condition, i.e. the liquid sticks to the plates at all times. At the rim, with $r = R$, the strain and strain rate is

$$\epsilon = \frac{\theta R}{h} \text{ and } \dot{\epsilon} = \frac{V}{h} \Rightarrow \dot{\epsilon} = \frac{\Omega R}{h} \quad (3.1.45)$$

where V and Ω is the general and angular velocity respectively. What happens when the upper plate rotates and the lower plate is stationary is a torsion of the liquid with a torsional moment, or torque, M , as well as a shear stress throughout the liquid as illustrated in figure 3.10b. This can be viewed as a torsion of a shaft where

$$\sigma = \frac{Mr}{J} \Rightarrow M = \frac{\sigma J}{r} \quad (3.1.46)$$

where J is the polar moment of inertia or the polar moment of area. In general, J can be calculated as the radius squared evaluated over the cross-sectional area, so that

$$J = \int_A r^2 d\mathbf{A} \quad (3.1.47)$$

This will give the expression for the torque as

$$M = \int_A \frac{1}{r} \sigma r^2 d\mathbf{A} = \int_A r \sigma d\mathbf{A} \quad (3.1.48)$$

which due to the cylindrical shape of the shaft can be expressed in polar coordinates as

$$M = \int_0^R \int_0^{2\pi} r \sigma r d\theta dr = \int_0^R r \sigma 2\pi r dr \quad (3.1.49)$$

If the liquid behaves as a Newtonian liquid, it can then be assumed that σ is linearly dependent on r throughout the sample along r , which makes it possible to define a constant, C , as $C = \sigma r$. This gives

$$M = \int_0^R r C r 2\pi r dr \quad (3.1.50)$$

This will give a total torque evaluated at the rim of the parallel plates as

$$M = 2\pi C \int_0^R r^3 dr = 2\pi C \frac{R^4}{4} = \frac{\pi C R^4}{2} \quad (3.1.51)$$

inserting $C = \sigma_r/R$, where σ_r is the shear stress at the rim of the plates, will give

$$M = \frac{\pi R^3}{2} \sigma_r \Rightarrow \sigma_r = \frac{2}{\pi R^3} M \quad (3.1.52)$$

The shear modulus at the rim of the plates is then given by

$$G = \frac{\sigma_r}{\epsilon_r} = \frac{2}{\pi R^3} \frac{M}{\epsilon_r} = \frac{2h}{\pi R^4} \frac{M}{\theta} \quad (3.1.53)$$

and the viscosity by

$$\eta_r = \frac{\sigma_r}{\dot{\epsilon}_r} = \frac{2hM}{\pi R^4 \Omega} \quad (3.1.54)$$

Finding the right parameters

When performing a frequency scan of the shear modulus, it is important to stay in the linear regime so that the equations from the above section apply. Otherwise one is dealing with non-linear rheology which is another matter entirely. A requirement for the linear regime is that the shear modulus must be independent of the size of the strain/displacement applied during the experiment.

This must be checked with a measurement of the shear modulus, where the strain is varied over several decades at a constant frequency. See figure 3.11a. Here strain percentage is used, which is just the strain times a hundred.

The figure shows that the shear modulus is constant as the strain is increased over several decades until the system reaches non-linearity when the $\gamma\%$ is almost equal to 1. Note that the strain here is denoted as γ . The slightly wobbly behavior with low strain is noise since at these values we are close to the instrument limit. Furthermore, as long as the $\gamma\%$ is within 0.01-0.4 when at 10 Hz the system is within the linear regime. This will however only be correct at 10 Hz since the linear regime shifts with frequency/temperature.

With increasing frequencies, the beginning of non-linearity will shift to lower strain and vice versa with decreasing frequency. This also means that the linear

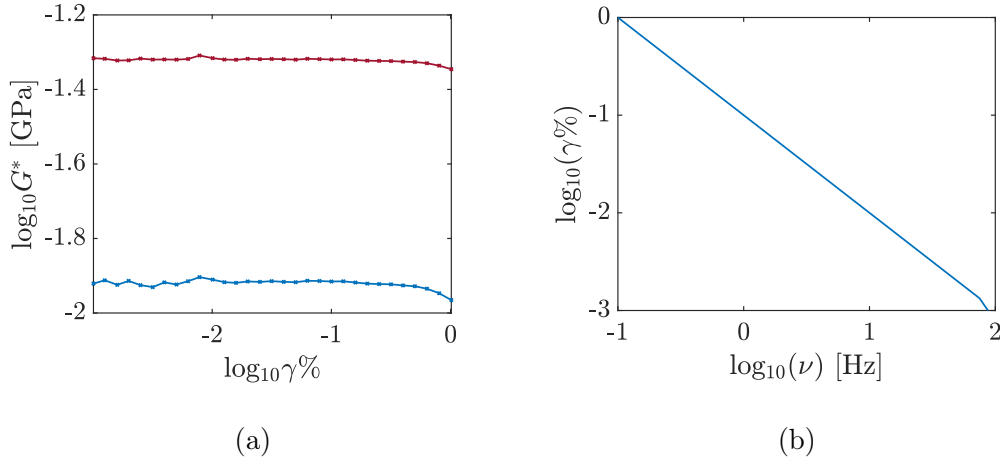


Figure 3.11: a) A plot showing the complex shear modulus of molecular liquid DC704 as a function of $\gamma\%$ at 10 Hz. Blue and red is the real and imaginary part respectively. It is seen how the shear modulus is constant with increasing strain up until the system becomes non-linear just before $\gamma\% = 1$. b) The logarithm of the strain percentage as a function of the logarithm of the frequency showing the relation between the two.

regime is highly dependent on the value of the shear modulus, since this changes with frequency. In practice this has the consequence that staying in the linear regime during a frequency scan where the shear modulus can change with several orders of magnitude can be quite challenging and will depend on the chosen geometry of the plates and strain range. The following is an analysis of how to systematically find the right parameters in order to stay in the linear regime as the frequency/temperature changes.

The equation for the shear modulus, equation (3.1.53), shows the relationship between the parameters M , R , γ_r and θ . Where G is an intrinsic property of the liquid, the other parameters are connected to the instrument and the geometry of the plates. In a strain controlled experiment, the two parameters that can be varied are the radius of the plates, R , and the strain, γ_r , or in this case the strain percentage, $\gamma\%$. Since the frequency varies logarithmically, the first thing to notice is that the strain should also vary logarithmically, but with opposite sign. This is due to the fact that with increasing frequency the start of the non-linear regime moves to decreasing strain values. An example of this can be seen in figure 3.11b, where both frequency and $\gamma\%$ varies over three decades.

The start and end values for the strain can be found by looking at the ratio between the shear modulus at high and low frequencies. If the radius is kept constant through the frequency scan, the ratio between the high and low shear modulus, G_1 and G_2 with corresponding strain γ_1 and γ_2 will be

$$\frac{G_1}{G_2} = \frac{2M}{\pi R^3 \gamma_1} \frac{\pi R^3 \gamma_2}{2M} = \frac{\gamma_2}{\gamma_1} \quad (3.1.55)$$

As an example, let a strain that is in the linear regime when $G_1 = 1\text{GPa}$ be

equal to 0.008 $\gamma\%$. Then, if $G_2 = 0.01$ GPa, the corresponding correct strain to use would be

$$\frac{G_1}{G_2} = \frac{\gamma_2}{\gamma_1} = 100 \Rightarrow \gamma_2 = 100\gamma_1 = 100 \cdot 0.008 = 0.8 \quad (3.1.56)$$

The result is not surprising, and the method is a good way to estimate the needed start and end values in the strain controlled experiment. However, a problem arises if the variation in shear modulus becomes so large that the corresponding strain becomes too small or too large. E.g. if $G_1 = 1.2$ GPa at 100 Hz and $G_2 = 6 \cdot 10^{-6}$ GPa at 0.005 Hz, then the minimum start strain at 100 Hz is around $\gamma_1 = 0.005$, which is the instrument limit. The corresponding strain at 0.01 Hz will then be $\gamma_1 = 1000$ which will be too high, since strains at this level could violate the non-slip assumption. A direct consequence of this is that it will not be possible to measure over this wide range of frequencies in this example.

Traditionally the way around this problem is to change temperature which will shift the shear modulus curve accordingly, so that another part of the curve is in the experimental window. The time-temperature superposition principle can then be applied to create the full shear modulus curve. However, this method only applies to cases where the shape of the curve is temperature independent which in many cases is not true. This is the reason why, in this thesis, the shear modulus will be combined with measurements performed with the piezoelectric shear modulus gauge (PSG) so that full curves at each temperature will be measured giving the temperature dependence of the shear modulus.

A consequence of this is that the shear modulus will have to be measured with the parallel plate rheometer over a very wide range of moduli and frequencies, which as just explained poses a problem. The solution to this could be to change another parameter besides the strain. A look at equation (3.1.53) shows that an obvious suggestion is the radius of the plates, since even a small change in radius will create a large difference due to the cubic term. Take the example from before with $G_1 = 1.2$ GPa with $\gamma_1 = 5 \cdot 10^{-3}$ and $G_2 = 6 \cdot 10^{-6}$ GPa. This resulted in a strain of $\gamma_2 = 1000$. However, if the radius can be varied then

$$\frac{G_1}{G_2} = \frac{R_2^3 \gamma_2}{R_1^3 \gamma_1} = 2 \cdot 10^5 \quad (3.1.57)$$

If e.g. the start radius, R_1 , is 2mm and the end radius, R_2 , is 12mm, then

$$\gamma_2 = \frac{2 \cdot 10^5 \gamma_1 R_1^3}{R_2^3} = 4.6\gamma\% \quad (3.1.58)$$

at 10^{-3} Hz, which is a very reasonable strain.

Challenges with the rheometer

This section will describe some of the challenges encountered during the work with the conventional rheometer at RUC and Dortmund for this thesis. This is because even though the principle behind the method is simple and straight

forward, technical challenges can make it difficult to obtain trustworthy and reproducible results.

In principle the PPR can measure very small values of shear modulus, since the instrument limits allow for the measurement of very small displacement and forces. Values as small as down to 1 Pa in shear modulus have been measured on ionic liquids in for example a study in 2011 by N. V. Pogodina et al. [45]. By going this low in modulus it will be possible to measure and discern low frequency relaxation signals as for example sub-alpha relaxational modes.

Therefore, the method was implemented in this work to combine with shear modulus data measured by the PSG which, as mentioned in the above sections, can only measure accurately at much higher moduli. A combination of the two methods would therefore give very accurate data over a broad range of frequencies and moduli. But in practice it turned out to not be so easy to go down in modulus and get high quality data.

Reproducibility In order to get a sense of the instrument and to test how far down in modulus it was possible to measure, test measurements were performed on the molecular liquids 5PPE, DC704 and squalane. These three liquids are easy to supercool and in the case of 5PPE and DC704 do not have any known secondary slow or fast relaxations. This detail was important since it makes it possible to follow the terminal mode down in modulus and thus make sure that the data are still trustworthy.

This is not always the case since systematic errors can make the data deviate from the terminal mode. An example of this can be seen in figure 3.12a where a difference in strain rate gives quite different results of the low frequency flank of the alpha relaxation in Pyr18-TFSI. This is most clearly seen in the real part of the modulus.

The first step was to test reproducibility between the PPR and the PSG. This was done at first with all three molecular liquids (5PPE, DC704 and squalane). Some examples of results for 5PPE, DC704 and squalane can be seen in figure 3.12. Here we see that for 5PPE and DC704 it was possible to reproduce PSG results with the PPR and even go further down in modulus. That was especially true for the 5PPE data where the PPR can measure two decades further down in modulus. This way of combining PSG and PPR data was also utilized in literature with success [18].

The reproducibility on the PPR itself was also good. For squalane, however, there was less success in both the reproducibility and quality of the data, also reproducibility on the PPR itself. The reason for this difference was not clear, but perhaps it had something to do with the lower temperature that squalane was measured at. The origin of this reasoning is that it was discovered that at low temperatures ice formed on the surface of the rods and the liquid layer connecting the rods through this ice layer. This was despite the fact that there is a high flow of dry and cold nitrogen in the sample environment, but still water somehow managed to enter and freeze on the rods and the liquid layer.

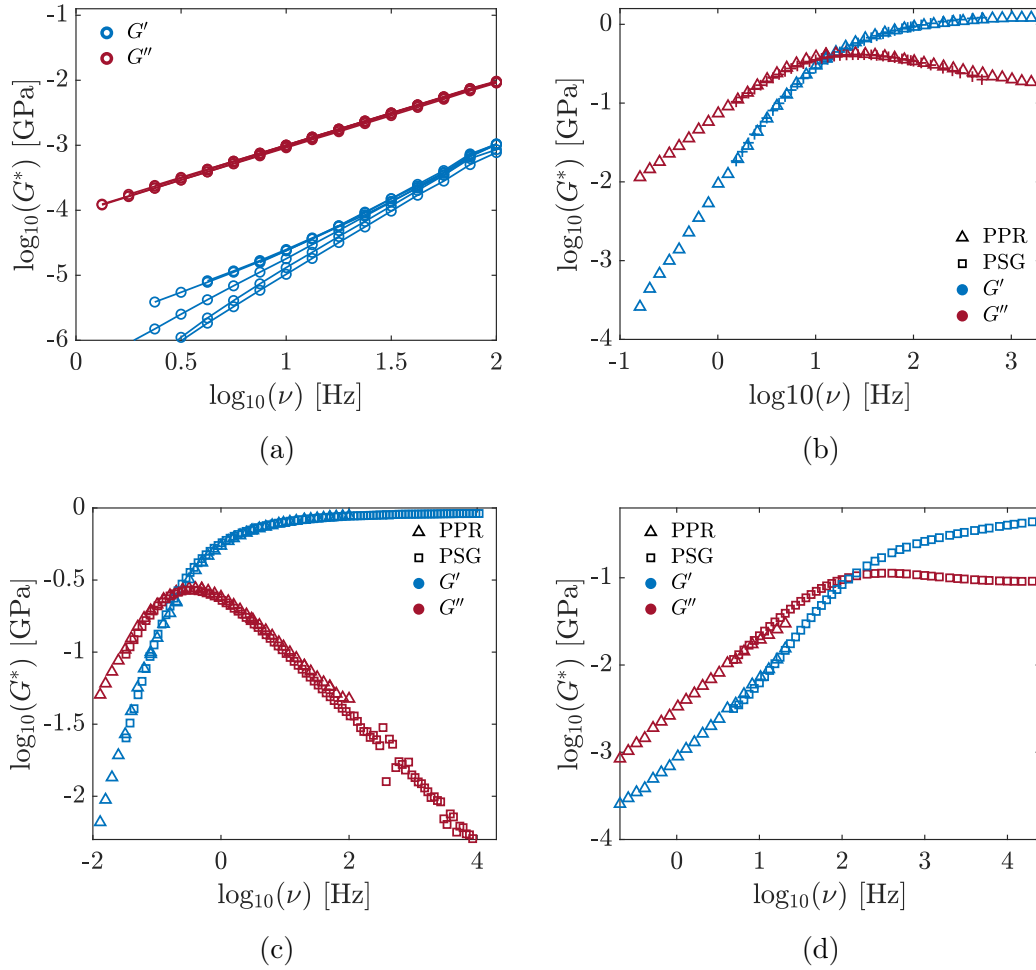


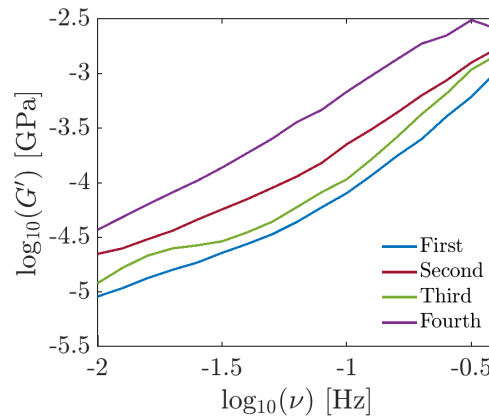
Figure 3.12: a) Real and imaginary part of the shear modulus for Pyr18-TFSI measured with a PPR at 210 K. The difference between the data sets is the strain rate showing that the results clearly depend on the chosen strain rate. b) Shear modulus for 5PPE measured with the PPR and PSG (PSG data taken by Tina Hecksher and borrowed with permission) showing good reproducibility and that the PPR results go around 2 decades further down in modulus. c) Shear modulus for DC704 at 210 K measured with PPR and PSG also showing good reproducibility. d) Shear modulus for squalane at 178 K measured with the PPR and PSG (PSG data taken by Tina Hecksher) showing that for this liquid both reproducibility and quality of the PPR data were low.

RTIL Measurements on RTIL with the PPR at RUC was also challenged with low reproducibility where an example is shown in figure 3.13a. Here four identical test measurements were performed in quick succession with very different resulting shear modulus. The measurements do show a low modulus that could be the cause of errors, but it would not explain the large discrepancy between the repeating measurements.

To support this statement figure 3.12a show a low degree of reproducibility

at low moduli for Pyr18-TFSI (measurements performed at DTU), but in this case all the curves collapse at higher moduli and then gradually start to deviate from one another as opposed to figure 3.13a where all curves are different at all frequencies. Note that both figures show modulus curves over 1.5 decades in frequency.

The reason behind the low degree of reproducibility could be the before mentioned ice formation on the sides of the rod and the liquid layer, but it could also be due to crystallization of the sample, since some of the RTIL are very prone to cold-crystallization.



(a)

5

Figure 3.13: a) Real part of the shear modulus for Pyr14-TFSI measured with the PPR for repeated measurements with identical instrument settings. It shows a low degree of reproducibility.

Unfortunately, it was not within the time scope of this project to work out the technical difficulties related to reproducibility in the measurements performed on RTIL with the PPR. However, it was possible to get more trustworthy and usable results at DTU with the rheometer that they have there. This made it possible to combine PPR and PSG results, extending the shear modulus curve further down in modulus and frequency.

The difference between measuring at our in-house PPR and at the one used at DTU was three-fold. Firstly, the cooling system at DTU made sure that the sample environment was significantly drier, and so no ice was forming on the surface of the rods and the liquid. Secondly, there was a transparent window installed in the instrument at DTU making it possible to visually inspect if the sample has crystallized or not, which happened often.

Thirdly, it was possible with a customized add on to the instrument software for the DTU instrument to change the strain percentage logarithmically over the logarithmically changing frequency in one frequency scan. So, if one were to measure from 0.1Hz \rightarrow 100Hz at a given temperature the instrument could also change the strain percentage logarithmically going from 10 γ % \rightarrow 0.1 γ % during that scan. This was very useful since the same strain rate cannot be used

throughout several decades of frequencies, as was also discussed in a previous section.

In conclusion it can be said that measuring the complex shear modulus of supercooled RTIL with a parallel plate rheometer is not a trivial task. The principle behind is rather simple, but multiple technical challenges make performing successful and trustworthy results difficult. This was also pointed out by Pogodina and coworkers in their study from 2011 [45]: *"It is worthy to mention that experimental rheology of IL and glass-formers in general in the vicinity of glass transition is very complex"*. Fortunately, it is possible and can give results going far down in modulus and thus combine with results from the PSG giving a large frequency range of decent quality data.

3.2 Dielectric spectroscopy

Dielectric spectroscopy is a powerful and very precise experimental method that has been used extensively in the glass-forming as well as the ionic liquid community for decades. The topic on its own is complex and lengthy and so this section will only provide a brief overview of the theory behind and the method in general, with emphasis on how it was used in this thesis. The section will be based on the book by F. Kremer and A. Schönenhals from 2003 [35] unless stated otherwise.

3.2.1 Theory of dielectric relaxation

At the very beginning is the relation connecting the dielectric displacement, \mathbf{D} , and the electric field, \mathbf{E} . For small field strengths this relation reads

$$\mathbf{D} = \varepsilon^* \varepsilon_0 \mathbf{E} \quad (3.2.1)$$

where ε_0 is the permittivity of vacuum and ε^* is the complex dielectric function which is essentially the property that is probed by dielectric spectroscopy. For a periodic electrical field we have that

$$\varepsilon^*(\omega) = \varepsilon'(\omega) - i\varepsilon''(\omega) \quad (3.2.2)$$

where ε' and ε'' is the real and imaginary part of the dielectric permittivity respectively.

To further understand the dielectric response in a material it is necessary to define the polarization, \mathbf{P} , which is the dielectric displacement originating from the response of a material to an external electric field. \mathbf{P} is defined as

$$\mathbf{P} = (\varepsilon^* - 1)\varepsilon_0 \mathbf{E} = \chi^* \varepsilon_0 \mathbf{E} \quad (3.2.3)$$

where χ^* is the dielectric susceptibility. Note that in general $\varepsilon^*(\omega)$ is a tensor, but in an isotropic liquid it can be treated as a scalar since the macroscopic polarization is parallel to the electric field.

The macroscopic polarization can be related to the microscopic one through the expression

$$\mathbf{P} = \frac{1}{V} \sum \mathbf{p}_i \quad (3.2.4)$$

where i denotes all dipole moments in the system. When a molecule has a permanent dipole moment, μ , which can be oriented by an applied electric field, then equation (3.2.4) becomes

$$\mathbf{P} = \frac{N}{V} \langle \boldsymbol{\mu} \rangle + \mathbf{P}_\infty \quad (3.2.5)$$

where N denotes the whole number of dipoles in the system, $\langle \mathbf{u} \rangle$ is the mean dipole moment and \mathbf{P}_∞ contains the combined contribution from induced electronic and atomic polarization which takes place on a very fast time scale. Equation (3.2.5) is what is called rotational polarization and is the quantity that is of interest here.

The complex dielectric function, $\varepsilon^*(\omega)$ is accordingly to linear response theory a compliance function in relation to other compliance function, e.g. shear mechanical compliance. The related dielectric complex modulus is $M^*(\omega)$ and is given by

$$M^*(\omega) = \frac{1}{\varepsilon^*(\omega)} \quad (3.2.6)$$

Analyzing the spectrum When analyzing the dielectric spectrum, it is important to know that there are three different contributions: 1) The microscopic fluctuations of molecular dipoles, 2) the translational diffusion of mobile charge carriers and 3) the separation of charges at interfaces which gives rise to electrode polarization. The latter is not an inherent property of the material but an artifact added to the relaxation spectrum.

For the first contribution, the fluctuations, it is possible to theoretically describe the spectrum using a Debye function, which assumes a simple exponential decay in the relaxation of the dipoles. In the frequency domain it is given by

$$\varepsilon^*(\omega) = \varepsilon_\infty + \frac{\Delta\varepsilon}{1 + i\omega\tau_D} \quad (3.2.7)$$

where ε_∞ is the high frequency limiting dielectric permittivity, ε_s is the low frequency limiting dielectric permittivity and $\Delta\varepsilon = \varepsilon_s - \varepsilon_\infty$ is the dielectric strength. The Debye model is plotted in figure 3.14 as the blue and red solid line, as well as the three permittivity constants. The peak in the imaginary part is called the loss peak and it relates directly to the relaxation time of the dipole moments given as $\tau_D = 1/(\omega_\alpha)$ where ω_α is the frequency at the peak. This relaxation time is often called the alpha relaxation time.

In a lot of cases, however, the dielectric spectrum cannot be described with the Debye model since the decay of the relaxations is not a simple exponential but rather a stretched exponential, just as with the shear modulus. Instead the

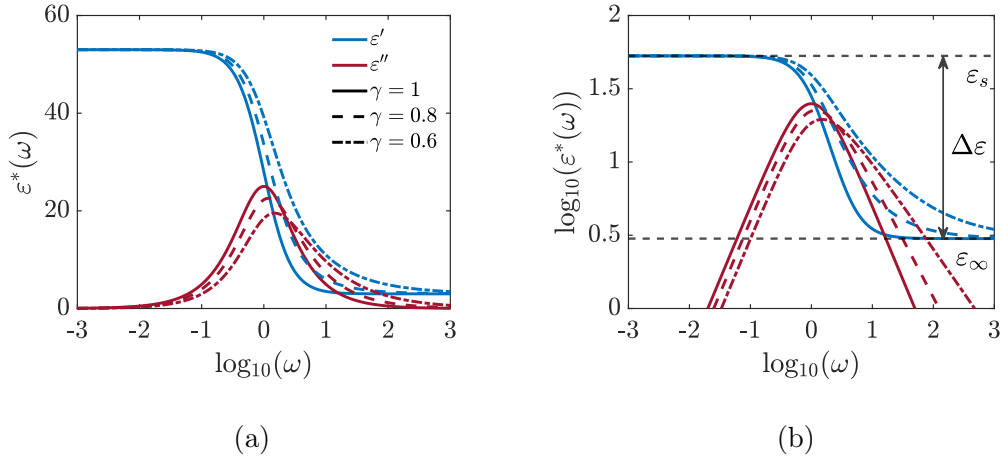


Figure 3.14: A sketch of the model version of the real (blue) and imaginary (red) part of the complex dielectric permittivity as a function of angular frequency. Three different versions is shown; the Debye function with $\gamma = 1$ and the Cole-Davidson function with γ of 0.8 and 0.6. a) is the linear-log plot and b) is the log-log plot also showing the values for ϵ_s , ϵ_∞ and $\Delta\epsilon = \epsilon_s - \epsilon_\infty$.

spectrum can be described using other models like the Cole-Cole model

$$\epsilon^*(\omega) = \epsilon_\infty + \frac{\Delta\epsilon}{1 + (i\omega\tau_{CC})^\beta} \quad (3.2.8)$$

where β is a stretching parameter between 0 and 1, or the Cole-Davidson function [38] which reads

$$\epsilon^*(\omega) = \epsilon_\infty + \frac{\Delta\epsilon}{(1 + i\omega\tau_{CD})^\gamma} \quad (3.2.9)$$

where γ is a parameter between 0 and 1. The Cole-Davidson function is illustrated in figure 3.14 as the dashed and dashed-dotted line with a γ of 0.8 and 0.6 respectively. It shows clearly how the stretching parameter smooths out the edges of ϵ' and the loss peak of ϵ'' . With $\gamma = 1$ the original Debye function is retrieved.

Thirdly there is the Havriliak-Negami function which is a combination of the previous two and so reads

$$\epsilon^*(\omega) = \epsilon_\infty + \frac{\Delta\epsilon}{(1 + (i\omega\tau_{HN})^\beta)^\gamma} \quad (3.2.10)$$

where $0 < \beta$ and $\beta\gamma \leq 1$. Note that in general all parameters of the relaxation process are temperature dependent.

If there are additional relaxation processes in the spectrum, e.g. a faster β relaxation, the spectrum can be fitted with a sum of the relaxation functions.

Conductivity The second contribution is as mentioned fluctuations of mobile charge carriers which give rise to conductivity. This is especially important when

measuring on ionic liquids since all the ions to some degree are mobile charge carriers.

Using Ohm's law, $\mathbf{j} = \boldsymbol{\sigma}^* \mathbf{E}$, where \mathbf{j} is the current density and $\boldsymbol{\sigma}$ is the complex conductivity, and the fact that \mathbf{j} is equivalent to $\frac{\partial \mathbf{D}}{\partial t}$ it can be shown with a periodic electric field of $E(t) = E_0 \exp(-i\omega t)$ that

$$\sigma^* = i\omega \varepsilon_0 \varepsilon^* \quad (3.2.11)$$

which in turns imply that

$$\sigma' = \varepsilon_0 \omega \varepsilon'' \text{ and } \sigma'' = \varepsilon_0 \omega \varepsilon' \quad (3.2.12)$$

For pure electronic conduction there is no contribution to the real part of the dielectric permittivity but there is to the imaginary part. Here the permittivity will increase linearly with decreasing frequency as $\varepsilon''(\omega) = \sigma_0 / (\varepsilon_0 \omega)$, where σ_0 is the steady state conductivity or DC conductivity. A theory which can be applied to conductivity data is the Random Barrier Model developed by J. Dyre [27]. This will be explained in detail in section 10.1.

The conduction can also be seen in the modulus representation, where the loss peak in the imaginary part of the modulus is directly linked to the conductivity and so, the relaxation time of the conduction process can be deduced in the same manner as from the dielectric permittivity.

Ionic liquids, which are subjects of study in this thesis, exhibit a very large conductivity that in most cases will completely obscure the relaxation processes of the liquids, and so only details about the conductivity are available for analysis. There exists a way to get around the ohmic conductivity and thus reveal relaxation processes hidden beneath, since the ohmic conductivity can be viewed as a contribution added to only the imaginary part of the relaxation spectrum. It can be shown that [46]

$$\varepsilon''_{der}(\omega) = -\frac{\pi}{2} \frac{\partial \varepsilon'(\omega)}{\partial \ln(\omega)} \quad (3.2.13)$$

where $\varepsilon''_{der}(\omega)$ is the so-called derivative representation of ε'' and is a first order approximation of the Kramer-Kronig relation [47]. It holds for broad peaks like the alpha relaxation and secondary relaxations and will suppress the ohmic conduction as well as make the relaxation peaks sharper and more clearly discernable. The loss peak of ε'' matches that of ε''_{der} and so this is a powerful method to find relaxation times of dielectric spectra that was otherwise obscured by conductivity. The technique does however not remove electrode polarization which can still obscure results in the low frequency range.

3.2.2 Broadband dielectric spectroscopy

The dielectric constant, ε^* , can be probed experimentally with Broadband Dielectric Spectroscopy (BDS) by realizing that the relation between this and the

frequency dependent complex capacitance, C^* , is

$$\varepsilon^*(\omega) = \frac{C^*(\omega)}{C_0} \quad (3.2.14)$$

where C_0 is the capacitance of the empty capacitor of the experimental setup. In this study a simple parallel plate capacitor was used so that the measured capacitance can be expressed as follows

$$C^*(\omega) = C_0 \varepsilon^*(\omega) = \frac{\varepsilon_0 A}{d_0} \varepsilon^*(\omega) \quad (3.2.15)$$

From this the dielectric permittivity of the liquid can be directly calculated from the measured capacitance. With a sinusoidal applied electric field of $E^*(\omega) = E_0 \exp(i\omega t)$, the capacitance is given as

$$C^*(\omega) = \frac{1}{i\omega Z^*(\omega)} \quad (3.2.16)$$

where $Z^*(\omega)$ is the complex impedance of the system given as

$$Z^*(\omega) = \frac{U^*(\omega)}{I^*(\omega)} \quad (3.2.17)$$

Details on the setup can be seen in [48, 49] and that setup can measure frequencies from $10^{-3} - 10^6$ Hz which is an impressive range as compared to dynamic mechanical spectroscopy. In important detail about the experimental setup used in this thesis is that the same cryostat was used for both BDS and DMS measurements. A consequence of this is that the temperature control in both methods is the exact same and so differences in dynamics between the two methods are not due to differences in temperature.

3.2.3 Finding the conductivity

To find the conductivity, σ_0 , from the BDS results, the real part of the complex conductivity is used. σ_0 is the value of the low frequency plateau in σ' which in this thesis was found by first differentiating σ' , identifying the region where this derivative is equal to or very close to zero (typically below 0.05) and then average the σ' value in this region.

An example of this can be seen in figure 3.15. Here a) shows the derivative of σ' with respect to the logarithm of the frequency, b) shows the found average values of σ' in the plateau region seen as black, solid lines.

3.3 Neutron scattering

This chapter will give the very basic principles behind neutron scattering followed by a section describing the principle behind measuring the mean square

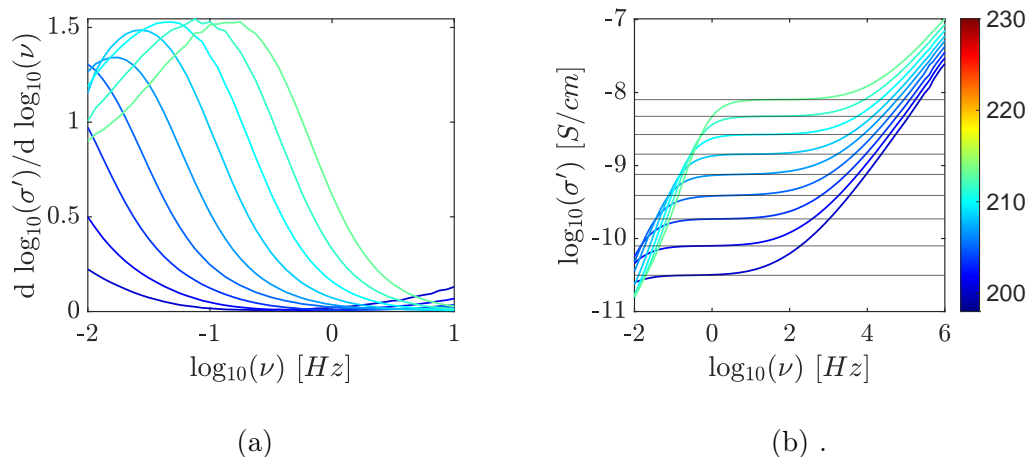


Figure 3.15: a) is $d \log_{10}(\sigma)/d \log_{10}(\nu)$ as a function of $\log_{10}(\nu)$ to see where the slope is zero or close to zero (constant conductivity). b) is the frequency dependent conductivity shown with the DC conductivity plateau, σ_0 , found from the derivative (black, solid lines).

displacement with neutron scattering. It will as such not be an introduction to the theory behind neutron scattering and for this the reader is referred to other works, e.g. *Introduction to the Theory of Thermal Neutron Scattering* by G. L. Squires (2012) [50] and *Theory of Neutron Scattering from Condensed Matter* by Stephen W. Lovesey [51]

The chapter will end with a section about quasi-elastic neutron scattering as well as the backscattering principle and instrumentation, which are the parts of neutron scattering most relevant for this thesis.

3.3.1 Basic principles

Neutron scattering is a powerful experimental tool that allows the user to determine structure and dynamics of materials on an atomic and molecular level. This is due to the fact that the wavelength of the neutron matches that of inter-atomic and inter-molecular distances.

Another strong advantage of neutron scattering is that the neutron interacts with the nuclei of the atoms in such a way that the cross section varies significantly across different species of atoms. A consequence of this is that neutron scattering can tell the difference between e.g. hydrogen and deuterium, something that is not possible with for example x-ray scattering.

A disadvantage to using neutrons in scattering experiments is that it can only be done at large scale facilities, since it requires either a nuclear reactor or a spallation source where heavy elements are hit by high-energy photons.

It is possible to calculate a neutron's energy and wavelength with the de-

Broglie relation

$$\lambda = \frac{h}{m\mathbf{v}} = \frac{2\pi}{|\mathbf{k}|} \quad (3.3.1)$$

where h is Planck's constant, m is mass of the neutron, \mathbf{v} is the velocity of the neutron and \mathbf{k} is the so called wavevector. The momentum is related to the wavevector as $\mathbf{p} = \hbar\mathbf{k}$ and so the energy of the neutron is given as $E = \frac{\hbar^2 k^2}{2m}$.

3.3.2 Basic scattering theory

Scattering theory is based on the fact that wave-particle duality makes it possible to describe neutrons as both a particle and a wave. The first is important in the case of detecting the neutron and the latter in the case of the scattering incident itself. This is because scattering in its essence is the interference of waves.

Let an incoming neutron wave with wavevector \mathbf{k}_i and known energy E_i hit a sample. The wave will hit the atoms of the sample and scatter off of the nuclei in spherical waves with wavevector \mathbf{k}_f and energy E_f and then be detected. The now known difference between the incoming and outgoing wave will provide information about the sample, e.g. exchange of energy. A fundamental property is thus the scattering vector which is the difference between the wave vector of the incoming and outgoing wave, $\mathbf{Q} = \mathbf{k}_i - \mathbf{k}_f$. These three vectors are the building blocks of the scattering triangle, illustrated in figure 3.16, and the angle between \mathbf{k}_i and \mathbf{k}_f is the scattering angle, θ [52].

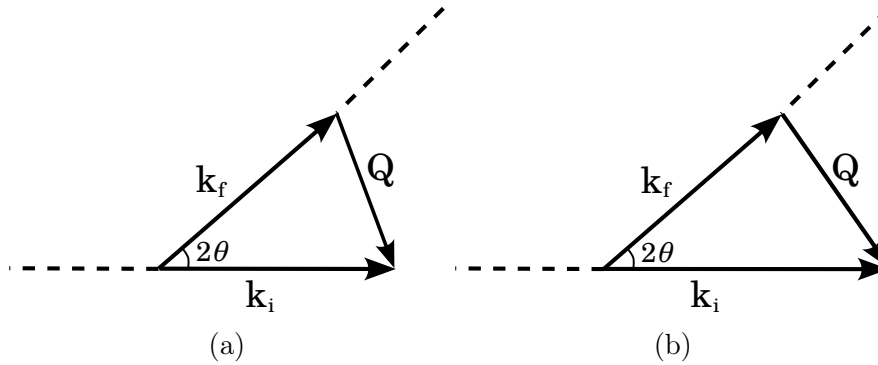


Figure 3.16: The scattering triangle with incoming wavevector, \mathbf{k}_i , outgoing wavevector, \mathbf{k}_f , scattering vector, \mathbf{Q} , and scattering angle, θ . a) is elastic scattering where $\mathbf{k}_i = \mathbf{k}_f$ and b) is inelastic scattering where $\mathbf{k}_i \neq \mathbf{k}_f$.

If $\mathbf{k}_i = \mathbf{k}_f$ then no energy has been transferred to the sample in the scattering event and the scattering is therefore elastic. If on the other hand energy has been transferred, so that $\mathbf{k}_i \neq \mathbf{k}_f$, then the scattering is inelastic and the difference in energy between incoming and outgoing wave contain information about the now excited state of the sample.

The relation between the momentum transfer and the scattering angle is

$$Q^2 = k_i^2 + k_f^2 - 2k_i k_f \cos\theta \quad (3.3.2)$$

and the energy transfer is

$$\hbar\omega = E_i - E_f = \frac{\hbar^2}{2m}(k_i^2 - k_f^2) \quad (3.3.3)$$

The scattering vector, \mathbf{Q} , is also called momentum transfer, and is together with the energy of the incoming and outgoing wave the basic quantity in a neutron scattering experiment.

3.3.3 Cross section and the structure factor

The quantity that is actually measured in a neutron scattering experiment is the scattering cross section. A thorough description of this complex quantity is well out of scope with this thesis, but shortly put is it the number of neutrons scattered per second into a solid angle, $d\Omega$, with final energy between E and $E + dE$ over the flux of incident neutrons, Φ . This can also be written as

$$\frac{d^2\sigma}{d\Omega dE} \quad (3.3.4)$$

where σ is the cross section with dimensions of area.

The total scattering cross section is given as

$$\frac{d^2\sigma}{d\Omega dE} = N \frac{k_f}{k_i} \frac{\sigma_{coh}}{4\pi} S_{coh}(\mathbf{Q}, \omega) + N \frac{k_f}{k_i} \frac{\sigma_{inc}}{4\pi} S_{inc}(\mathbf{Q}, \omega) \quad (3.3.5)$$

where N is the number of particles, σ_{coh} and σ_{inc} is the coherent and incoherent cross section respectively given as

$$\sigma_{coh} = 4\pi \bar{b}^2 \text{ and } \sigma_{inc} = 4\pi (\bar{b}^2 - \bar{b}^2) \quad (3.3.6)$$

where b is the so-called scattering length. The bar denotes the average value. The scattering length is a complex number where the imaginary part represents absorption and the real part describes how much the neutron "sees" the nucleus. The real part can be positive or negative depending on the attractive or repulsive nature of the scattering interaction. The unit is area and usually it is represented in the special unit femtobarn which in SI-units is 10^{-45}m^2 . The actual values of the scattering lengths are experimentally determined quantities since there is not yet any theory of nuclear forces capable of theoretically determine the scattering lengths [50].

$S_{coh}(\mathbf{Q}, \omega)$ and $S_{inc}(\mathbf{Q}, \omega)$ are the coherent and incoherent dynamic structure factor respectively given as [51]

$$S_{coh}(\mathbf{Q}, \omega) = \frac{1}{2\pi\hbar} \int_{-\infty}^{\infty} I_{coh}(\mathbf{Q}, \omega) e^{-i\omega t} dt \quad (3.3.7)$$

and

$$S_{inc}(\mathbf{Q}, \omega) = \frac{1}{2\pi\hbar} \int_{-\infty}^{\infty} I_{inc}(\mathbf{Q}, t) e^{-i\omega t} dt \quad (3.3.8)$$

I_{coh} and I_{inc} are the coherent and incoherent intermediate scattering functions respectively given as

$$I_{coh}(\mathbf{Q}, t) = \frac{1}{N} \sum_{i,j} \langle e^{-i\mathbf{Q}\cdot\mathbf{r}_i(0)} e^{i\mathbf{Q}\cdot\mathbf{r}_j(t)} \rangle \quad (3.3.9)$$

and

$$I_{inc}(\mathbf{Q}, t) = \frac{1}{N} \sum_j \langle e^{-i\mathbf{Q}\cdot\mathbf{r}_j(0)} e^{i\mathbf{Q}\cdot\mathbf{r}_j(t)} \rangle \quad (3.3.10)$$

where $\langle \dots \rangle$ denotes a correlation function, $\mathbf{r}_{i/j}$ is the distance to the j 'th/ i 'th nucleus. It is in equation (3.3.9) seen that the coherent scattering depends on the correlation between positions of the same nucleus at different times as well as the correlation between the positions of different nuclei at different times. In other words the coherent scattering gives the interference effects in the scattering event.

In contrast to this it is seen in equation (3.3.10) that the incoherent scattering only depends on the correlation between positions of the same nucleus at different times, or in other words the self-correlation. It tells about how much the same nucleus has moved after a certain amount of time [50].

3.3.4 Separation of motion

This section will describe specific limiting behavior and simple models relevant for this work in order to connect the scattering signal with motions of molecules in the supercooled liquids. Only the case of incoherent scattering from single-scatterers will be considered, and so the subscripts *inc* and *i* will be omitted.

Elastic scattering in a solid In the case of glasses and highly viscous liquids it is reasonable to assume that there is no diffusion of the molecules on the experimental time scale and so the only movement comes from vibrations around a fixed position in space. This way the modeling of the scattering in glass-forming liquids can be limited to evolve around solids, ordered or disordered.

In the case of the disordered solid the equilibrium position of the vibration is not well defined but it is possible to write a time dependent position vector as [53]

$$\mathbf{r}(t) = \mathbf{r}_e + \mathbf{u}(t) \quad (3.3.11)$$

where the first term is time independent equilibrium position of the particle and the second term is a time dependent position of the particle from its equilibrium position.

Inserting this into equation (3.3.10) will give

$$\begin{aligned} I(\mathbf{Q}, t) &= \langle e^{-i\mathbf{Q}\cdot[\mathbf{r}_e+\mathbf{u}(0)]} e^{i\mathbf{Q}\cdot[\mathbf{r}_e+\mathbf{u}(t)]} \rangle \\ &= \langle e^{-i\mathbf{Q}\cdot\mathbf{u}(0)} e^{i\mathbf{Q}\cdot\mathbf{u}(t)} \rangle e^{-i\mathbf{Q}\cdot\mathbf{r}_e} e^{i\mathbf{Q}\cdot\mathbf{r}_e} \\ &= \langle e^{-i\mathbf{Q}\cdot\mathbf{u}(0)} e^{i\mathbf{Q}\cdot\mathbf{u}(t)} \rangle e^{i\mathbf{Q}\cdot[\mathbf{r}_e-\mathbf{r}_e]} \\ &= \langle e^{-i\mathbf{Q}\cdot\mathbf{u}(0)} e^{i\mathbf{Q}\cdot\mathbf{u}(t)} \rangle \end{aligned} \quad (3.3.12)$$

where it is clearly seen that the incoherent scattering intensity contains no information about the position of the particles but only the dynamics.

In the long time limit it is then assumed that there is no correlation of the particles between $t = 0$ and $t \rightarrow \infty$. It is furthermore assumed that the ensemble average, $\langle \dots \rangle$ is time independent and the intensity is then

$$I(\mathbf{q}, t) = \langle e^{2\mathbf{Q}\cdot\mathbf{u}} \rangle \quad (3.3.13)$$

where the factor $\langle e^{2\mathbf{Q}\cdot\mathbf{u}} \rangle$ is called the Debye-Waller factor.

Further assumptions can now be made in order to give a more explicit expression for the Debye-Waller factor. The first one is that in disordered systems the average of $\mathbf{Q}\cdot\mathbf{u}$ will be independent on the direction of \mathbf{Q} . The second one is that the vibrations of the particles can be modelled with a Gaussian distribution. With this the scattering intensity becomes [53]

$$I(\mathbf{Q}, t) = \exp\left(-\frac{Q^2\langle u^2 \rangle}{3}\right) \quad (3.3.14)$$

From this it is possible to extract the mean square displacement, $\langle u^2 \rangle$, from the scattering intensity.

3.3.5 QENS

Quasi-elastic neutron scattering, or QENS, is a method used to measure the dynamic relaxation processes in a system. The timescale of the observed dynamics is defined by the instrumental resolution function which will be the minimum measurable energy exchange [54]. At low energy resolution, high energy neutrons will probe fast motions and vice versa with a high energy resolution.

In QENS the scattering intensity is observed as a broadening of the elastic signal around zero energy transfer, i.e. the elastic peak. This broadening around the elastic peak is related to a characteristic time of the relaxation process in question. Molecular motions slower than the resolution function will to the observer be a part of the elastic signal, while dynamics faster than the window will be a part of an approximately flat background signal.

In QENS the incoherent part of the scattering function, $S(\mathbf{Q}, \omega)$, will contain information about the spatial and temporal correlation between identical molecules. This can be further divided into four terms; vibrational, rotational and translational motion plus the experimentally determined instrumental resolution function [54]. The broadening of the elastic signal due to rotational and translational motion can, to a very good approximation, be modelled by Lorentzian functions.

Figure 3.17a show the measured scattering function in a QENS experiment at three different temperatures. At a low temperature, T_1 , the signal is mainly elastic and the QENS peak is narrow. At increasing temperature, T_2 and T_3 , motion starts to increase in the sample resulting in a broadening of the elastic peak which is almost entirely gone at T_3 .

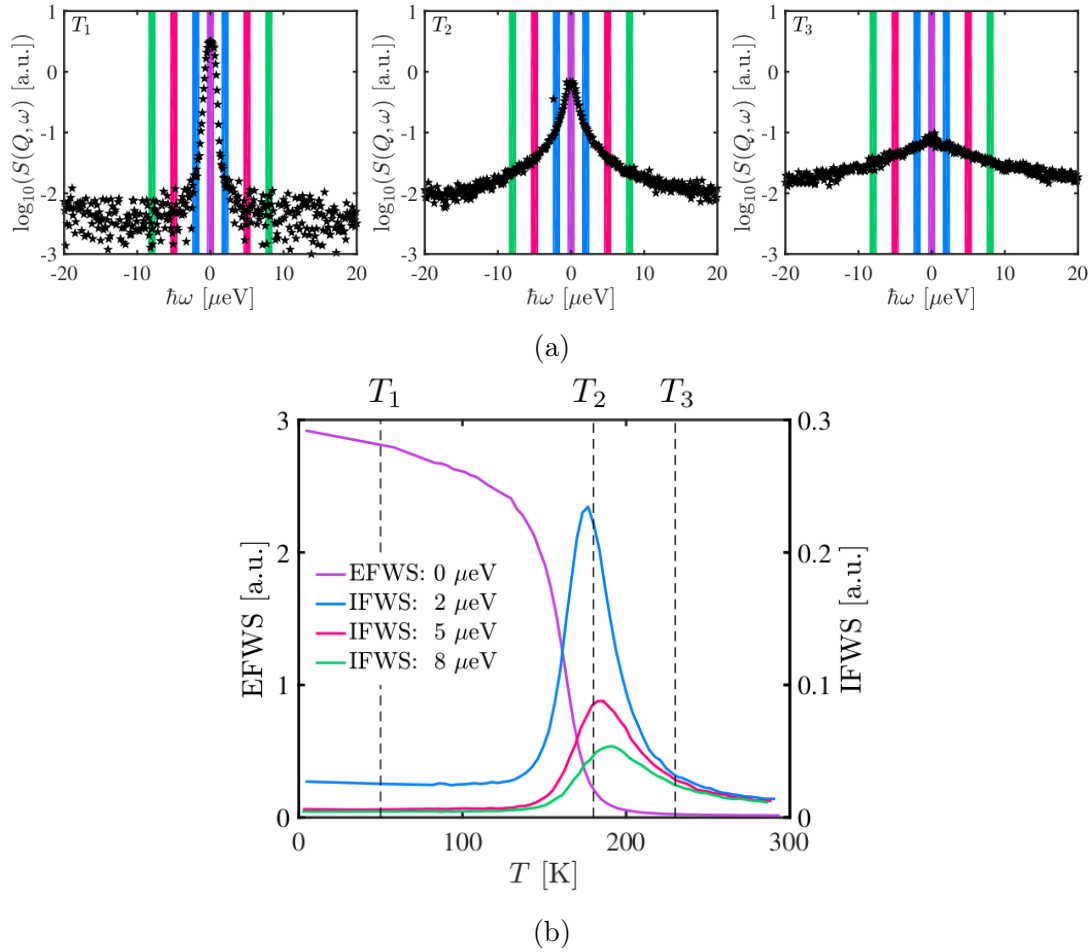


Figure 3.17: a) Examples of full QENS spectra measured on a liquid at three different temperatures with the instrument IN16b located at ILL. b) EFWS and IFWS spectra where the temperatures from a) are marked with black, dashed lines. Note that the vertical colorbars in a) refer to the FWS spectra in b). Both figures are from [12].

If the energy transfer is held fixed and the scattering intensity measured at different temperatures it is called a Fixed Window Scan (FWS). This can give specific temperature dependence of the relaxational modes in the sample and is the specific method used in this thesis. Figure 3.17b illustrates the concept. Here the elastic (purple) signal is shown together with three different inelastic signals with an energy transfer of 2 (blue), 5 (red) and 8 (green) μeV respectively.

The elastic signal (EFWS) gives the temperature dependence of the elastic peak. At low temperatures it is at its highest, with the inelastic signal being almost zero, as was also illustrated in figure 3.17a. As the temperature increases the elastic signal decreases until it is completely gone at high temperatures. EFWS can be used to determine the mean square displacement of the molecules in the sample. This analysis will be explained in more detail in chapter 11.

The three inelastic signals (IFWS) exhibit a peak which position depends

on the specific energy transfer and reveals dynamical signatures. A detailed description of this will be given in chapter 11.

3.3.6 Backscattering

The instrument used for measuring EWFS and IFWS in the RTIL studied in this thesis was IN16b located at Institut Laue-Langevin (ILL), Grenoble, France. IN16b is a backscattering instrument capable of measuring quasi-elastic neutron scattering and probing dynamics on the nano second timescale.

Backscattering was originally proposed by Heinz Maier-Leibnitz in 1966 [55] and the basic concept is to make use of scattering with a Bragg angle of 90° for the selection and analysis of the neutron wave. A scattering angle of 90° means that $2\theta = 180$ and thus \mathbf{k}_f travels in the direct opposite direction of \mathbf{k}_i , hence the name backscattering.

The advantage of using a Bragg angle of 90° , for the selection and analysis of neutrons, is that the wavelength band, $\Delta\lambda$, becomes very narrow meaning that the instrument can obtain a very high energy resolution. As mentioned before, a high energy resolution makes it possible to access lower energy motions or longer time scales [56], in this case around a nanosecond. This may not sound like a long time scale, but it is significantly longer than the time scale accessible by for example time-of-flight instruments, which is in the order of a pico second.

Limitations in the accessible dynamic range is on the lower side the achievable energy resolution and on the upper side the maximum energy transfer. For IN16b with an energy resolution of $\Delta E_{res} = 0.8\mu\text{eV}$ this is $\pm 30\mu\text{eV}$ giving an effective Q -range of 0.1-1.8 μeV .

Chapter 4

Room Temperature Ionic Liquids

The purpose of this chapter will be to give a general introduction to room temperature ionic liquids (RTIL). This includes general features that apply across different families of RTILs including what is already known about dynamics as well as structure.

RTILs are simply salts that are molten at around room temperature and were developed back in the 1970s and 80s [57–59]. The specific temperature limit to when a molten salt is accepted as a RTIL is not sharply defined, but a 100 degrees Celsius is generally accepted. This means that RTILs are comprised entirely of ions and in that sense, they do not differ from simple molten salts [60].

This is of course in practice not completely true, since a liquid of 100% purity is not practically possible and so the RTILs will not be comprised *entirely* of ions. A practical approach is of course necessary and so a purity of above 95% is a requirement. Preferably as high as 99% for high-quality/sensitive work [60].

The ions that RTILs consist of are typically an organic cation with one or more alkyl chains of varying lengths together with an inorganic anion which can be both symmetric and asymmetric. A study shows that the alkyl chain reduces the melting temperature of the liquid due to a destabilization of the crystalline packing structure [61] and so the low melting point can be explained by this.

The requirement that RTILs consist of a large cation and an inorganic anion of course limits the number of possible configurations, but the number of potential RTILs is still huge. Figure 4.1 show a selection of cations and anions which, when combined, will form RTILs. Just from this small selection it is clear that a large variety of liquids can be created. Each family of RTILs, e.g. RTILs with an imidazolium cation, will have its own unique physical properties such as viscosity, conductivity, chemical stability, and so forth and the potential applications will therefore also vary with this.

This fact makes it very desirable to develop methods that can predict physical properties in RTILs since it is immensely time consuming, and in practice impossible, to actually synthesize and characterize every single combination of cations and anions. This is one of the reasons why it is still very relevant to study this class of liquids.

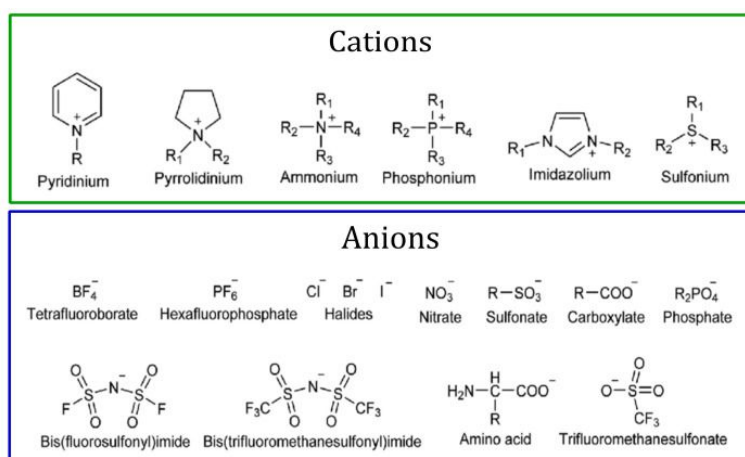


Figure 4.1: A range of different cations and anions that all can be combined creating a large variety of different RTILs. This is just a small selection of cations and anions from which one can create RTILs. From [62].

4.1 General properties

Even though the properties of RTILs vary significantly across different families it is still possible to sum up some of the most general ones, which will be done in the following.

Viscosity The viscosity varies greatly across different RTILs, but it is in general high due to van der Waal forces, hydrogen bonding and Coulombic forces. The viscosity is at least ten times higher than that of water and often significantly greater, which can be a hindrance with regards to application [60].

Vapor pressure One very significant property of RTILs is their negligible vapor pressure causing them to have low flammability. This is a desirable property in applications such as rechargeable Li-ion batteries since it increases the safety to have a non-volatile liquid which emits almost no vapors [60].

Electrochemical RTILs have in general good electrochemical stability and relatively high ionic conductivity that enables their use in batteries, supercapacitors, fuel cells, solar cells and so on [60].

Conductivity and ion transport The transport of electroactive species in a RTIL is of paramount importance in applications such as batteries and it is therefore important to understand the effects of, for example, structure on the ion conductivity. The increase of aggregation in RTILs will decrease the level of conductivity below that which would be expected if all the ions could move around freely [60].

4.2 Structure

The structure of RTILs is an important area of investigation when it comes to understanding this complex and versatile class of liquids. The x-ray structure factor of RTILs reveals three distinct peaks, where two of them are present in general and the third only in some special cases. This can be seen in figure 4.2 which shows examples of the computationally derived structure factor.

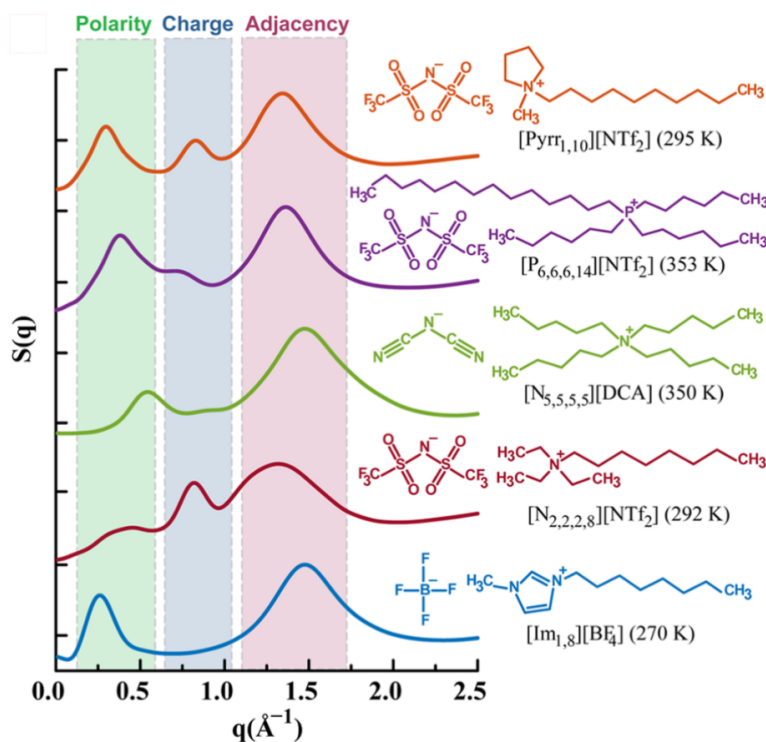


Figure 4.2: Computationally derived x-ray structure factor of five different RTILs showing the three distinct peaks; the main peak from adjacent molecules, the charge alternation peak and the polarity alternation or pre-peak. From [63].

The peak at highest Q -values is called the main peak or adjacency peak and is related to the smallest structure. The origin of this peak is simply the periodic distance between neighboring molecules. This peak is also present in conventional solvents such as methanol.

The intermediate peak is the charge alternation peak, and it arises from the alternation of charges in the ions. This peak is more complicated in nature since it is a combination of peaks and anti-peaks arising from alternation of charges of equal and opposite sign, respectively. A consequence of this is also that the charge peak is not always present when measuring the structure factor. Not because there is no charge alternation, there always is in RTILs, but because the peak and anti-peaks cancel each other out. In fact, the charge alternation peak is the signature of RTILs [63].

The peak at lowest Q -value, and thus at the longest distance in real space, is the polarity alternation peak also called the pre-peak. The origin of this peak

is the heterogeneities that arise from polar and apolar regions in the liquid, where the polar region forms a network of the cation heads and the anions and the apolar regions form from the cation tail. These regions are formed in some RTILs when the apolar part of the cation is large enough to separate the polar network into distinct regions which are also referred to as mesoscale aggregates. The pre-peak often appears when the apolar alkyl chain of the cation is longer than five carbon atoms [64].

An important thing to note about the pre-peak is that, just as with the charge alternation peak, it consists as a combination of peaks arising from polar-polar plus apolar-apolar alternation as well as an anti-peak arising from polar-apolar alternation. As a consequence, peaks and anti-peaks can cancel each other out and there will be no pre-peak in the structure factor even though polar-apolar heterogeneities exist [63].

A pre-peak related to mesoscale structure was first experimentally discovered by A. Triolo et al. in 2007 [65] and has since then been confirmed in multiple studies [66–69]. The position of the pre-peak is generally around a few nm^{-1} giving a real space correlation distance of around 10–30 Å, which is very large for a liquid [69]. Furthermore, the size of these mesoscale structures has been shown to increase with increasing alkyl chain length [65,67].

4.3 RTILs in this work

The RTILs measured in this thesis will be presented here in order to give a quick overview.

Pyr14-TFSI 1-butyl-1-methylpyrrolidinium bis(trifluoromethanesulfonyl)imide (Pyr14-TFSI) is seen in figure 4.3 and is a well-studied liquid in the pyrrolidinium family with numerous publications [68–83] presenting results with a broad variety of measuring techniques. It has a T_g of 185 K and a melting temperature of $T_m = 254$ K.

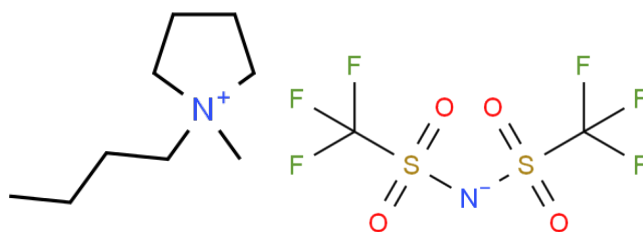


Figure 4.3: 1-butyl-1-methylpyrrolidinium bis(trifluoromethanesulfonyl)imide (Pyr14-TFSI)

The x-ray structure factor exhibits two peaks which are the charge alternation and main peak, i.e. this sample has no pre-peak. NMR studies however have shown that a small degree of mesoscale aggregates does appear in this liquid [71].

In this work the liquid has been studied using dynamic mechanical spectroscopy (DMS), broadband dielectric spectroscopy (BDS), quasi-elastic neutron scattering (QENS) and calorimetric techniques.

Pyr15-TFSI 1-pentyl-1-methylpyrrolidinium bis(trifluoromethanesulfonyl)imide (Pyr15-TFSI) is seen in figure 4.4. It has a high tendency to crystallize and is thus very difficult to supercool. It crystallized during dynamic mechanical spectroscopy and broadband dielectric spectroscopy measurements and it was only possible to supercool with the thermalization calorimetry technique due to the very fast cooling rate. Consequently, it was only possible to deduce the glass transition and melting temperature as $T_g = 188$ K and $T_m = 285$ K.

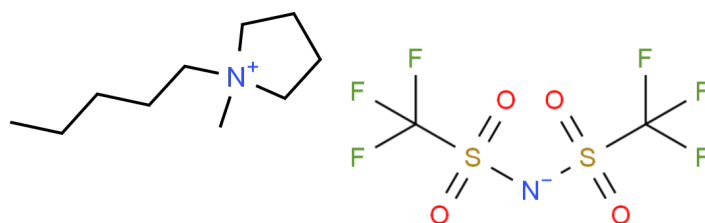


Figure 4.4: 1-pentyl-1-methylpyrrolidinium bis(trifluoromethanesulfonyl)imide (Pyr15-TFSI)

This tendency to crystallize and consequently not supercool was also the case in another study [80].

Pyr16-TFSI 1-hexyl-1-methylpyrrolidinium bis(trifluoromethanesulfonyl)imide (Pyr16-TFSI) is seen in figure 4.5 and has also been studied before with various techniques [68, 71, 80, 82, 83]. It is the first liquid in the Pyr1*n*-TFSI series to show a pre-peak in x-ray structure factor [68] and it has been confirmed to have a significant degree of mesoscale aggregation [71].

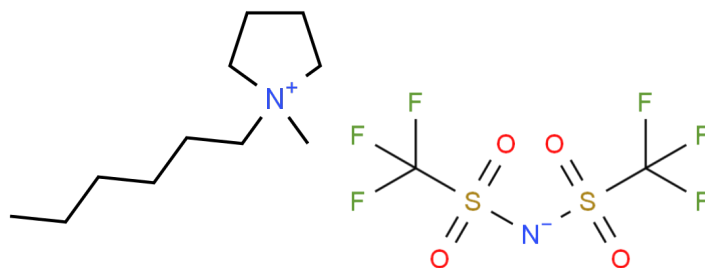


Figure 4.5: 1-hexyl-1-methylpyrrolidinium bis(trifluoromethanesulfonyl)imide (Pyr16-TFSI)

The liquid was in this work measured with DMS, BDS and thermalization calorimetry (TC), where the latter showed $T_g = 186$ K and $T_m = 276$ K.

Pyr18-TFSI 1-octyl-1-methylpyrrolidinium bis(trifluoromethanesulfonyl)imide (Pyr18-TFSI) is seen in figure 4.6 and has been studied before with various techniques [68, 71, 80, 83, 84]

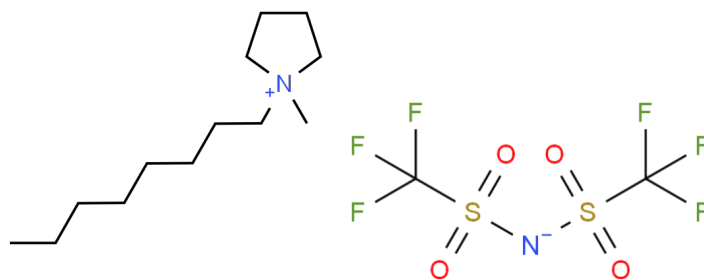


Figure 4.6: 1-octyl-1-methylpyrrolidinium bis(trifluoromethanesulfonyl)imide (Pyr18-TFSI)

As with Pyr16-TFSI the x-ray structure factor shows the three standard peaks for RTILs with long alkyl chain length; the pre-peak, the charge alternation peak and the main peak [68]. NMR studies show that there is pronounced mesoscale aggregate formation [71] as expected.

It has in this study been measured with DMS, BDS and TC where the latter showed a $T_g = 191$ K and $T_m = 259$ K.

Pmim-BF₄ 1-propyl-3-methylimidazolium tetrafluoroborate (Pmim-BF₄) is seen in figure 4.7. Even though the imidazolium family of RTILs is probably one of the most well studied, there is only very limited number of studies on supercooled Pmim-BF₄ [85].

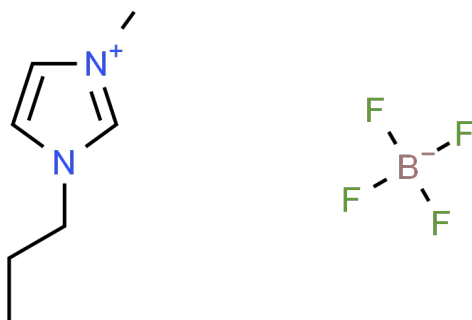


Figure 4.7: 1-propyl-3-methylimidazolium tetrafluoroborate (Pmim-BF₄)

Pmim-BF₄ has in this study been measured with DMS, QENS and TC, where TC results showed a $T_g = 180$ and no cold-crystallization.

Omim-BF₄ 1-propyl-3-methylimidazolium tetrafluoroborate (Pmim-BF₄) is seen in figure 4.8. This liquid has been thoroughly studied in literature [31,84,86, 87] and was for example among the ionic liquids studied in the first experimental evidence of the existence of a pre-peak in the x-ray structure factor [65].

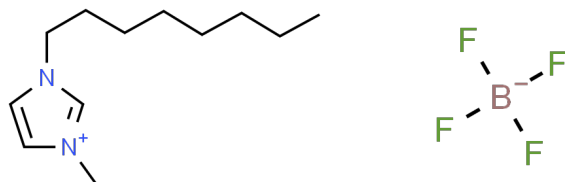


Figure 4.8: 1-octyl-3-methylimidazolium tetrafluoroborate (Omim-BF₄)

In this work the liquid has been studied with DMS, BDS and TC techniques where the latter showed a $T_g = 189$ K and no crystallization.

Bpyr-BF₄ 1-butylpyridinium tetrafluoroborate (Bpyr-BF₄) can be seen in figure 4.9. It was in this study only successfully measured with the TC method which showed $T_g = 189$ K and $T_m = 250$ K.

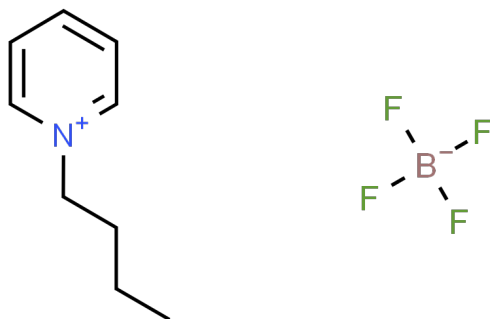


Figure 4.9: 1-butylpyridinium tetrafluoroborate (Bpyr-BF₄)

Emim-TCM 1-ethyl-3-methylimidazolium tricyanomethanide (Emim-TCM) can be seen in figure 4.10. It was in this study also only successfully measured with the TC method which showed $T_g = 184$ K and $T_m = 271$ K.

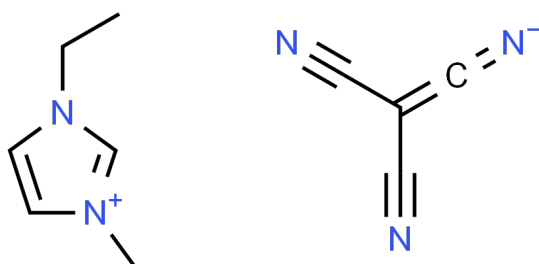


Figure 4.10: 1-ethyl-3-methylimidazolium tricyanomethanide (Emim-TCM)

Chapter 5

Molecular mimic

This chapter will be based on the paper by Frederik Philippi et al. [88] published in 2022. It will give a quick overview of the content of the paper and then focus more in detail on my contribution, which was density measurements under high pressure.

One very important property of RTILs is the viscosity since the practical application of ionic liquids, in for example batteries, depends highly on viscosity [60, 89]. A natural consequence of this is a high demand of tools to describe, optimize and predict viscous flow of ionic liquids, and indeed great effort has been put into this over the years [90–96]. One way to understand the underlying mechanism of why high viscosity arises in RTIL is to compare directly with conventional molecular liquids. This is the method implemented in the presented paper.

The general idea is to synthesize a molecular liquid with similar structure to the ionic liquid, a so-called molecular mimic, and then compare viscosity between the two. The molecular mimic is in other words a charge neutral version of the ionic liquid and this makes it possible to directly and experimentally investigate the consequence of the charged anion and cation on viscosity. See figure 5.1 for a schematic of the ionic liquid and molecular mimic investigated in this work.

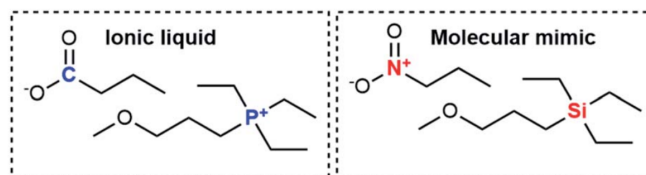


Figure 5.1: The ionic liquid/molecular mimic combination, where the difference between the two is indicated with blue and red [88].

At first the densities of the RTIL and the molecular mimic were measured at ambient pressure and at room temperature (25°C). The result was a density of 0.874(1) g/cm³ and 1.032(1) g/cm³ for the molecular mimic and ionic liquid respectively. Viscosity at ambient pressure and room temperature was measured

to be 0.99(4) mPa s and 217 mPa s for the molecular liquid and ionic liquid respectively, which gives a difference in viscosity of a factor of around 200.

There will be three different values of viscosity to be compared in this study, i.e. viscosity of the 1) molecular mimic at ambient pressure (MM), 2) the molecular mimic under isodensity conditions (MM^{hp}) and 3) the ionic liquid at ambient pressure (IL). This in turn gives two viscosity differences, i.e. MM→MM^{hp} for the jump in viscosity between 1) and 2) and MM^{hp}→IL for the jump between 2) and 3). In order to identify the isodensity conditions pressure-volume measurements were performed on the molecular mimic, which was my main contribution and shall be described in detail in the following.

5.1 Pressure-volume measurements

5.1.1 Method

The density of the molecular mimic under high pressure was measured to find the isodensity conditions using a U111 high pressure pump and an MV1-30 pressure chamber, both provided by Unipress in Poland. The sample is loaded into a cylindrical container with a movable piston at one end and the container is then submerged into enclosed pressure fluid which is connected to a high-pressure pump. The increasing pressure moves the piston inwards, compressing the liquid sample, during which the displacement of the piston is recorded. The density change is then calculated using the absolute mass and the change in volume of the sample due to the increase in pressure. Measurements were performed from 0–350 MPa at 25°C.

5.1.2 Results

I measured on two different samples to test reproducibility, and each sample was measured twice on an isotherm and once on an isobar. However due to issues with the cooling process the isobar from the first sample is not useful.

First sample The mass of the first sample was $M_{sample,1} = 11.335$ g. The density was calculated using the simple formula

$$\rho = \frac{M_{sample}}{(h - D)\pi r^2} \quad (5.1.1)$$

where h is the length of the cylinder containing sample to begin with, D is the displacement of the piston due to increase of the pressure and r is the radius of the cylinder containing the sample. Note that there is an uncertainty of +/- 1 mm on h , which is 4.1 mm, giving an uncertainty of around 2.4%. Because of this, it could be an advantage to measure the absolute density of the liquid at ambient pressure and 25°C in order to get a more accurate estimate of the start volume of the sample. Then recalculate the density at each data point with the start-volume minus the displacement volume given as $V_{dis} = D\pi r^2$.

The resulting density for the first sample can be seen in figure 5.2. Here we see a smooth increase in density with pressure and there is good reproducibility seen as a small difference in the first and the second measurement. The first measurement was from 0-300 MPa and the second from 0-330 MPa.

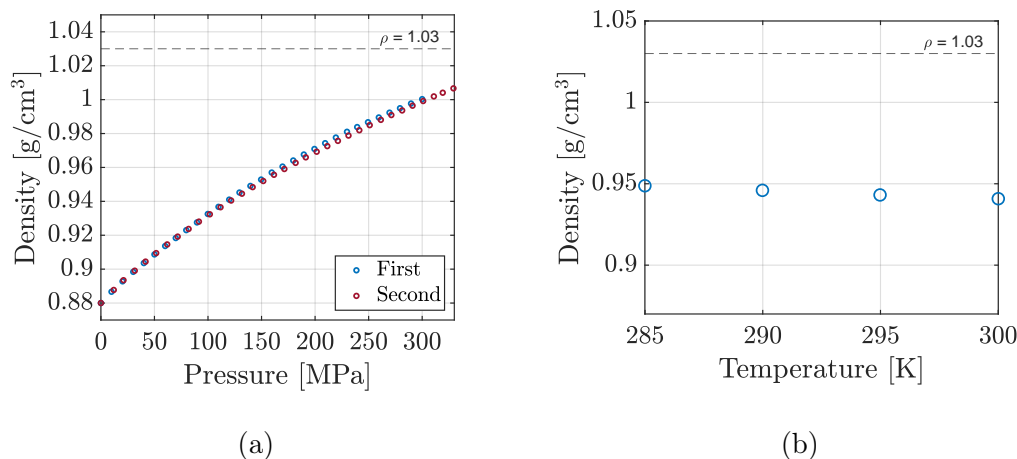


Figure 5.2: a) Density as a function of pressure on an isotherm with a temperature of 25°C on the first sample. Blue is from the first and red is for the repeated/second measurement. b) Density as a function of temperature on an isobar with a pressure of 100 MPa, first sample. For both plots, the dashed line is the density of the ionic liquid.

In order to see at what pressure the density of the molecular mimic will reach that of the ionic liquid, a fit of the data to the Tait equation was made. The Tait equation reads [97, 98]:

$$\rho(T, P) = \left(V_0 e^{\alpha_0 T} \left(1 - C \ln \left(1 + \frac{P}{b_0 e^{-b_1 T}} \right) \right) \right)^{-1} \quad (5.1.2)$$

where V_0 , α_0 , C , b_0 and b_1 are fitting parameters.

The best-fit parameters were then used to extrapolate the data all the way up to 500 MPa, giving a final density of the molecular mimic higher than that of the ionic liquid. The result for both measurements can be seen in figure 5.3. The vertical dashed line is the pressure at which the density of the molecular mimic is 1.03 g/cm³. This is at 414 MPa and 425 MPa for the first and the second measurement, respectively.

The best-fit parameters used for the extrapolation can be seen in table 5.1.

Second sample The mass of the second sample was $M_{sample,2} = 11.3150$ g. The density was again calculated using equation (5.1.1). The result for both the isotherm and the isobar can be seen in figure 5.4. The measurement on the isobar worked well this time, however, as can be seen in figure 5.4b, the density decrease with decreasing temperatures is much too small to reach even near the

Fit parameter	First	Second
V_0	1.12	1.12
α_0	$5.08 \cdot 10^{-4}$	$5.40 \cdot 10^{-4}$
C	0.108	0.109
b_0	170	177
b_1	$6.5 \cdot 10^{-3}$	$5.9 \cdot 10^{-3}$

Table 5.1: A table showing the found best-fit parameters when fitting the data to the Tait equation for both the first and the second measurement on the first sample.

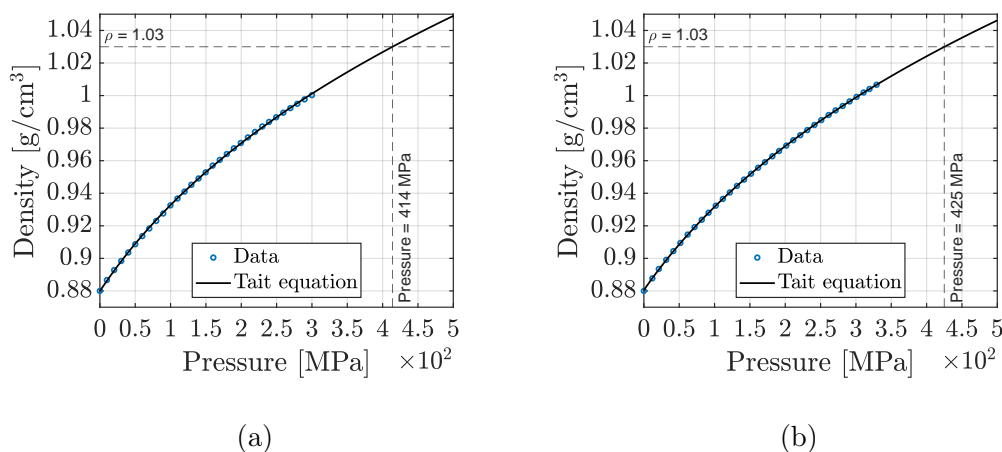


Figure 5.3: Density as a function of pressure for the first sample on an isotherm with a temperature of 25 °C. a) and b) are for the first and second measurement respectively. Black solid line is an extrapolation made with a fit to the Tait equation and dashed lines are from where the extrapolation intersects with the density of the ionic liquid.

isodense conditions and so the focus will be on the isotherm measurement. Here we see a smooth increase in density with pressure, see figure 5.4a and there is good reproducibility between the first and the second measurement. Both measurements were from 0-350 MPa.

To find the pressure with isodense conditions, the data was again fitted to the Tait equation and the best-fit parameters were then used to extrapolate the data all the way up to 500 MPa. The result for both measurements can be seen in figure 5.5. The vertical dashed line is the pressure at which the density of the molecular mimic is 1.03 g/cm³. This is at 430 MPa for both measurements. The best-fit parameters can be seen in table 5.2

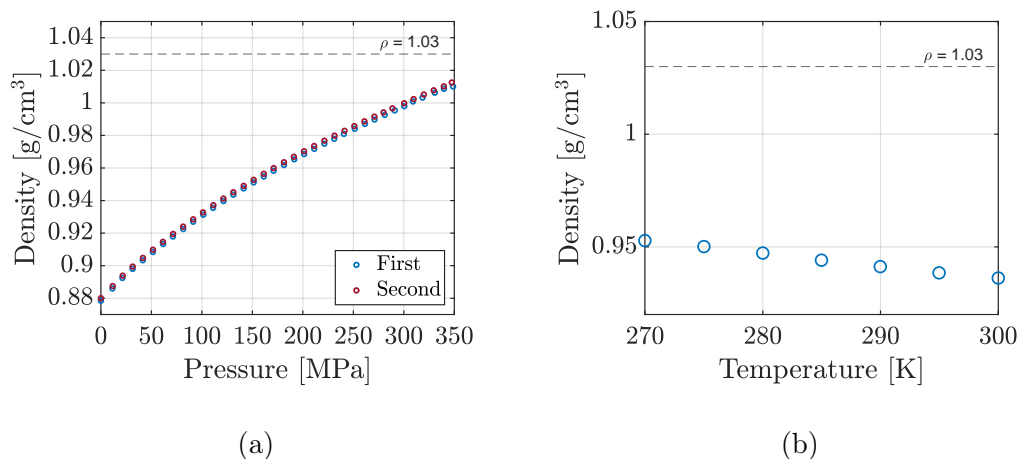


Figure 5.4: a) Density as a function of pressure on an isotherm with a temperature of 25°C for the second sample. Blue is from the first and red is for the repeated/second measurement. b) Density as a function of temperature on an isobar with a pressure of 100 MPa, second sample. For all plots, the dashed line is the density of the ionic liquid.

Fit parameter	First	Second
V_0	1.12	1.13
α_0	$5.46 \cdot 10^{-4}$	$4.63 \cdot 10^{-4}$
C	0.107	0.107
b_0	171	174
b_1	$6.2 \cdot 10^{-3}$	$6.8 \cdot 10^{-3}$

Table 5.2: A table showing the found best-fit parameters when fitting the data to the Tait equation for both the first and the second measurement on the second sample.

5.1.3 Discussion and conclusion

As hinted, the use of an isobar to find the change in density is not feasible in this case and thus the focus will be in the four measurements on an isotherm. All four measurements are very similar which is also evident in the small difference between the four set of best-fit parameters, even between the two different samples. This of course shows the robustness of the results.

Regarding which of the four measurements should be used, I would choose a combination of the two from the second sample, since the reproducibility here is highest. This reproducibility is also confirmed through the extrapolated pressure giving isodense conditions, since it is identical in the two separate measurements (430 MPa). This marks the end of my contribution to this work.

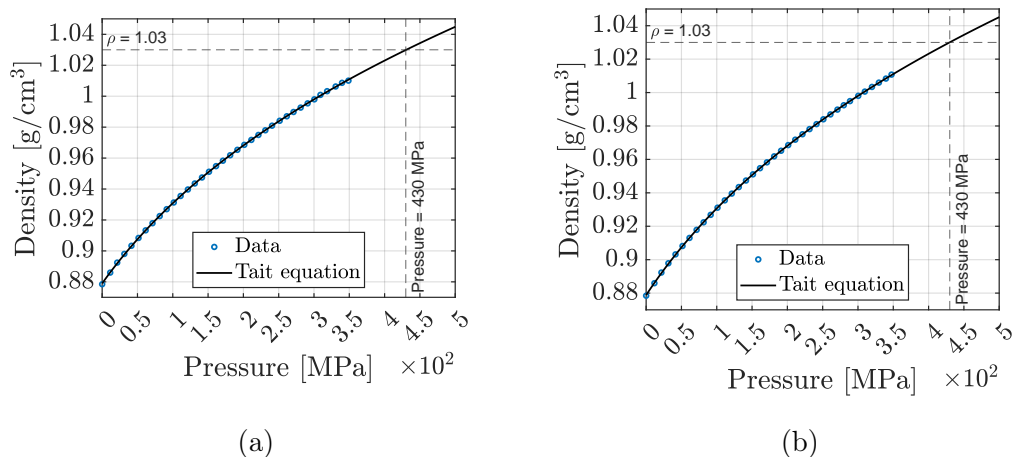


Figure 5.5: Density as a function of pressure for the second sample on an isotherm with a temperature of 25 °C. a) and b) are for the first and second measurement respectively. Black solid line is an extrapolation made with a fit to the Tait equation and dashed lines are from where the extrapolation intersects with the density of the ionic liquid.

The resulting pressure where the molecular mimic has a density identical to that of the ionic liquid was in the final paper reported to be 460 MPa. This result was found from fitting both measurements on the second sample simultaneously to the Tait equation and lead to a measurement of the viscosity of the molecular mimic under high pressure (up to 500 MPa) using a falling body viscometer. The result was a viscosity of 13.6 mPa s. This leads to the main finding of the paper; that the total increase in viscosity from the molecular mimic to the ionic liquid (by a factor of 219) can be divided into two contributions; increase from $MM \rightarrow MM^{hp}$ with a factor of 14 and again from $MM^{hp} \rightarrow IL$ with a factor of 16. This means that these two different increases in viscosity, the first from indirect effects of the Coulombic compaction and the second from direct effects of the charge network, are of equal importance. This result should be applicable for ionic liquids in general since Coulombic compaction and the formation of a charge network will be present in any case.

Finally, this paper also leads to the conclusion that a good model for transport properties in an ionic liquid should be able to predict the difference between the ionic liquid and the molecular mimic at isodense conditions.

Chapter 6

Calorimetric measurements

This chapter will present details from calorimetric measurements by use of Differential Scanning Calorimetry and Thermalization Calorimetry. It will begin with a description of the two methods followed by results and finally a discussion. The aim is to establish thermodynamic properties of the different ionic liquids studied in this thesis.

6.1 Differential Scanning Calorimetry

The Differential Scanning Calorimetry (DSC) method is a standard technique for measuring calorimetric properties of liquids such as the characteristic temperatures; melting temperatures, T_m , glass transition temperature, T_g , crystallization temperature, T_c , percent crystallinity, χ_c , heat capacity, C , heats of fusion, ΔH_m , and phase diagrams. It has the great advantage of providing quantitative measurements with high sensitivity and with a controlled heating rate [99].

The principle of the DSC is to measure the change of the *difference* of the heat flow rate between the sample and a reference sample, while both are being subjected to a controlled temperature change [100]. This is why the method is called *differential* scanning calorimetry and the principle increases the sensitivity of the method, since there is no need to take into consideration contributions from diverse thermal effects [99]. What is actually measured in a DSC instrument is a temperature difference given as difference in voltage through a thermocouple. The DSC instrument used in this thesis was a heat flux DSC with a disk-type measuring system.

The visual representation of the results from a DSC measurement is the normalized (to sample mass) heat flow as a function of temperature. This gives a heat flow curve with distinct features that can establish the thermodynamic properties mentioned in the beginning of this section. The so called isothermal baseline is what is measured if the heat flow is constant due to no difference between the sample and the reference. The glass transition can be seen as a dip in the heat flow when there is a transition from one isothermal baseline to another. This happens due to a change in specific heat from the glassy state to the liquid state and will also be further explained in section 6.2. T_g can then

be defined as either the onset of the dip or as the midpoint. In this work it is defined as the temperature at the midpoint of the transition.

Crystallization is a first-order exothermic phase transition and is seen as a peak in the heat flow. As with the glass transition, the crystallization temperature, T_c , can be determined in two ways; as the onset of the peak or as the position of the peak. For this work, the onset temperature was chosen. Another possibility with DSC is to calculate the energy that was released in the crystallization process by integrating the crystallization peak.

Melting is as opposed to crystallization an endothermic phase transition and is thus seen as a sharp decrease in the heat flow. As with crystallization, the melting temperature, T_m , is determined at either the onset of the decrease or at the minimum in heat flow. For this work T_m was defined as the minimum of the melting curve. It is also possible to find the energy used in the melting process by integrating the curve starting from the beginning of the melting process to the end of it (when the heat flow is back to the isothermal baseline).

All DSC measurements were performed at Chalmers Technical University, Göteborg, Sweden. The DSC device used was from TA-instrument with a temperature range of 93-823 K, temperature accuracy of ± 0.1 °C, baseline noise < 1 μ W and with a resolution of 60mW/°C. A typical sample size is around 10 mg.

6.2 Thermalization Calorimetry

The Red Box is the name of a Thermalization Calorimetry (TC) instrument that was developed at Roskilde University [101] and the most distinct feature is a red, metal box, hence the name. Despite its humble appearance it holds great potential when you want to characterize calorimetric properties of liquids, since the setup is simple as well as quick and easy to use. In the process of writing this thesis the shear mechanical properties was measured on several ionic liquids with completely unknown calorimetric properties such as T_g and T_m . So, in order to find the temperature range in which the liquid properties could be accessed in the super cooled region, I had to look in the blind. This was in many ways very time consuming and so I turned to the Red Box for assistance.

The Red Box works by measuring the rate of change in temperature by the use of a thermocouple inserted into the liquid sample. This gives the relative change in specific heat and so reveals exothermic and endothermic processes when plotting dT/dt as a function of T . An exothermic process happens during crystallization and appears as a peak/increase in dT/dt whereas an endothermic process happens during melting and appears as a sharp decrease in dT/dt .

The Red Box works by measuring the difference of temperature relative to ambient temperature using a thermocouple. This thermocouple measures the change in voltage which is caused by a change in temperature. The liquid sample is loaded into a small test tube and the thermocouple is placed in this tube such that it is covered by the liquid. The test tube is then sealed and submerged

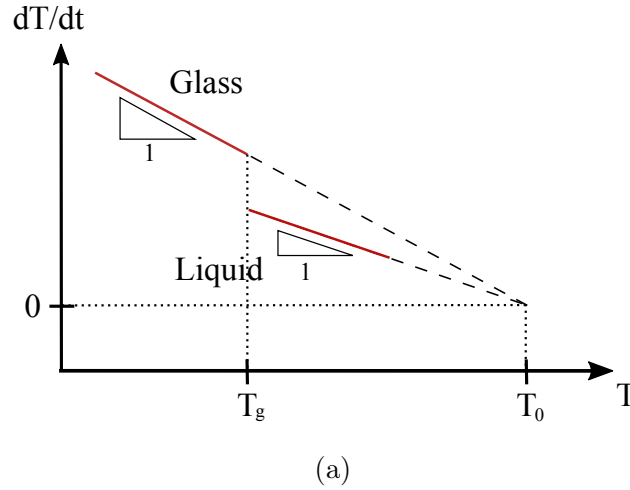


Figure 6.1: A schematic of the rate of change of temperature as a function of temperature. The two red lines show heating with constant specific heat in the glassy state (largest slope) and the liquid state (smallest slope). The jump between these lines is the glass transition and happens at the temperature T_g . Dashed lines show the linear relationship of dT/dt between the two points $(T, dT/dt)$ and $(T_0, 0)$. The slope of the lines is the inverse of the apparent specific heat, $(R_0C)^{-1}$. Inspired by figure 1 in [101].

into liquid nitrogen causing the whole sample and thermocouple to cool to a temperature of 77 K. After this, the test tube is removed from the nitrogen and placed inside a hole in an insulated box made from expanded polystyrene causing the sample to slowly heat due to the temperature gradient between the sample and the surroundings outside of the box. Note that the hole in the insulated box had been pre-cooled to 77 K. When the sample thus passively heats from 77 K all the way up to room temperature, the rate of change of temperature is measured, giving one the change of specific heat of the sample.

The data can be directly interpreted since the rate of change in temperature, dT/dt , is inversely proportional to the specific heat of the sample, C , when there is a given heat current input of $P(t) = dQ/dt$. The specific heat is defined as $\Delta T = \frac{1}{C}Q$, where Q is the heat. Combining the time derivative of this definition with Fourier's law of thermal conduction, $P(t) = -\frac{1}{R_0}(T(t) - T(0))$, the rate of change in temperature becomes

$$\frac{dT(t)}{dt} = -\frac{1}{R_0C}(T(t) - T_0) \quad (6.2.1)$$

where R_0 is the temperature independent thermal resistance of the experiment, T_0 is the target temperature and $T(t)$ is the sample temperature. When C is constant, dT/dt as a function of T will be a straight line between a point $(T, dT/dt)$ and the end point $(T_0, 0)$ with $1/(R_0C)$ as the slope. When/if C changes, the slope of the line will also change. This happens for example at the glass transition, where the sample goes from having a lower to a higher specific

heat. This is illustrated in figure 6.1. Here two different red lines illustrate the rate of change with two different specific heat values, one from the glassy state and one from the liquid state. The change in slope between the two states is clearly illustrated with the two, different triangles. In a real measurement, this change between the states will be seen as a sudden "dip" in the measured dT/dt . The apparent specific heat, R_0C , can be derived from the data by finding the slope of the dT/dt curve.

A detailed description of the method and setup can be found in the study by B. Jakobsen et al. [101].

6.3 Results

The following shows calorimetric results for a series of ionic liquids measured both with DSC and with the TC-method. The purpose of these measurements was to characterize the liquids and to get an overview of the different thermodynamic properties. T_c was in all cases found as the onset temperature and T_m as the minimum in the melting curve.

For the DSC measurements, the liquid was loaded into a small pan and sealed before the measurement. Procedure was cooling with a rate of 20 K/min down to 173 K, then an isothermal step of 5 minutes followed by ramping with 10 K/min to 313 K, but only the heating process is portrayed in the figure. DSC was measured on Pyr14-TFSI and Pyr18-TFSI.

The result for Pyr14-TFSI can be seen in figure 6.3a. T_g is seen as a small dip in the heat flow in the ramping around 185 K for Pyr14-TFSI. The DSC measurements also show the cold-crystallization at 216 K and a melting process split into two separate processes at 246 K and 254 K respectively. For Pyr18-TFSI the glass transition is at 191 K, there is cold-crystallization at 232 K and a melting in one single process at 258 K.

Ten ionic liquids as well as the molecular liquid squalane have been measured with the TC-method. The reason for choosing to measure on squalane for comparison to a liquid with well-defined glass transition and no cold-crystallization. The result from squalane can be seen in figure 6.2.

When measuring dielectric spectroscopy on neat Pyr15-TFSI it proved to be impossible to find a temperature range where the sample did not crystallize in the supercooled region. The results from the Red Box measurements clearly indicates why: The liquid has a very high and broad crystallization peak at 216 K, just after the glass transition as well as a much smaller peak at 199 K, see figure 6.3b. This result is one of the reasons why it was implemented to measure on new ionic liquids with the Red Box before proceeding with any further experimental methods. It is time consuming to find T_c and T_m with for example dielectric spectroscopy but the Red Box reveals these characteristics within only the hour it takes to perform the experiment.

Pyr14-TFSI mixed with $x = 0.05$ and $x = 0.10$ molar fraction of Li-TFSI respectively (called Pyr14x005 and Pyr14x01) gave two very different results,

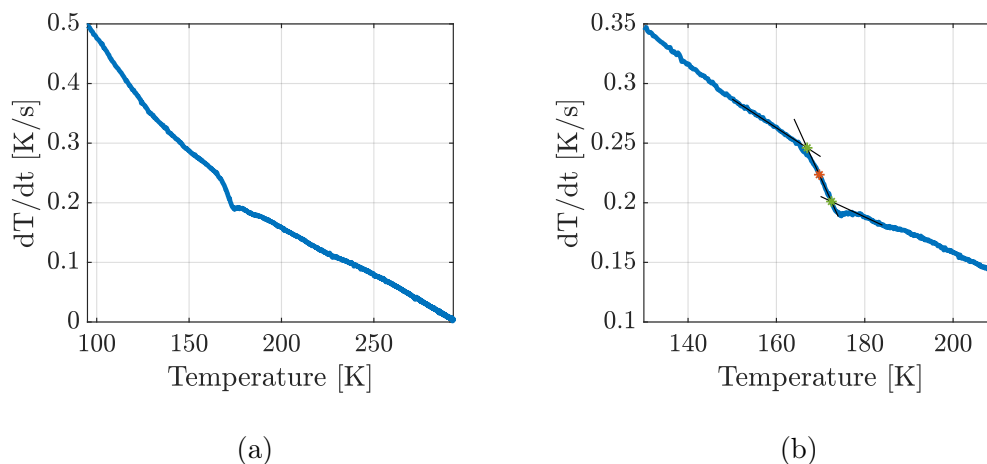


Figure 6.2: Squalane. Showing an example with no cold-crystallization and a clear glass transition at 170 K. b) is a zoom in on the data around the glass transition, where the green asterisk shows the intersections between the black lines found from a linear fit to that section of the curve. Orange asterisk is the midpoint T_g .

as can be seen in figure 6.4. For Pyr14x005 $T_g = 187$ K and there is a clear cold-crystallization process with $T_c = 222$ K. The peak is rather broad and is almost immediately followed by a messy and partial melting sequence spanning a temperature range of around 25 K. This makes it difficult to determine an exact melting temperature.

For Pyr14x01 it is another case. Here T_m is rather specific with two distinct melting curves at 254 K and 264 K. However, where the liquid crystallizes before this melting is not clear from the results. It could seem to happen gradually starting at just above $T_g = 192$ K and all the way to the melting, as seen by very small, subsequent peaks in the curve.

Pyr18-TFSI mixed with a molar fraction of $x = 0.2$ (Pyr18x02) and $x = 0.4$ (Pyr18x04) Li-TFSI respectively have been measured and, as with Pyr14-TFSI mixed with Li-salt, give very different results depending on the amount of Li-salt concentration, see in figure 6.5. For Pyr18x02 the glass transition is not easy to discern but seems to be at 204 K. This transition is followed by a small degree of cold-crystallization starting at 214 K and T_m is found to be 273. Pyr18x04 looks much like squalane with no detectable cold-crystallization or melting. The whole curve is very smooth and there is a clear glass transition at $T_g = 220$ K.

Finally, the three ionic liquids used for the second neutron scattering measurement, see section 11.2, were characterized in order to test if they supercool. This is not a bullet proof way to test if the liquids can supercool in the neutron scattering experiment since the cooling rate will be different there. With TC the cooling rate is very fast and uncontrolled where as in the neutron scattering measurements the cooling rate is controlled and slower. The difference in cooling rate, plus the difference in sample holder texture, can cause very different

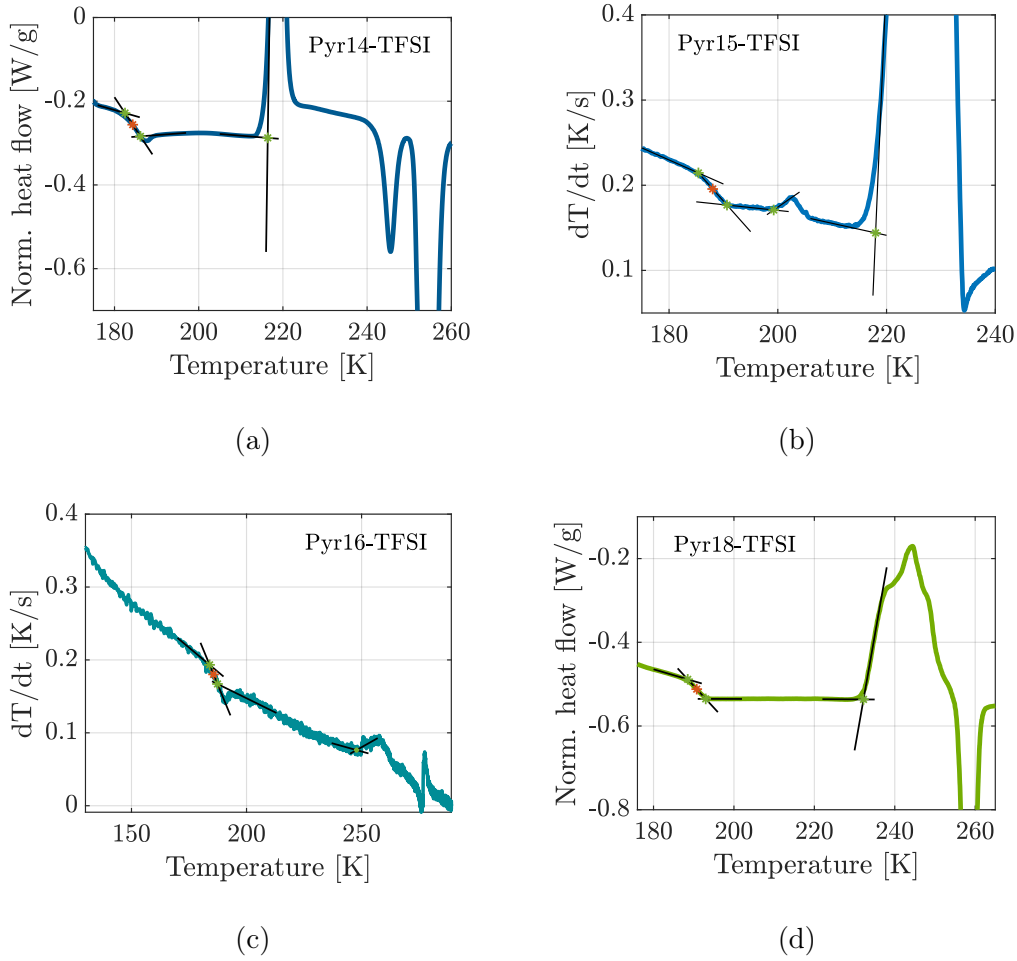


Figure 6.3: Results from DSC measurements on Pyr14-TFSI and Pyr18-TFSI as well as TC measurements on Pyr15-TFSI and Pyr16-TFSI. Green asterisk show the intersections between the black lines which are found from a linear fit to that section of the curve. The orange asterisk is the midpoint between the two green asterisks and mark the glass transition temperature.

amounts of cold-crystallization. In this sense, the DSC instrument would be better to characterize the liquids, since here the cooling rate can be controlled and thus be set to mimic the neutron scattering experiment.

The results can be seen in figure 6.6. The plots show a zoom in on the area around the glass transition and the cold-crystallization and reveal that all three liquids were supercooled and entered the glassy state. Pmim-BF₄ shows no cold-crystallization which corroborates findings in literature [85]. This is opposed to Bpyr-BF₄ and Emim-TCM, which both has a rather narrow supercooled temperature region and large cold-crystallization peaks.

Unfortunately, it turned out that only Pmim-BF₄ stayed liquid during the neutron scattering experiment. This could indicate that a large cold-crystallization and a narrow temperature range between the glass transition and this cold-

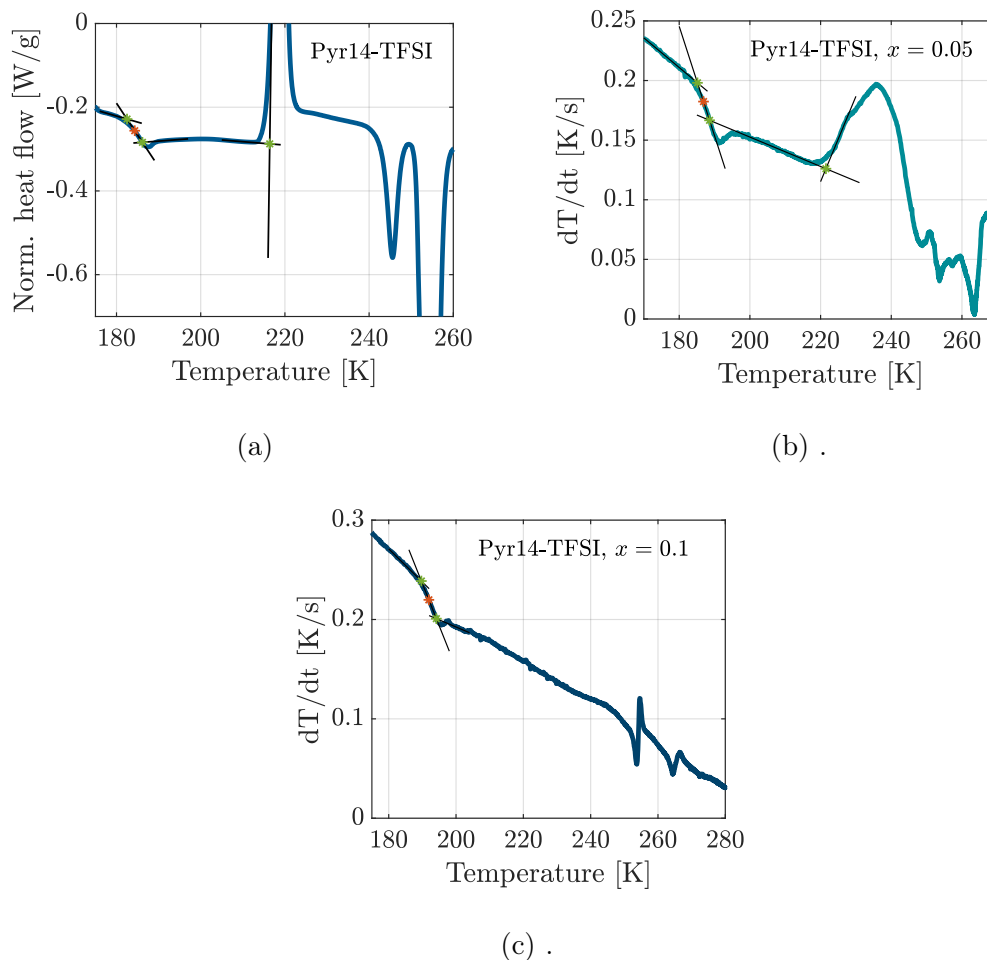


Figure 6.4: a) is neat Pyr14-TFSI, b) is Pyr14-TFSI with $x = 0.05$ molar fraction Li-TFSI. T_g is 187 K. At 222 K, a large broad peak shows clear cold-crystallization followed by partial melting in the range of 248-274 K. c) is Pyr14-TFSI with $x = 0.1$ molar fraction Li-TFSI. T_g is at 192 K and there is a clear partial melting of the crystal in the range of 250-268 K. In between a cold-crystallization necessarily takes place but it is difficult to discern due to an apparent lack of a crystallization peak. For both figures, the green asterisk shows the intersections between the black lines which are found from a linear fit to that section of the curve. Orange asterisk is the midpoint T_g .

crystallization in the TC measurements lead to a higher risk of cold-crystallization during cooling in the neutron scattering instrument.

6.4 Discussion

The DSC and TC results for all liquids measured in this study have been collected in table 6.1 and here clear trends in T_g can be detected. For the pyrrolidinium series with increasing alkyl-chain length T_g increases with increasing chain length

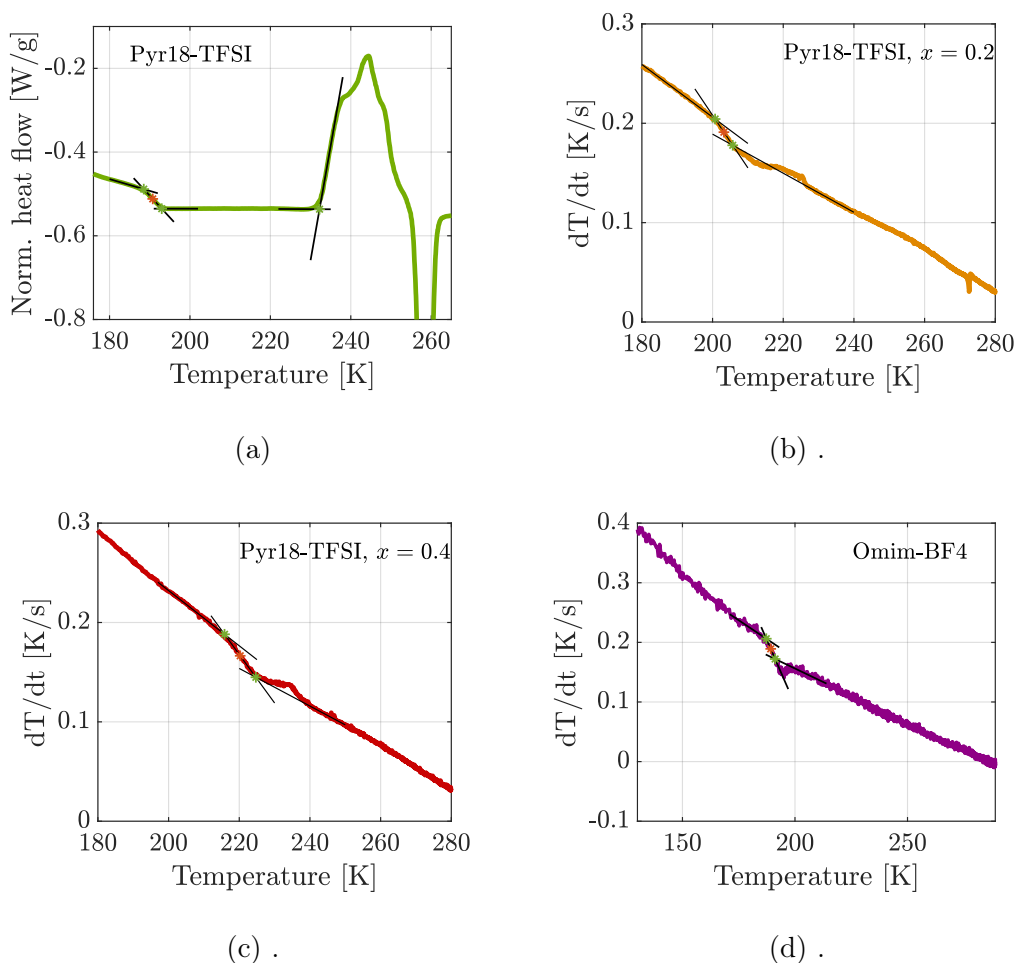


Figure 6.5: a) Neat Pyr18-TFSI. b) Pyr18-TFSI with $x = 0.2$ molar fraction Li-TFSI. T_g is a little hard to discern but the standard method gives a $T_g = 203$ K. At 214 a partial cold-crystallization sets in and T_m is at 272 K. c) Pyr18-TFSI with $x = 0.4$ molar fraction Li-TFSI. $T_g = 220$ K and there seems to be no detectable crystallization and melting in this liquid. The green asterisk shows the intersections between the black lines which are found from a linear fit to that section of the curve. Orange asterisk is the midpoint T_g .

except for Pyr15-TFSI which has a higher T_g than Pyr16-TFSI. For the two Li-salt mixed series T_g increases as well with increasing Li-salt concentration. This relation between T_g and increasing alkyl chain length/Li-salt concentration was also found for 1-alkyl-3-imidazolium tetrafluoroborate [102], Pyr14-TFSI mixed with Li-salt [70], 1-alkyl-3-methylimidazolium bis(trifluoromethane)sulfide [103] and Pyr1*n*-TFSI with $n = 4, 5, 6$ and 8 [80].

This systematic increase in T_g is especially interesting when comparing to the viscosity of the RTILs since viscosity also increases when increasing chain-length for imidazolium based RTILs [104–106] and Li-salt concentration in Pyr14-TFSI and Pyr18-TFSI.

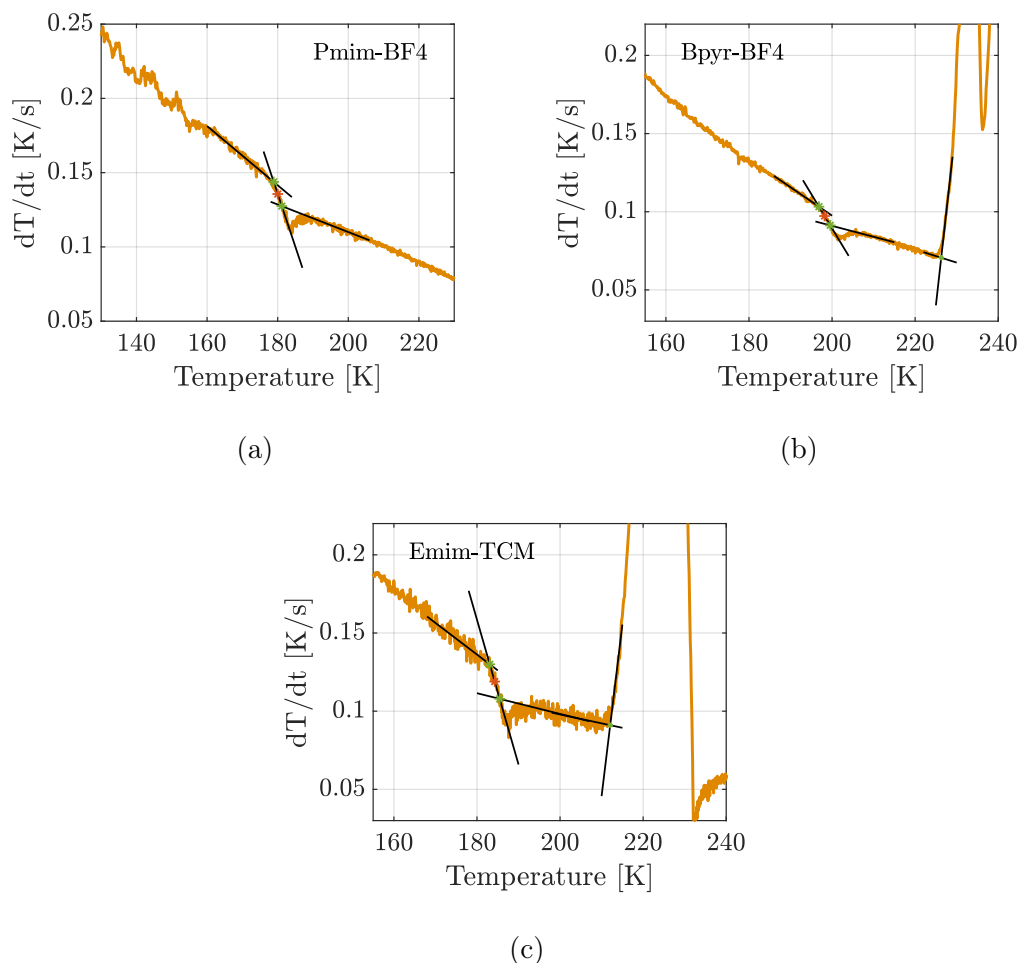


Figure 6.6: a) Pmim-BF4 with $T_g = 180$ K and not cold-crystallization. b) Bpyr-BF4 with $T_g = 198$, $T_c = 226$ K and $T_m = 259$ K. c) Emim-TCM with $T_g = 184$ K, $T_c = 212$ K and $T_m = 271$ K.

For the other two characteristics found from the calorimetric measurements, T_c and T_m , the picture is not so clear. There is no discernible systematic connection between the chemical composition and the transition temperatures. It is especially puzzling in the Pyr1*n*-TFSI series where Pyr15-TFSI has a T_c much closer to T_g than in both Pyr14-TFSI and Pyr18-TFSI.

The exception to this lack of systematic connection is Pyr14-TFSI and Pyr18-TFSI mixed with Li-salt where crystallization is suppressed with increasing Li-salt concentration. This effect is especially clear for Pyr18-TFSI mixed with Li-salt where crystallization is suppressed going from neat Pyr18-TFSI to 20% Li-salt concentration and even further suppressed going with 40% Li-salt concentration where there is no crystallization at all. The effect is less clear with Pyr14-TFSI mixed with Li-salt.

Another interesting thing to note in the Li-salt mixed Pyr14-TFSI series is that T_m is the same in both ionic liquids, and that the first of the two melting

temperatures are identical to the second melting temperature in neat Pyr14-TFSI. An explanation to this is however not within the scope of this thesis, but the result is contrary to literature which shows a slight decrease in T_m with increasing Li-salt concentration [107].

Liquid	T_g	T_c	T_m
Squalane	170	non	non
Pyr14-TFSI	185/184	216	246/254
Pyr15-TFSI	188	199	283/285
Pyr16-TFSI	186	248	276
Pyr18-TFSI	191/191	232	259
Pyr14-TFSI, $x = 0.05$ Li-TFSI	187	222	254/264
Pyr14-TFSI, $x = 0.1$ Li-TFSI	192	?	254/264
Pyr18-TFSI, $x = 0.2$ Li-TFSI	203	214	273
Pyr18-TFSI, $x = 0.4$ Li-TFSI	220	non	non
Pmim-BF4	180	non	non
Omim-BF4	189	non	non
BPyr-BF4	198	226	250
Emim-TCM	184	212	271

Table 6.1: A table showing the three characteristic temperatures, T_g , T_c and T_m , for squalane and several RTILs as found from the calorimetric measurements. All values are in Kelvin. For Pyr14-TFSI and Pyr18-TFSI the two T_g values were found both from DSC and TC measurements respectively.

Chapter 7

Comparative analysis, Pyr1*n*-TFSI

Room Temperature Ionic Liquids (RTILs) are complex in their structure and chemical composition when comparing to molecular liquids such as cumene or DC704. They are binary mixtures of anions and often large and bulky cations where the charge of both gives rise to not only competing interactions but also short- and long-range structures.

This is seen in the x-ray structure factor of RTILs where in general, in addition to the standard main peak arising from the nearest neighbor interaction, two additional peaks can be observed. The charge peak at intermediate Q -values related to charge alternation, which is also the signature of RTILs, and the pre-peak at even lower Q -values which is related to long range structures on the length scale of 10-30 nm. The question is then, if this complexity in structure and chemical composition is reflected in the dynamics of the RTILs?

One way to gain further insight into this complicated class of liquids, and to answer the question, is to measure the same response function on a series of the same type of RTILs but with small systematic changes to the chemical composition. This way, changes in the measured dynamic signal can be directly linked to the change in chemical composition. The reason for using this method is two-fold. Firstly, it makes it possible to say something concrete about the molecular origin of the dynamic modes and secondly, systematic behavior of the dynamics can be linked to systematic behavior as measured with other methods such as x-ray scattering.

This chapter will present results on a homologous series of pyrrolidinium-based RTILs with different measuring methods to look at systematic changes, and to compare results between response functions and to literature. The series is 1-alkyl-1-methylpyrrolidinium bis(trifluoromethanesulfonyl)imide with alkyl chain length, n , of 4, 6 and 8 carbon atoms, also called Pyr1*n*-TFSI.

Figure 7.1 shows how the charge peak and the pre-peak change with increasing alkyl chain length. The charge peak decreases and the pre-peak increases with increasing alkyl chain length, showing a drastic change in structure with a change of the alkyl group on the pyrrolidinium ring.

Studies with shear mechanical and dielectric measurements on supercooled Pyr1*n*-TFSI with $n = 4, 6$ and 8 have been performed before [80], but with

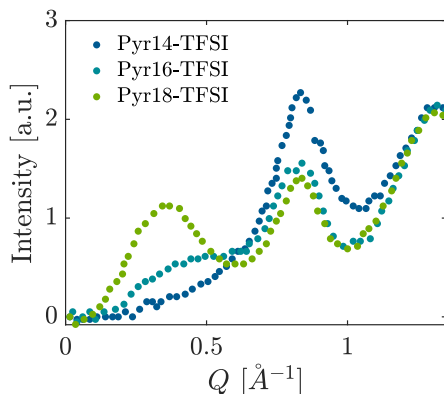


Figure 7.1: X-ray scattering structure factor for the homologous series Pyr1*n*-TFSI to show the change in structure with increasing alkyl chain length. The charge peak decreases and the pre-peak increases going from Pyr14-TFSI to Pyr18-TFSI. Data from [68].

no focus on the high-frequency dynamics of the shear mechanics. This is due to the fact that conventional rheometers have an upper limit in frequency of around a 100 Hz, a problem avoided by the use of the PSG. This study will, as a consequence, for the first time compare high-frequency shear mechanical results to those obtained by broadband dielectric measurements on RTILs.

The chapter is divided into three parts related to the method used to investigate the dynamic modes; dynamical mechanical spectroscopy (DMS), broadband dielectric spectroscopy (BDS) and the two combined. Each of the three parts will start by presenting individual results on the three liquids in this series; Pyr1*n*-TFSI with $n = 4, 6$ and 8 followed by a comparative analysis.

7.1 Dynamic Mechanical Spectroscopy

This section will go through some of the common features for the three liquids presented in this chapter. Both with regards to storage, sample preparation and shear modulus measurements.

7.1.1 Method

All three liquids used in the Pyr1*n*-TFSI series were of 99.9% purity, purchased from Solvionic and used as received. Previous studies [108] have shown that Pyr14-TFSI is highly hygroscopic and therefore quickly absorbs water when it is exposed to moisture. This was assumed to also apply to Pyr16-TFSI and Pyr18-TFSI and therefore all preparation and storage of the samples took place inside a glove box with an inert, dry nitrogen atmosphere.

Two frequency sweeps were made at all temperatures with a spectrum taking around 1 hour if going to 10 mHz and around 10 h if going to 1 mHz. There was

a waiting time between each sweep of 10 minutes. At each temperature it was made sure that no change was seen between these two spectra which indicates that no crystallization had taking place.

The shear modulus was measured with a closed-cycle cryostat [48] where also the subsequent BDS measurements took place, making a direct comparison between results from the two methods possible.

7.1.2 Pyr14-TFSI

The first ionic liquid studied in this work is 1-butyl-1-methylpyrrolidinium bis-(trifluoromethanesulfonyl)imide (Pyr14-TFSI) which is well studied with various other techniques [69–75]. T_m and T_g is 254 and 185 K respectively as measured in this work by differential scanning calorimetry (DSC). The shear mechanical data on Pyr14-TFSI from this section have also been published in a previous study [95].

The liquid has a small degree of mesoscale structures due to the alkyl-chain length which are visible in NMR measurements [71] but not in x-ray scattering experiments [69]. Furthermore the x-ray signal shows a charge alternation peak [69]. It was also found in this study that the supercooled liquid is highly prone to cold-crystallization around 192-254 K in the shear measurements and at 216-254 K in the DSC measurements.

Because the liquid is prone to cold-crystallization the method was to cool it rapidly down to 190 K since previous tests showed no crystallization below this temperature. Subsequently, the spectra in the supercooled state were measured in cooling with 2 K steps from 190-180 K.

Spectra in the glassy state were measured on a new sample by cooling to 188 K and then measuring a spectrum which collapsed with the 188 K spectrum from the previous measurement. Spectra were then measured at 178 K and 177 K. The waiting time between the 188 K and 178/177 K measurement was 24 hours. Two spectra were just as before measured at each temperature where each spectrum took approximately 10 hours to measure and importantly no aging was observed in the modulus between the two spectra at the same temperature.

Fig. 7.2 shows the real and imaginary part of the shear modulus for Pyr14-TFSI in the temperature range 177 K to 190 K plotted on a log-linear and a log-log scale. The alpha relaxation is seen as an increase in the real part of the modulus and as a prominent peak in the imaginary part. Both of these features move to lower frequencies upon cooling as was also expected.

The spectra reveal a prominent and high intensity beta relaxation at high frequencies close to 10 kHz. A beta relaxation like this is commonly seen in other liquids [16, 109]. The beta relaxation appears to be temperature independent in position and amplitude in the liquid state, whereas it has a small change in both intensity and position in the glassy state.

There is also an additional feature in the shear spectra located around 0.1 Hz. It is low in intensity and appears as a small shoulder around 182 K and then becomes more evident around 178 K. The mode appears to have weak or

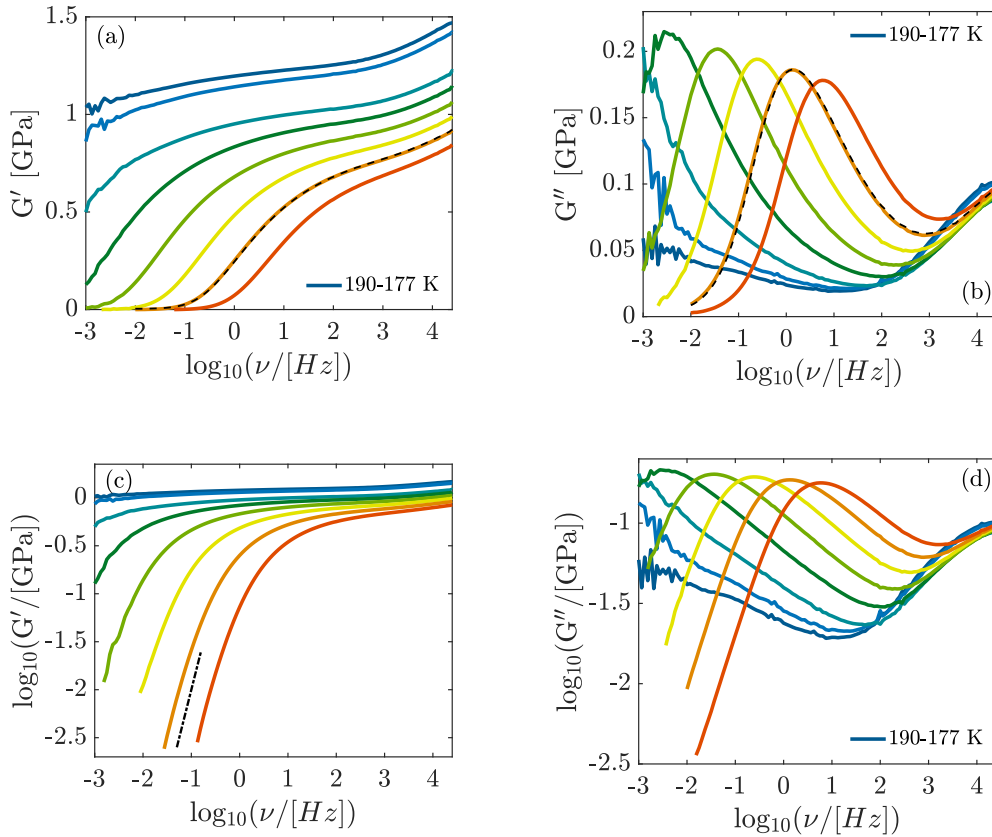


Figure 7.2: The complex shear modulus of Pyr14-TFSI plotted as the a) real part, b) imaginary part, c) logarithm of the real part and d) logarithm of the imaginary part. Data were taken at temperatures ranging from 177-190 K. Black dashed line on top of the 188 K curve is from the second measurement at 188 K which was followed by measuring in the glass at 178 and 177 K.

maybe even no temperature dependence, but since it is merged with the alpha relaxation it is hard to judge precisely.

Finally, it can be seen that at frequencies below the alpha relaxation the signal enters viscous flow with the characteristic power law behaviors in real and imaginary part [18].

7.1.3 Pyr16-TFSI

The second liquid in this series is 1-hexyl-1-methylpyrrolidinium bis(trifluoromethanesulfonyl)imide (Pyr16-TFSI). T_g was measured with thermalization calorimetry to be 186 K and T_m to be 276 K.

As mentioned before this liquid has been studied before with DMS [80] and it shows pronounced mesoscale aggregation as seen by NMR [71] and a pronounced pre-peak in the x-ray structure factor [68]. Due to cold-crystallization it was only possible to measure shear modulus in the temperature range of 198-182 K,

where the lower limit is due to the liquid going too deep into the glassy state.

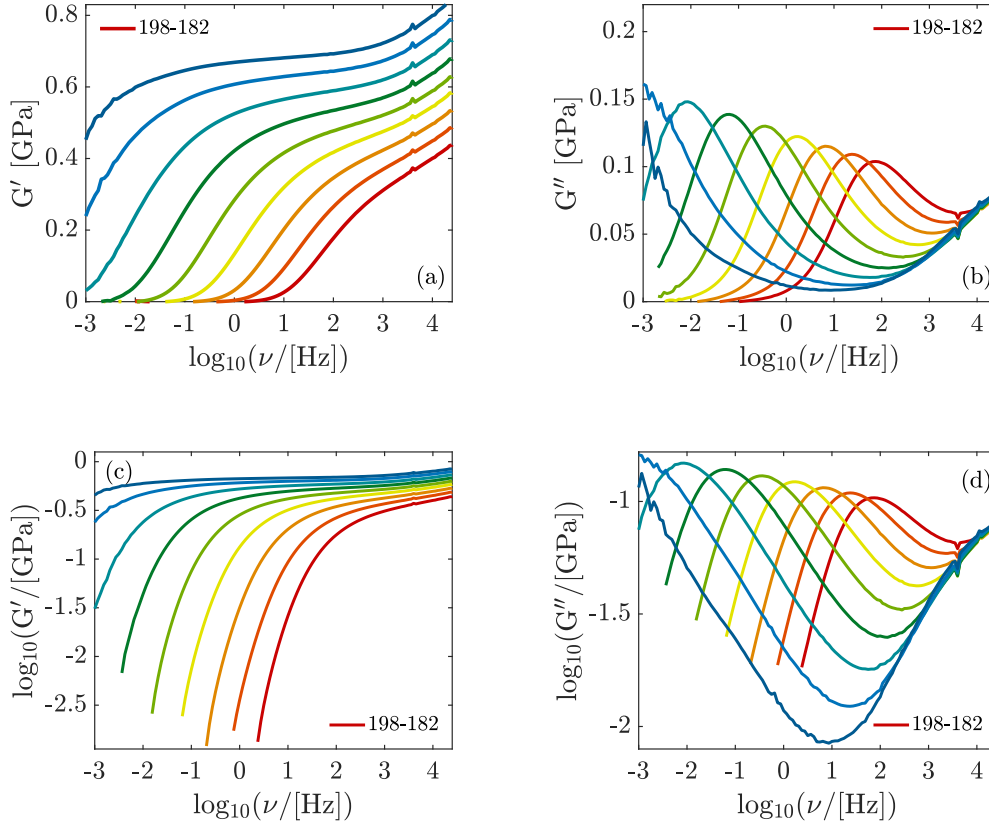


Figure 7.3: The complex shear modulus for Pyr16-TFSI from 198-182 K in steps of 2 K. a) and b) are a lin-log plot. c) and d) are log-log plots.

The results from the shear modulus measurements taken on the PSG for Pyr16-TFSI can be seen in figure 7.3. The data clearly show a standard, temperature dependent alpha relaxation with an increasing intensity at decreasing temperature. At 182 K the alpha relaxation has moved out of the frequency window.

The spectra also reveal what seems to be a temperature independent beta relaxation at high frequencies. It appears to have a maximum in intensity at around 10 kHz, but the relaxation peak is outside of the frequency window which makes it difficult to discern any specific properties. No additional features are seen in the spectra which reach the terminal mode at the six highest temperatures.

7.1.4 Pyr18-TFSI

The second liquid in this series is 1-octyl-1-methylpyrrolidinium bis(trifluoromethanesulfonyl)imide (Pyr18-TFSI). T_g was measured with thermalization calorimetry to be 191 K and T_m to be 259 K.

As with the other two liquids in the series, Pyr18-TFSI has been measured before in literature [69,80,84]. It shows even more pronounced mesoscale aggregation than Pyr16-TFSI [71] which is also seen as an increase of the pre-peak in the x-ray structure factor [68]. Pyr18-TFSI is also prone to cold-crystallization and so liquid measurements could only take place from 200-184 K. See figure 7.4 for the results on shear modulus as measured with the PSG.

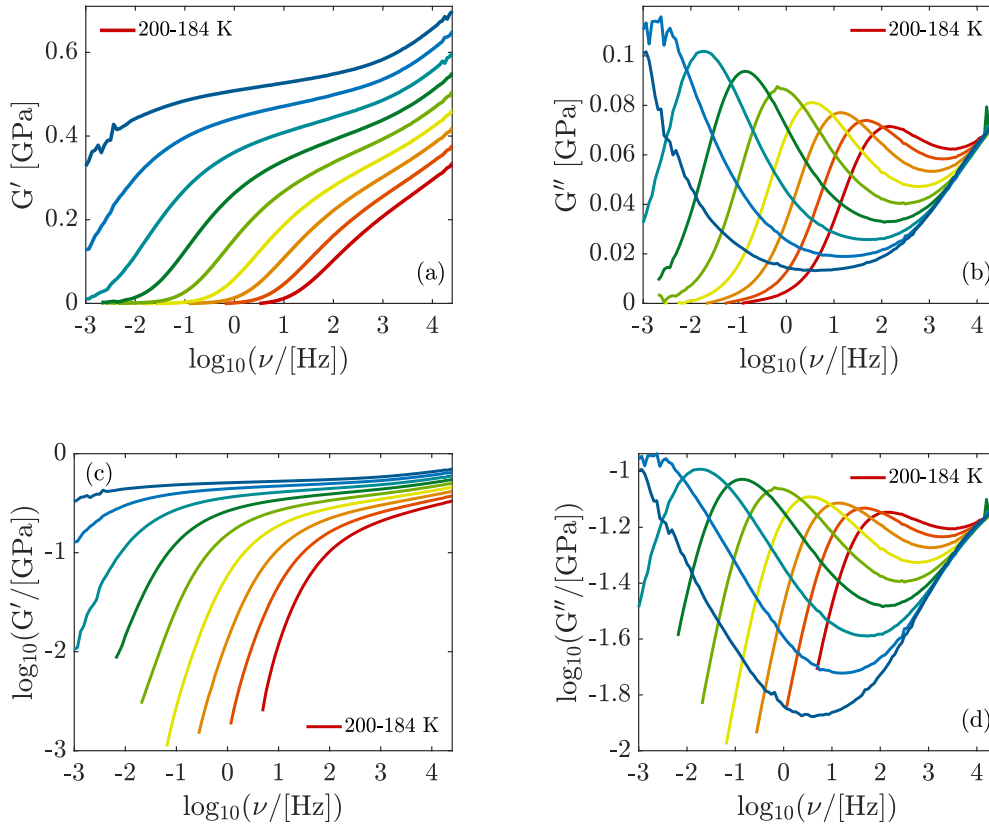


Figure 7.4: The complex shear modulus of neat Pyr18-TFSI plotted as the a) real part, b) imaginary part, c) logarithm of the real part and d) logarithm of the imaginary part. Data were taken at temperatures ranging from 200-184 K.

As with Pyr14-TFSI and Pyr16-TFSI the data reveals two distinct relaxations: 1) an alpha relaxation that is temperature dependent with increased intensity as the temperature is decreased and 2) a very high intensity beta relaxation at frequencies around 10 kHz. Again, the peak of the beta relaxation is out of the experimental window and only the left flank is measured. This also makes it difficult to deduce the exact position, intensity and temperature dependence, but, by visual inspection it would seem that it is much less temperature dependent than the alpha relaxation. Only these two relaxational modes are seen and all spectra reach the terminal mode after the alpha relaxation.

7.1.5 Alpha relaxation

The first and obvious property to compare across the three liquids in the series is the alpha or structural relaxation. It is a primary feature of a liquid and is therefore a good starting point of a comparative analysis.

The alpha relaxation can be found by different analytical methods. One is to fit the spectra to a model expression containing the alpha relaxation time as a fitting parameter. In this work the spectra at all temperatures were attempted fitted to an electrical circuit model containing a contribution from both an alpha and beta relaxation [109] in order to extract the time scales of both dynamic modes. It was unfortunately not possible to obtain a reliable fit at all temperatures due to the peak of the beta relaxation being out of the frequency window.

Instead, the time scales for the alpha relaxation of the three liquids were found as $\tau_\alpha = 1/(2\pi\nu_{max})$, where ν_{max} is the frequency at the alpha relaxation peak. This frequency was found by fitting the imaginary part of the shear modulus just around the alpha relaxation peak to a second-degree polynomial. This is a purely phenomenological method and only serves to find the top point of the peak itself. The resulting alpha relaxation times can be seen in figure 7.5.

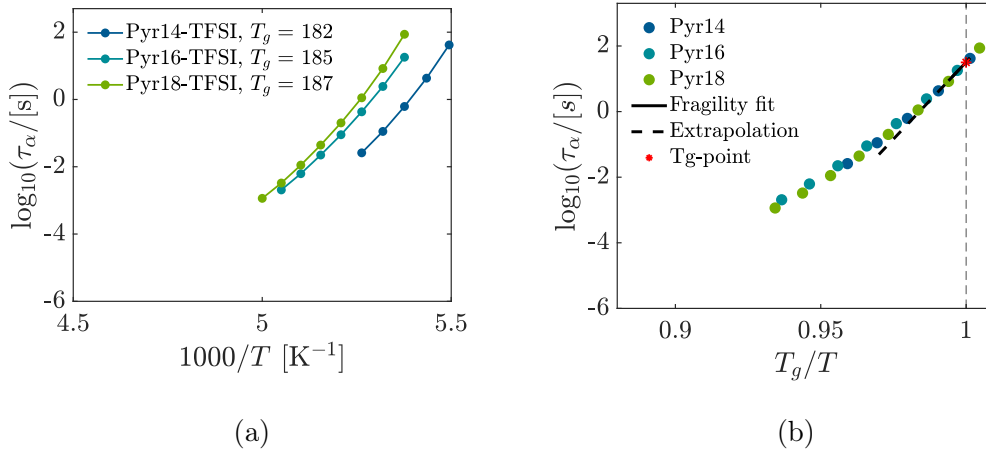


Figure 7.5: a) Alpha relaxation times for three Pyr1*n*-TFSI RTILs shown as a function of inverse temperature. The fragility was found using a definition of T_g as where $\log_{10}(\tau_\alpha) = 1.5$. b) Same as in a) with temperature scaled to T_g showing a collapse of data at all temperatures. It also shows T_g (red asterisk) and the resulting linear fit (black solid line) to find the isobaric fragility index which in this case is $m_p = 90 \pm 5$. Black dashed line is an extrapolation of the fragility fit.

As expected Pyr1*n*-TFSI slows down with increasing alkyl chain length, as was also the case in the study by T. Wu et al. [80]. Another common feature between this study and literature is that the relative increase in alpha relaxation time is not systematically linked to number of carbon atoms in the alkyl chain.

This is seen in figure 7.5a where there is a larger slowing down between Pyr14-TFSI and Pyr16-TFSI than between Pyr16-TFSI and Pyr18-TFSI.

The glass transition temperatures were found to be 182 K, 185 K and 187 K for Pyr14-TFSI, Pyr16-TFSI and Pyr18-TFSI respectively. T_g was defined as the temperature at which $\log_{10}(\tau_\alpha) = 1.5$. For Pyr14-TFSI and Pyr18-TFSI this T_g point was found by interpolating between the two coldest temperatures and for Pyr16-TFSI it was found by extrapolating beyond the coldest measured temperature. This increase in T_g with increasing alkyl chain length confirms findings in literature [80].

In order to compare the temperature dependence of the alpha relaxation time in the series, the data from figure 7.5b have been scaled to the found T_g , see figure 7.5b. The temperature dependence of the three liquids is very similar and hard to distinguish by eye. Consequently, the isobaric Angell fragility index, m_p , given as [8,9]

$$m_p = \left. \frac{d \log_{10}(\tau_\alpha)}{d T_g/T} \right|_{T=T_g} \quad (7.1.1)$$

was calculated for all three liquids simultaneously. Again, T_g was defined as where $\log_{10}(\tau_\alpha) = 1.5$.

The result was an isobaric fragility index of $m_p = 90 \pm 5$. The reason behind the uncertainty is that the resulting slope, found from best-fit parameters, is highly sensitive to the number of data points just around T_g chosen to be included in the fit. There is no definitive objective way to select the correct number of data points/temperature interval to be included in the fragility fit and so, this degree of flexibility is reflected in the uncertainty of ± 5 . The fragility index will be presented with uncertainties found from this principle in the rest of the thesis.

The resulting fragility index is slightly higher than in literature where m_p was found to be 82, 81 and 86 for Pyr14-TFSI, Pyr16-TFSI and Pyr18-TFSI respectively, but with a defined T_g as $\log_{10}(\tau_\alpha) = 1$. The lower defined T_g value could explain this discrepancy, but it could alternatively be due to the higher number of data points around T_g in this study.

7.1.6 Beta relaxation

It is clear that all three ionic liquids have a secondary relaxation at high frequencies at around 10 kHz, a relaxation that is here named the beta relaxation. This dynamic mode appears in all cases to be relatively temperature independent, since the curves at all temperatures collapse around this beta relaxation peak. In the shear modulus representation it is not clearly resolved and so, quantitative properties cannot be deduced.

It is however possible to draw some preliminary conclusions from visual inspection. There is a systematic increase in intensity of the beta relaxation as seen relative to the alpha relaxation with increasing alkyl chain length. Note that a comparison of the absolute value of G^* across samples is difficult since it can vary with 5-10% due to small deviations in the filling degree of the transducer from sample to sample [41].

Another feature is that the separation between the alpha and beta relaxation seems to increase with increasing alkyl chain length. This is most visible at lower temperatures where there is almost a plateau between the two relaxations in Pyr18-TFSI.

Compliance Another way to look at the data is to convert it to the complex compliance representation, which is the inverse of the shear modulus, $J^*(\omega) = 1/G^*(\omega)$. The beta relaxation is much better resolved in the imaginary part of the shear compliance, J'' , for all three liquids, as can be seen in figure 7.6.

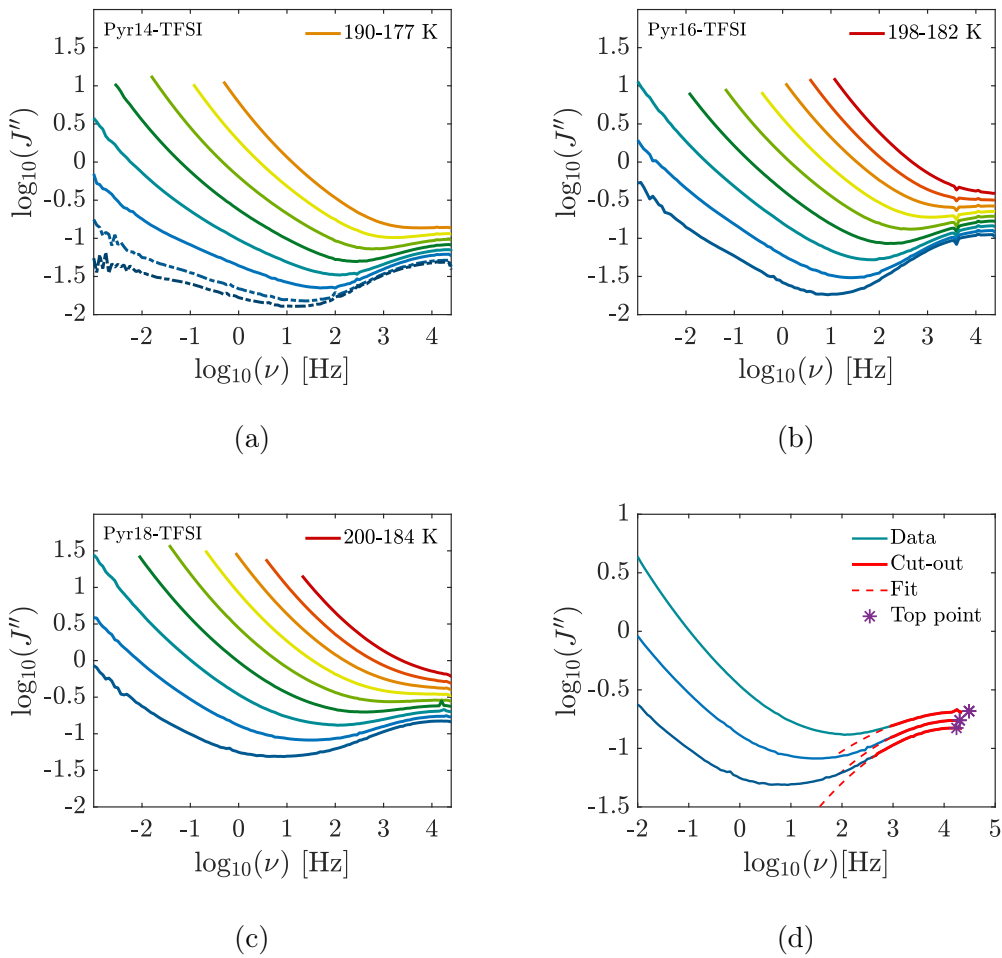


Figure 7.6: The imaginary part of the complex compliance, J'' , for a) Pyr14-TFSI, b) Pyr16-TFSI and c) Pyr18-TFSI. In this representation, the beta relaxation is better resolved than in the shear modulus making it possible to discern the actual peak. d) is an example of the procedure to find the beta relaxation time. The red, solid line is the data fitted to a second-degree polynomial (red, dashed line). The purple asterisk is the resulting top point giving the relaxation time.

The beta relaxation time was found by the same method as with the alpha

relaxation, i.e. fitting the logarithm of the just around the peak to a second-degree polynomial. The choice of fit function is somewhat arbitrary, but it works well when the objective is to only find the peak position. An example of this procedure can be seen in figure 7.6d, where the red, solid line is the data used in the fitting and the red, dashed line is the second-degree polynomial plotted using best-fit parameters. The purple asterisk is the resulting top point found from best-fit parameters showing that the method works reasonably well. A drawback of this method is that the relaxation time can only be found for temperatures where the relaxation peak is within the frequency window.

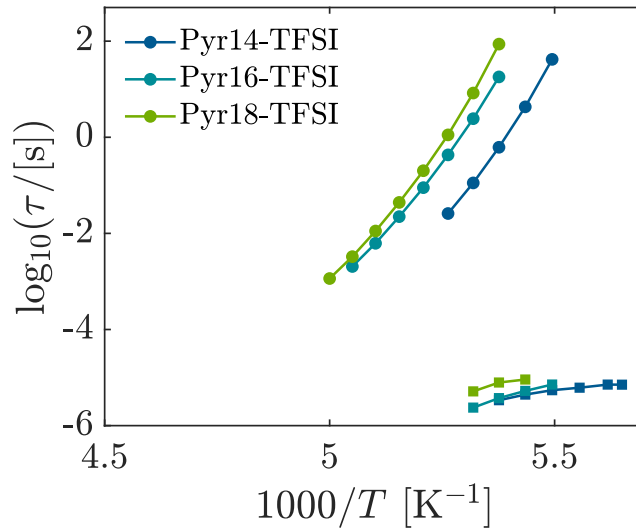


Figure 7.7: An Arrhenius plot showing the alpha relaxation (circles) as found from shear modulus and beta relaxation (squares) as found from shear compliance, for the three liquids in the series. Both dynamic modes slow down with increasing alkyl chain length.

The resulting relaxation times are shown in an Arrhenius plot in figure 7.7 for both the alpha relaxation time as found by shear modulus and the beta relaxation as found from the shear compliance. The results confirm the preliminary conclusion that the beta relaxation is close to temperature independent and that it slows down with increasing chain length. Furthermore, there is a weak temperature dependence of the beta relaxation which is Arrhenius in nature.

Due to this observation, it is possible to find an activation energy of the beta relaxation, E_β , according to the Arrhenius relation

$$\tau = \tau_0 e^{E_\beta/RT} \quad (7.1.2)$$

where τ_0 is a characteristic time and R is the gas constant.

The resulting activation energies are 9.74 kJ/mol, 22.6 kJ/mol and 17.7 kJ/mol for Pyr14-TFSI, Pyr16-TFSI and Pyr18-TFSI respectively with corresponding τ_0 values of $1.8 \cdot 10^{-12}$ s, $8.5 \cdot 10^{-21}$ s and $2.5 \cdot 10^{-17}$ s. The τ_0 values for

Pyr16-TFSI and Pyr18-TFSI are unphysical and the activation energies in these two cases can therefore not be trusted.

This is the first time that DMS measurements have made it possible to reveal quantitative properties about a beta relaxation in RTIL.

7.1.7 TTS

The first criterion for simplicity in glass-forming liquids was presented in chapter 2 and states, that for a liquid to be simple it must obey time-temperature-pressure superposition (TTPS). This is an expansion of time-temperature superposition which means, that the shape of the relaxation spectrum is constant at all temperatures. TTPS is thus a constant spectral shape at all temperatures *and* pressures, but since the RTILs in this thesis were only measured at ambient pressure, it was only possible to test TTS. This is still a reasonable way to test the first criterion for simplicity since a liquid exhibiting TTS will most likely also exhibit TTPS. Note that it is the first time TTS can be tested in shear modulus results of RTILs, due to the extraordinary frequency range of the PSG.

Figure 7.8 shows a TTS plot of the logarithm of the real and imaginary part of the shear modulus for all three liquids in the Pyr1*n*-TFSI series. Both the real and imaginary part of the spectra at all temperatures were scaled to a point in the imaginary part, which lies 30% down in modulus from the alpha relaxation peak to the low-frequency side of the peak (called *lp*). The reason behind this choice of scaling was, that the alpha relaxation is broadened slightly due to the merging of the beta relaxation at higher temperatures in Pyr18-TFSI. A scaling on the low-frequency side of the alpha relaxation peak thus gives a better collapse of data.

The figure shows qualitatively the same trend for all three liquids; almost perfect TTS for the alpha relaxation, but not for the beta relaxation. This is observed as a nice collapse of data around the alpha relaxation peak, which extends to the high-frequency side of the peak in a frequency range depending on temperature. The collapse of data worsens with increasing temperature, and this is interpreted as being due to the beta relaxation increasingly merging with the alpha relaxation. This interpretation is supported by visual inspection of figure 7.8, where there is a mastercurve extending from the terminal mode to around 10 kHz for all three liquids. At each temperature, the curve systematically starts to deviate from this mastercurve, going into a minimum of equal distance to the mastercurve and then increase towards the beta relaxation peak. This shows that the beta relaxation is most likely responsible for the deviation from TTS.

Consequently, only the alpha relaxation can be said to exhibit simple behavior and thus, that the three RTILs do not comply to the criterion of complete TTS. This is not surprising since the Arrhenius plot in figure 7.7 shows a much weaker temperature dependence of the beta relaxation compared to the alpha relaxation. That the alpha relaxation seems to obey TTS in all three liquids supports the idea that this is a general behavior in glass-forming liquids [4].

These results also show that, even though the RTILs studied in this chapter

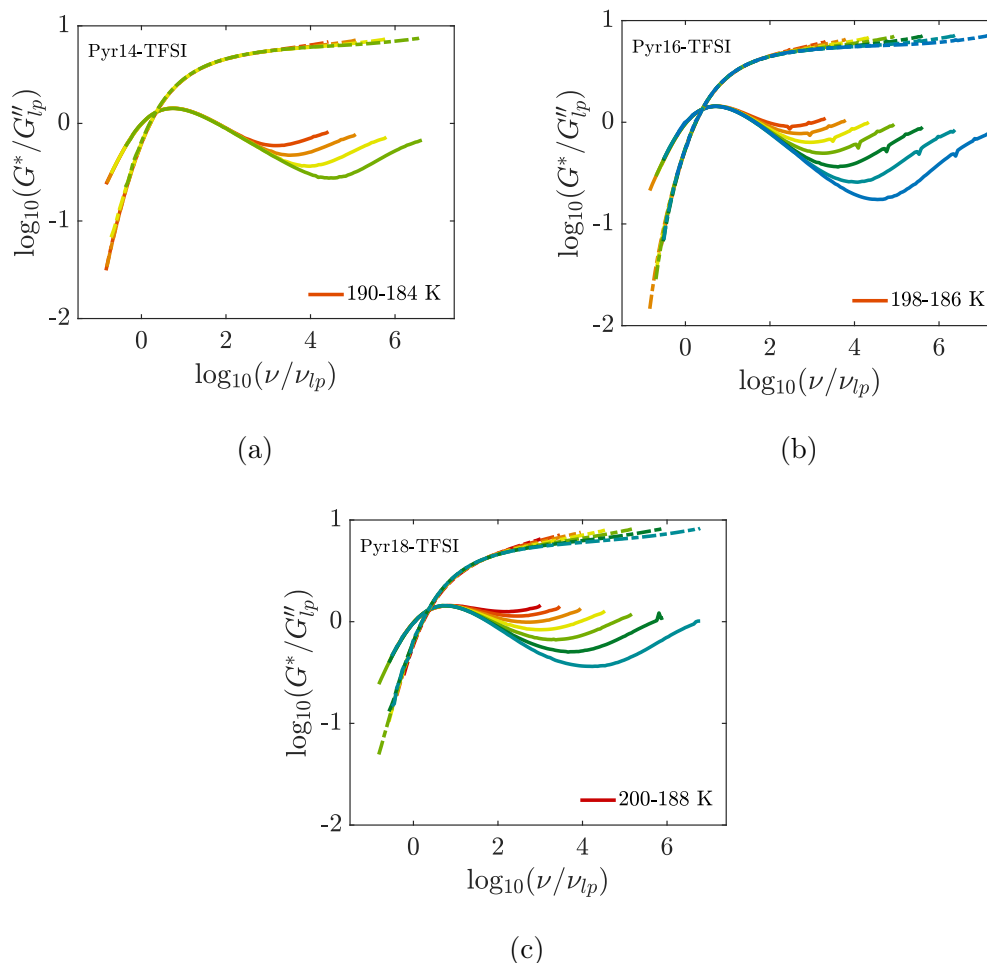


Figure 7.8: TTS plot of the logarithm of the real (dashed-dotted) and imaginary (solid) part of the shear modulus for the three liquids in the Pyr1*n*-TFSI series. All temperatures have been scaled to a point in the modulus which lies 30% in modulus below the alpha relaxation peak on the low frequency side (lp). It shows a high degree of TTS for the alpha relaxation in all three liquids which is not present for the beta relaxation.

do not exhibit complete simple behavior as for example DC704, the behavior of the relaxation spectra seen in figure 7.8 still match that of non-associated molecular liquids like squalane [109] and polyisobutylene [16].

7.2 Broadband Dielectric Spectroscopy

7.2.1 Method

This section will go through the common procedure when measuring BDS on the three ionic liquids in the series. All BDS measurements were performed in the same cryostat [48] as the DMS measurements making a direct comparison of

time scales possible, since the temperature control is the exact same in the two cases.

As with the DMS measurements, all three ionic liquids used in the Pyr1*n*-TFSI series was of 99.9% purity, purchased from Solvionic and used as received, plus, all preparation and storage of the samples took place inside a glove box with inert, dry nitrogen atmosphere.

The BDS data will not be presented for the individual liquids in separate subsections as with the DMS data, but instead be divided into the different representations used. The reason is that there are four different representations; complex permittivity, ε^* , the derivative of complex permittivity, $\varepsilon''_{der} = (-\pi/2)(\partial\varepsilon'/\partial\ln(f))$, the dielectric modulus that is $M^*(\omega) = 1/\varepsilon^*(\omega)$ and conductivity. All four representations can reveal different aspects of the results and will each time be presented in comparison to the other ionic liquids in the series.

7.2.2 Alpha relaxation

The alpha relaxation is in the dielectric permittivity obscured by the high conductivity in all three ionic liquids, see figure 7.9 where ε'' is shown as dashed lines. The conductivity contribution to the spectra can however be removed by using the derivative representation, ε''_{der} , which is explained in detail in section 3.2.

A dynamic mode is present in all three ionic liquids at all temperatures, seen as a shoulder in the spectra, just before electrode polarization enters the signal, and this mode was identified as the alpha relaxation. Note that the electrode polarization is not an intrinsic feature of the dielectric permittivity, but an experimental artifact dependent on the geometry of the capacitor. The relaxation times of this mode was found by fitting the logarithm of ε''_{der} just around the alpha relaxation peak to a second-degree polynomial and then identifying that $\tau_{\alpha,d} = 1/(2\pi\nu_{max})$. This choice of fitting function is purely phenomenological and only serves to find the peak position, see figure 7.9d for an example showing that the method yields reasonable results. For Pyr18x02 there is only a shoulder in ε''_{der} which will increase the uncertainty of the found alpha relaxation with this method.

The resulting relaxation times have been plotted together with the alpha relaxation time from the shear modulus data in figure 7.10. For all three ionic liquids the time scale of the alpha relaxation in BDS, $\tau_{\alpha,d}$, matches that of the structural relaxation as found from the shear modulus, $\tau_{\alpha,s}$, well, despite small differences. Furthermore, the alpha relaxation is faster in the shear modulus. These findings agree with results from literature on other ionic liquids [31, 110, 111] and non-associated molecular liquids [33].

$\tau_{\alpha,d}$ for all three liquids has been scaled to T_g , which was defined as where $\log_{10}(\tau_{\alpha,d}) = 1$, see figure 7.10b. As with the alpha relaxation found from the shear modulus, all three curves collapse when scaled to T_g which justifies the calculation of a single isobaric fragility index found from a collected dataset. This was found to be $m_p = 67 \pm 4$, which is lower than the fragility found from

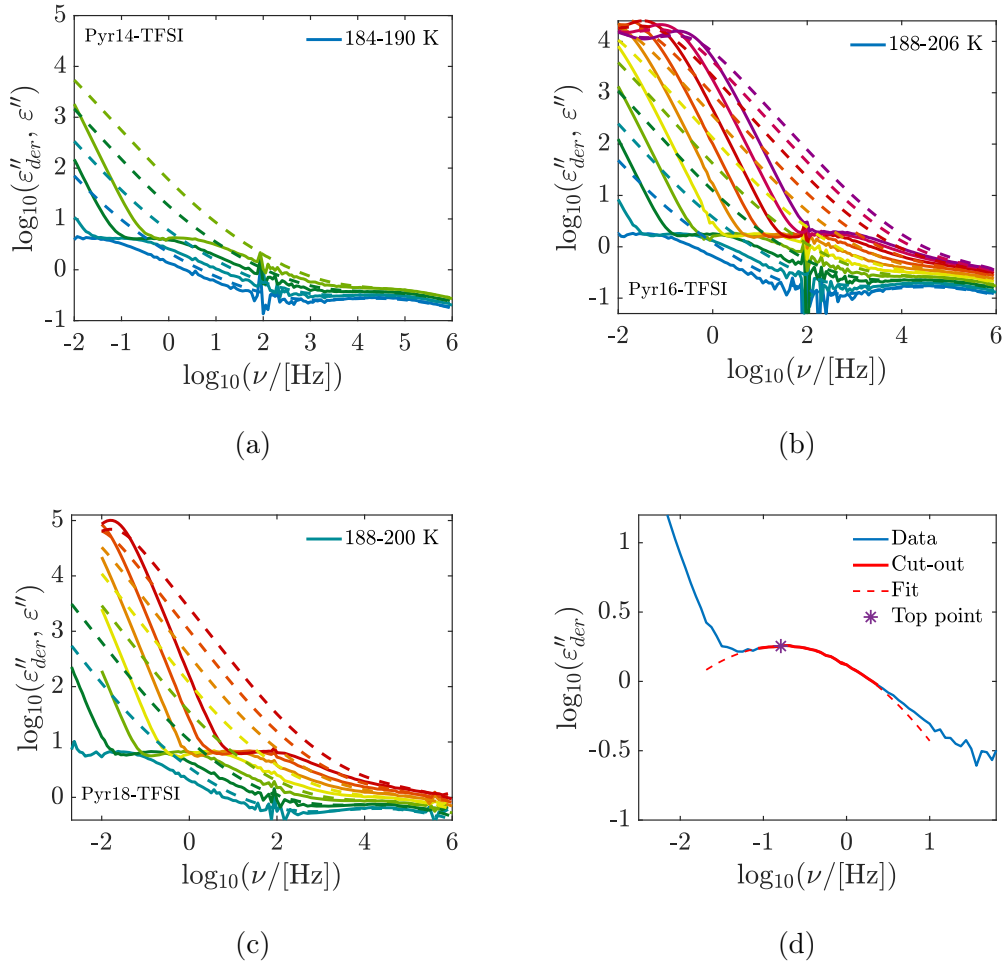


Figure 7.9: The derivative representation of the complex permittivity (solid lines) for a) Pyr14-TFSI, b) Pyr16-TFSI and c) Pyr18-TFSI shown together with the imaginary part of the complex permittivity (dashed lines) for comparison. d) is an example of the alpha relaxation time found from the top point (purple asterisk) of a second-degree polynomial (dashed red) fitted to the data around the peak (solid red).

shear modulus.

7.2.3 Beta relaxation

Figure 7.9 also reveal a secondary relaxation at high frequencies in all three liquids. This was expected since a previous study concludes that, if a beta relaxation is present in the shear modulus, it will also be present in the dielectric permittivity [16].

A quick comparison with the shear compliance data, which is the mechanical equivalent of the dielectric permittivity, shows that this beta relaxation share some similarities with the mechanical data. The peak is located around 10 kHz

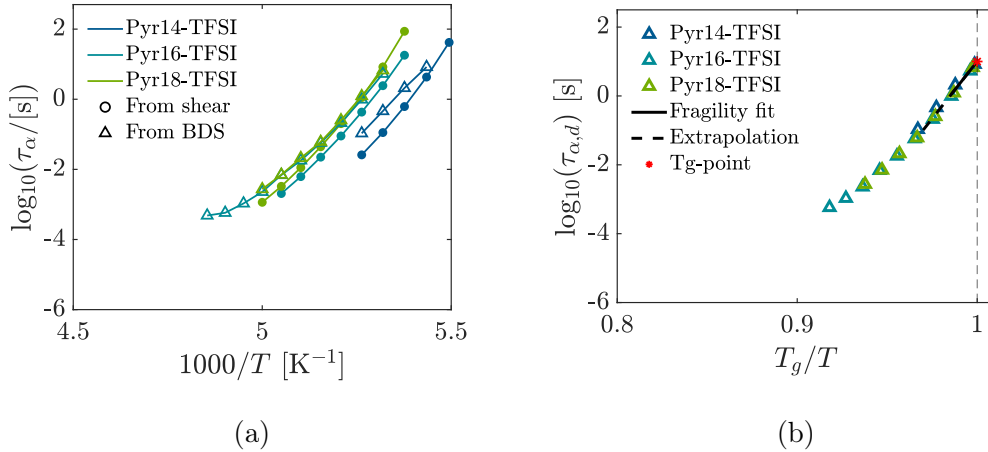


Figure 7.10: a) An Arrhenius plot of the alpha relaxation time for neat Pyr14-TFSI, Pyr16-TFSI and Pyr18-TFSI found by shear modulus (circles) and by the derivative representation of the dielectric permittivity (triangles). It shows a good agreement between the alpha relaxation times found from the two different response functions. b) the dielectric alpha relaxation time from a) in an Arrhenius plot scaled to T_g showing the linear fit to find the fragility index (black solid) and T_g (red asterisk). The resulting fragility index is $m_p = 67 \pm 4$.

and appears almost temperature independent. The beta relaxation is more pronounced in the complex electric modulus representation, M^* , see figure 7.11, where it appears as a clear peak that merges with the conductivity peak at higher temperatures.

The beta relaxation times have been found in the imaginary part of both representations, i.e. ε'' and M'' , by fitting the logarithm of the data just around the beta relaxation peak to a second-degree polynomial and using the relation $\tau_{\beta} = 1/(2\pi\nu_{max})$, where ν_{max} is the frequency at the peak. See figure 7.11d for an example of the fitting procedure. It was attempted, without success, to fit the dielectric data to a model based expression and so, this simple method of just finding the peak position in order to extract the relaxation time was chosen.

The resulting relaxation times can be seen in figure 7.12 together with the alpha and beta relaxation times from the DMS measurements. Only the beta relaxation found from ε'' at the lowest temperature has been included since it was not possible to find a clear peak position at higher temperatures. This problem was not present when finding the beta relaxation from M'' . Figure 7.12c and 7.12d are zoom in on the beta relaxation for clarity.

There is a clear overlap of the beta relaxation found from the different response functions. Especially for Pyr14-TFSI, where the data points from M'' is hard to distinguish from data points for J'' . This is a clear indication that the beta relaxation seen in the shear mechanical measurements has the same origin as the beta relaxation seen in the dielectric measurements. Furthermore, this is the first time such a connection has been made in RTILs, since it is only possible

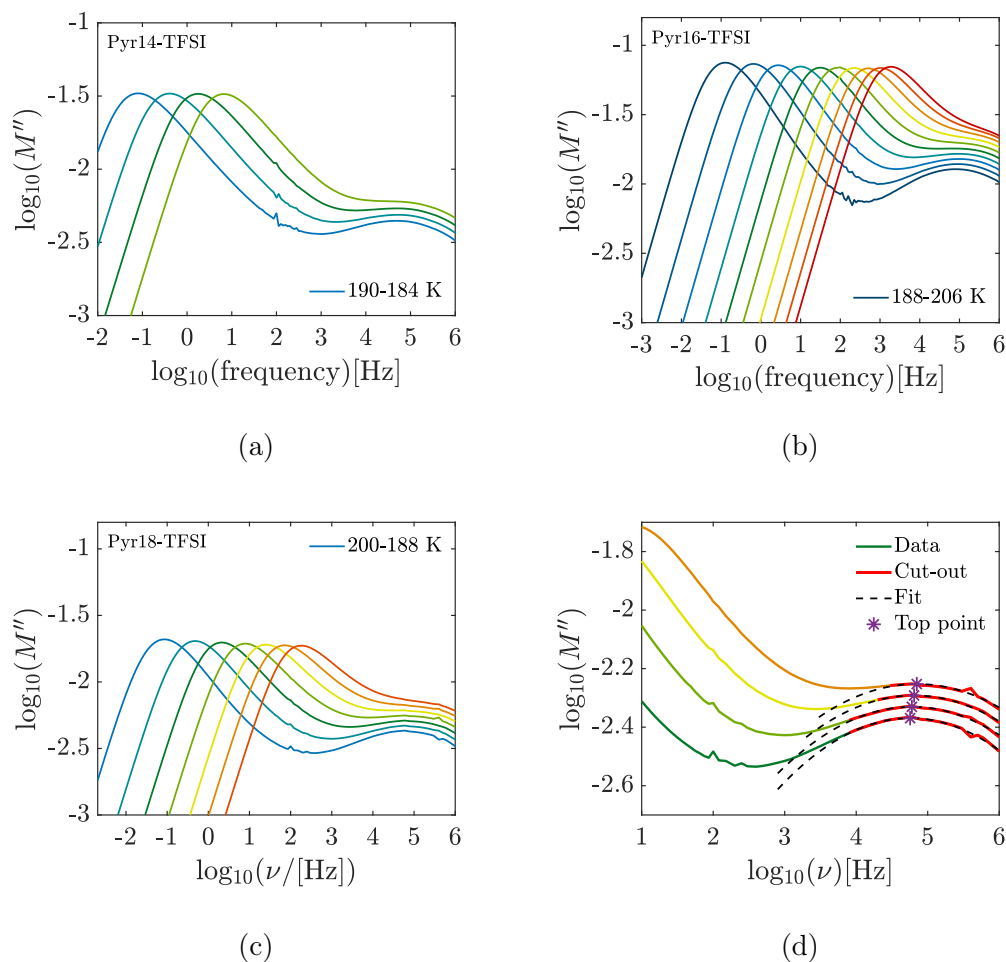


Figure 7.11: Imaginary part of the complex modulus for a) Pyr14-TFSI, b) Pyr16-TFSI and c) Pyr18-TFSI showing both a pronounced conductivity peak and a beta relaxation at higher frequency that merges with the conductivity peak at higher temperatures. d) is an example of the fitting procedure in order to find the relaxation time where a section of the spectrum (red, solid) is fitted to a second-degree polynomial (dashed) to find the top point (asterisk).

to resolve the high-frequency shear mechanical dynamics with the PSG.

Another interesting feature is that the beta relaxations in the three different liquids are very similar in both time scale and temperature dependence, where the latter is still of an Arrhenius nature. They are difficult to distinguish from each other by eye and it appears as though there is just one common temperature dependence. This indicates that the origin of the beta relaxation is identical in the three liquids.

The activation energy has for the sake of completeness been found for the BDS beta relaxation in all three liquids and the result is $E_{\beta,d} = 2.65, 5.12$ and 4.74 kJ/mol for Pyr14-TFSI, Pyr16-TFSI and Pyr18-TFSI respectively with corresponding τ_0 of $6.0 \cdot 10^{-8}$ s, $1.1 \cdot 10^{-9}$ s and $2.7 \cdot 10^{-9}$ s. It was expected to find

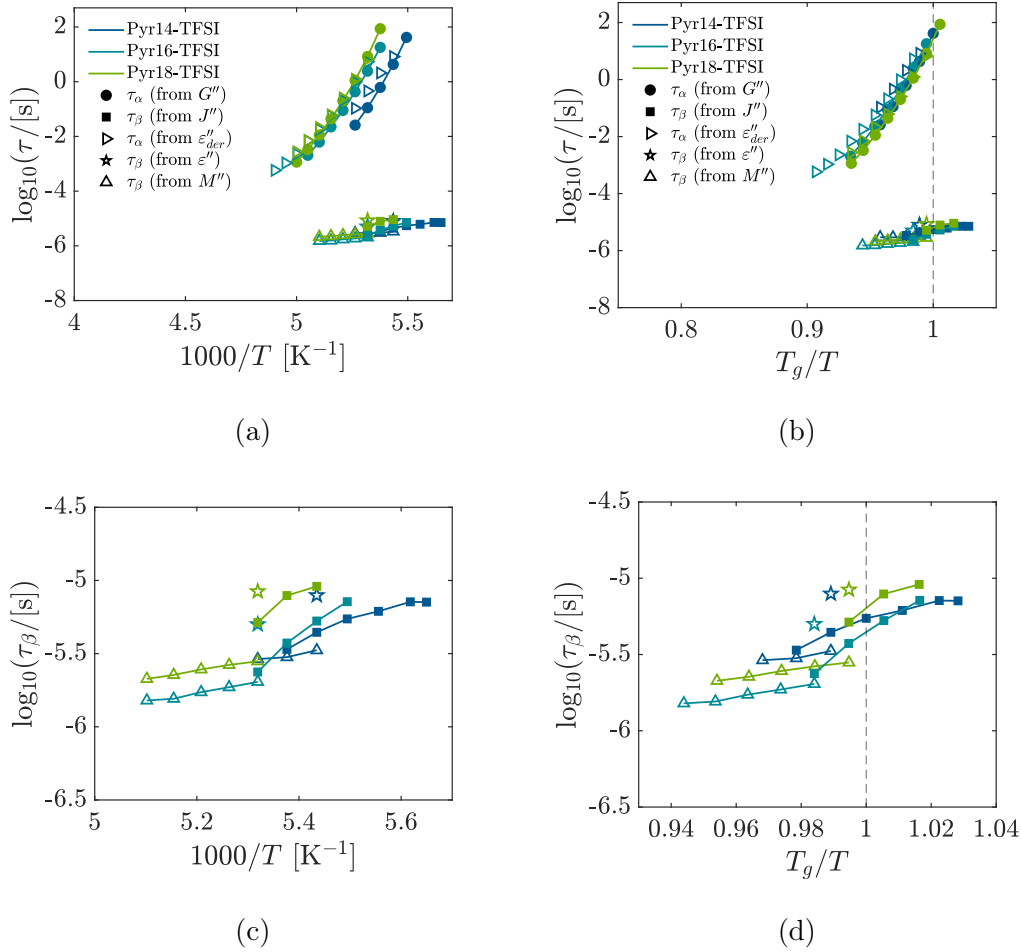


Figure 7.12: The alpha and beta relaxation times for Pyr14-TFSI, Pyr16-TFSI and Pyr18-TFSI found by shear modulus (circles), shear compliance (squares), dielectric permittivity (right pointing triangle and star) and electric modulus (triangles) plotted in an Arrhenius plot. It clearly shows a significantly lower temperature dependence of the beta relaxation time compared to the alpha relaxation. Only the coldest temperature for the beta relaxation time found from ε'' has been included, since this is the only temperature where the fit was able to find a reliable relaxation top point. For M'' it was the first three (Pyr14-TFSI) and the first five (Pyr16-TFSI and Pyr18-TFSI) temperatures that this applied to. c) and d) is a zoom in around the beta relaxation times.

activation energies changing systematically with increasing chain length as was the case in a study on imidazolium based RTILs [111]. In that study the activation energies were found in a similar way, but deep into the glassy state.

7.2.4 Conductivity

The final way of representing the dielectric data is as mentioned before conductivity, $\sigma(\omega) = i\omega\varepsilon_0\varepsilon^*(\omega)$. The advantage of this representation is that ionic transport properties are directly displayed, and it is possible to find the steady state conductivity, σ_0 , which is a basic property of RTILs.

Due to cold-crystallization it was only possible to measure in a limited temperature range. As with the shear mechanical measurements the procedure was to cool down rapidly to around T_g and then measure in heating steps of 1-2 K until crystallization started.

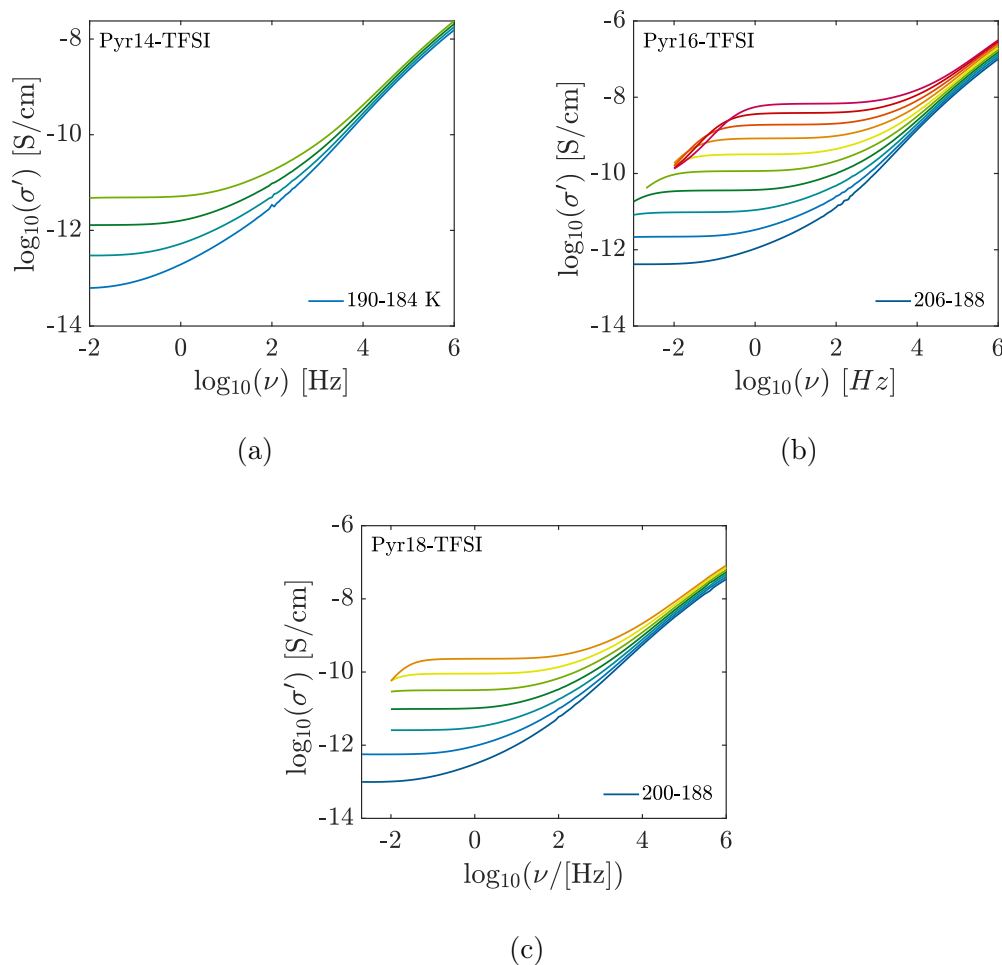


Figure 7.13: Real part of the complex conductivity for a) Pyr14-TFSI, b) Pyr16-TFSI and c) Pyr18-TFSI showing the frequency dependence with the steady state conductivity as the plateau between electrode polarization at low temperatures and a steady increase in conductivity at high frequencies.

In literature it is standard to present the steady state conductivity and thus deduce the effect of for example a systematic change of cation alkyl chain length, mixing with Li-salt, mixing with other types of RTIL and so forth. One of

the reasons is that knowing the steady state conductivity is paramount when designing new electrolytes for future Li-batteries.

See figure 7.13 for plots of the real part of the conductivity for the three liquids in the series. The steady state conductivity, σ_0 , was calculated for the three liquids at all measured temperatures as described in section 3.2. The resulting conductivity plotted as a function of inverse temperature can be seen in figure 7.14a. The figure shows a somewhat surprising result since the high temperature conductivity does not decrease systematically with decreasing alkyl chain length as expected. The reason could be that the measurement setup was not optimized at high temperatures.

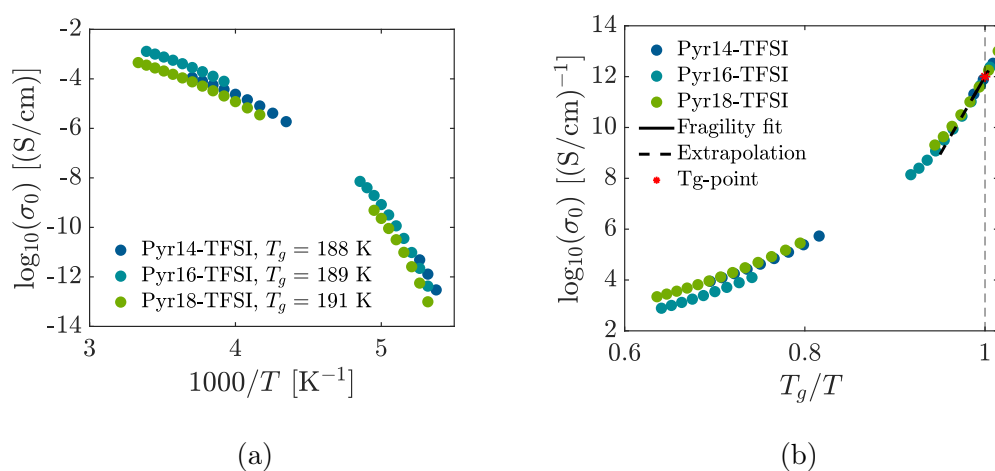


Figure 7.14: a) the conductivity as a function of inverse temperature for the three RTILs in the series. b) The inverse of conductivity as a function of inverse temperature is scaled to T_g . T_g was found as the temperature where $\log_{10}(1/\sigma_0) = 12$ (red asterisk) and the fragility index was found from a linear fit (black solid) around this T_g giving $m_p = 63 \pm 3$.

At low temperatures, below the no-man's land created by cold-crystallization, the picture is different. Here there is a clear decrease in steady state conductivity with increasing alkyl chain length. The temperature dependence of conductivity is however very similar between the three liquids which confirms findings from literature [80]. This is clarified in figure 7.14b where the plot has been scaled to T_g found as where $\log_{10}(1/\sigma_0) = 12$. This definition of T_g gives a slightly higher T_g than in the shear mechanical data, and it indicates that a value of $\log_{10}(1/\sigma_0) = 12$ is too low. This value was however chosen to avoid extrapolation of the conductivity data.

T_g was found to be 188 K, 189 K and 191 K for Pyr14-TFSI, Pyr16-TFSI and Pyr18-TFSI, respectively. A common isobaric fragility index was found from the collected data of all three liquids, since the temperature dependence for these at low temperatures is very close to identical. The result is a fragility of $m_p = 63 \pm 3$ which is close to the one found by the dielectric alpha relaxation time of 67 ± 4 .

7.3 Coupling between shear and conductivity

This section will analyze the relation between the shear mechanical alpha relaxation time and the steady state conductivity to find the decoupling between the two. This was done by plotting the inverse conductivity and alpha relaxation time in the same plot with two y-axes, to investigate how much they collapse, see figure 7.15.

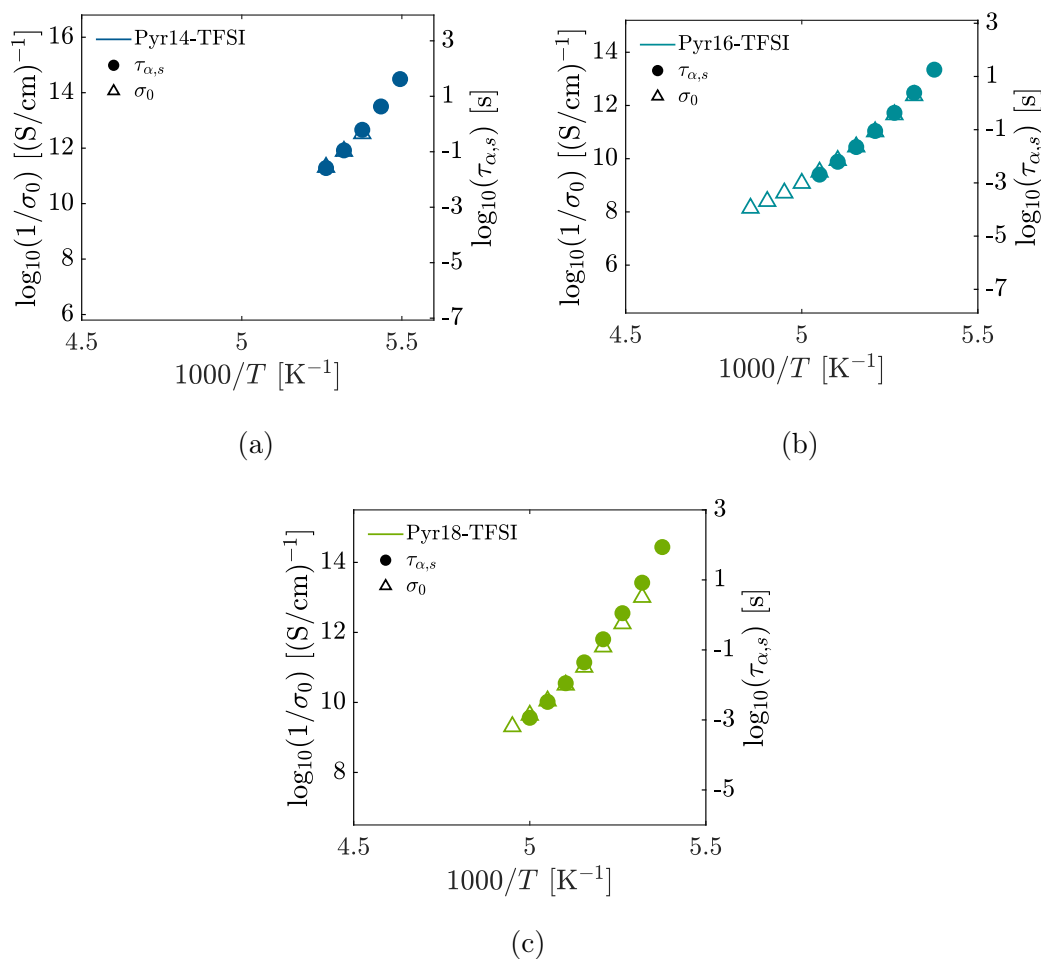


Figure 7.15: The inverse conductivity (triangles) together with the shear mechanical alpha relaxation time (circles) for all three liquids in the Pyr1*n* series with $n = 4$ (a), $n = 6$ (b) and $n = 8$ (c). The two axes have been scaled so that the data collapse at the second highest temperature, and there is an equal number of decades on both axes. There is a decoupling between the inverse conductivity and the alpha relaxation time as T_g is approached for all three liquids.

In all three cases the two y-axes were scales so that $1/\sigma_0$ and $\tau_{\alpha,s}$ collapse at the second highest temperature, in order to follow the temperature development as the temperature is lowered. Note that both y-axes display an equal number of decades to allow direct comparison between the two properties.

For all three liquids the decoupling between conductivity and alpha relaxation time increases as T_g is approached, even though this effect is tiny in Pyr14-TFSI and Pyr16-TFSI. This corroborates findings from literature [112], where the conductivity diffusion coefficient in Bmim-TFSI decoupled from the structural relaxation time when T_g was approached. This decoupling is however not general for RTILs as another study found complete coupling between the conductivity and structural relaxation for a wide variety of RTILs [113].

Time-scale index The logarithm of the alpha relaxation times found with shear modulus and the derivative of the dielectric permittivity, as well as the inverse conductivity, have been scaled for each temperature to the logarithm of $\tau_{\alpha,d}$. This was to quantify the decoupling of the timescales between the three properties. This quantification is called a time-scale index [114], and it reveals very clearly if there is a decoupling seen as a difference in temperature dependence of the alpha relaxation time, as measured with DMS or BDS, and the inverse conductivity. Note that the inverse conductivity is not a time, but it can be included in the time-scale index if shifted properly to the alpha relaxation time, as was done in figure 7.15. This way, the temperature dependence, but not the absolute value, of the inverse conductivity can be compared to the alpha relaxation time found from shear and dielectric spectroscopy.

The resulting time-scale index can be seen in figure 7.16. It shows a decoupling of the alpha relaxation times across all three liquids even though it is less pronounced in Pyr14-TFSI and Pyr16-TFSI. The overall change in alpha relaxation time and inverse conductivity is however still relatively small compared to an overall slowing down of the dynamics of around 5 decades. In Pyr16-TFSI and Pyr18-TFSI the scaled inverse conductivity support the tendencies found in the scaled dielectric alpha relaxation times, but there is less decoupling of the inverse conductivity than the dielectric alpha relaxation time in Pyr14-TFSI. The latter is probably due to the large error related to finding the dielectric alpha relaxation time.

An important point to make is that the alpha relaxation was in all cases found with a purely phenomenological method, i.e. fitting the data around the alpha relaxation peak to a second-degree polynomial. This is a somewhat naive way of finding the alpha relaxation time, since the merging of the alpha and the beta relaxation peak can obscure the actual location of the former.

This problem was bypassed in a study from 2021 where the time-scale index was calculated for squalane, which also has a high intensity beta relaxation [33]. In order to avoid the effect of the beta relaxation, they used the terminal mode instead of the alpha relaxation peak when finding the time-scale index. This way, the decoupling almost vanished and squalane was shown to follow the second criterion for simplicity.

Using this method showed no change in decoupling in Pyr14-TFSI and Pyr16-TFSI, but for Pyr18-TFSI, where the temperature dependence of the time-scale index is largest, the decoupling decreased when using the terminal mode, see figure 7.16c. It decreased so much that it seemed to match that of Pyr14-TFSI

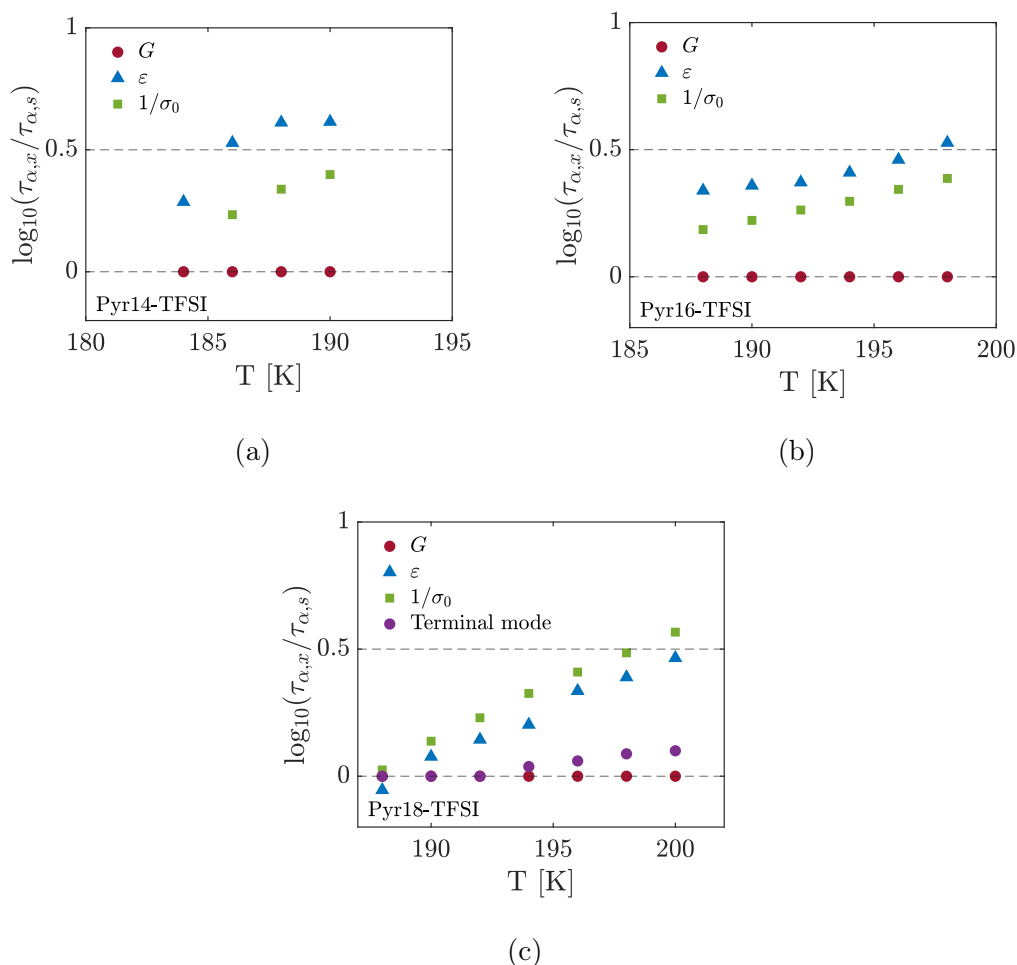


Figure 7.16: The alpha relaxation time for Pyr14-TFSI, Pyr16-TFSI and Pyr18-TFSI found by shear modulus (red) and the derivative of the dielectric permittivity (blue) as well as the steady state conductivity (green) scaled to the alpha relaxation time of the shear modulus. This is called the time-scale index and shows the quantitative degree of decoupling between the alpha relaxation measured with the two response functions. It shows decoupling in all three liquids but to a lesser degree in Pyr16-TFSI.

and Pyr16-TFSI. When looking at the shear modulus of the three liquids in the series, it is also evident that the beta relaxation is much larger relative to the alpha relaxation in Pyr18-TFSI. This indicates that the larger decoupling seen here is due to the effect of the beta relaxation.

The terminal mode time was found by first scaling the imaginary part of the shear modulus to the alpha relaxation peak position. Then manually shifting these normalized spectra in frequency to obtain a collapse of data at the low frequency flank of the alpha relaxation peak, instead of the peak. The time scales were then derived by applying this shift factor relative to the relaxation time at the lowest temperature, where the separation of the alpha and beta

relaxation is biggest.

7.4 Overview

In order to get an overview of the different results in this chapter, the calculated parameters have been collected in table 7.1. For Pyr16-TFSI and Pyr18-TFSI T_g is four degrees higher as found by conductivity and in Pyr14-TFSI it is six degrees higher.

Liquid	$m_p, \tau_{\alpha,s}$	$m_p, \tau_{\alpha,d}$	m_p, σ	$T_g, \tau_{\alpha,s}$	$T_g, \tau_{\alpha,d}$	T_g, σ
Pyr14-TFSI	90 ± 5	67 ± 4	63 ± 3	182	184	188
Pyr16-TFSI	90 ± 5	67 ± 4	63 ± 3	185	187	189
Pyr18-TFSI	90 ± 5	67 ± 4	63 ± 3	187	188	191

Table 7.1: A table showing the isobaric fragility index, m_p , and the glass transition temperature, T_g , for all liquids measured with DMS and BDS. T_g was for the shear mechanical data defined as $\log_{10}(\tau_{\alpha,s}) = 1.5$ and for the dielectric data as $\log_{10}(\tau_{\alpha,d}) = 1$ and $\log_{10}(1/\sigma_0) = 12$.

Liquid	E_β, G'' [kJ/mol]	E_β, M'' [kJ/mol]
Pyr14-TFSI	9.74	2.65
Pyr16-TFSI	22.6	5.12
Pyr18-TFSI	17.7	4.73

Table 7.2: A table showing the activation energy of the beta relaxation, E_β , found in DMS and BDS measurements for the three ionic liquids in the series.

7.5 Discussion

Simplicity Two criteria for simplicity in glass-forming liquids were tested on Pyr14-TFSI, Pyr16-TFSI and Pyr18-TFSI in this chapter; the requirement of TTS and the constant time-scale index. The first showed that, even though the shear mechanical relaxation spectra did not exhibit complete TTS due to a weaker temperature dependence of the beta relaxation, the alpha relaxation does obey the TTS principle.

The second criterion for simplicity was not completely met either, which was shown in two ways; with a time-scale index showing a temperature dependence and with a significant difference in isobaric fragility index calculated for the shear

alpha relaxation time ($m_p = 90 \pm 5$) and both the dielectric alpha relaxation time ($m_p = 67 \pm 4$) and the steady state conductivity ($m_p = 63 \pm 3$).

It was not expected that the RTILs studied in this chapter would meet the requirements for simplicity and thus be viewed as "zeroth order" liquids, but it is assessed that the deviation from simplicity is not large. With the TTS spectra seen in figure 7.8 it is likely that the high degree of simplicity is only interrupted by the beta relaxation. Therefore, it is suggested that the whole spectrum could be theoretically explained by adding a term, which accounts for the beta relaxation to the basic, simple behavior of the alpha relaxation. What this extra term should be of course depends on the molecular nature of the beta relaxation.

In relation to simplicity in RTILs it was in chapter 2 suggested to test the criterion for simplicity in Pyr1*n*-TFSI with increasing chain length and thus increasing complexity in the microscopic structure. The degree of simplicity seen in Pyr14-TFSI do not, with respect to TTS, change across chain length. The decoupling between the alpha relaxations was analyzed in two ways; first the time-scale index and here the degree of simplicity did not change systematically with increasing chain length when using the terminal mode instead of the alpha relaxation time. Second way was the fragility index, where the temperature dependence of both $\tau_{\alpha,s}$, $\tau_{\alpha,d}$ and $\tau_{\alpha,\sigma}$ was assumed to be identical across chain lengths. The conclusion is thus that the degree of complexity in the dynamics do not increase with increasing chain length.

Non-associated molecular liquids A main point of discussion in this study is whether or not the RTILs have dynamics that are similar to those of non-associated, molecular liquids like squalane or DC704. The x-ray structure factor seen in figure 7.1 will at first glance reveal that it originates from a RTIL due to the signature charge peak, but a similar effect cannot be seen in the dynamics.

The shear mechanical spectra with a prominent alpha relaxation and a large beta relaxation are very similar to for example squalane and for the dielectric permittivity and electric modulus the only indication that the resulting spectra do not originate from measurements of non-associated molecular liquids is the high conductivity contribution at low frequencies. These results show that this homologous series of pyrrolidinium based RTILs have dynamics resembling those of non-associated, molecular liquids. This result corroborates findings in literature [112].

Beta relaxation The presence of a secondary, high frequency or beta relaxation in RTILs is observed in literature when performing dielectric measurements. The main question asked in this regard is what the origin of this dynamic mode is, and one suggestion is that it is from intramolecular motions [110, 111]. This could in the case of pyrrolidinium based RTILs be the motion of the pyrrolidinium ring, the methyl chain, the alkyl chain and the anion.

A study on C_nC_1Im -TCM with $n = 2, 4, 6$ and 8 with BDS measurements showed a pronounced beta relaxation with an Arrhenius temperature dependence

in the imaginary part of the electric modulus [111]. The activation energy of this mode increased systematically with increasing alkyl chain length and with this, the beta relaxation was assigned to intramolecular motion of the alkyl chain. It was also shown that the beta relaxation did not change with changing the anion and so, the beta relaxation could not be from motion of the anion.

This conclusion of the beta relaxation being from intramolecular motions of the cation was supported in previous studies on imidazolium based RTILs [115,116] with similar arguments.

Studies on homologous series of quaternary ammonium and phosphonium ionic liquids [117,118] found beta relaxations with BDS and Depolarized Dynamic Light Scattering (DDLS) measurements. For the ammonium based liquids the beta relaxation was in all cases non-Arrhenius in nature as opposed to an Arrhenius nature in the phosphonium-based liquids, but for both series the conclusion was that the origin of the beta relaxation should be found in local fluctuations of the alkyl chains.

Since it is generally difficult to make conclusions that apply across different families of RTILs one should especially look at studies on pyrrolidinium based ones. A study from 2019 found a beta relaxation with an Arrhenius nature in a homologous series of Pyr1*n*-TFSI with $n = 4, 6$ and 8 [80]. The conclusion here was also that it originates in intramolecular motions of the alkyl chain since the activation energy increases systematically with increasing alkyl chain length. This could be explained by an increase in the steric hindrance of these local motions.

A study of dynamics in Pyr14-TFSI, by the author of this thesis and co-workers, showed with a combination of quasi-elastic neutron scattering on partly and fully deuterated cation and high-frequency DMS measurements that the beta relaxation of this RTIL is not related to either the single methyl group or the end methyl group on the butyl chain of the cation [95]. This is because the timescale of the beta relaxation is too slow to be related to these much faster dynamics. See chapter 11 for details. It was suggested that the origin of the beta relaxation is instead intramolecular motion of the anion or even a so-called genuine Johari-Goldstein beta-relaxation [16,119]. The latter is backed by a study on pyrrolidinium based RTILs from 2019 where it was concluded that the beta relaxation is based on intermolecular motion and that it is ionic in nature [110].

In this work the beta relaxation time is very similar and hard to distinguish across different chain lengths, as is seen in figure 7.12, suggesting a common origin. This could be dynamics from the anion which is the only molecular constant across all three liquids, but it cannot be said with certainty.

Conductivity and alpha relaxation When looking at the resulting steady state conductivity of this homologous series of pyrrolidinium based RTILs in the high temperature region the conductivity does not decrease systematically with increasing alkyl chain length. The reason could be that the measuring setup was not optimized to measure at high temperatures.

At low temperatures however, below the no-man's land of cold-crystallization, the conductivity decrease with decreasing temperature as was also seen in literature for the same liquids [80]. When looking at the to T_g scaled plot the three conductivity curves collapse which shows a similar temperature dependence across alkyl chain length.

Furthermore, in this temperature region it is also possible to discuss the relationship between the conductivity and the structural relaxation time since both were measured here. This was in this study done with two analysis methods; 1) to find the isobaric fragility index in both the conductivity and alpha relaxation time, 2) by plotting the steady state conductivity in the same plot as the alpha relaxation time.

The first method showed a fragility index of the shear mechanical alpha relaxation time, $\tau_{\alpha,s}$, significantly higher than the one found from steady state conductivity, i.e. $m_p = 90 \pm 5$ and 63 ± 3 respectively. This difference in fragility cannot alone be explained by the fact that the glass transition temperature found from steady state conductivity is 6 K higher than the one found from $\tau_{\alpha,s}$. Instead it indicates a decoupling of $\tau_{\alpha,s}$ and σ_0 close to the glass transition. A similar decoupling was found in literature in the same liquids [80].

The second method shows that for all three liquids the coupling between conductivity and structural relaxation decreases with decreasing temperature. An effect most pronounced in Pyr18-TFSI and less pronounced in Pyr16-TFSI where there is a higher degree of coupling. This decreasing coupling as T_g is approached confirms the difference in fragility between the two response functions.

7.6 Conclusion

This chapter presents results on the dynamics of a homologous series of pyrrolidinium based RTILs, i.e. Pyr1*n*-TFSI with $n = 4, 6$ and 8 , measured with dynamical mechanical and broadband dielectric spectroscopy in order to make a comparative analysis when changing the chemical composition. This was to shed light on whether or not the complexity in the structure of RTILs is reflected in the dynamics and to see if the origin of the different dynamic modes observed in these RTILs could be revealed.

In the shear mechanical results, two modes were found in Pyr16-TFSI and Pyr18-TFSI and three modes in Pyr14-TFSI, where the slowest mode was identified as the structural, or alpha, relaxation time in all three liquids. The isobaric fragility index was calculated for all three liquids simultaneously and gave $m_p = 90 \pm 5$. The second slowest mode in Pyr14-TFSI could not be quantified and so no further analysis was performed on this.

The fastest mode, named the beta relaxation, in the shear mechanical measurements on all three liquids could be quantitatively analyzed when using the compliance representation. This showed that the beta relaxation is Arrhenius in nature and very similar in both temperature dependence and time scale across chain lengths.

The beta relaxation was also present in the BDS measurements of all three liquids and this is the first time that a direct comparison of the beta relaxation found in BDS and DMS measurements can be made in a series of RTILs. The beta relaxation in the BDS measurements showed similar behavior to the DMS measurements with an Arrhenius temperature dependence. The activation energies were shown to be 2.65, 5.12 and 4.73 kJ/mol for Pyr14-TFSI, Pyr16-TFSI and Pyr18-TFSI respectively. The origin of the beta relaxation was discussed, and the close overlap of the beta relaxation times across all three liquids suggest a common origin, which could possibly be by dynamics from the anion.

The steady state conductivity was also analyzed. Pronounced cold-crystallization made sure that results were divided into a high and low temperature region with a no-man's land in between. The low temperature region showed a steady state conductivity, that systematically decreased with increasing alkyl chain length, and which collapsed when scaled to T_g . This low temperature conductivity was also compared to the alpha relaxation times in order to investigate a coupling between the two. It showed a large degree of coupling that however did decrease as the temperature approached T_g which is consistent with findings from literature.

Furthermore, the criteria for simplicity in glass-forming liquids were investigated and it was found, that there is a high degree of simplicity in these pyrrolidinium based RTILs and that this degree of simplicity do not change significantly across alkyl chain length. The only exception from this is a higher degree of decoupling between shear alpha relaxation time and inverse conductivity in Pyr18-TFSI, but this higher degree vanishes when using the terminal mode instead of the alpha relaxation time.

It is finally concluded that the dynamic behavior of this series of pyrrolidinium based RTILs across both shear mechanical and dielectric measurements do not reflect the complex structure as seen in the x-ray structure factor. Instead, the dynamics resemble those found in non-associated molecular liquids.

Chapter 8

Comparative analysis, Pyr18-TFSI with Li-TFSI

This chapter will further investigate the complex nature of RTILs and the implications on mechanical and dielectric properties. Pyr18-TFSI has a cation with an alkyl chain length of 8 carbon atoms and previous studies show that the x-ray structure factor contains a pre-peak which is directly linked to the heterogeneities of mesoscale aggregates in the liquid.

A way to further increase this already existing complexity in the structure of the liquid is to introduce a third component; lithium ions. In practice this is done by mixing the ionic liquid Pyr18-TFSI with the salt Li-TFSI, where the latter then dissolves in the liquid. Since the anion in both the liquid and the salt is TFSI, the final mixture will be one consisting of three components. The reason for choosing Li-salt specifically is that with their low-flammability, high thermal stability, low vapor pressure and high ionic conductivity RTILs are a promising candidate for electrolytes in the next generation of rechargeable Li batteries [69].

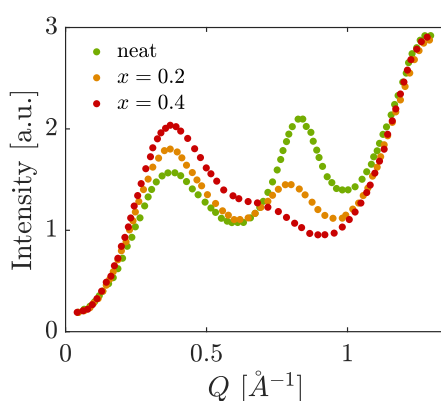


Figure 8.1: X-ray scattering structure factor for the series Pyr18-TFSI mixed with Li-salt in molar fractions of $x = 0.2$ and $x = 0.4$ in order to show the development of the scattering pre-peak and charge peak. Data from [69].

For the RTILs to be used as electrolytes in rechargeable batteries, Li-ions need

to be added. This however introduces undesirable changes to the liquid properties such as an increase in viscosity and a decrease in ionic conductivity [87]. A study by L. Aguilera et al. also discovered in 2015 [69] that an increase in Li-salt concentration will increase the x-ray structure factor pre-peak and thus increase the amount of mesoscale aggregation. This can be seen in figure 8.1 where the pre-peak, which is directly linked to the mesoscale aggregates, increases with increased Li-salt concentration.

Another feature of the x-ray structure factor is that the charge alternation peak decreases which again reflects changes in the structure of the liquid when increasing the amount of Li-salt.

With this in mind, it is interesting to see what the effect of this increased Li-salt concentration is on the transport and shear mechanical properties of Li-salt and RTIL mixtures since there is a clear effect on the microscopic structure. An investigation of this kind could then possibly connect the effects on the microscopic scale with those on the macroscopic scale and also see if the increased complexity in the structure is reflected in the dynamics. This has been done before with Li-salt and Pyr14-TFSI mixtures [107, 120], but never before with Li-salt and Pyr18-TFSI.

The chapter will be divided into three parts related to the method used to investigate the dynamic modes; Dynamic Mechanical Spectroscopy (DMS), Broadband Dielectric Spectroscopy (BDS) and the two combined. The three parts will start by presenting individual results on the three liquids in this series; Pyr18-TFSI with a Li-TFSI molar fraction of $x = 0.2$ and $x = 0.4$ followed by a comparative analysis of these liquids. It will furthermore connect to the results found in the previous chapter.

8.1 Dynamic Mechanical Spectroscopy

8.1.1 Method

The method used for the DMS measurements was the same as described in subsection 7.1.1 with an addition regarding the RTIL Li-salt mixture: The Li-TFSI, or lithium bis(trifluoromethanesulfonyl)imide, used in the Pyr18-TFSI Li-salt mixtures was of 99.9% purity, extra dry and from Solvionic. Both Pyr18-TFSI and the Li-salt was used as bought with storage and sample preparation including mixing taking place in a glove box with dry, inert atmosphere. DMS results on neat Pyr18-TFSI is presented in chapter 7.

8.1.2 Pyr18-TFSI with $x = 0.2$ Li-TFSI

The first RTIL and Li-salt mixture was Pyr18-TFSI with a molar fraction of $x = 0.2$ Li-salt, henceforth called Pyr18x02. This specific mixture is sparsely studied in literature with the only, to his author knowledge, publication being the one by Aguilera and co-workers from 2015 [69]. Here the x-ray structure

factor was measured showing an increase in the pre-peak intensity and a decrease in charge peak intensity when comparing to the neat liquid.

Thermalization calorimetry (TC) measurements showed a T_g of 203 K and T_m of 273 K with sparse amounts of cold-crystallization. Despite of these TC results the liquid was prone to a high degree of cold-crystallization in the PSG and so, the DMS measurements took place by rapid cooling past the temperature region with cold-crystallization and then measuring in cooling with 2 K steps.

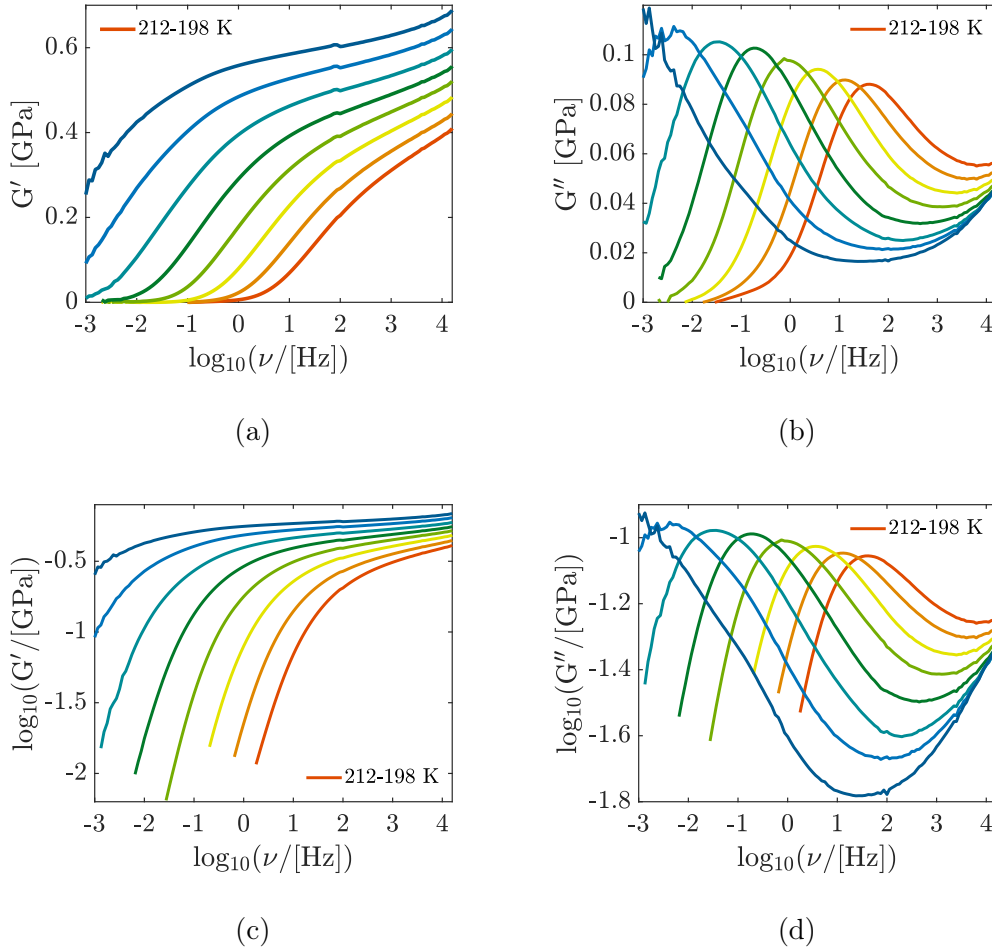


Figure 8.2: The complex shear modulus of Pyr18-TFSI mixed with $x = 0.2$ Li-TFSI plotted as the a) real part, b) imaginary part, c) logarithm of the real part and d) logarithm of the imaginary part. Data were taken at temperatures ranging from 212-198 K and measured in cooling.

The shear mechanical results measured in this work for Pyr18x02 can be seen in figure 8.2. The alpha relaxation is seen as an increase in the real part of the shear modulus and as a prominent and highly temperature dependent peak in the imaginary part. The peak move to lower frequencies with decreasing temperature.

A high intensity secondary relaxation at high frequencies is also visible at

all measured temperatures. The peak of this beta relaxation is well outside of the frequency window and only the low-frequency wing of the peak is measured. Despite of this it still appears to be relatively temperature independent, at least when compared to the alpha relaxation.

In addition to these two prominent features in the spectra, a third feature also appears as a shoulder in the high-frequency part of the alpha relaxation. This feature is only visible at low temperatures when the alpha relaxation has moved below 1 Hz.

8.1.3 Pyr18-TFSI with $x = 0.4$ Li-TFSI

The second RTIL and Li-salt mixture was Pyr18-TFSI with a molar fraction of $x = 0.4$ Li-salt, from now on called Pyr18x04. This specific mixture is as with Pyr18x02 also sparsely studied in literature with the study by Aguilera and co-workers from 2015 [69] being the only example known to the author of this thesis. Here the x-ray structure factor showed a further increase in the pre-peak intensity and a further decrease in charge peak intensity when comparing to the neat liquid with the latter being almost completely gone at this Li-salt concentration.

TC measurements on the liquid showed a T_g of 220 K and no cold-crystallization. This tendency to supercool with no crystallization also applied to the measurements with the PSG and so it was possible to measure spectra in cooling at 12 temperatures, i.e. from 234-212 K in steps of 2 K.

The resulting DMS measurements can be seen in figure 8.3. The lin-log plots of both G' and G'' show a clearly resolved alpha relaxation as a steady increase in the real part of the modulus and as prominent peak in the imaginary part.

The beta relaxation which was also seen in Pyr18x02 have moved further out of the frequency window and the left flank can only be seen at low temperatures. Furthermore, there is no third high-frequency feature seen in this liquid as was the case with Pyr18x02.

8.1.4 Alpha relaxation

The first property to compare is the alpha relaxation across the three liquids in the series, since it is an obvious starting point. Figure 8.4 shows the alpha relaxation times for the three measured ionic liquids with different concentrations of Li salt, where the alpha relaxation time was found as $\tau_\alpha = 1/(2\pi\nu_{max})$, where ν_{max} is the frequency at the alpha relaxation peak. This frequency was found by fitting the imaginary part of the shear modulus just around the peak to a second degree polynomial and then use the top point to get ν_{max} . This choice of fitting function is purely phenomenological and only serves to find the peak position.

Figure 8.4a shows that the alpha relaxation slows down dramatically with increased Li-salt concentration. This slowing down is so prominent that there is almost no overlap in temperature between the alpha relaxation time of the

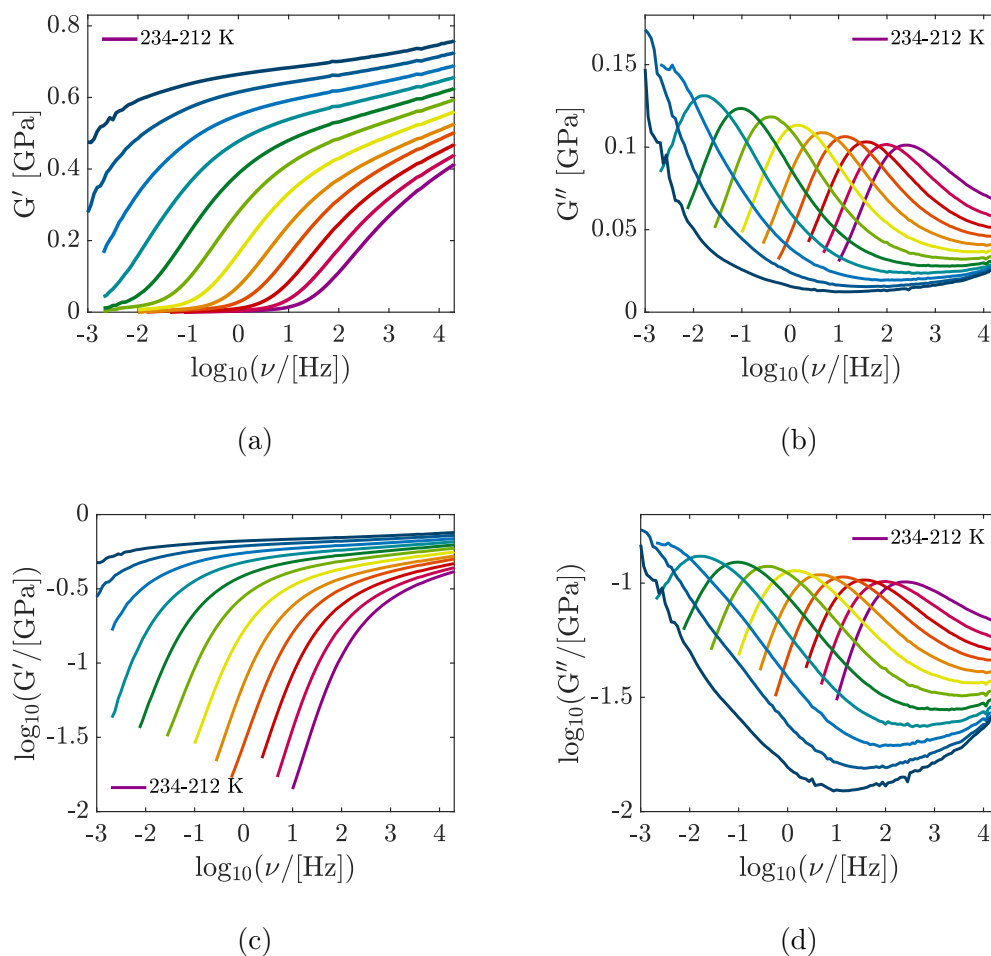


Figure 8.3: The complex shear modulus for Pyr18-TFSI with $x = 0.4$ Li-TFSI from 234-212 K. a) and b) are a lin-log plot. c) and d) are log-log plots.

different liquids and the effect is much more pronounced than with increasing alkyl chain length as seen in chapter 7.

This slowing down is also reflected in the steep increase of T_g which increases with 13 K going from neat Pyr18-TFSI to Pyr18x02 and with 17 K going from Pyr18x02 to Pyr18x04. T_g was here defined as where $\log_{10}(\tau_\alpha) = 1.5$. For Pyr18x02 this point was found by extrapolation of data beyond the coldest measured temperature and for neat Pyr18-TFSI and Pyr18x04 it was found by interpolating between the two coldest temperatures.

To investigate the temperature dependence of the alpha relaxation time the temperature scale for all three ionic liquids were scaled to T_g found from the shear modulus measurements. The result can be seen in figure 8.4b and shows that the temperature dependence of all three ionic liquids is very similar.

In order to quantify this temperature dependence around T_g , the isobaric Angell fragility index, m_p , was calculated for all three liquids. Again, the Angell

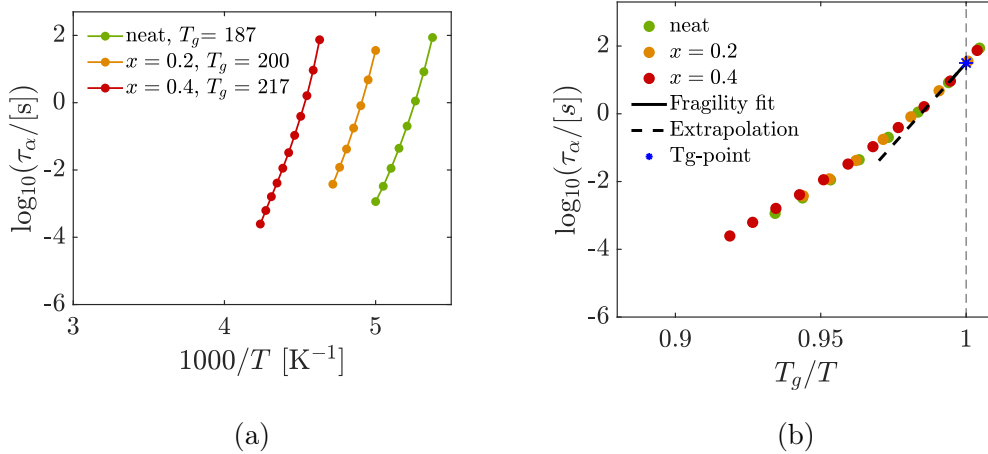


Figure 8.4: Alpha relaxation times as a function of inverse temperature. The fragility was found for all liquids using a definition of T_g as when $\log_{10}(\tau_\alpha) = 1.5$. a) is with $1000/T_g$ and b) shows the data scaled to T_g (blue asterisk) and with the fragility index found from a linear fit (black solid) to the collected data set of all three liquids.

fragility index is given as [8,9]

$$m_p = \left. \frac{d \log_{10}(\tau_\alpha)}{d T_g/T} \right|_{T=T_g} \quad (8.1.1)$$

where in this case the T_g defined as before mentioned was used in the calculation of m_p . Since the temperature dependence of the alpha relaxation by visual inspection appear to be almost identical for all three liquids it justifies the calculation of one collected fragility. The result is an isobaric fragility index of $m_p = 94 \pm 5$.

8.1.5 Beta relaxation

From the shear modulus results it is clear that all three ionic liquids have a secondary, high frequency relaxation here denoted the beta relaxation. The intensity of this dynamic mode decreases drastically from the neat Pyr18-TFSI to Pyr18x02 and in Pyr18x04 the beta relaxation is almost gone. This could be due to either a decrease of the beta relaxation itself or that the alpha and beta relaxation simply becomes more separated. Since the peak of the beta relaxation for all three liquids is outside of the experimental window it is difficult to quantify any properties of this dynamic mode.

Compliance The data have been converted to the shear compliance representation, i.e. the inverse of the shear modulus, in order to obtain more information on the beta relaxation since this approach proved useful for the Pyr18-TFSI series in chapter 7. The imaginary part of the shear compliance, J'' , shows the beta relaxation much better than the shear modulus, as can be seen in figure 8.5.

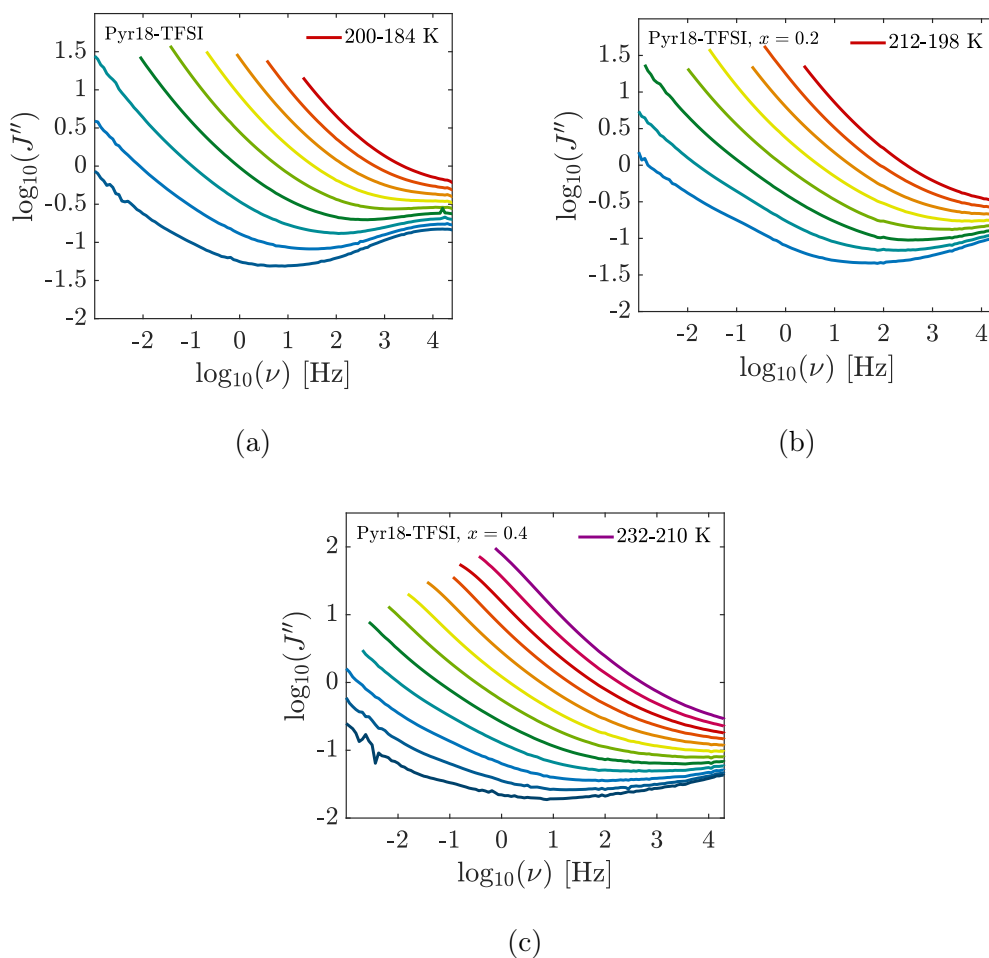


Figure 8.5: The imaginary part of the complex compliance, J'' . In this representation the beta relaxation is clearly better resolved than in shear modulus, but for the two liquids Pyr18x02 and Pyr18x04 the peak is still too far out of the frequency window. This is why there is no attempt to fit the beta relaxation in the compliance representation.

Still, the beta relaxation peak for Pyr18x02 and Pyr18x04 is still too far out of the frequency window to be discernible and so only quantitative properties from the beta relaxation in Pyr18-TFSI was obtained. The beta relaxation peak in this liquid was found by fitting the imaginary part of the compliance around the peak to a second-degree polynomial and then calculating the relaxation time using the top point frequency, ν_{max} as $\tau_{\beta} = 1/(2\pi\nu_{max})$. The result plotted together with the alpha relaxation times for all three liquids can be seen in figure 8.6.

8.1.6 TTS

Just as with the Pyr1*n*-TFSI series the Li-salt mixed Pyr18-TFSI series was also tested to see if it obeys the first criterion for simplicity, i.e. time-temperature

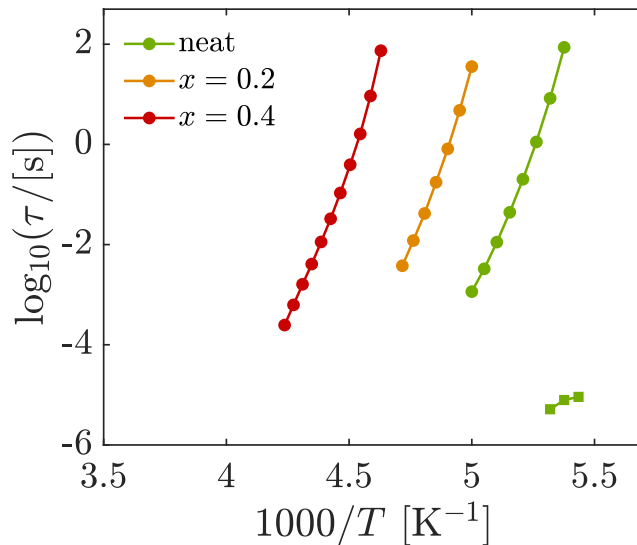


Figure 8.6: An Arrhenius plot showing the alpha relaxation (circles) as found from shear modulus and beta relaxation (squares) as found from shear compliance for the three liquids. Note that only Pyr18-TFSI has a discernible beta relaxation peak in the shear compliance.

superposition or TTS. The expansion of TTS, time-temperature-pressure superposition (TTPS), could not be tested since the RTILs in this study was only measured at ambient pressure.

Figure 8.7 shows a TTS plot of the logarithm of the real and imaginary part of the shear modulus for neat Pyr18-TFSI, Pyr18x02 and Pyr18x04. The data treatment was the same as in the previous chapter, meaning that the spectra at all temperatures were scaled to a point in the shear modulus, which lies 30% below the alpha relaxation peak to the low-frequency side of the peak, a point called lp .

The figure shows the same qualitative trend as was observed in the Pyr18-TFSI series; that the alpha relaxation nicely obeys TTS in all three liquids and that this does not apply to the beta relaxation. The latter was not expected since the temperature dependence of the beta relaxation is much weaker than the alpha relaxation. Again, consequently only the alpha relaxation can be said to exhibit signs of simple behavior, and the first criterion for a simple glass-forming liquid is not met in any of the five pyrrolidinium based RTILs studied in this thesis. That the alpha relaxation obeys TTS, however, supports the idea suggested in literature [4] that the structural relaxation exhibits a general behavior in glass-forming liquids.

These results show that even though the structure in the pyrrolidinium-based RTILs from this study have a complex structure, as observed in the x-ray structure factor, and even though they do not comply with the first criterion for

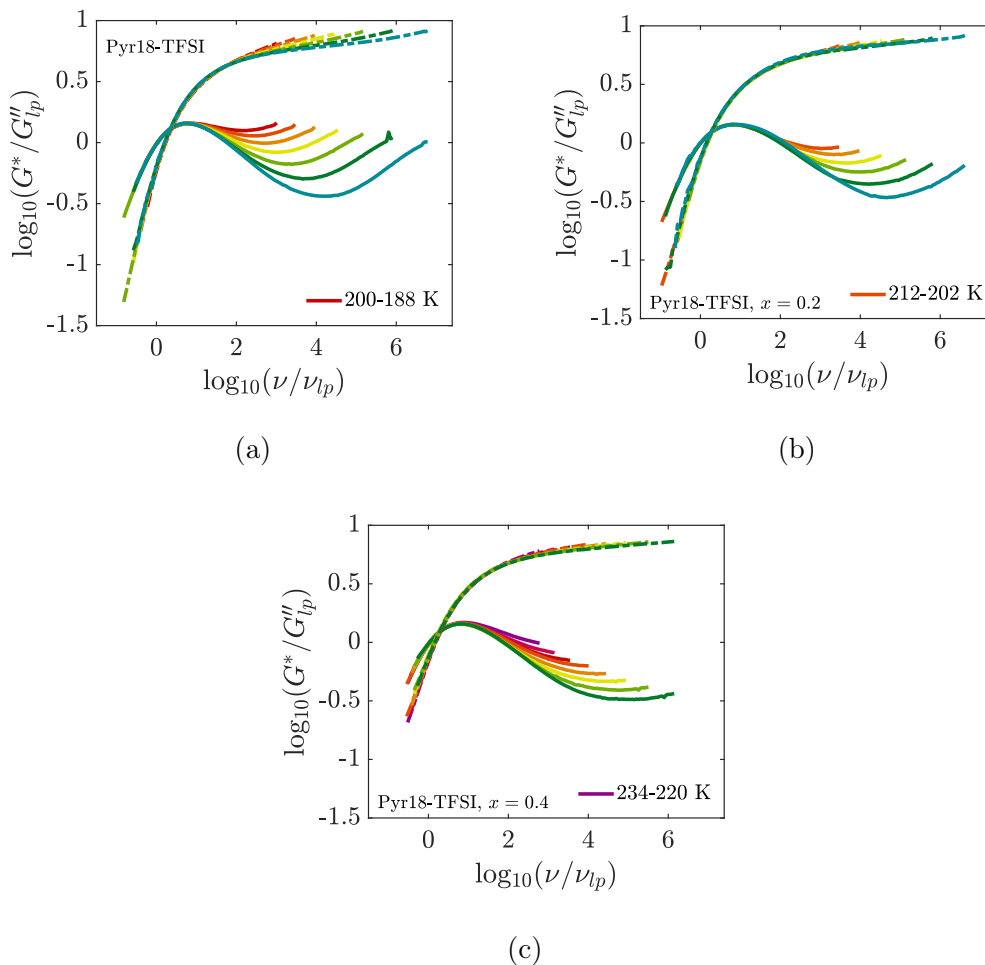


Figure 8.7: TTS plot of the logarithm of the real (dashed-dotted) and imaginary (solid) part of the shear modulus for the three liquids in the Pyr18-TFSI with Li-salt series. All temperatures have been scaled to a point in the modulus which lies 30% in modulus below the peak on the low frequency side (lp). It shows a high degree of TTS for the alpha relaxation in all three liquids which is not present for the beta relaxation.

simplicity, they still have a spectral relaxation similar to non-associated molecular liquids [11]. Furthermore, this applies across increasing chain length and increasing Li-salt concentration hinting that the dynamic behavior is independent of increasing structural complexity.

8.2 Broadband Dielectric Spectroscopy

8.2.1 Method

The method here is the same as described in subsection 7.2.1 with the addition that the Li-salt, lithium bis(trifluoromethanesulfonyl)imide, was with a purity

of 99.9%, purchased from Solvionic and used as bought. All storage, mixing and sample preparation took place inside a glove box with dry, inert nitrogen atmosphere.

As in chapter 7 the BDS data in this chapter will not be presented for the individual liquids in separate subsections, but instead be divided into four different representations of the data. The reason is that there are four different representations; complex permittivity, $\varepsilon^*(\omega)$, the derivative of complex permittivity, $\varepsilon''_{der} = (-\pi/2) \frac{\partial \varepsilon'}{\partial \ln(f)}$, the dielectric modulus that is $M^*(\omega) = 1/\varepsilon^*(\omega)$ and conductivity. All four representations can reveal various aspects of the results and will each time be presented in comparison to the other liquids in the series.

8.2.2 Alpha relaxation

The alpha relaxation is in the dielectric permittivity in all three liquids of the Li-salt mixed series obscured by a high DC conductivity contribution to the spectra. This is visible in figure 8.8 where the imaginary part of the permittivity, ε'' , is seen as dashed lines. This conductivity contribution to the spectra can be removed by using the derivative representation, ε''_{der} , a method explained in section 3.2.

Figure 8.8 shows that the derivative representation of the data reveal a dynamic mode at lower frequencies in all three liquids and at all temperatures. This mode is seen as a shoulder or a peak in the spectra at frequencies just above the electrode polarization. The relaxation times of this mode was found by fitting the logarithm of ε''_{der} around the shoulder/peak to a second-degree polynomial and then identifying that $\tau_{\alpha,d} = 1/(2\pi\nu_{max})$ where ν_{max} is the frequency of the peak, see figure 8.8d for an example of such a fitting. This choice of fitting function only serves to find the peak position since it was not possible to get reliable fits of the spectra to a model-based expression.

Note that for Pyr18x02 the absolute value of the permittivity is lower, possibly due to incomplete filling of the capacitor. As a consequence, the signal is more dominated by noise which is reflected in the found alpha relaxation times.

See figure 8.9 for the resulting dielectric alpha relaxation times in an Arrhenius plot together with the alpha relaxation times found from the shear modulus. It reveals that the alpha relaxation times, found from the two different measurements methods, agree quite well with the dielectric alpha relaxation being slower in all three liquids and having a weaker temperature dependence. There is especially in neat Pyr18-TFSI a high degree of overlap in the alpha relaxation time between the two response functions where the data collapse at the lowest temperature.

The dielectric alpha relaxation time, $\tau_{\alpha,d}$, for all three liquids has been scaled to T_g which in this case was defined as where $\log_{10}(\tau_{\alpha,d}) = 1$, and the results can be seen in figure 8.9. The three curves have very similar temperature dependence, but there is a slight difference between them which is not present in the alpha relaxation in the shear modulus. This is possibly due to the higher uncertainty in finding the alpha relaxation time from ε''_{der} . In Pyr18x02 this uncertainty was even higher due to the lower absolute value in the signal and as a result of this

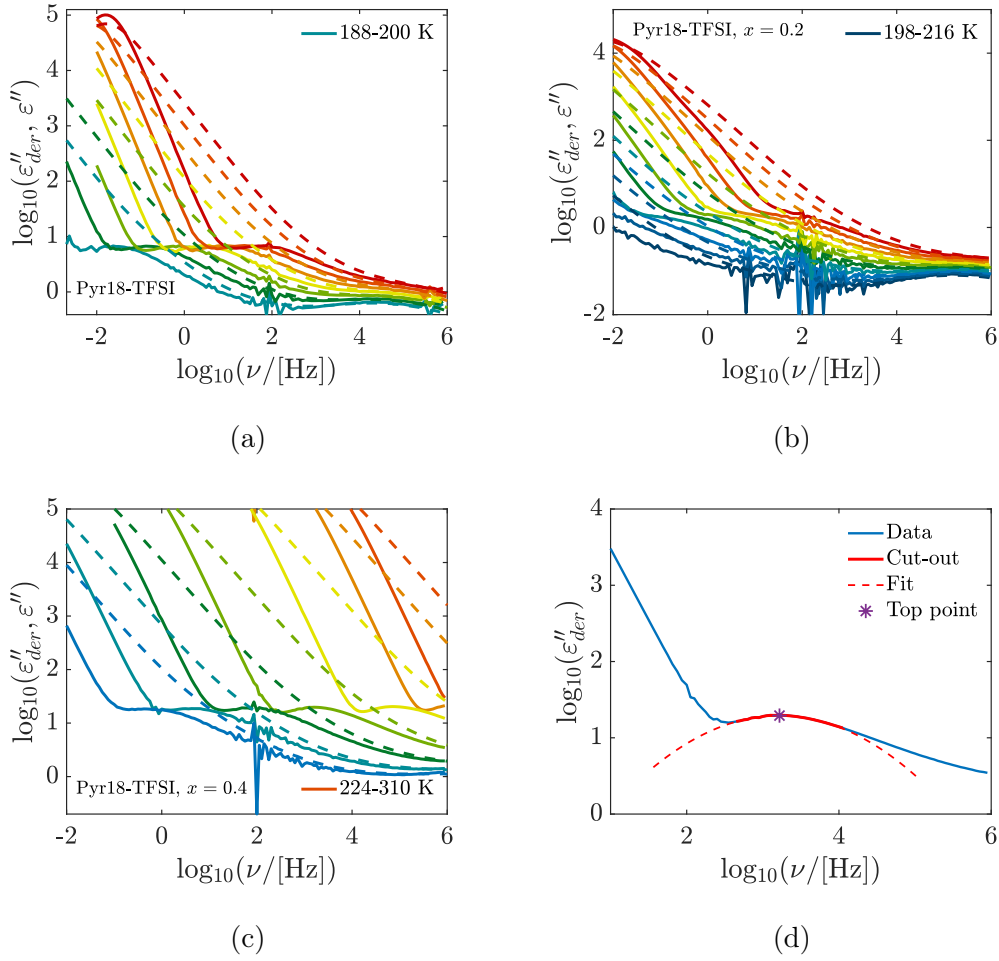


Figure 8.8: The derivative representation of the complex permittivity (solid lines) for a) Pyr18-TFSI, b) Pyr18-TFSI with $x = 0.2$ Li-TFSI and c) Pyr18-TFSI with $x = 0.4$ Li-TFSI shown together with the imaginary part of the complex permittivity (dashed lines) for comparison. d) is an example of the alpha relaxation time found from the top point (purple asterisk) of a second-degree polynomial (dashed red) fitted to the data around the peak (solid red).

no fragility index was found for this liquid.

For Pyr18-TFSI and Pyr18x04 the temperature dependence of the alpha relaxation time are still so similar that it justifies finding a collected fragility index for these two liquids. The result is a fragility of $m_p = 72 \pm 8$.

8.2.3 Beta relaxation

Figure 8.10 also reveals a secondary, high frequency relaxation in all three liquids. A qualitative comparison with the shear compliance data, which is the mechanical equivalent of the dielectric permittivity, show that this beta relaxation looks very similar in the two response functions. The peak is above 10 kHz and moves to

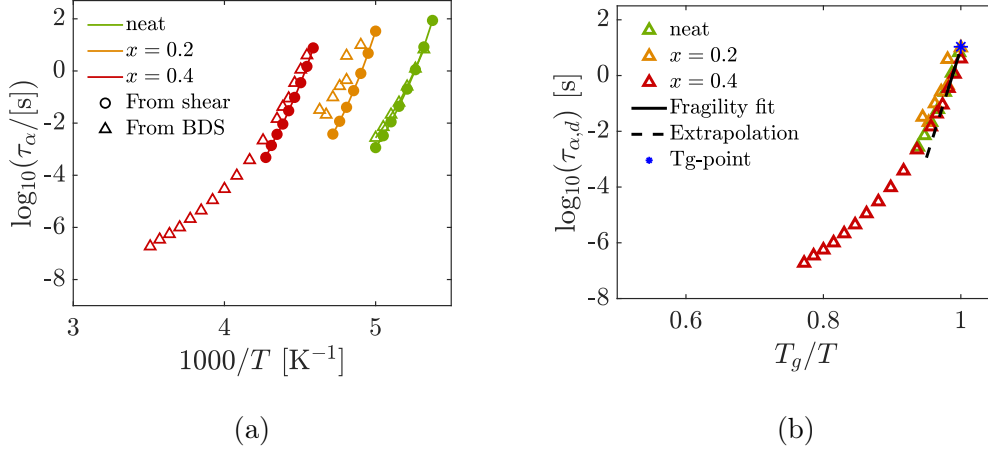


Figure 8.9: a) An Arrhenius plot of the alpha relaxation time for neat Pyr18-TFSI and Pyr18-TFSI with $x = 0.2$ and $x = 0.4$ molar fraction of Li-TFSI found by shear modulus (circles) and by the derivative representation of the dielectric permittivity (triangles). It shows a good overlap of the alpha relaxation times found from the two different measurement methods. b) the dielectric alpha relaxation time from a) in an Arrhenius plot scaled to T_g (blue asterisk) with the fragility found from a linear fit (black solid).

higher frequencies with increased Li-salt concentration and appears to be almost temperature independent. This is also similar to the beta relaxation that was found in the Pyr18-TFSI series.

The beta relaxation for all three liquids is much more pronounced in the modulus representation, $M^* = 1/\varepsilon^*$, see figure 8.11, where it appears as a clear peak which slowly merges with the conductivity peak as the temperature increases.

In order to quantify the beta relaxation in both the dielectric permittivity and modulus, the data just around the peak were fitted to a second degree polynomial in order to find the top point and thus the relaxation time. Then $\tau_{\beta,d} = 1/(2\pi\nu_{max})$, where ν_{max} is the frequency at the top point. The resulting relaxation times can be seen plotted together with the alpha and beta relaxation times found from the shear modulus and shear compliance respectively in figure 8.12. Note that only the beta relaxation time found from ε'' at the lowest temperature was included in the plot since the fit of ε''_{der} to a second-degree polynomial could not find the peak position at higher temperatures.

In all three liquids the beta relaxation across response functions and representations has very little temperature dependence and appear Arrhenius in nature with activation energies of the dielectric beta relaxation found from the modulus of 4.73, 7.53 and 8.70 kJ/mol for neat Pyr18-TFSI, Pyr18x02 and Pyr18x04 respectively with corresponding τ_0 of $2.6 \cdot 10^{-9}$ s, $1.7 \cdot 10^{-11}$ s and $2.4 \cdot 10^{-12}$ s. That the activation energies increase systematically with increase Li-concentration is an interesting result even though the increase is small.

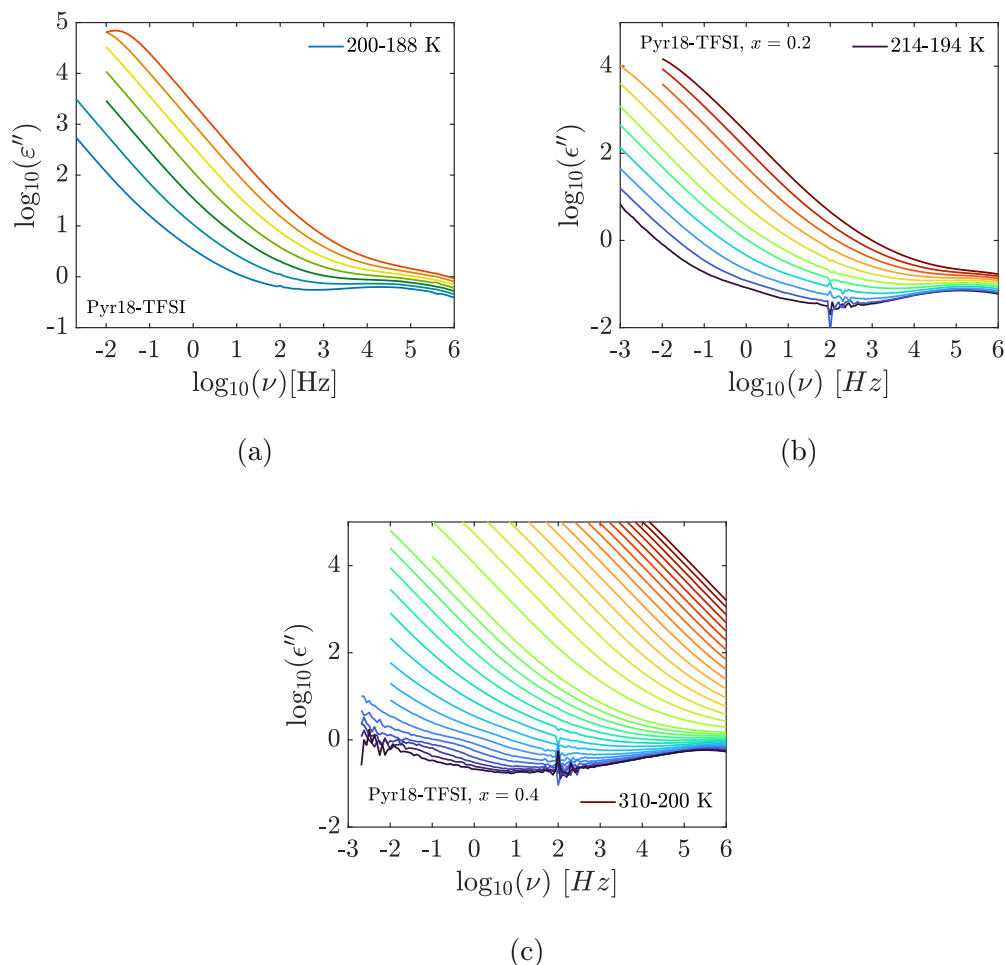


Figure 8.10: The imaginary part of the complex permittivity, ϵ'' for a) Pyr18-TFSI, b) Pyr18-TFSI with $x = 0.2$ Li-TFSI and c) Pyr18-TFSI with $x = 0.4$ Li-TFSI.

There is a clear overlap in the beta relaxation time between the shear compliance, the dielectric permittivity and the electric modulus in neat Pyr18-TFSI. This is a clear indication that the beta relaxation seen in the shear mechanical and dielectric data has the same molecular origin. For the two liquids mixed with Li-salt, there is an even better overlap of the beta relaxation time for the dielectric permittivity and the modulus, but here it was not possible to compare with the beta relaxation in shear compliance.

Looking at the difference in the beta relaxation times across Li-salt concentration, it is clear that it becomes faster with increased Li-concentration which is the opposite of the alpha relaxation. This decrease in relaxation time is most prominent going from neat Pyr18-TFSI to Pyr18x02 even though the change is small. When comparing the beta relaxation time in Pyr18x02 and Pyr18x04 this decrease is almost non-existing and so, the beta relaxation from the two ionic liquids with Li-salt is almost identical and with a similar temperature dependence.

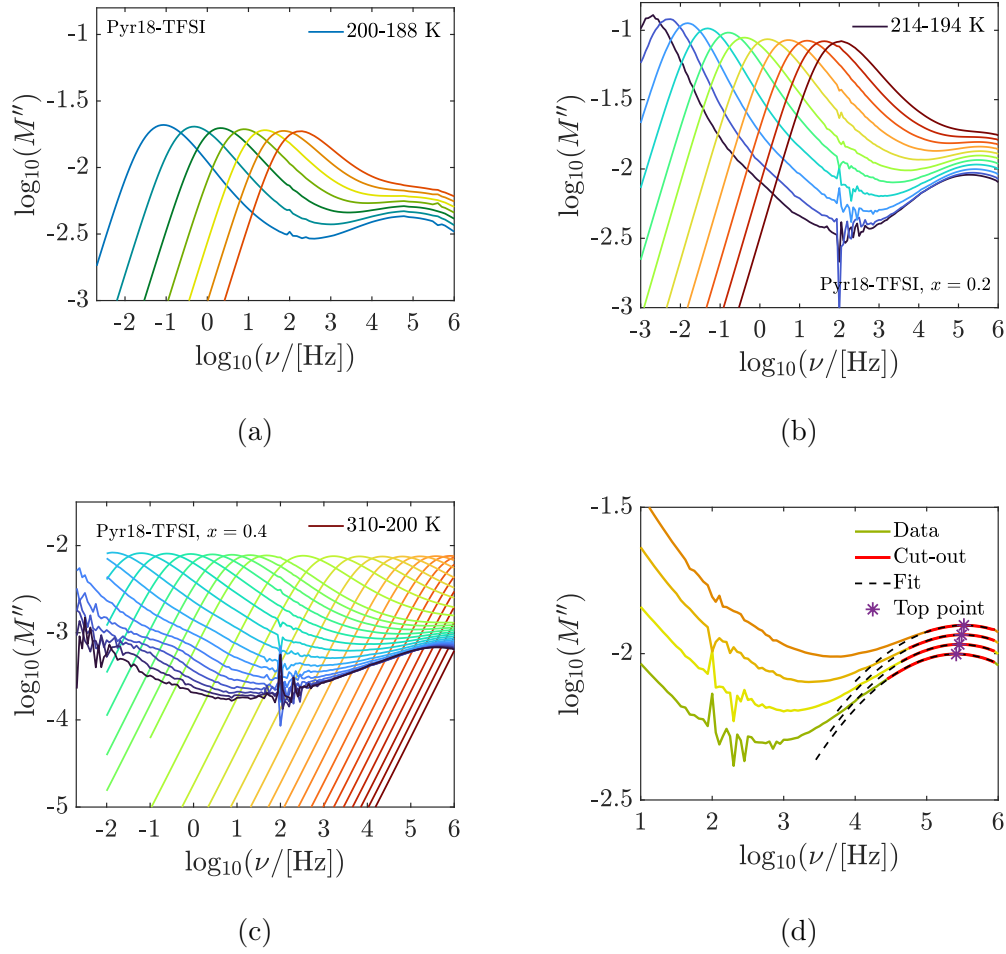


Figure 8.11: The imaginary part of the dielectric modulus, M'' , for a) Pyr18-TFSI, b) Pyr18-TFSI with $x = 0.2$ Li-TFSI and c) Pyr18-TFSI with $x = 0.4$ Li-TFSI. d) is an example of the fitting procedure used to find the relaxation time with the data round the peak (solid red) being fitted to a second degree polynomial (black dashed) to find the top point (purple asterisk), here with data from Pyr18-TFSI with $x = 0.2$ Li-salt.

The latter is also reflected in the activation energies.

That the alpha relaxation gets slower with increasing Li-salt concentration as opposed to the beta relaxation is made extra clear in figure 8.12b. Here all relaxation times are scaled to T_g and the decoupling of the alpha and beta relaxation is highlighted.

8.2.4 Conductivity

The last way of representing the data in this work is the conductivity given as $\sigma^*(\omega) = i\omega\varepsilon_0\varepsilon^*$. With this representation the transport properties in the form of ion conductivity will be displaced which can give information about for example

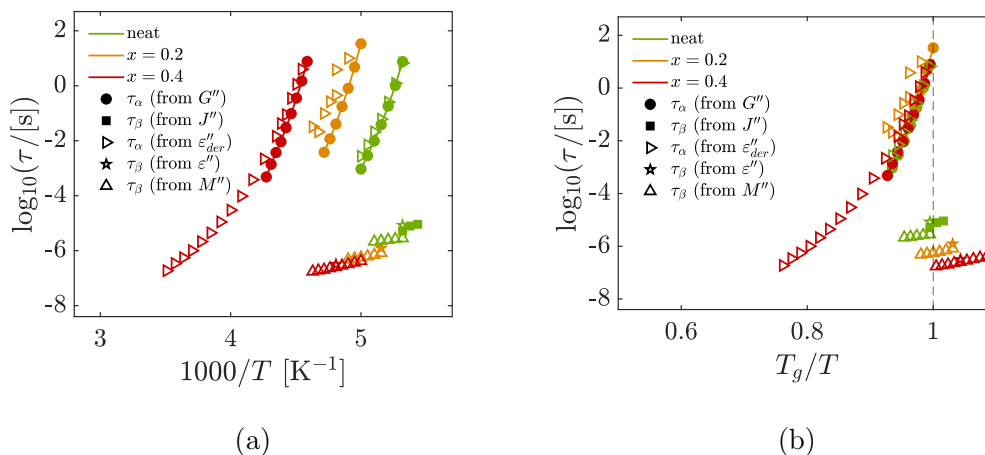


Figure 8.12: The alpha and beta relaxation times for neat Pyr18-TFSI, Pyr18x02 and Pyr18x04 found by shear modulus (circles), shear compliance (asterisk), by ε'' (squares) and by M'' (triangles) plotted in an Arrhenius plot. It clearly shows a significantly lower temperature dependence of the beta relaxation time compared to the alpha relaxation. Only the coldest temperature for the beta relaxation found from ε'' has been included, since this is the only temperature where it was possible to find a reliable top point.

the steady state conductivity, σ_0 . This is a basic property of RTILs and one that is often presented in literature.

Due to cold-crystallization it was only possible to measure in a limited temperature range for neat Pyr18-TFSI and Pyr18x02. In these two liquids the measurement protocol was to cool down rapidly to around T_g and then measure in heating steps of 1-2 K until crystallization started. Crystallization is completely suppressed in Pyr18x04 and it was possible to measure the conductivity in cooling all the way down to around T_g .

For liquid Pyr14-TFSI, Pyr24-TFSI and Pyr23-TFSI [70] as well as for Pyr15-TFSI [107] mixed with Li-salt the conductivity decreases with increasing Li-salt concentration. This decrease in conductivity is reported to be most likely due to a simultaneous increase in viscosity.

Figure 8.13 shows plots of the real part of the conductivity for Pyr18-TFSI, Pyr18x02 and Pyr18x04. For all three ionic liquids the spectra consist of a low-frequency electrode polarization shown as a dip in conductivity, followed by an intermediate conductivity plateau which is the steady state conductivity and ends with a high-frequency increase in conductivity.

The steady state conductivity, σ_0 , was calculated at all measured temperatures as described in section 3.2. The resulting conductivity plotted as a function of inverse temperature can be seen in figure 8.14. There is a clear decrease in conductivity with increasing Li-salt concentration. This is consistent with previous results on other pyrrolidinium based RTILs [70, 107], but it is the first time it has been shown in Pyr18-TFSI mixed with Li-salt. The decrease in conduc-

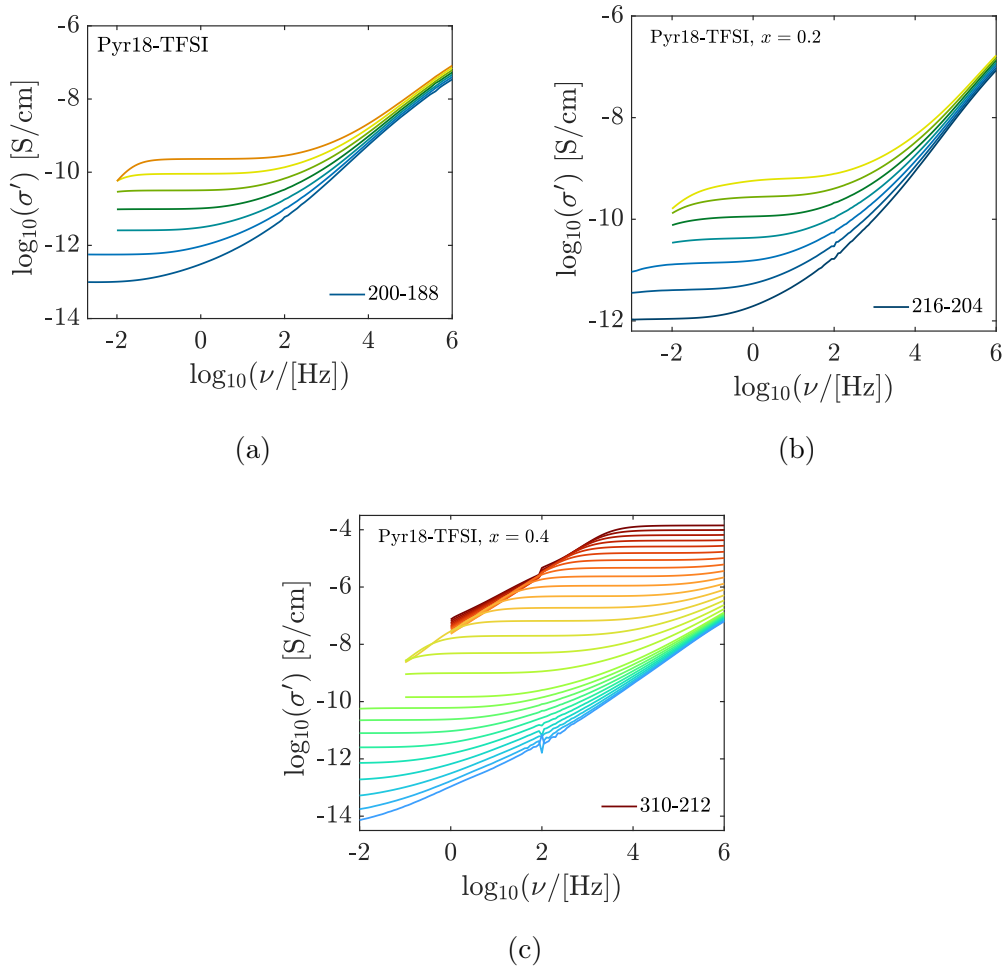


Figure 8.13: Real part of the complex conductivity of a) neat Pyr18-TFSI, b) Pyr18-TFSI with $x = 0.2$ molar fraction of Li-TFSI and c) Pyr18-TFSI with $x = 0.4$ molar fraction of Li-TFSI showing the steady state conductivity as a plateau in the spectra.

tivity becomes very pronounced at low temperatures, but in all three cases the temperature dependence of the conductivity appears to be similar.

This has been tested further by scaling the temperature to T_g found as where $\log_{10}(1/\sigma_0) = 12$. This definition of T_g gives a slightly higher T_g than in the shear mechanical data, and it indicates that a value of $\log_{10}(1/\sigma_0) = 12$ is too low. This value was however chosen as to avoid extrapolation of the conductivity data.

T_g was found to be 191 K, 204 K and 221 K for neat Pyr18-TFSI, Pyr18x02 and Pyr18x04 respectively and the to T_g scaled conductivity plot can be seen in figure 8.14b. Here it is clear that all three liquids exhibit a similar temperature dependence in the conductivity, especially at low temperatures close to T_g . That the three curves seem to collapse when scaling to T_g is consistent with results in a study on Pyr14-TFSI, Pyr24-TFSI and Pyr23-TFSI [70].

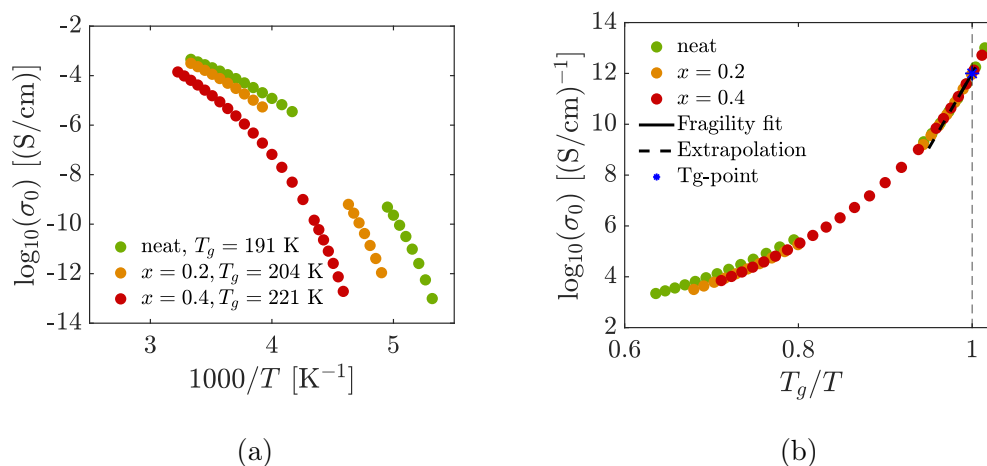


Figure 8.14: The inverse conductivity as a function of inverse temperature for three IL in the Li-mixed Pyr18-TFSI series. a) is inverse temperature and b) shows the data scaled to T_g (blue asterisk) with the fragility index found from a linear fit (black solid).

A common isobaric fragility index was found from the collected data since the temperature dependence of the three liquids at low temperatures by visual inspection is very close to identical. The result is a fragility of $m_p = 60 \pm 3$ with T_g defined as where $\log_{10}(1/\sigma_0) = 12$.

8.3 Coupling between shear and conductivity

This section will analyze the relation between the shear mechanical alpha relaxation time and the steady state conductivity in order to find the decoupling between the two. It was accomplished by plotting the inverse conductivity and alpha relaxation time in the same plot in order to analyze the temperature dependence of the decoupling between them, see the result in figure 8.15.

Note that the two y-axes are scaled so that $1/\sigma_0$ and $\tau_{\alpha,s}$ collapse at the second highest temperature, and that both y-axes display an equal number of decades to allow direct comparison of the temperature dependence between the two properties. For all three liquids the inverse conductivity and alpha relaxation time collapse at the first few measured temperatures, but then start to decouple as T_g is approached. The same tendency was seen in the Pyr1*n*-TFSI series even though the decoupling is more pronounced in the Li-salt mixed series, especially in Pyr18x02.

Time-scale index The time-scale index [114] for the shear and dielectric alpha relaxation time as well as the inverse conductivity were also found for the three RTILs in the Pyr18-TFSI mixed with Li-salt series. The results can be seen in figure 8.16 and show that the decoupling seen in the Pyr1*n*-TFSI series is also

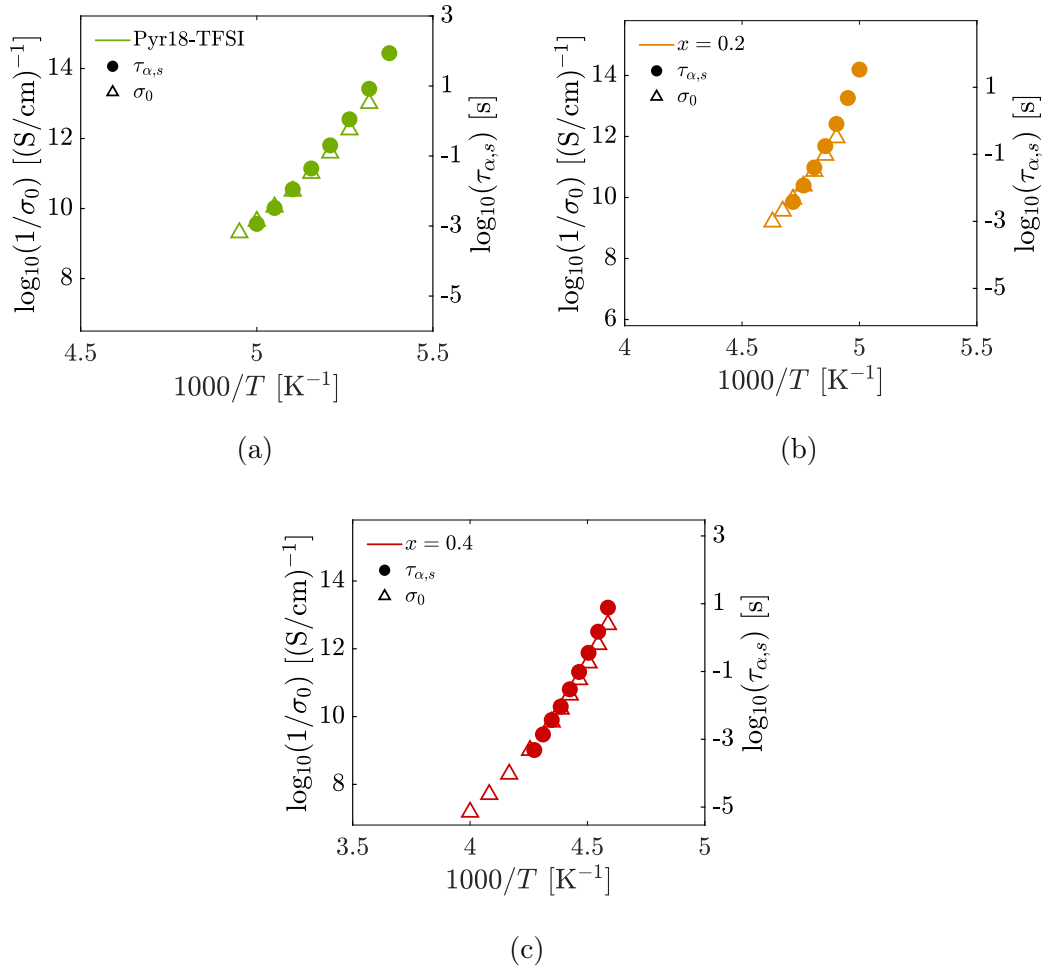


Figure 8.15: The inverse conductivity (triangles) together with the alpha relaxation time (circles) for all three liquids in the Li-salt mixed Pyr18-TFSI series. The two axes have been scaled so that the data collapse at the second highest temperature and there is an equal number of decades on both axes. There is a clear decoupling between the inverse conductivity and the alpha relaxation time in all three liquids as T_g is approached.

present when increasing the Li-salt concentration of Pyr18-TFSI mixed with Li-salt.

The degree of decoupling in Pyr18x02 and Pyr18x04 is less pronounced in the dielectric alpha relaxation time, as found from ε''_{der} , when compared to the inverse conductivity, which in the case of Pyr18x02 can be explained by the high uncertainty in finding the alpha relaxation time. Note that the dielectric time-scale index in Pyr18x02 was shifted 0.65 decades down in order to better show the temperature dependence relative to the shear alpha relaxation time and the inverse conductivity.

The degree of decoupling for the inverse conductivity relative to the shear alpha relaxation time, with an increase of around 0.5 decades in the time-scale

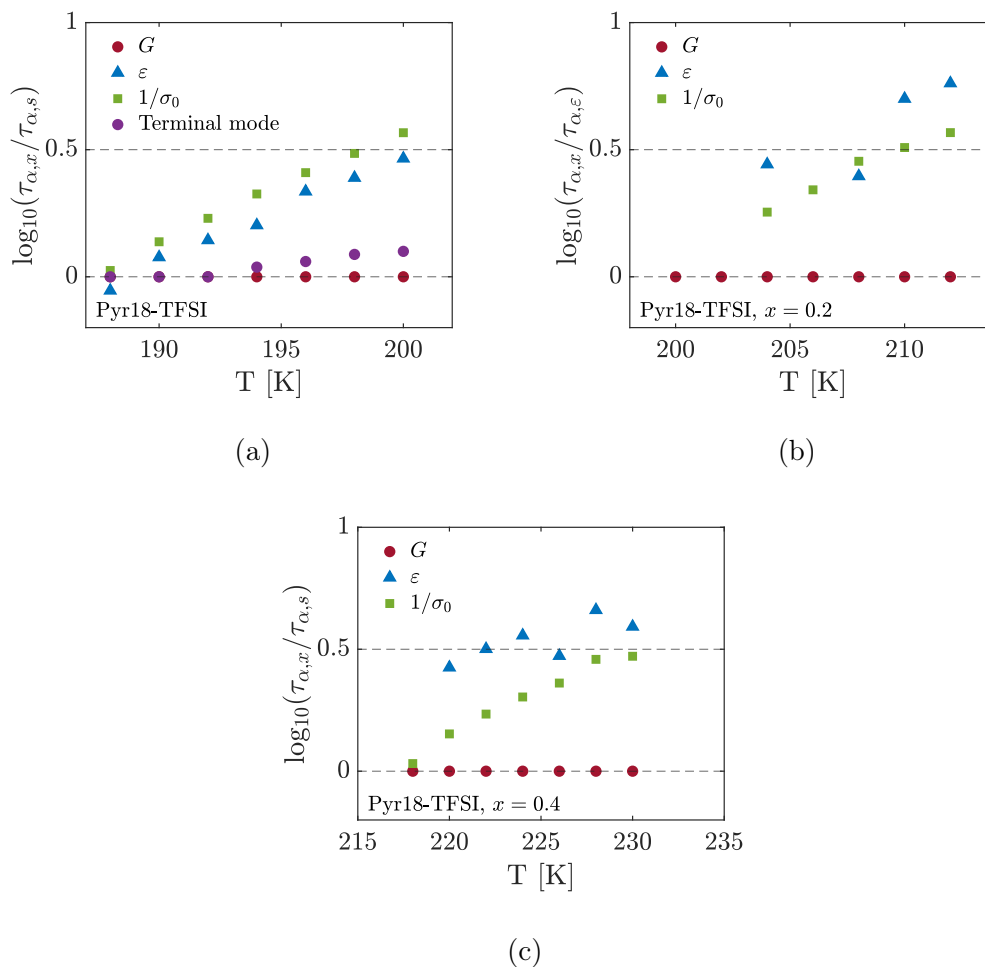


Figure 8.16: The logarithm of the alpha relaxation time for a) Pyr18-TFSI and Pyr18-TFSI mixed with b) $x = 0.2$ and c) $x = 0.4$ molar fraction of Li-TFSI found by shear modulus (red) and the derivative of the dielectric permittivity (blue) as well as the inverse conductivity (green) scaled to the alpha relaxation time of the shear modulus. This is called the time-scale index and shows the quantitative degree of decoupling between the alpha relaxation time measured with the two response functions and the inverse conductivity. All three ionic liquids show decoupling as a temperature dependence of the time-scale index.

index, is more or less the same in all three liquids and in the case of Pyr18-TFSI it matches that of the dielectric alpha relaxation. This picture changes when using the time scale of the terminal mode instead of the alpha relaxation time in Pyr18-TFSI, which decreases the decoupling. This is explained in more detail in the previous chapter, but it indicates that the beta relaxation is partially responsible for the decoupling in this liquid. In Pyr18x02 and Pyr18x04 there was no significant difference when using the time scale for the terminal mode compared to the alpha relaxation time which is probably since the alpha and beta relaxation are well separated in these two liquids.

With this in mind, it appears as though there is an increase in decoupling when increasing adding Li-salt to the neat Pyr18-TFSI, but there is no significant change when increasing the salt concentration from 20 to 40%.

8.4 Overview

To get an overview of the different results in this chapter, the basic parameters have been collected in table 8.1 and 8.2. For all three liquids T_g is four degrees higher when found with shear mechanical results as when found with conductivity.

Liquid	$m_p, \tau_{\alpha,s}$	$m_p, \tau_{\alpha,d}$	m_p, σ_0	$T_g, \tau_{\alpha,s}$	$T_g, \tau_{\alpha,d}$	T_g, σ_0
Pyr18-TFSI	94 ± 5	72 ± 8	60 ± 3	187	188	191
Pyr18x02	94 ± 5	-	60 ± 3	200	-	204
Pyr18x04	94 ± 5	72 ± 8	60 ± 3	217	220	221

Table 8.1: A table showing the isobaric fragility index, m_p , and the glass transition temperature, T_g , for all liquids measured with DMS and BDS. T_g was for the shear mechanical data defined as $\log_{10}(\tau_{\alpha,s}) = 1.5$ and for the dielectric data as $\log_{10}(\tau_{\alpha,d}) = 1$ and $\log_{10}(1/\sigma_0) = 12$.

Liquid	E_β, G'' [kJ/mol]	E_β, M'' [kJ/mol]
Pyr14-TFSI	9.74	2.65
Pyr16-TFSI	22.6	5.12
Pyr18-TFSI	17.7	4.73
Pyr18x02	-	7.53
Pyr18x04	-	8.70

Table 8.2: A table showing the activation energy of the beta relaxation, E_β , found in DMS and BDS measurements for the three liquids in the series.

8.5 Discussion

Simplicity As in the previous chapter, two criteria for simplicity in glass-forming liquids were tested but this time on neat Pyr18-TFSI and Pyr18-TFSI mixed with $x = 0.2$ and $x = 0.4$ molar fraction of Li-TFSI. The criteria were the requirement of TTS and the constant time-scale index. The first corroborated the result seen in the Pyr1*n*-TFSI series; that even though the shear mechanical

relaxation spectra did not exhibit complete TTS, due to a weaker temperature dependence of the beta relaxation, the TTS principle was followed with the alpha relaxation.

The second criterion for simplicity, no decoupling between response functions, also corroborated the results from the Pyr1*n*-TFSI series. The time-scale index for both alpha relaxation times and inverse conductivity is clearly temperature dependent for all three Li-concentrations.

The consequence is that in both series the dynamics do not completely meet the requirements for simple behavior, but only to some degree. Again, it was not expected that the RTILs in this study, or RTILs in general, meet the criteria for simple behavior and thus be viewed as "zeroth order liquids", but there is still a degree of simplicity present. This is seen as 1) the alpha relaxation complying to TTS and 2) a time-scale index with a relatively weak temperature dependence. As the alpha relaxation changes 5-6 order of magnitude the time-scale index for the conductivity changes around 0.5 decade and the dielectric alpha relaxation time changes around 0.25-0.5 decade.

When increasing the Li-salt concentration in Pyr18-TFSI, the x-ray structure factor reveals a significant change in structure seen as an increase of the pre-peak and a decrease of the charge peak. This change in structural complexity is, however, not reflected in the degree of simplicity present in the dynamics of these liquids, which is an intriguing result. There is a slight increase in decoupling when adding Li-salt to Pyr18-TFSI, seen in the time-scale index, but this decoupling do not increase further with increased salt concentration.

Non-associated molecular liquids With the study of this series of Pyr18-TFSI mixed with Li-salt it is possible to expand on the conclusion, that the Pyr1*n*-TFSI series exhibit a dynamic behavior similar to non-associated molecular liquids. As with the Pyr1*n*-TFSI series, the large change in the structure is not at first glance reflected in the dynamics. There are two prominent dynamic modes in the shear mechanical spectra, the alpha and beta relaxation, except for a small intermediate mode in Pyr18x02, seen as a shoulder in the spectra at low temperatures.

The alpha relaxation slows down significantly with increasing Li-salt concentration, but the temperature dependence is close to unchanged. So much that the alpha relaxation times in the three liquids cannot be distinguished, and a fragility index was calculated for all of them collected.

The same picture is repeated in the steady state conductivity. Here there is, as with the alpha relaxation, a slowing down of the conductivity with increasing Li-salt concentration, but the temperature dependence is close to identical across the three liquids. This is seen as a collapse of all three σ_0 curves when scaled to T_g .

A feature in the Pyr18-TFSI mixed with Li-salt series, which deviates from non-associated molecular behavior, is the presence of a slow mode in the shear mechanical spectra of Pyr18x02 and Pyr18x04. The intensity of the slow mode increases with increasing Li-salt concentration and thus, introduces a complexity

not present in non-associated molecular liquids like squalane or cumene. This will be shown and explained in detail in chapter 9.

Beta relaxation The presence of a high frequency beta relaxation in the dielectric signal has been observed before in different families of RTILs and one of the aims in this study is to investigate the origin of this dynamic mode. If the beta relaxation has an intramolecular origin then it can be the motion of 1) the pyrrolidinium ring, 2) the methyl chain, 3) the alkyl chain and 4) the anion, as was also mentioned earlier in chapter 7.

Several studies end at the conclusion that the beta relaxation seen in the dielectric signal originates from motion of the alkyl chain on the cation [111, 115–118], but these are all studies on a different family of RTILs.

When focusing on results on the beta relaxation in pyrrolidinium based RTILs, there are two different conclusions found in literature. The first is that the beta relaxation originates in the alkyl chain of the cation [80] and the second is that it is the dynamic signal of intermolecular motion or a so-called genuine Johari-Goldstein (JG) beta relaxation [110].

That the beta relaxation in pyrrolidinium based RTILs is the dynamic signal of JG-modes was also one of the suggestions to the origin of this relaxation in a study of neat Pyr14-TFSI by the author of this thesis and co-workers [95]. Here a combination of quasi-elastic neutron scattering on a partly and fully deuterated cation and high-frequency DMS measurements showed that the beta relaxation of this RTIL is not related to either the single methyl group or the end methyl group on the butyl chain of the cation [22]. The reason for this is that the time scale of the beta relaxation is too slow to be related to these much faster dynamics. It was however also suggested that the origin was dynamics from the anion TFSI.

If the origin is the TFSI anion, then the beta relaxation should be invariant when changing the cation and keeping the anion constant. An invariance in the beta relaxation time was indeed seen in the Pyr1*n*-TFSI series as described in chapter 7 and this invariance continues across Li-concentration as well. This is illustrated in figure 8.17 where all five RTILs in the two series have been plotted together in an Arrhenius plot, showing both the alpha and beta relaxation times from both shear mechanical and dielectric measurements. A common feature is that the beta relaxation depends very little on both alkyl chain length and Li-salt concentration across response functions and representations. It even appears almost as a single beta relaxation with a weak temperature dependence. In a temperature interval where the alpha relaxation changes with up to ten orders of magnitude compared to 1-2 for the beta relaxation.

The to T_g scaled plots, i.e. figure 8.17b and 8.17d, illustrate that the beta relaxation is measured all the way from the liquid state well into the glassy state. The temperature dependence seems constant across T_g meaning that there is no kink in the beta relaxation time at T_g . The to T_g scaled plots, furthermore underline the decoupling between the alpha and the beta relaxation.

The above points indicate a common origin of the beta relaxation which is to

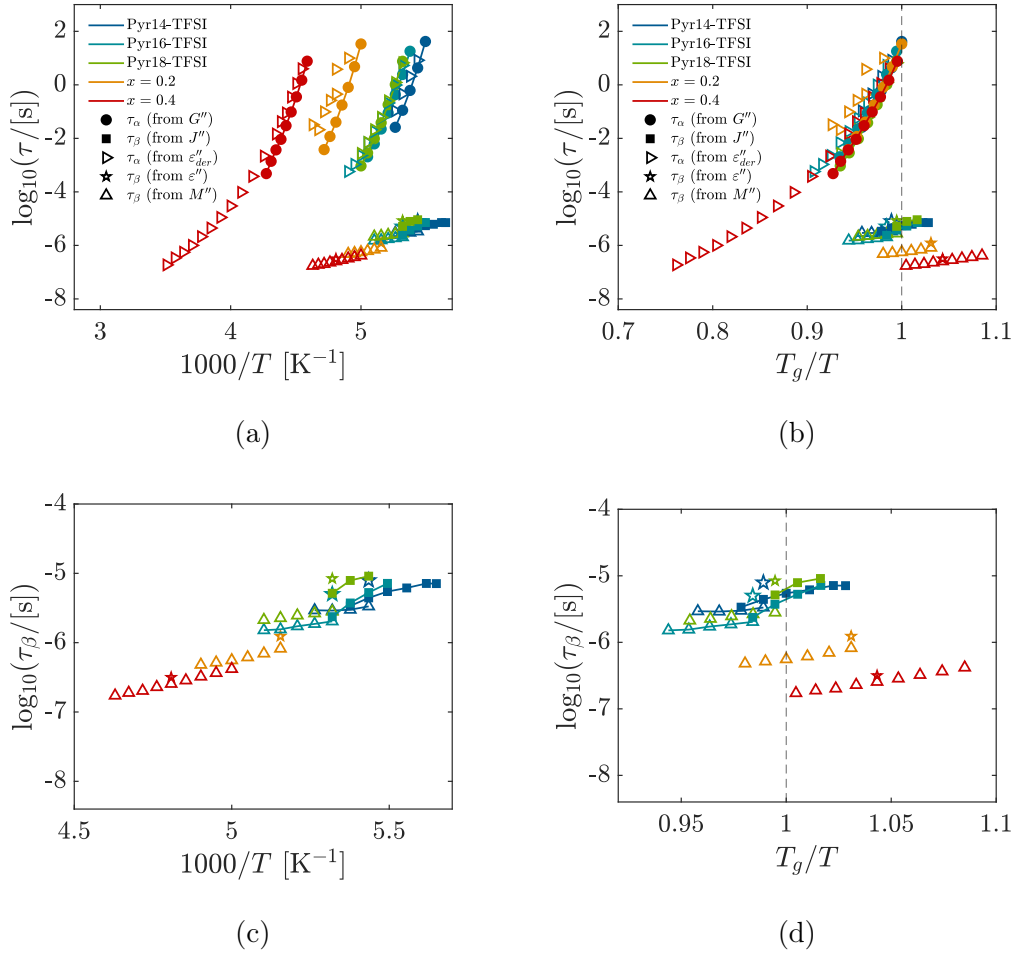


Figure 8.17: Arrhenius plot of the alpha and beta relaxation time from both shear mechanical and dielectric measurements for all five pyrrolidinium based ionic liquids, i.e. Pyr14-TFSI, Pyr16-TFSI, Pyr18-TFSI and Pyr18-TFSI with $x = 0.2$ and $x = 0.4$ molar fraction of Li-TFSI. a) and c) is as a function of inverse temperature and b) and d) is as a function of inverse temperature scaled to T_g . c) and d) are zoom in around the beta relaxation.

a very small degree affected by the cross over from viscous liquid to the glassy state and which has a low activation energy. A candidate which complies with these requirements is small rotations in the anion.

Figure 8.17 furthermore shows that both the shear and dielectric alpha relaxation for all five ionic liquids collapse almost perfectly when scaled to T_g , which is also reflected in the similar fragility indexes of the shear and dielectric alpha relaxation, respectively.

Conductivity and the alpha relaxation When looking at the steady state conductivity in the series of Pyr18-TFSI mixed with Li-salt there is a clear decrease in conductivity with increasing Li-salt concentration. This is consistent

with the picture of the conductivity being related to the mobility of charge carriers and so the systematic increasing in viscosity with increasing Li-salt concentration is reflected here. This results also matches what is found in literature [70, 107].

A further discussion regarding the steady state conductivity is its coupling with the structural relaxation time. This was in this study investigated with two analysis methods; 1) to find the isobaric fragility index in both the conductivity and alpha relaxation time and 2) by plotting the steady state conductivity in the same plot as the alpha relaxation time.

The first method shows a fragility index of the shear mechanical alpha relaxation time which is higher than the one found from steady state conductivity, i.e. $m_p = 94 \pm 5$ with $\tau_{\alpha,s}$ compared to 72 ± 8 with σ_0 for neat Pyr18-TFSI and Pyr18x04, respectively. It was not possible to find a conductivity fragility index for Pyr18x02. This difference in fragility indicates a decoupling of $\tau_{\alpha,s}$ and σ_0 close to the glass transition, just as with the Pyr1*n*-TFSI series. This is consistent with findings from literature on a series of Pyr1*n*-TFSI with $n = 4, 6$ and 8 [80]

The second method gives a more complex picture of the coupling between conductivity and the structural relaxation, since it can be investigated with change in temperature. Figure 8.15 shows that the decoupling between the two dynamic properties increase as T_g is approached. This general increase in coupling as T_g is approached is consistent with results from literature [80, 110].

8.6 Conclusion

This chapter presents results on the dynamics of a series of Pyr18-TFSI mixed with Li-TFSI in molar fractions of $x = 0.2$ (Pyr18x02) and $x = 0.4$ (Pyr18x04) measured with dynamical mechanical and broadband dielectric spectroscopy. This forms the basis of a comparative analysis with a systematical increase of the Li-salt concentration.

In the shear mechanical results, two modes were found in all three liquids where the slowest mode was identified as the structural or alpha relaxation time. A third relaxation mode was also present in Pyr18x02 at intermediate frequencies as a low frequency shoulder only visible at low temperatures. Further analysis on this mode was not performed.

The isobaric fragility index was calculated for all three liquids simultaneously and gave a collected fragility of $m_p = 94 \pm 5$. The fastest mode, named the beta relaxation, in the shear mechanical measurements could only be quantitatively analyzed for Pyr18-TFSI, since in Pyr18x02 and Pyr18x04 it had moved out of the frequency window in both the modulus and compliance representation. The beta relaxation for Pyr18-TFSI is Arrhenius in nature and has an activation energy, E_β , of 17.7 kJ/mol. The beta relaxation was also present in the BDS measurements and showed an Arrhenius temperature dependence in all three liquids. The activation energies were found to be 4.73, 7.53 and 8.70 kJ/mol for

Pyr18-TFSI, Pyr18x02 and Pyr18x04 respectively.

The alpha and beta relaxation times for both the Pyr1*n*-TFSI and the Pyr18-TFSI mixed with Li-salt series across response functions were plotted in an Arrhenius plot. This indicated that the beta relaxation has a common origin in all five ionic liquids, and that this origin is small rotations in the anion TFSI.

The steady state conductivity was furthermore analyzed. Pronounced cold-crystallization ensured that results were divided into a high and low temperature region with a no-man's land in between for neat Pyr18-TFSI and Pyr18x02, but crystallization was completely suppressed in Pyr18x04. The conductivity decreased with increasing Li-salt concentration, which was expected as the viscosity increases with increasing Li-salt. This is consistent with findings in literature on Pyr14-TFSI and Pyr15-TFSI mixed with Li-salt [70,107]. The low temperature conductivity was then compared to the alpha relaxation times in order to investigate a coupling between the two. It showed that the decoupling increases as T_g is approached in all three liquids.

Two criteria for simplicity were tested; the TTS principle and constant time-scale index. Neither criterion was met completely, but there was nevertheless a degree of simplicity in all three liquids, seen as TTS around the alpha relaxation and a time-scale index with relatively low temperature dependence. This degree of simplicity did not change systematically with increasing Li-salt concentration.

It is finally concluded that even though the alpha and beta relaxation, as well as the steady state conductivity, seen in all three liquids behaves as in non-associated molecular liquids, a level of complexity is introduced with increasing Li-salt concentration. The reason is that a slow mode in the shear mechanical spectra appears in Pyr18x02 and increases with increasing Li-salt concentration.

Chapter 9

Looking for the slow mode

This chapter will further describe the relaxations in room temperature ionic liquids (RTIL). As opposed to the in chapter 7 and 8 previously described fast relaxations, where the frequency is higher than that of the alpha or structural relaxation, this chapter will focus on the relaxations that are slower than the alpha relaxation.

The chapter will be separated into several parts. First there is an introduction which gives an overview of the studies in literature investigation slow relaxations in RTIL. This leads up to new data from this study and ends with a discussion which aims to shed light on the current status when talking about slow relaxations in RTIL.

9.1 Introduction

9.1.1 The pre-peak and mesoscopic structure

One of the original questions asked in this PhD project was to see if ionic liquids have low-frequency dynamics associated with their mesoscopic structure. This is a part of the overall question which aims to answer if ionic liquids have dynamics similar to those of simple liquids as well as non-associated molecular liquids.

The origin of this research question was general considerations in my research group regarding further research on ionic liquids. At that time, it was known that certain mono-hydroxy alcohols exhibited a low-frequency, sub alpha relaxation dynamic signal in the dynamic mechanical rheology (DMS) measurements [18]. This low-frequency signal is what will be referred to as the slow mode in the following. This slow mode in mono-hydroxy alcohols was related to mesoscale structures in the liquid [19] and it was therefore obvious to ask the question if there was a similar signal in ionic liquids.

It was at this time well known that there existed a pre-peak in the x-ray structure factor in ionic liquids in general [65], and in pyrrolidinium and bis(trifluoromethanesulfonyl)imide based ionic liquids especially [63, 68, 69, 83, 121], which was suggested being connected to mesoscale structures created by polar and non-polar regions. This connection between the structure factor pre-peak and

the formation of polar-nonpolar regions in the liquid has since then been confirmed several times [63, 67, 121, 122]. It has also been shown that an increase in alkyl chain length above three carbon atoms will increase the shear viscosity in imidazolium based RTIL [104–106]. The main question is therefore if these mesoscopic structures have a dynamic signal in for example dielectric and mechanical spectroscopy.

9.1.2 Literature overview

Since the discovery of mesoscopic structures in RTIL multiple research groups have investigated the low-frequency response of these. In 2009 D. Turton et al. [123] registered a slow mode in OKE and dielectric measurements of Emim-BF₄, Emim-DCA and Bmim-DCA which they assigned to mesoscale aggregates. The signal from the slow mode was intense in the OKE spectra but very weak in the dielectric signal and this implied that fluctuations in the mesoscale aggregates introduced a major change in the polarizability of the aggregates but only a small change in the macroscopic dipole.

This study was further supported by T. Sonnleitner et al. in 2014 [124] in a another combined dielectric and OKE study which showed sub-alpha relaxation dynamics in several RTILs. This study contained some interesting facts, namely that the sub-alpha relaxation peak was dominating in the OKE spectra but hardly discernible in the dielectric spectra and 2) that there was a clear difference between the imidazolium and the pyridinium/pyrrolidinium based IL. In the imidazolium ILs the sub-alpha relaxation was clearly present whereas in the pyridinium/pyrrolidinium ILs it was completely absent. Note however that the liquids found in these studies are not known to have a pre-peak in the structure factor.

Slow mode is due to mesoscale aggregates The following paragraphs will give a timeline of the studies where first of all a slow mode was detected in a RTIL and second of all where this slow mode was attributed to being the dynamic signal from mesoscale aggregates.

2011 A study by N. V. Pogodina et al. [45] aimed to make an in depth investigation on the dynamics of RTIL with rheology. They found a bimodal behavior in the shear modulus of both tri-isobutyl-methyl-phosphonium (TMP-Tos) and 1-butyl-1-methylimidazolium tetrafluoroborate (Bmim-BF₄) by identifying a slope in G'' significantly different from that of the terminal mode and by fitting the spectra to a model with two distinct slopes.

The fast mode was identified as the structural relaxation and the slower mode, which had a peak in G' at around 10^4 Pa, assigned to cooperative ion motion, or in other words, the motion of the mesoscale aggregates.

This conclusion was later criticized by R. Tao and S. L. Simon in a study on rheology of RTIL four years later in 2015 [125]. Tao and Simon pointed out that their own data and the data from Pogodina et al. have large errors at low

frequencies due to limitations in the phase angle measurement. This is because close to the terminal mode of the liquid the phase angle, δ , approaches 90° which results in large errors in $G' = G^* \cos(\delta)$. Furthermore, the liquid Bmim-BF₄ was later measured in a study by T. Cosby et al. [31] in which there was no discernible slow mode in the DMS signal.

2014 P. J. Griffin et al. studied methyltrioctylammonium bis(trifluoromethanesulfonyl)imide (N8881-TFSI) [126] by Broadband Dielectric Spectroscopy (BDS), Dynamic Mechanical Spectroscopy (DMS) and Depolarized Dynamic Light Scattering (DDLs) in order to look for the slow mode. They found nothing in BDS and DMS, but a bimodal spectrum showed up in DDLs which was, to this author's knowledge, the first time anyone had detected such a signal. The slow mode found in DDLs was attributed to mesoscale aggregate dynamics.

2015 This study was followed by some of the same authors in a study the year after on octyltriethylammonium bis(trifluoromethane-sulfonyl)imide (N2228-TFSI) and octyltriethylphosphonium bis(trifluoromethane-sulfonyl)imide (P2228-TFSI) with BDS and DDLs [117]. They observe a slow mode in the DDLs signal but this time also in the BDS signal, which was the first observation of a slow mode in the dielectric spectra of RTIL. Only the slow mode measured with BDS was however assigned to be the dynamic signal of mesoscale aggregates.

2017 A combined BDS and DMS study on a series of imidazolium based RTIL by T. Cosby et al. [31] showed a slow mode in the BDS signal of Omim-TFSI, Hmim-TFSI, Omim-BF₄ and Hmim-BF₄, so with alkyl chain lengths of six and eight. It did not appear in the RTIL with alkyl chains of shorter lengths. A clear slow mode was also detected in the DMS measurements for Omim-BF₄, and this liquid has a pre-peak in the x-ray structure factor [65].

This was the second time a slow mode was observed in DMS, but contrary to the study by Pogodina et al. the slow mode measured by Cosby et al. had its peak in G'' at a value two decades higher in modulus and the error in the signal was significantly lower, which was seen as a very small scatter of data points in the master plot. The time scales of the slow mode from the BDS measurements correlated with those obtained by neutron spin echo measurements of the mesoscale aggregates and so Cosby et al. concluded that the slow mode stems from long-lived mesoscopic structures. This conclusion was however questioned in a later study by the same group [127]. Here they mention a simulation study by T. Yamaguchi from 2018 [91] which shows that the slow mode in shear viscosity of imidazolium based IL with the TFSI anion is from the local decay of the charge alternation mode.

2018 The year after the same research group publishes a combined BDS and DMS study on another series of phosphonium RTILs [128] with the same anion. The cation was either triethyl-alkyl-phosphonium or tributyl-alkyl-phosphonium with the alkyl chain being either octyl (TEOP and TBOP) or dodecyl (TEDP

and TBDP). All four liquids exhibit a pre-peak in the x-ray structure factor but only the two of them (TEOP and TEDP) had a slow mode in the BDS measurements.

The question raised in this study was therefore; if a pre-peak in the structure factor is linked to the formation of mesoscale aggregates and the slow mode is the signal of these aggregates if they are long-lived, then why is there no slow mode in TBOP and TBDP? Two liquids which are shown to have a pre-peak.

The authors found the explanation in a detailed analysis of the x-ray structure factor. Here they showed, using the Tanford equation [129], that there could be a disruption of the mesoscale aggregates in the tributyl-alkyl phosphonium. This led to the conclusion that the pre-peak on its own is not enough in order to show if there are long-lived mesoscale aggregates. None of the RTIL in the study showed a slow mode in DMS.

2019 Cosby et al. [130] observed a slow mode in both DMS and BDS measurements on a series of binary RTIL mixtures where Omim-BF₄ was mixed with 30, 50 and 70 mol% of Emim-BF₄. Furthermore, a pre-peak was measured in the static structure factor obtained by x-ray scattering for all mixtures as well as the neat Omim-BF₄.

The slow mode showed systematic behavior with increased mixing percentage in the BDS signal but not in the DMS signal. Furthermore, the pre-peak decreased in intensity with increasing Emim-BF₄ percentage and this systematic change was reflected in the slow mode in the DMS signal. The conclusion from this study was also that the slow mode should be attributed to fluctuations of the mesoscale aggregates at time scales longer than that of the alpha relaxation.

2020 A very similar study was published by M. Musiał et al. [111] on 1-alkyl-3-methylimidazolium tricyanomethanide (C_nMim-TCM) with alkyl chain length of 2, 4, 6, 8 and 16. They found a slow mode in the BDS signal on liquids with an alkyl chain length above 4 with the same systematic behavior as the scattering structure pre-peak from the same liquids. They detected no slow mode in the DMS measurements.

2021 A similar study was performed by T. Cosby et al. [127] on a series of Lewis-acidic 1-alkyl-3-methylimidazolium chloroaluminate IL (C_nMim-Al₂Cl₇) with alkyl chain length of 2, 4, 6 and 8 as well as 1-alkyl-3-methylimidazolium chloride (C_nMim-Cl) with alkyl chain length of 6 and 8.

A slow mode was found by DMS only in Omim-Cl but by BDS in all the liquids where the signal was 15 times stronger in the liquids with a Cl anion as compared to the liquids with AlCl₃ anion. Two different slow modes were observed in the AlCl₃ based liquids; a low and a high temperature one. The slow mode was in all cases attributed to the dynamics of mesoscale polar/non-polar aggregates.

Slow mode from something else The next paragraphs will give examples of studies where at first a slow mode was detected in RTIL and second how this slow mode was attributed to something else than the mesoscale aggregates.

2019 A different approach to explaining the origin of the slow mode was taken in two studies by F. Pabst et al. The first one from 2019 is a direct comment on the Cosby et al. paper from 2017.

Pabst et al. measured on Omim-BF₄ as well as C_nMim-TFSI with $n = 3, 8, 10$ and 12 with BDS and DDLS and found that when comparing time scales from their study with data from the study by Cosby et al. it was shown that the bimodal spectrum stems from a separation in relaxation time of the cation and anion, with the cation being the slowest one of the two. Pabst et al. however did find in their DDLS measurements what they ascribed as a genuine mesoscale aggregate signal at even lower frequencies.

2021 The second study is from 2021 and concentrates on BDS measurements on Omim-BF₄, Omim-TFSI, Pyr18-TFSI, N2228-TFSI and N8881-TFSI. They found a slow mode in all liquids except for N8881-TFSI.

In order to add to the discussion if wether or not the slow modes stems from the mesoscale aggregates which are related to the pre-peak, Pabst et al. investigated the pressure dependence of the slow mode of Omim-BF₄ and Pyr18-TFSI and compared it to the pressure dependence of the pre-peak. They found that for both liquids the pressure dependence was not the same for the pre-peak and the slow mode. The pre-peak decreased with pressure but the shape of the dielectric spectra were invariant under compression.

Furthermore, the temperature dependence of the slow mode in Omim-BF₄ was not the same as that of the pre-peak. The authors thus reach the conclusion that the slow mode seen in the dielectric spectra was not connected to movements of aggregates probed by x-ray scattering.

An overview of the studies which aimed to measure a slow mode in RTIL can be seen in table 9.2. This includes liquids with and without a pre-peak as well as liquids where a slow mode was looked for but without any luck.

9.1.3 Opposing views

The literature overview clearly shows that even when a slow mode is found in the dynamic signals of RTILs there is not a clear agreement in the community on the interpretation on the origin of this mode. So even though the discovery of a slow relaxation in the dynamic signal of RTILs is over a decade old at this point, the origin of this mode and how it should be interpreted is still an open question that requires more targeted research.

This is why the rest of the chapter will focus on results from this study and how they fit into the previous studies on slow modes in order to get a clearer overview. Furthermore, the aim is also to shed more light on whether or not

the slow mode is the dynamic signal of the mesoscale structures. A discussion about the different views taken by researchers in literature and how these look in relation to results from this study will also be included.

9.2 Results

The following section will show results in the two RTILs series obtained in this study, i.e. the Pyr1*n*-TFSI with $x = 4, 6$ and 8 and the Pyr18-TFSI mixed with Li-salt in molar fractions of $x = 0.2$ and $x = 0.4$. Results from both series are here shown together since it paints a more complete picture with regards to the slow dynamics.

Shear mechanical data on the Pyr1*n*-TFSI is found in literature [80] and that study also investigated the existence of a slow mode in Pyr18-TFSI inspired by the previous findings in Omim-BF₄ [31]. A master plot of the shear modulus data of Pyr18-TFSI showed no presence of a slow mode even though the data extend down to a kPa in the real part of the shear modulus.

This study will take the search for a slow mode in the pyrrolidinium based RTILs a step further by introducing Pyr18-TFSI mixed with Li-salt in high concentrations. X-ray data show that by increasing the concentration of Li-salt in Pyr18-TFSI the intensity of the pre-peak will increase. Furthermore the method used to measure the shear modulus in this work is different than previous studies on the Pyr1*n*-TFSI liquids and so for completeness shear modulus data on Pyr14-TFSI, Pyr16-TFSI and Pyr18-TFSI are presented in the following analysis.

9.2.1 Dynamic Mechanical Spectroscopy

The data from shear modulus measurements can be seen in a scaled plot in figure 9.1. The plot has been scaled in both modulus and frequency to a data point at each temperature that lies 30% in modulus down in the low frequency side of the alpha relaxation peak. This ensured that a possible broadening of the alpha relaxation peak due to merging of the beta relaxation peak would not influence the low frequency side of the spectra.

The figure contains data from the two series Pyr1*n*-TFSI with $n = 4, 6$ and 8 and Pyr18-TFSI mixed with Li-salt of a molar fraction of $0, x = 0.2$ and $x = 0.4$. Data from two other liquids have also been included in order to compare results: The first one is the simple molecular liquid DC704 which contains no relaxations other than the alpha relaxation [131] and the second one is Omim-BF₄ which is known to have a slow mode in the shear modulus [31]. This comparison serves to clarify the existence of a slow mode in the pyrrolidinium based RTILs.

In order to quantify the low frequency signal and to confirm/deny the existence of a slow mode in the pyrrolidinium based liquids, the low frequency flank of the real part of the shear modulus for all seven liquids has been fitted to a first-degree polynomial to find the slope of this part of the spectra.

The method for doing so was as follows: Take the derivative of $\log_{10}(G')$ with respect to the logarithm of the frequency in order to see the change in modulus

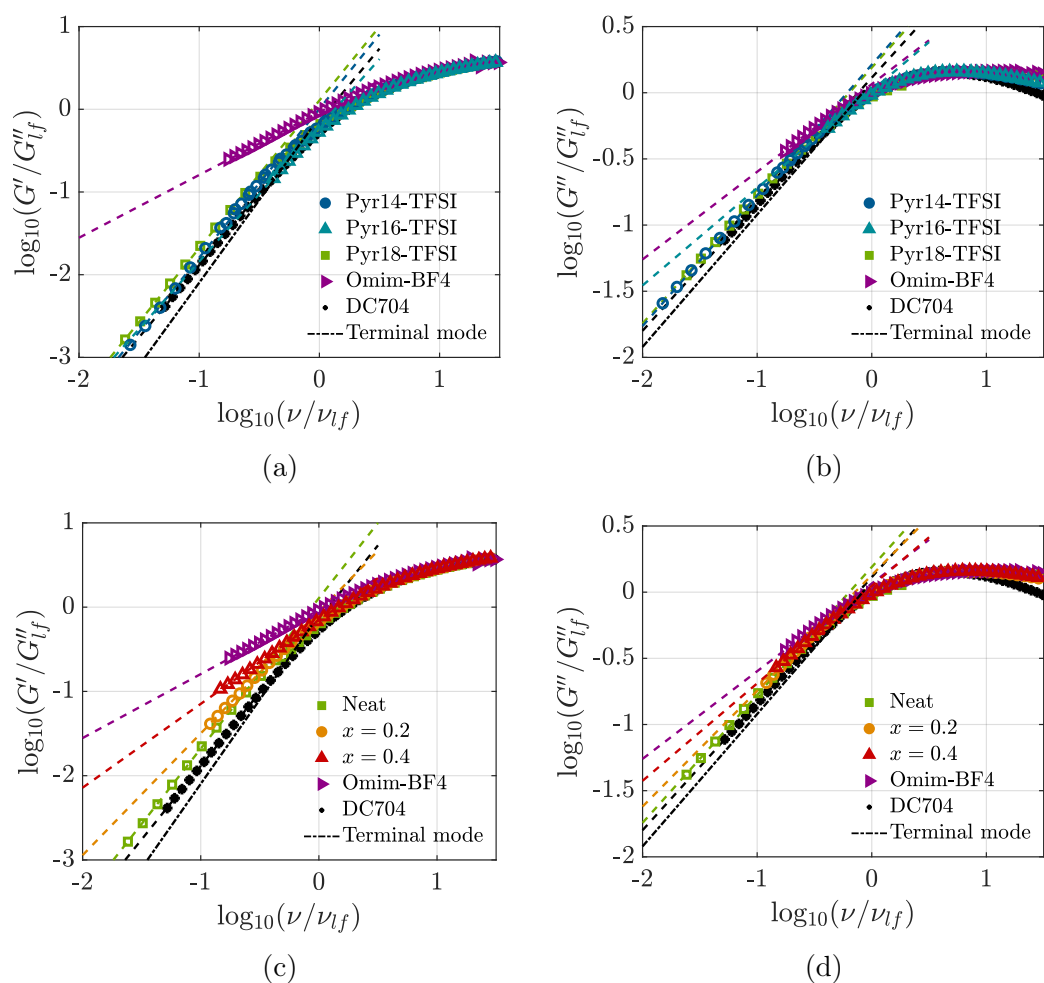


Figure 9.1: Scaled shear modulus for the Pyr1*n*-TFSI and Pyr18-TFSI Li-salt series with each curve being from a single temperature. Both shear modulus and frequency have been scaled to a point that lies 30% below the top point of the alpha relaxation peak (denoted G''_{lf} and ν_{lf}). Dashed lines are linear fits to the low frequency flank of the alpha relaxation peak.

with frequency. The region at frequencies below the alpha relaxation peak, where the slope of $\log_{10}(G')$ stayed close to constant, was then identified. The data in the region with constant slope was then fitting to a first order polynomial in order to find the actual value of this slope. The reason for choosing this specific method was to quantify the choice of data to be included in the fit to eliminate as much subjectivity as possible.

The stability of the fit was investigated by including different frequency ranges within the linear, low-frequency part of the curve to be included in the fit. This showed a stable fit with a maximum error of ± 0.03 , except for in Pyr16-TFSI where it was ± 0.13 . The resulting slopes can be seen in table 9.1 and show what figure 9.1 visualizes. Firstly, that there is no slow mode in Pyr14-TFSI, Pyr16-TFSI and Pyr18-TFSI since they have a slope in G' at the low frequency

side of the alpha relaxation peak close to that of DC704 and close to 2 which is the theoretical value for the terminal mode, i.e. fully viscous behavior. Secondly, that there is a clear slow mode in Omim-BF4 seen as a slope of G' close to 0.8 and thirdly that a slow mode starts to appear in Pyr18x02 and increases in intensity in Pyr18x04.

Liquid	slope G'	% of Pyr14-TFSI	Liquid	slope G'	% of Pyr18-TFSI
DC704	1.75	97	DC704	1.75	99
Pyr14-TFSI	1.80	100	Pyr18-TFSI	1.77	100
Pyr16-TFSI	1.63	91	Pyr18x02	1.45	82
Pyr18-TFSI	1.77	98	Pyr18x04	0.995	56
Omim-BF4	0.759	42	Omim-BF4	0.759	43
Pmim-BF4	1.22	68	Pmim-BF4	1.22	69

Table 9.1: A table showing the slope of the low frequency flank of real part of the shear modulus for both pyrrolidinium series plus Omim-BF4, Pmim-BF4 and DC704.

In this work the two ionic liquids Pmim-BF4 and Omim-BF have also been measured in order to investigate if the existence of a pre-peak could be connected to the existence of a slow mode in the relaxation spectra. The two liquids are similar except for the alkyl chain on the imidazolium ring which has three and eight carbons, respectively. A pre-peak has been shown in Omim-BF4, but no pre-peak exists in Bmim-BF4 [65], that is with four carbons in the alkyl chain, and so, it is in this study assumed that no pre-peak exists in Pmim-BF4 either.

The real part of the shear modulus has been plotted for Omim-BF4 at 190 K and Pmim-BF4 at 180 K as measured with the PSG together with literature data for Omim-BF4 [31]. The PSG data was treated in the same way as in figure 9.1 and literature data shifted in both modulus and frequency in order to collapse with the PSG data at the alpha relaxation peak. The data is also shown together with the data from the simple, molecular liquid DC704 and the dashed line is the terminal mode, see figure 9.2.

From this plot it is clear that a slow mode exists in both Omim-BF4 and Pmim-BF4 despite the fact that Pmim-BF is assumed to have no pre-peak in the structure factor. Furthermore, the data from Pmim-BF4 falls almost on top of Omim-BF4. The calculated slope of the low frequency side of the alpha relaxation peak is 0.909 for Pmim-BF4 as compared to 0.775 for Omim-BF4, so in this respect the slow mode is less pronounced in Pmim-BF4, but it is far from the slope of 1.70 seen in DC704.

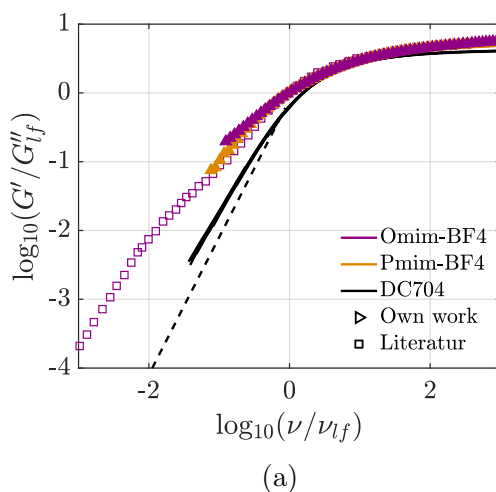


Figure 9.2: The real part of the shear modulus for Omim-BF4 at 190 K and Pmim-BF4 at 180 K as measured with the PSG together with literature data on Omim-BF4 as measured with a conventional rheometer and shown as a master plot. Black solid line is PSG data from DC704, a simple molecular liquid with no sub-alpha relaxation. Black dashed line is the terminal mode.

9.2.2 Broadband Dielectric spectroscopy

The six RTILs from this study were also measured using BDS to see if there was a slow mode in the dielectric signal. This has been observed before, as was also mentioned in the introduction, and so these experiments were repeated on the liquids from this study in order to expand the knowledge about the slow mode in different response functions.

The resulting spectra will only be shown here in the derivative representation of the dielectric permittivity due to the low frequency signal being obscured by a high conductivity contribution in the ionic liquids. The derivative permittivity, $\varepsilon''_{der} = -(\pi/2) \left(\frac{d \varepsilon'(\omega)}{d \ln \omega} \right)$ can be seen in figure 9.3.

The figure shows two relaxation modes in all five liquids in the two pyrrolidinium series; a slow and temperature independent one which is identified as the alpha relaxation. This has been confirmed by comparing the time scales of this slow relaxation to the time scale of the alpha relaxation found from the shear modulus, see chapter 7 and chapter 8.

The time scale of the second, fast relaxation in the five pyrrolidinium liquids is also seen in the other representations of the dielectric data and coincides with that of the fast relaxation in the shear modulus, the one that has been labeled the beta relaxation. See chapter 8 and chapter 7. Therefore the bimodal behavior in the derivative representation of the dielectric data for all five pyrrolidinium liquids can be explained as being the alpha and beta relaxation and thus not the alpha relaxation and a slow mode.

A lack of a slow mode in the dielectric results does however not mean that it does not exist in these liquids. It could be that the slow mode is simply hidden

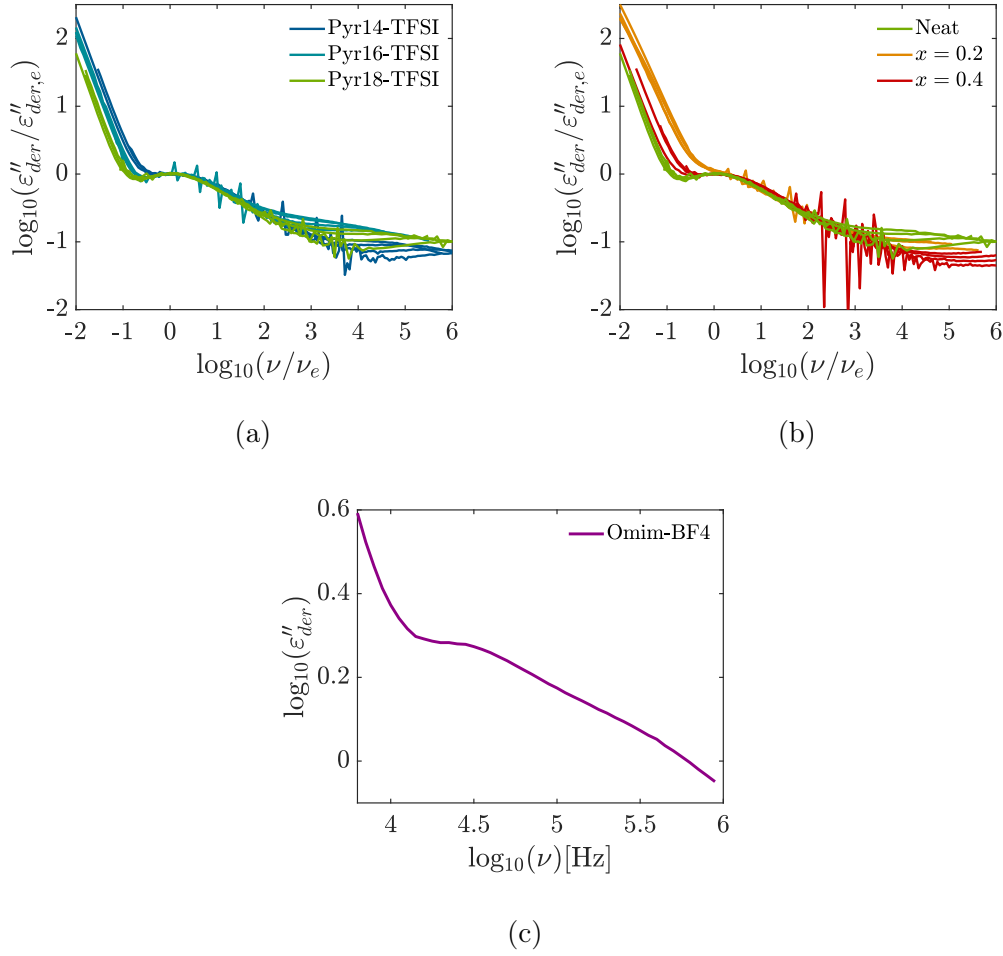


Figure 9.3: The logarithm of the derivative of the dielectric permittivity, ϵ''_{der} as a function of frequency both scaled to the low frequency peak, for the two series; a) Pyr1*n*-TFSI with $n = 4, 6, 8$. Temperature range is for Pyr14-TFSI; 184-190 K, for Pyr16-TFSI; 194-200 K and for Pyr18-TFSI; 188-194 K. b) is Pyr18-TFSI doped with Li-salt with a Li-salt molar fraction of $x = 0.2$ and $x = 0.4$. Temperature range is for neat Pyr18-TFSI; 188-194 K, for Pyr18x02; 210-216 K and for Pyr18x04; 220-228 K. c) shows the result from Omim-BF4 at 235 K.

below the high intensity electrode polarization that in these measurements sets in at frequencies just below the alpha relaxation. This is an explanation also suggested in the study by F. Pabst et al. from 2021 [84].

The results can readily be compared to BDS results on Pyr18-TFSI at 263 K from a study by F. Pabst et al. [84]. A bimodal behavior is also shown here, but the two relaxation peaks are only separated by around a decade in frequency. The study identifies the slow relaxation with dipolar reorientation of the cation and not as a relaxation of the mesoscale aggregates. Note that it was not possible to see the dynamics in the BDS signal at 263 K in this study since at this high

temperature electrode polarization completely dominates the spectrum.

ε''_{der} for Omim-BF₄ at 235 K measured as a part of this study can be seen in figure 9.3c and it clearly shows bimodal behavior where the two modes are separated by approximately one order of magnitude. This behavior matches qualitatively with the result from the studies by T. Cosby et al. [31] and F. Pabst et al. [84].

9.3 Discussion

The main question asked in this chapter is whether the slow mode seen in the dielectric, shear mechanical and light scattering measurements on RTILs has its origin as the dynamic signal of the mesoscale aggregates. These aggregates have been shown to exist in RTILs with alkyl chain lengths of the cation of 6 carbon atoms and longer, typically.

The relaxation of these aggregates would logically be slower than that of the individual molecules, the latter being the structural or alpha relaxation. The reason behind this argument is that collectively the molecules will be slower than on an individual basis. Consequently, the relaxation of the aggregates should appear as a peak in the imaginary part of the measured response at lower frequencies than the alpha relaxation, resulting in a bimodal behavior of the spectrum.

Results from literature This bimodal behavior has now been observed in BDS, DMS and DDLs measurements of various RTILs in studies going back to 2011. There are two different views with opposing opinions when it comes to interpreting these bimodal spectra, as was shown in the overview in the introduction of this chapter. One saying that the sub-alpha or slow mode is the dynamic signal of the mesoscale aggregates and one saying that it has a completely different origin. The second view does not say that there is no slow mode at all, just that the sub-alpha relaxations observed to this point in time is not the dynamic signal of the mesoscale aggregates but rather something else.

The arguments for assigning the slow mode to the relaxation of mesoscale aggregates are multiple. Some studies assign the slow mode to the dynamic signal of the aggregates simple due to the fact that the time scale of the slow mode is slower than that of the alpha relaxation [31, 45, 126].

Another argument is that the onset of the slow mode in a series with increasing alkyl chain lengths matches that of the onset of the x-ray structure factor pre-peak [111, 117, 127, 130]. A matching behavior between the pre-peak and the slow mode could indicate a similar origin, and since the pre-peak has been shown to be directly linked to the formation of mesoscale aggregates, it is thus an obvious conclusion to reach that also the slow mode comes from the aggregates.

More complex arguments are also given in this discussion such as the time scale of the slow mode being matched to those found from NSE measurements directly probing the mesoscale aggregates [31] and also that a systematic change

in the dielectric strength parameter, found from fitting the dielectric spectra, can be directly linked to changes in the shape of the mesoscale aggregates [127,130].

Fewer studies have contradicted these arguments, saying that the observed slow mode in BDS, DMS and DDLs measurements cannot readily be assigned to the dynamic signal of the mesoscale aggregates. Two studies come with a different interpretation. F. Pabst et al. in 2019 [86] concluded that the slow mode observed by T. Cosby et al. in 2017 is instead from a separation of the cation and anion relaxation times so that the slow mode is from cation relaxation. This argument was supported by comparing time scales of the dynamic modes across different liquids and response functions.

The other study is from 2021 and also by F. Pabst et al. [84]. Here the observed bimodal behavior found in BDS measurements of Omim-BF₄ and Pyr18-TFSI did not have the same pressure dependence as the pre-peak. It was therefore concluded that the origin of the pre-peak and the slow mode could not be the same, and so the slow mode must be contributed to another kind of dynamics than one arising from movement of the mesoscale aggregates.

Furthermore, the conclusion that a slow mode was even present in the DMS data in the study by N. V. Pogodina et al. [45] was later criticized in a study by R. Tao and S. L. Simon [125], saying that errors in the measurements at low moduli makes such a conclusion impossible.

Results from this study At first, for the three RTILs in the Pyr1*n*-TFSI series there is no significant difference between the slopes of the low frequency flank of the alpha relaxation in G'' . In fact, the slopes of these liquids lie close to the slope for DC704, a simple molecular liquid which exhibits no slow mode. There is a small deviation from this picture in Pyr14-TFSI, whose slope is a little higher than that of the other ILs in the series, as well as DC704, but it is not significant.

It should also be noted here that none of the slopes reach 2 which is the theoretical value for a fully viscous behavior in the log-log plot, also known as the terminal mode (shown as a black dashed-dotted line in figure 9.1). This is however not unusual [125] but in this case it demonstrates the relatively high uncertainty in comparing the low frequency slopes of the liquids to the terminal mode.

In any case there is a clear difference between the slope of the Pyr1*n*-TFSI IL and Omim-BF₄, which has been shown to have a slow mode. This indicates that there is no slow mode in the Pyr1*n*-TFSI series and that the shear modulus signal goes directly to the terminal mode of the alpha relaxation peak. This confirms the results found by W. Tu et al. [80] and T. Sonnleitner et al. [124].

A different picture is seen in the Pyr18-TFSI mixed with Li-salt series. Here there is a clear decrease in the slope of the low frequency flank with increasing Li-doping. This is also confirmed visually in figure 9.1. Pyr18x02 has a slope intermediate between the neat Pyr18-TFSI and Pyr18x04, indicating that a slow mode starts to develop at 20% Li-salt concentration and increases in intensity with increasing Li-salt concentration.

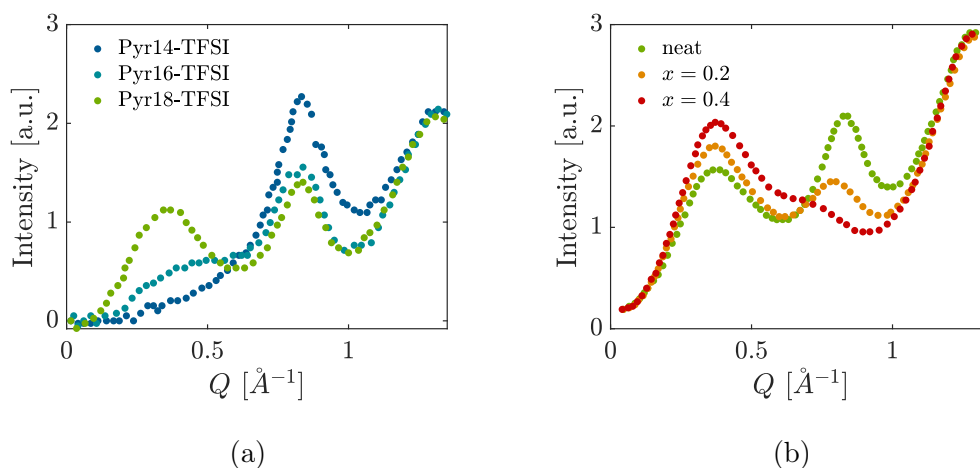


Figure 9.4: X-ray scattering structure factor for the two liquid series Pyr1*n*-TFSI and Pyr18-TFSI mixed with Li-salt in order to show the development of the scattering pre-peak. Data from a) and b) are from [68] and [69] respectively. The two different measurements of neat Pyr18-TFSI (green) have been shown to be similar, see Appendix D.

Following the conclusion that a slow mode is observed in Pyr18x02 and Pyr18x04 but not in Pyr14-TFSI, Pyr16-TFSI and Pyr18-TFSI it is obvious to look at the x-ray static structure factor for the same liquids. If the slow mode is indeed the dynamic signal of long-lived mesoscale aggregates, then an increase in the pre-peak should be reflected as an increase in the slow mode intensity.

The x-ray structure factor found in literature for both ionic liquid series can be seen in figure 9.4. Figure 9.4b specifically shows that the pre-peak increases in intensity with increasing Li-salt concentration, with Pyr18x02 being intermediate of neat Pyr18-TFSI and Pyr18x04. Furthermore, this matches findings from NMR studies of Pyr1*n*-TFSI mixed with Li-salt showing that the degree of mesoscale aggregate formation increases with increasing Li-salt concentration [71]. This systematic increase in intensity of the pre-peak, as well as an increase in the mesoscale aggregates with increasing Li-salt concentration, is reflected in the DMS slow mode as can be seen in the slope of the low-frequency flank of G' , see table 9.1.

This behavior is however not present in the Pyr1*n*-TFSI series. Figure 9.4a show that the pre-peak in the static structure factor increases systematically with increasing alkyl-chain length, but in the DMS signal there is no significant difference in the low-frequency slope of G' between Pyr16-TFSI and Pyr18-TFSI, see table 9.1. This do not mean that the origin of the slow mode being mesoscale aggregates can be excluded for the Pyr1*n*-TFSI series. Instead, an explanation for the lack of slow mode in Pyr14-TFSI, Pyr16-TFSI and Pyr18-TFSI when there is an increase in the pre-peak intensity could be that the pre-peak intensity needs to be higher for the signal to be detected with DMS and BDS. When combining the pre-peak intensity for both series it seen that the pre-peak increases systemati-

cally with increasing alkyl chain length and also increases Li-salt concentration. With this in mind, it could be that the intensity of the pre-peak in Pyr18-TFSI is simply the onset of the mesoscale aggregates being detectable in the dynamic signal.

It should furthermore be added to the discussion that one should take extra care when comparing time scales of the same liquid across different response functions, which is a preferred way of labeling the different dynamic modes of the BDS, DMS and DDLS measurements. This was for example done in the study by T. Cosby et al. [31] when concluding that the slow mode signal in the DMS results from Omim-BF₄ comes from the mesoscale aggregates.

This can be problematic as was shown in a study by L. Roed et al. [33] that the time scales of the alpha relaxation of the same liquid measured in the same cryostat differs significantly across response functions/methods. Furthermore, in supercooled liquids close to the glass transition the alpha relaxation is extremely temperature dependent and can easily move a decade in time with only a 2 K temperature change.

Combined An overview of the many different reported results from literature and this study on the slow mode can be seen in table 9.2. The table shows if a slow mode was observed in BDS, DMS and/or DDLS respectively for the given liquid or if there are no known results. Note that both liquids with and without a pre-peak in the x-ray structure factor have been included.

It is difficult to distinguish a clear pattern of any kind when looking through the table. There are even a few liquids where the literature disagrees on whether or not there even is a slow mode present. Furthermore, even liquids with not pre-peak exhibit a slow mode in one or more response functions.

This, combined with the above presented discussion on both the literature findings and the results from this study, leads to the conclusion that the origin and nature of the slow mode in RTIL is still very much an open topic. It cannot be simply concluded that the presence of a slow mode in either the BDS, DMS and/or DDLS signal is directly linked to the dynamic signal of mesoscale aggregates in RTIL. The results from table 9.2 also implies that making conclusions across different species of RTIL is problematic, as this class of liquids is very diverse. This is also a point made out by M. Musiał and co-workers in a study from 2020 where they end the conclusion saying "*...that the behavior of ILs is complex, difficult to generalize, and we still have to treat each IL family individually*" [111].

9.4 Conclusion

This chapter presents results on slow, sub-alpha dynamics in BDS, DMS and DDLS measurements on various RTILs both reported in literature and found in this study. This sub-alpha dynamic mode is called the slow mode and has previously been associated with the dynamic signal of mesoscale aggregates in

the liquid. These aggregates are known to exist and is the heterogeneity behind the so-called pre-peak in the x-ray structure factor.

In this study it was found that a slow mode exists in the DMS measurements of Pyr18-TFSI mixed with 20 and 40 % Li-salt, but not in DDLs measurements on Pyr18-TFSI mixed with 40% Li-salt. No slow mode was detected in the DMS measurements of Pyr1*n*-TFSI liquids with $n = 4, 6$ and 8. The BDS measurements on all liquids were inconclusive due to high electrode polarization except for in Omim-BF₄ where a slow mode was detected.

A method to investigate if the observed slow mode in RTILs has its origin in the mesoscale aggregates, is to look at the systematic change of the pre-peak with varying chemical composition and see if it matches the change in the slow mode. This was done for the two series in this study; the Pyr1*n*-TFSI with $n = 4, 6$ and 8 as well as Li-salt mixed Pyr18-TFSI. The increase in pre-peak intensity with increasing alkyl chain length in the first series did not match the results on the slow mode, since no slow mode was detected in these liquids. For the Li-salt mixed Pyr18-TFSI, however, there was an increase in the slow mode intensity which followed an increase in the pre-peak.

One explanation for this difference between the two RTIL series is that the pre-peak intensity for the Pyr18-TFSI mixed with 20% and 40% Li-salt is increasingly higher than neat Pyr18-TFSI which again is higher than in Pyr16-TFSI and Pyr14-TFSI. So it could be that the pre-peak intensity in Pyr18-TFSI is the threshold value for the mesoscale aggregate signal being intense enough to show up in the shear mechanical measurements. Another explanation could be that the mechanism behind the slow mode seen in Pyr18-TFSI mixed with Li-salt is simply not present in neat Pyr1*n*-TFSI with $n = 4, 6$ and 8.

Combining this with results from literature clearly shows that it cannot be concluded if the slow mode detected in various RTILs is the dynamic signal of mesoscale aggregates. It can be in certain cases, but in other cases the picture is much less clear. This supports the idea that one must take care when making generalized conclusions across different types of RTILs, since it is very diverse class of liquids.

Another important conclusion, which can be made from this investigation of the slow mode, is that the RTILs exhibit a dynamic behavior somewhat more complicated than what was initially thought in the previous chapters. At least for the Pyr18-TFSI mixed with Li-salt, where a slow mode is present and so, the dynamics no longer match those of non-associated molecular liquids like squalane and polyphenyl ether (PPE) [109, 131, 132].

Instead, the dynamic behavior of Pyr18-TFSI mixed with Li-salt mimics that of complex systems with supra-molecular hydrogen-bonded structures as seen in several studies [18–21]. This conclusion is independent of whether the slow mode seen in this study originates from the mesoscale aggregates, from a separation of the relaxation of the cation and anion or from something else entirely.

An interesting thing to note with regards to the slow mode is that, even though there is a slow mode in the shear modulus of Pyr18x04, the liquid still obeys TTS in the low frequency region. This can be seen in the TTS plot

in chapter 8. It is surprising that the temperature dependence of the alpha relaxation time and the slow mode are so similar, especially since it observed in imidazolium based RTILs, that the slow mode measured with DDLS did not obey TTS [86].

Liquid	BDS	DMS	DDLS	Source
TMP-Tos	?	+	?	[45]
Pmim-BF4	?	+	?	this work
Bmim-BF4	-	+/-	?	[45]/ [31]
Hmim-BF4	+	-	+	[31]
Omim-BF4	+	+	+	[31], [86], [84]
Hmim-TFSI	+	?	?	[31]
Omim-TFSI	+	?	+	[31], [86]
Demim-TFSI	?	?	+	[86]
Domim-TFSI	?	?	+	[86]
Pyr14-DCA	+	?	?	[124]
Pyr14-TFSI	-	-	?	this work
Pyr16-TFSI	-	-	?	this work
Pyr18-TFSI	+	-	?	this work, [84], [80]
Pyr18-TFSI, 20% Li-salt	?	+	?	this work
Pyr18-TFSI, 40% Li-salt	?	+	-	this work
Hmim-TCM	+	-	?	[111]
Omim-TCM	+	-	?	[111]
TEOP-TFSI	+	-	?	[128]
TEDP-TFSI	+	-	?	[128]
TBOP-TFSI	-	-	?	[128]
TBDP-TFSI	-	-	?	[128]
Emim-Al2Cl7	+	-	?	[127]
Bmim-Al2Cl7	+	-	?	[127]
Hmim-Al2Cl7	+	-	?	[127]
Omim-Al2Cl7	+	-	?	[127]
Hmim-Cl	+	-	?	[127]
Omim-Cl	+	+	?	[127]
Emim-DCA	+	?	?	[124]
N8881-TFSI	-	-	+	[126], [84]
N2228-TFSI*	+	?	-	[117], [84]
P2228-TFSI*	+	?	-	[117]
Omim/Emim-BF4 30%	+	+	?	[130]
Omim/Emim-BF4 50%	+	+	?	[130]
Omim/Emim-BF4 80%	+	+	?	[130]

Table 9.2: Overview of RTILs where a slow mode was investigated in BDS/DMS/DDLS. +, - and ? means a slow mode, no slow mode and not tested, respectively. Liquids in shaded gray rows do not exhibit a pre-peak in the x-ray structure factor. * Pre-peak in a similar IL (P666,14-TFSI).

Chapter 10

Simplicity of spectral shapes

One of the ways to investigate simplicity in the dynamics of liquids is to look at the spectral shape of the relaxation spectrum. A requirement for simplicity, as stated in chapter 2 is that the spectral shape is identical for different response functions. A way to test this is to look at and compare the shape of the structural relaxation in for example dielectric and shear mechanical spectroscopy. Another way is to test the Random Barrier Model, which before has been tested with success on ionic liquids even though it is a model that describes conductivity in solid matter.

10.1 Random Barrier model

The Random Barrier Model was originally created by Jeppe Dyre in 1985 [26, 27] and further developed throughout the years by him and Thomas Schröder at Roskilde University [28, 133–136], where the newest revised version from 2008 gives an expression that accurately describes conductivity in the entire frequency range. But before we come to that expression let us first briefly go through the basic concepts of the RBM.

The model aims to give a simple basis for the conductivity in disordered solids at low temperatures and to reproduce some of the universal features of conductivity, including the steady-state conductivity plateau at low frequency as well as the high-frequency increase in conductivity which follows an approximate power law with an exponent less than one. An exponent which increases slightly with increasing temperature.

The RBM begins with five basic assumptions: 1) The charge carriers in the solid have no interaction at all, not even self-exclusion, 2) charge carrier motion takes place exclusively on a cubic lattice, so motion only takes place between lattice sites, 3) all lattice sites have the same energy and are therefore in that sense equally preferred, 4) only nearest-neighbor jumps are allowed and 5) the jump rates have a random activation energy with distribution $p(e)$. This has been visualized in one dimension in figure 10.1.

Here we see a charge carrier (black dot) that resides at one lattice site (on the cubic lattice). Between lattice sites are energy barriers with heights that

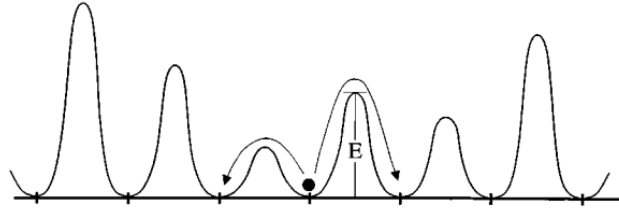


Figure 10.1: A visualization of the RBM in one dimension. The charge carrier (black dot) jumps from lattice site to lattice site by overcoming an energy barrier of random height. From [133].

are randomly distributed and the charge carrier can then jump to either side, to the nearest-neighbor sites on the lattice, illustrated by the black arrows. This is done by overcoming the energy barriers. The charge carrier can then either jump back to the same site again or jump further along the lattice.

A central conclusion in the RBM is that the universal ac-conductivity in the extreme disorder limit is caused by an underlying percolation cluster. By extreme disorder limit it is meant that $k_B T$ is much smaller than the relevant energy barriers. In order to understand what this percolation cluster is, one can imagine a network of connections between lattice sites. At low temperatures the particles prefer to jump across low energy barriers which means that there are areas of the cubic lattice that the particles will avoid, and these areas do therefore not contribute to the overall conductivity since they are not connected [133]. The part of the lattice that is connected, however, is so called fat percolation cluster and it was shown in the RBM paper from 2008 [28] that all of the fat percolation cluster contributes to the ac conductivity.

Another conclusion is that when the reduced frequency, $\tilde{\omega}$, is above 1, the fat percolation cluster appears fractal, since the particles move less than the correlation length. But below one the particles have more time and can move longer than the correlation length, so that the fat percolation cluster now appears homogeneous. A consequence of this is that the entire frequency range need to be described by two terms, one for each case. The final expression for the conductivity in disordered solids, covering all frequency ranges, is (in reduced units)

$$\ln \tilde{\sigma} = \frac{i\tilde{\omega}}{\tilde{\sigma}} \left(1 + 2.66 \frac{i\tilde{\omega}}{\tilde{\sigma}} \right)^{-1/3} \quad (10.1.1)$$

where $\tilde{\omega} = \omega \Delta \varepsilon \varepsilon_0 / \sigma_0$ and $\tilde{\sigma} = \sigma(\omega) / \sigma_0$. Here $\Delta \varepsilon$ is the dielectric strength, ε is the vacuum permittivity and σ_0 is the steady-state conductivity. In conventional units this gives the expression

$$\ln \frac{\sigma^*(\omega)}{\sigma_0} = \frac{i\omega \tau_{RBM} \sigma_0}{\sigma^*(\omega)} \left(1 + 2.66 \frac{i\omega \tau_{RBM} \sigma_0}{\sigma^*(\omega)} \right)^{-1/3} \quad (10.1.2)$$

where τ_{RBM} is a characteristic time and together with σ_0 they are scaling factors that move the function up/down in conductivity and frequency, but there are

no shape-parameters, which mean that the RBM expression really captures the universal behavior of ac-conductivity. It has been shown to work very well on simulations and experimental data, both for the real and the imaginary part [28, 31, 35, 126, 137, 138]. Eq. (10.1.2) has been solved numerically by Schröder and Dyre and the solution can be found in the supplemental material to the paper *Ac hopping conduction at extreme disorder takes place on the percolating cluster* by Schröder and Dyre [28].

The RBM in the version seen in equation (10.1.2) has here been tested on the conductivity spectra for the two series of RTILs (which was presented in chapter 7 and 8) as well as on Omim-BF₄. Results can be seen in figure 10.2. The TTS plot was made by scaling in conductivity to the steady-state conductivity and the frequency to the peak frequency of the modulus peak in M'' , as was done in Sangoro et al. [137]. See chapter 7 and 8 for details on the steady state conductivity. The modulus conductivity peak was found by fitting the logarithm of the electric modulus to a second-degree polynomial just around the peak itself.

The RBM prediction is seen as a thick, black dashed line and is from equation (10.1.2). It was manually scaled in conductivity and frequency for each liquid to collapse with data just around the conductivity peak. The figure shows a very general behavior in all six liquids; at low frequencies, the electrode polarization creates an increase in conductivity not described in the RBM, and so a fit in this frequency region is not expected. When the steady state conductivity enters the spectra, the RBM do however collapse nicely with data through several orders of magnitude in frequency. This is especially pronounced for Omim-BF₄ where the collapse continues four decades above the conductivity peak.

The fit to the RBM is a little worse in the pyrrolidinium based liquids where a deviation begins around 2-3 decades above the conductivity peak, a deviation that tends to increase with temperature. It has previously been found that the RBM fits conductivity data for imidazolium based RTILs several decades above the conductivity peak [29, 112, 127, 139], which agrees well with data from this study.

It is clear that at high temperatures and increasing frequency the fit to the RBM starts to deviate significantly. The reason for this effect is not clear, but it could be due to the beta relaxation which is very pronounced in the pyrrolidinium based liquids but of much less intensity in Omim-BF₄. This secondary relaxation merges increasingly with the conductivity at higher temperatures and could therefore be the cause behind the temperature dependent deviation. This is supported by the fact that for Omim-BF₄ the fit to the random barrier model is better.

10.2 Fluidity and spectral shapes

Complex fluidity is another way of representing shear rheology data and is simply the inverse of the complex viscosity, η^* , which is calculated from the shear modulus as $\eta^* = G^*/(i\omega)$. This means that the fluidity informs about the flow

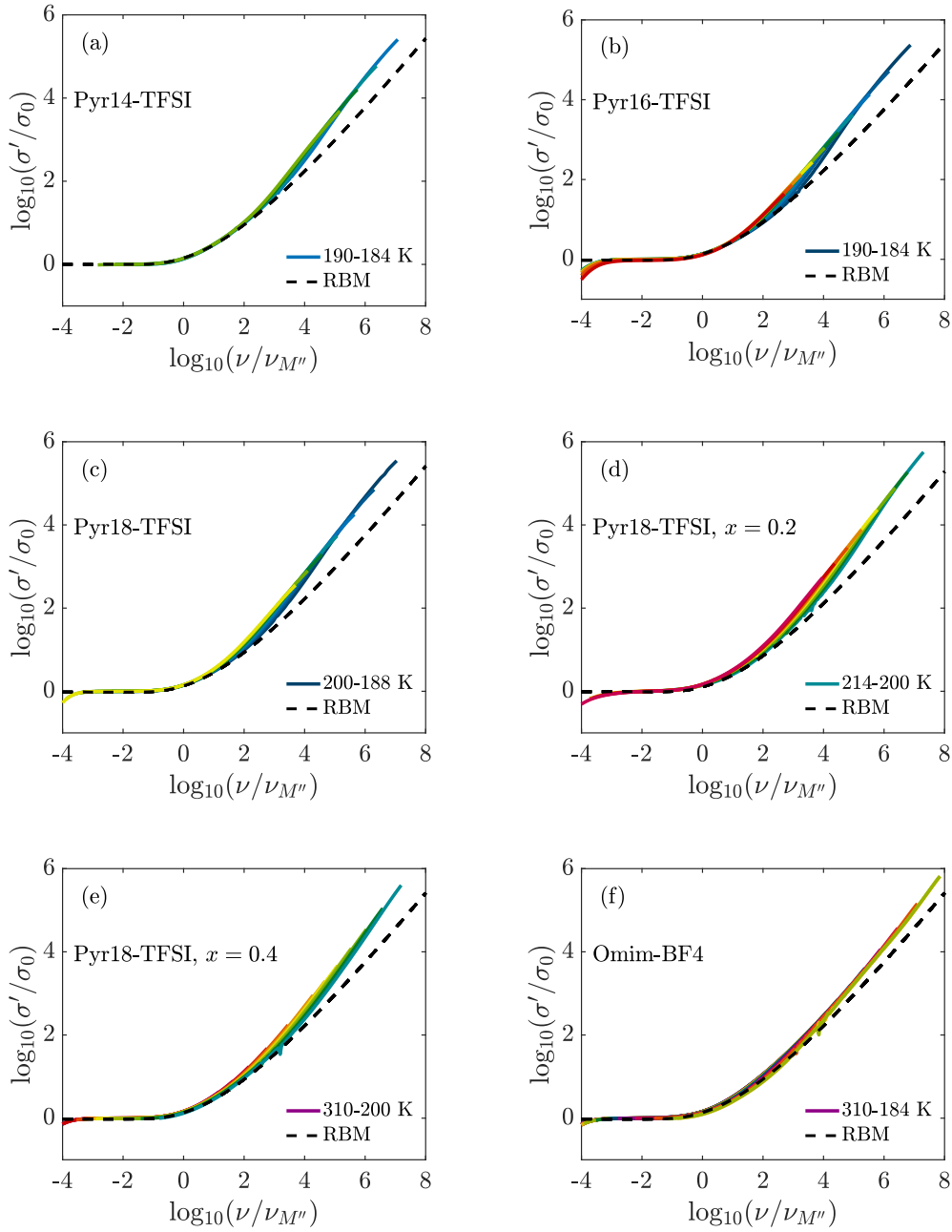


Figure 10.2: The real part of the complex conductivity scaled to σ_0 and frequency scaled to the conductivity peak in M'' for six RTILs. The black dashed line is the prediction by the RBM, which is seen to hold very well below and around the conductivity peak.

of the liquid. The real part of the fluidity, F' , is generally characterized by a low frequency behavior where the fluidity reaches a plateau, the so-called fluidity plateau, F_0 , which characterizes the steady state flow.

What is interesting in the following is that the shear fluidity is the mechanical

counterpart of the complex electric conductivity, $\sigma^*(\omega)$ [24], and when looking at data from fluidity and conductivity, the spectral shapes are remarkably similar. They also share some fundamental properties as a steady state plateau at low frequencies and a transition to a high frequency increase.

Furthermore, both the dielectric conductivity, σ , and the shear fluidity, F , are connected to the self-diffusion coefficient of migrating molecules. This is described with the Stokes-Einstein and the Nernst-Einstein relation respectively [140]. This also means that the fluidity can be expressed in terms of the mean square displacement [24]. It could therefore be interesting to ask the question, if the RBM, which successfully describes conductivity in liquids, can be applied to shear fluidity?

This question was formulated by S. P. Bierwith, R. Böhmer and C. Gainaru in 2017 and the remarkable answer was 'yes'. In this study they applied the RBM to shifted fluidity master curves for several simple molecular liquids. Note that none of these liquids have a discernible secondary relaxation mode, but only the characteristic alpha relaxation, and that all liquids obey time-temperature superposition.

A remarkable feature is that when transforming the RBM to apply for fluidity, i.e. $\sigma^*(\omega) = F^*(\omega)$ and $\sigma_0 = F_0$, the fluidity data collapse with the transformed RBM prediction. A consequence of this is that the universality previously reported for electric conductivity have a counterpart in the mechanical flow of liquids. This is even more remarkable when remembering that the RBM contains no shape-factors and only two shift factors, i.e. σ_0 and τ_{RBM} .

This analysis was further extended in a study by C. Gainaru in 2019 [25]. Here the RBM was tested on a large number of liquids from a wide variety of classes of liquids showing excellent agreement between data and the RBM prediction at frequencies above the alpha relaxation. The main conclusion from this study was that the spectral shape simplicity is shared by a large variety of liquids at frequencies larger than the alpha relaxation frequency, ω_α , and that this spectral shape can be well described by the RBM.

Simplicity should be understood in this regard as significant reduction of parameters needed to describe the viscous flow in liquids across several decades in frequency and several classes of liquids. In fact, only two parameters are needed to describe the fluidity spectra when the data fits the RBM prediction, i.e. F_0 and τ_α .

Of course, in order to draw more general conclusions on this simplicity of the spectral shape of fluidity, one needs to include more categories of glass-forming liquids. With this it would also be of interest to investigate how far into the subdiffusive region, i.e. at frequencies higher than ω_α , this simplicity holds. This is the motivation for in the following to apply this RBM based analysis to the fluidity data of the RTILs investigated in this thesis. This will especially shed light on the spectral shape at higher frequencies, since the PSG technique (see section 3.1.4) allows for measurements far above the usual limit of a 100 Hz.

The fluidity plateau, F_0 , was found by first finding the derivative of the fluidity with respect to frequency and then identifying the region, where the

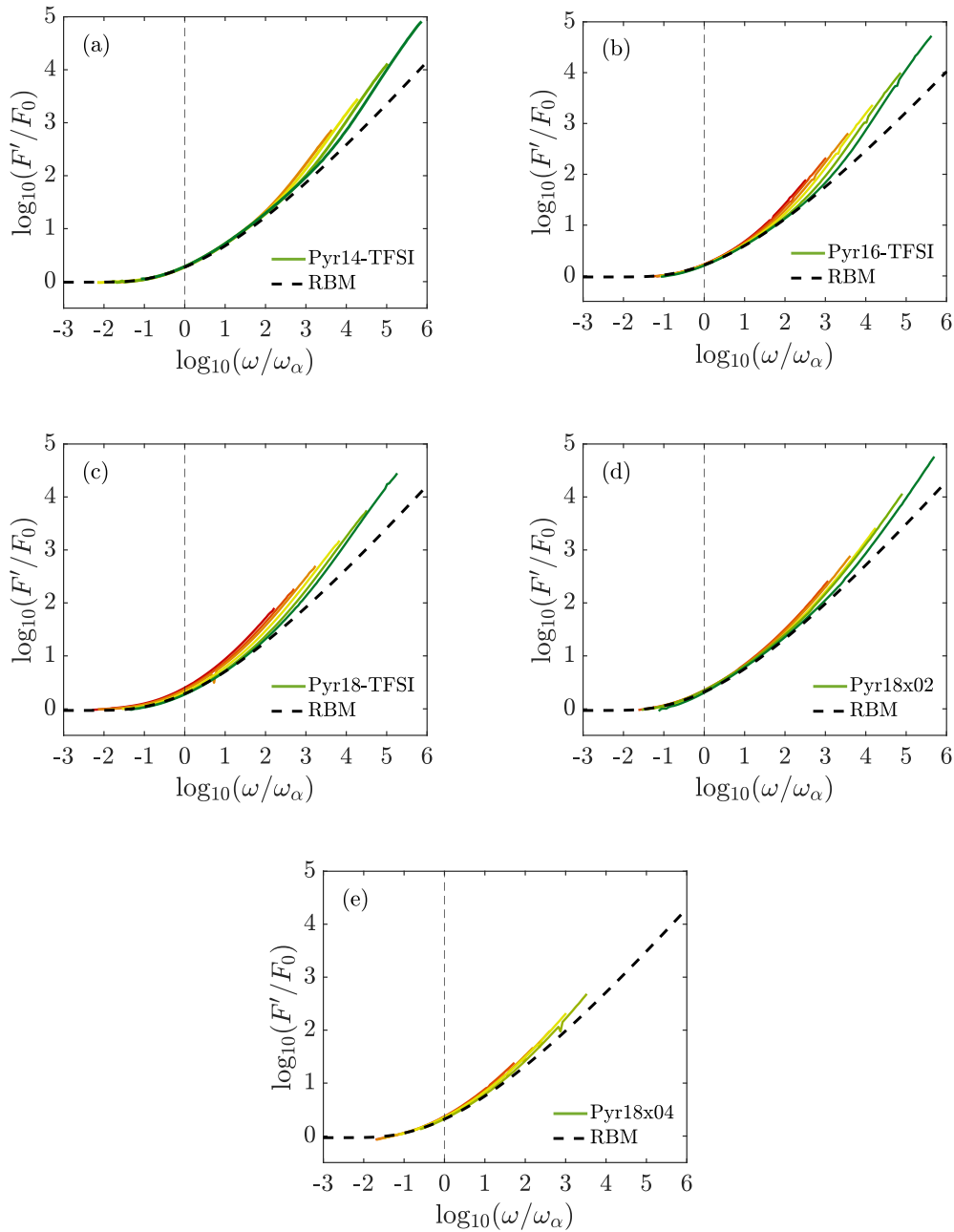


Figure 10.3: The real part of the complex fluidity scaled to the low frequency fluidity plateau, F_0 and frequency scaled to the alpha relaxation peak, ω_α . The thick, black dashed line is the prediction by the RBM seen in equation (10.1.2). All liquids display a good agreement with the RBM prediction at low temperatures up to around 3 decades above the alpha relaxation peak where a clear deviation sets in. This deviation starts at lower frequencies with higher temperatures.

change in fluidity was zero or very close to zero. The fluidity value in this

region was then averaged to give the actual value of the plateau. To create the collapse, the real part of the fluidity at all temperatures was scaled to F_0 and the frequency scaled to the alpha relaxation peak frequency. The result for data on the five pyrrolidinium based RTILs, i.e. Pyr14-TFSI, Pyr16-TFSI, Pyr18-TFSI and Pyr18-TFSI mixed with $x = 0.2$ and $x = 0.4$ molar fraction of Li-TFSI, can be seen in figure 10.3. Note that for Pyr18-TFSI with $x = 0.4$ molar fraction of Li-TFSI, called Pyr18x04, it was only possible to reach the fluidity plateau at the warmest temperatures. The color coding is the same used when presenting the shear mechanical data in for example chapter 7, meaning that the warmest temperatures have reddish colors and the coldest have bluish colors.

The RBM prediction is shown as a thick, black dashed line and is from equation (10.1.2). It has been manually scaled in fluidity and frequency for each liquid in order to collapse with data from the coldest temperature just around the alpha relaxation frequency. The predictions show a good agreement with data below and around the alpha relaxation peak for all RTILs.

As the frequency increases to around 3 decades above the alpha relaxation peak a discrepancy between data and the RBM prediction begins. The fluidity increase changes frequency dependence and becomes steeper creating a significant deviation from the RBM prediction which thus increases with frequency. This effect is for all RTILs increasingly more pronounced at higher temperatures.

This behavior can be directly compared to literature [25] where data from one ionic liquid and one ionic melt have been included. Here there was no deviation between data and the RBM prediction, not even at frequencies almost four decades in frequency and two decades in the scaled fluidity above the alpha relaxation peak.

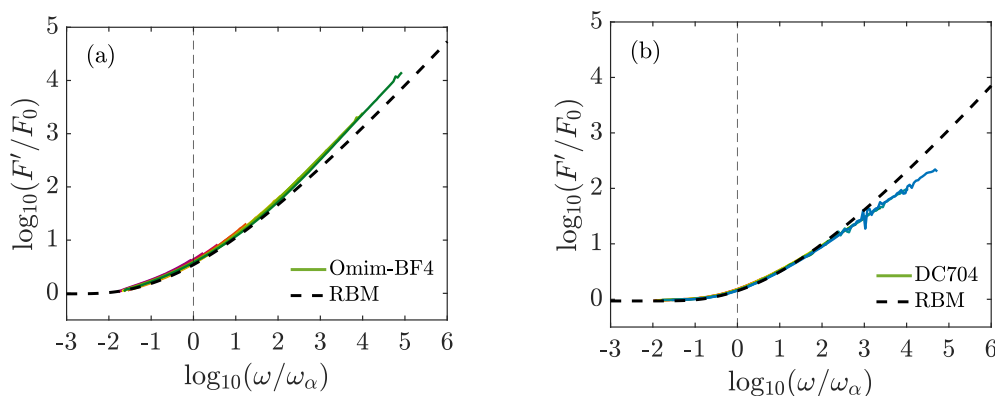


Figure 10.4: The real part of the complex fluidity scaled to the low frequency fluidity plateau and frequency scaled to the alpha relaxation peak. The thick, black dashed line is the prediction by the RBM seen in equation (10.1.2). a) is data from Omim-BF4 which has a low-intensity beta relaxation and b) is from the molecular liquid DC704 with no visible beta relaxation and complete TTS in the spectrum.

An explanation could be found in the difference between the data collection and analysis. In contrast to the literature data, data in this study were measured with the PSG as continuous isothermal spectra up to 30 kHz and this creates two significant differences; the fluidity data are not presented as masterplots and there is a pronounced beta relaxation.

That the beta relaxation is responsible for the deviation from the RBM prediction is supported by the fact that the beta relaxation increasingly merges with the alpha relaxation at increasing temperatures. This matches the increasing deviation between prediction and data at higher temperatures. Furthermore, the deviation from the RBM prediction is smaller in Pyr18x02 and Pyr18x04 where the beta relaxation is further separated from the alpha relaxation.

To test this further, the same data analysis was applied to fluidity data from the RTIL Omim-BF₄, which has a much less pronounced beta relaxation, and the molecular liquid DC704, which has no visible beta relaxation plus complete TTS in the relaxation spectrum. Both can be seen in figure 10.4 and it shows a significant different behavior than the RTILs in figure 10.3.

Omim-BF₄ shows a much smaller deviation from the RBM at higher frequencies, even though the difference begins at roughly the same scaled frequency. The deviation from the RBM prediction also prevails in DC704, but due to the scaled fluidity having a *less* steep frequency dependence than the RBM. Furthermore, the deviation from the RBM prediction in DC704 is temperature independent. This corroborates the idea of the beta relaxation and the related breakdown of TTS being the cause of the deviation from the RBM prediction at higher frequencies and temperatures in all RTILs.

Comparing to conductivity In order to test the second criterion for simplicity in glass-forming liquids, that the spectral shape is identical for different response functions, the test of the RBM is compared between conductivity and shear fluidity, i.e. the results from figure 10.2 and 10.3. If the data follows the RBM prediction in both conductivity and fluidity, then the criterion for simplicity is definitely met. But the shape could also be identical if a deviation from the RBM is identical across response functions.

At first glance, the conductivity and shear fluidity data follow the same trend when testing the RBM. There is a good agreement with the theoretical prediction at the σ_0/F_0 plateau, which continues around 3 decades up in frequency and 2 decades in conductivity/fluidity. After this, the data starts to deviate from the RBM prediction and this deviation continues to increase with frequency and temperature. This is less pronounced for the liquid Omim-BF₄ in both response functions and that could, as mentioned, be due to the beta relaxation in Omim-BF₄ being much lower in intensity than in the five pyrrolidinium-based liquids.

Qualitatively, all six RTILs exhibit the same behavior when comparing to the RBM in both conductivity and fluidity, which supports that the spectral shape is identical across response functions. There are small differences, but these appear to be more related to the beta relaxation, which is corroborated when comparing the conductivity and fluidity spectra for Omim-BF₄, where the

beta relaxation intensity is low. Here the spectra for the two response functions are indistinguishable.

RBM in other representations In light of the discoveries by Gainaru and co-workers, Schröder and Dyre authored a paper where they study how well the RBM describes low-temperature mean square displacement in a crystallization-resistant modification of the Kob–Andersen binary Lennard-Jones mixture [136].

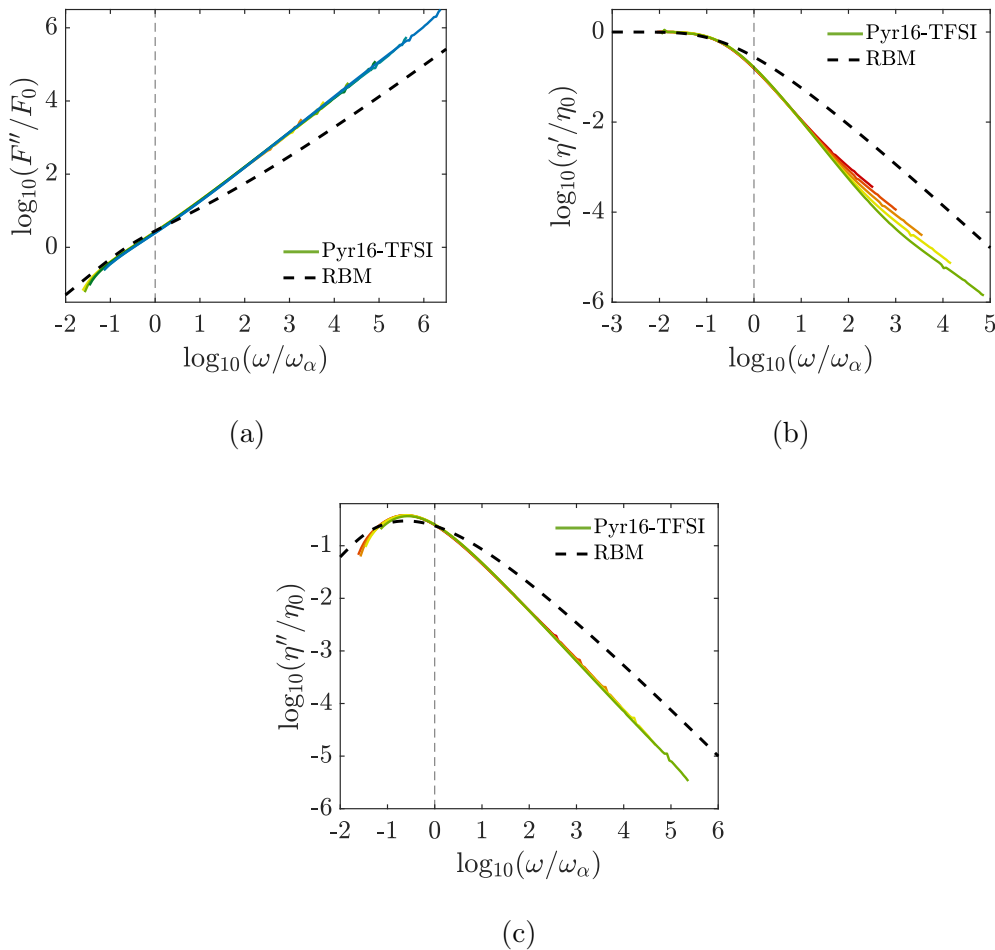


Figure 10.5: Shear mechanical data for Pyr16-TFSI with frequency scaled to the alpha relaxation peak where a) is imaginary part of the fluidity scaled to F_0 , b) and c) is the real and imaginary part of the shear viscosity respectively scaled to η_0 . Thick, black dashed line is the RBM prediction, which is these representations of the data does not work well.

In this study was found that the RBM describes the liquid MSD well in this system if one adds a constant, the so-called "plateau parameter", β , which reflects the cage-rattling contribution. This new expression for the MSD can be related to the experimental fluidity data by two assumptions: 1) the RBM describes the liquid MSD (which was confirmed by simulations) and 2) the Stokes-Einstein

relation between diffusion and viscosity is also correct, i.e. that the macroscopic shear viscosity controls the microscopic frictional forces. Then MSD is directly linked to fluidity and the spectral shape simplicity of the fluidity as found by Gainaru and co-workers can be explained.

But a question then arrives. If the simulation data requires this β parameter in order to show universality, then why was it not needed in the work by Gainaru and co-workers? Schrøder and Dyre suggest that the answer to this question can be found if one looks at the expression for the fluidity derived directly from the expression for MSD: $\tilde{F}(\tilde{\omega}) = \tilde{F}_{RBM}(\tilde{\omega}) + i\omega\tilde{\beta}$, where tilde denotes a suitable scaling.

It is seen in this expression that the β parameter is not included in the real part of the fluidity which is what Gainaru and co-workers studied. It could be that the imaginary part is not universal because β is not universal, and a consequence of this would be that the *imaginary* part of the fluidity will not be well described by the RBM. This would then also be true for viscosity, which is just the inverse of the complex fluidity.

This has been tested in the following on the data for Pyr16-TFSI in both ways, i.e. both the imaginary part of the fluidity as well as the complex viscosity. The results can be seen in figure 10.5. Here it is clearly seen that the RBM does not describe data well, and the spectral shape simplicity does not apply to these representations of the data.

Nevertheless, it is puzzling that a very simplistic model designed to explain ac conductivity in disordered solids can reproduce fluidity results around the alpha relaxation in such complex glass-forming liquids as RTILs and the reason behind is still an open question to be answered in the future [136].

10.3 Conclusion

The conclusion from this analysis is, that the random barrier model prediction works well for the real part of the conductivity for all pyrrolidinium-based ionic liquids studied in this work, as well as for the imidazolium based ionic liquid Omim-BF₄, just around the conductivity peak. Data, however, starts to deviate from the model prediction as frequency and temperature is increased, and this deviation is qualitatively the same for all liquids.

Another conclusion is that, in the diffusive region and a few decades into the sub diffusive region, the spectral shape simplicity for the real part of the shear fluidity, that in literature was observed, is also present in the RTILs studied in this thesis.

But contrary to literature this coincidence stops into the subdiffusive region, i.e. around 3 decades above the alpha relaxation peak, and it worsens with increasing frequency and temperature. The reason behind the difference in results from this thesis and literature could be because the method used to measure shear modulus in this study, the PSG, can resolve the high frequency beta relaxation. This secondary relaxation is not considered in the RBM, and it was not present

in literature data.

Furthermore, a comparison between the test of the RBM in the conductivity and fluidity data show that the spectral shapes to a large degree are identical. The small differences are most likely due to the beta relaxation, meaning that the criterion for simplicity is met for the alpha relaxation.

Finally, it is shown that, as suggested by Schröder and Dyre, the spectral shape simplicity does not hold for the imaginary part of the fluidity as well as for the complex viscosity. The reason for this could be that in the mathematical expression for these representations of the data a non-universal parameter is included which is not present in the real part of the fluidity.

Chapter 11

Quasi-elastic neutron scattering

This chapter will show results, discussion and conclusion from the incoherent neutron scattering measurements on two room temperature ionic liquids (RTIL), i.e. Pyr14-TFSI and Pmim-BF₄. All of the experiments were performed on the backscattering instrument IN16B located at Insitute Laue-Langevin (ILL) in Grenoble, France. The raw neutron scattering data were reduced using the LAMP software package [141].

11.1 Pyr14-TFSI

quasi-elastic neutron scattering was performed on four different samples of Pyr14-TFSI, each with different degrees of deuteration. All samples were synthesized at Department of Chemistry, Saarland University, Germany by Daniel Rauber and Prof. Rolf Hempelmann. Experiments were performed by Henriette W. Hansen and Filippa Lundin. All data analysis was performed by the author of this thesis. The data and analysis from this section was also published in [95].

A quick overview of the four samples of different deuteration, which is also visually presented as inserts in figure 11.1:

- D0: The fully protonated sample. Results will be from the whole cation.
- D3: Partial deuteration, where only the methyl arm is deuterated. This sample will show results from the pyrrolidinium ring and the butyl arm.
- D9: Partial deuteration, where the butyl arm is deuterated. This sample will then show results from the pyrrolidinium ring and the methyl group.
- D12. Partial deuteration, where both the butyl arm and methyl group is deuterated, so that results will be from the pyrrolidinium ring only.

Elastic fixed window scans (EFWS) were measured with an energy resolution of $\Delta E \approx 0.8 \mu\text{eV}$ and this corresponds to a timescale of the dynamics of around 5 ns. Inelastic fixed window scans (IFWS) [142] were measured with an energy off-set of $E_{IFWS} = 2 \mu\text{eV}$ which gives a time of $1/\omega_{IFWS} = 1/(E_{IFWS}/\hbar) =$

$3.3 \cdot 10^{-10}$ s. The Q -range was with both EFWS and IFWS 0.19 - 1.90 \AA^{-1} . To avoid crystallization the samples were measured in cooling and covered the temperature range 10 - 310 K with a cooling rate of 0.5 K/min.

It is assumed in the analysis of incoherent neutron scattering that there is no coherent scattering present which is a reasonable assumption for Pyr14-TFSI. The reason for this is that it contains a large fraction of hydrogen which is an element with a very high percentage of incoherent cross section. But a problem arises in the deuterated liquids since deuterium mainly scatters coherently. A consequence of this is that the increased value of deuterium will decrease the incoherent cross section. Specifically, the percentage of incoherent scattering will be reduced from 91% in D0 to 76% in D12.

Table 11.1 provides an overview of the incoherent contribution from each sample. Here it can also be seen that the incoherent scattering from the TFSI anion can be neglected since, compared to the incoherent scattering of the entire liquid, it is very low. Therefore, it is mainly the dynamics of the cation that will be probed with inelastic neutron scattering in this study.

It is expected that there will be three different kinds of dynamics in the cation and therefore, the total dynamics will be a combination of 1) the global diffusion of the center-of-mass of the cation and 2) local motions due to ring wagging and rotation of the butyl-chain and the methyl-group [143].

Note finally that all EFWS and IFWS intensities were normalized to the elastic intensity at the lowest temperature measured.

Sample	σ_{scat}	σ_{inc}	σ_{coh}	$\sigma_{\text{inc}}/\sigma_{\text{scat}}$ [%]
D0	1768	1606	161.3	91
D3	1545	1372	172.8	89
D9	1098	902.4	195.8	82
D12	875.1	667.8	207.3	76
TFSI	65.7	0.522	65.2	0.8

Table 11.1: The neutron scattering cross sections for the four different samples of Pyr14-TFSI. All scattering cross sections are in barn.

11.1.1 Inelastic fixed window scans

The results from the temperature dependent inelastic fixed windows scans will be presented in this section. Figure 11.1 shows results for the four different deuterations of Pyr14-TFSI at different Q -values. The incoherent scattering is well above 70% in all cases and therefore most of the signal can be assumed to come from hydrogen atoms in the molecules. This means that data on the D12 liquid is mainly sensitive to dynamics originating in the pyrrolidinium ring and will thus give direct information on the alpha relaxation of the liquid. This

is because the pyrrolidinium ring is assumed to be linked to the center-of-mass motion of the cation.

There is in all four samples a prominent main mode around 300 K, but in D0, D3 and D9 the presence of other, additional modes appear. These additional modes, which all appear at lower temperatures, are assumed to be connected to the butyl and methyl arm since these are part of the molecules which can move around. These assumptions are also supported by the fact that the scattering cannot detect movement from the anion and so dynamics from this molecule can be ruled out.

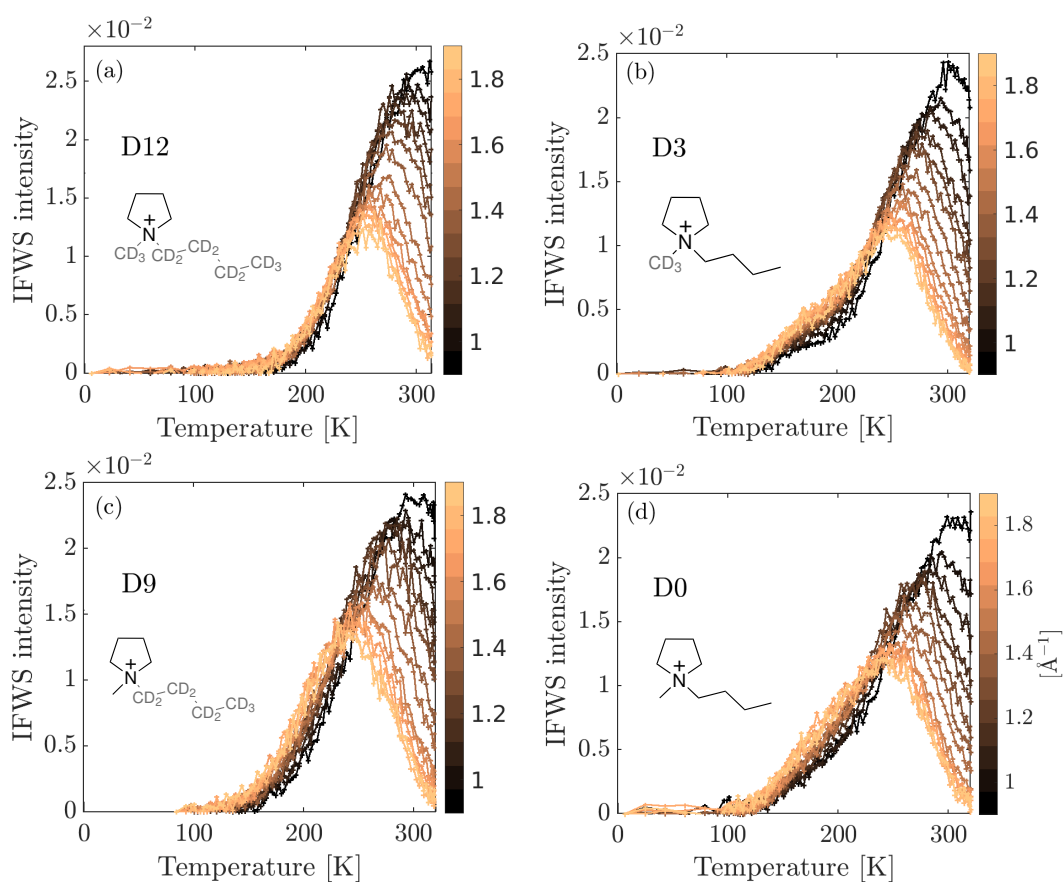


Figure 11.1: IFWS intensity for the whole Q -range (light to dark, see the color bar in units of \AA^{-1}) and for all four deuterations of Pyr14-TFSI. a) D12, b) D3, c) D9 and d) D0. Intensity was normalized after subtracting background to the lowest temperature elastic signal and the 4 lowest Q -values were excluded due to the data at these Q -values being noisy and disrupting the whole picture of the Q -dependence. The main peak present in all samples is Q -dependent and decrease in intensity with higher Q -values. Two additional Q -independent modes are present in the D3 and D9 liquids at lower temperatures.

It is clearly seen that the high temperature peak present in all samples is Q -dependent, shifts to lower temperature and decreases in intensity with increasing Q -value. This suggests that the origin of this dynamic mode is diffusive [142].

A conclusion which also corroborates the interpretation that the mode is indeed the alpha or structural relaxation of the liquid.

The position of the additional dynamic modes seen as low-temperature shoulders in the D9, D3 and D0 liquids appear to be Q -independent, but the intensity increases with increasing Q -values. An interpretation of this is that these low-temperature modes originate in local motions of the molecules. This interpretation would be consistent with the assumption that the dynamic mode originates from the butyl and methyl groups [142].

To summarize the interpretation of the data so far, there are three different modes in the IFWS data of the non-deuterated liquids, D0: The pyrrolidinium ring that is assumed to be linked to the center-of-mass of the cation molecule, the methyl group motion and the motion of the butyl chain. This interpretation of the data is also consistent with a recent interpretation of IFWS data by Busch et al. [143].

In order to separate the different dynamic modes from each other, the data from the D12 liquid have been fitted to a single Gaussian function at each Q -value. The choice of using a Gaussian is purely phenomenological but it clearly fits the data well and can therefore be used to interpolate between data points in the spectra in order to obtain information at intermediate temperatures.

Note that the D12 data were normalized relative to the other three samples so that a direct comparison was made possible. This normalization was chosen such that the right side of the main peak for all four samples (D0, D3, D9 and D12) collapse. This is reasonable since it is assumed that there are no additional dynamics in any of the samples at temperatures above the activation of the main peak.

The normalization value was chosen by hand, which is not ideal, but results from both the activation energy and τ_0 were robust to this high temperature flank normalization in the following fitting routine. See figure 11.2 to see the Gaussian fits to the D12 data at all Q -values.

See figure 11.5a to see an example of the data from the three samples D3, D9 and D12 after this normalization and with the Gaussian fit to the D12 data, all at $Q = 1.3\text{\AA}^{-1}$. This shows that the interpolation of the D12 data makes it possible to subtract the D12 intensity from the D3 and D9 intensity at all Q -values separately. This is seen in 11.5b where the D3-D12 and D9-D12 data are obtained through the following procedure: Fit the D12 data at each Q with a Gaussian function to get the interpolation between data points, subtract this interpolation from the D3 and D9 data at each Q and then sum over all Q for D3 and D9.

Figure 11.3 shows the D3 with the interpolated D12 data subtracted for each Q -value as a function of temperature. The dashed line marks the highest temperature included in the following fit to the suggested model in eq. 1. Above this, the residual is less than 50% of the total signal, i.e. $(D3-D12)/D12 < 50\%$, and the data is no longer trustworthy which is also evident in the figure, since 1) a Q -dependence appears and 2) the intensity goes below zero.

This whole procedure makes it possible to separate the main mode from the

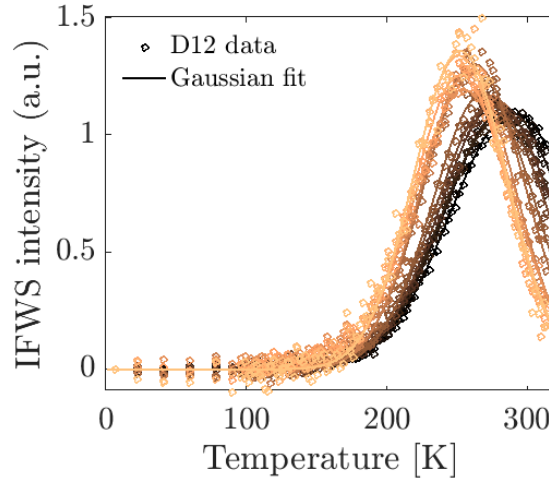


Figure 11.2: IFWS intensity for the D12 sample (circles) shown for a Q -range of 0.95 \AA^{-1} (dark) to 1.9 \AA^{-1} (light) with the corresponding fit to a Gaussian function (solid lines) at each Q -value.

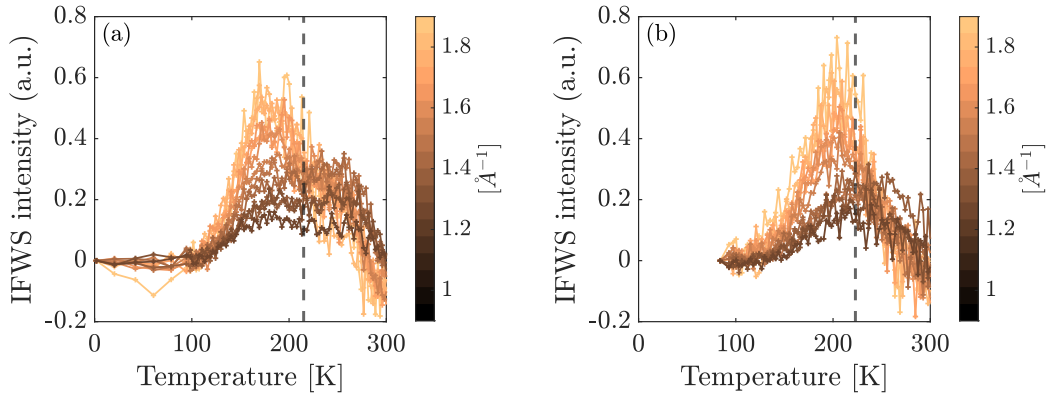


Figure 11.3: IFWS intensity as a function of temperature for a) D3-D12 and b) D9-D12 at each Q -value. The data are summed over Q and then fitted to the suggested model in equation (11.1.1). Black dashed line marks the highest temperature included in the fit to the model.

secondary mode in the D3 and D9 sample and it there are two additional dynamic modes which are separated from the main mode of the pyrrolidinium ring, where the former is seen as a peak in intensity around 184 K and 208 K, see figure 11.5.

The simplest assumption which can be made here is that these localized motions have a Lorentzian spectral shape. This will then lead to the following equation describing the IFWS-signal [142, 143]

$$I(T) = e^{-aT} \cdot \left[I_0 \frac{1}{\pi} \frac{\tau(T)}{1 + \tau(T)^2 \omega_{IFWS}^2} \right] \quad (11.1.1)$$

where $\tau(T)$ is the temperature dependent relaxation time and ω_{IFWS} is the angular frequency given by the energy off-set at which the data is acquired, $\omega_{IFWS} = \Delta E/\hbar$. The exponential pre-factor is the temperature dependent Debye-Waller factor where a is found from a linear fit to the low temperature region of the logarithm of the elastic intensity, see figure 11.4.

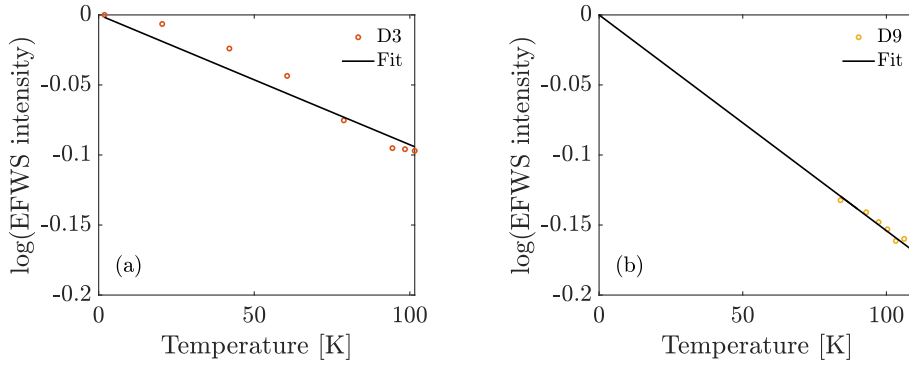


Figure 11.4: The logarithm of the over Q summed EFWS intensity as a function of temperature for a) D3 data and b) D9 data. Both data sets are at low temperatures. The solid black line is a fit to the function $-aT$ in order to find the pre-factor a .

Assuming that the temperature dependence is Arrhenius in nature will give a relaxation time as

$$\tau(T) = \tau_0 e^{E_a/RT} \quad (11.1.2)$$

where R is the universal gas constant, τ_0 is the high temperature limit of the relaxation time and E_a the activation energy of the local dynamics. Combining equation (11.1.1) and equation (11.1.2) will give a model with τ_0 , E_a and I_0 as free parameters. This is furthermore in addition to the parameter a , which is found from the EFWS data. This approach was proposed in 2012 by B. Frick et al. [142], and has also recently been used by M. Busch et al. to analyze a set of IFWS data on another RTIL [143].

Figure 11.5b shows the fits (black solid lines) of the D3-D12 and D9-D12 data. To quantify the temperature region to be included in the fit, it was only performed where the residual signal is at least 50% of the total one (i.e. (D3-D12)/D12 > 50%). The model shown in equation (11.1.1) gives an excellent fit with a τ_0 in the picosecond range which is physically reasonable value.

Furthermore, the model gives the activation energies for the localized motions which are found to be $E_a = 7.8$ kJ/mol for the D3 liquid and $E_a = 9.1$ kJ/mol for the D9 liquid. These activation energies show good correspondence with previous studies on the fully protonated RTIL N-butylpyridinium bis(trifluoromethanesulfonyl)imide [143–145], which is a liquid very similar to the one in this study with the exception that the cation ring only has the alkyl-chain and not the methyl-group seen on the pyrrolidinium ring.

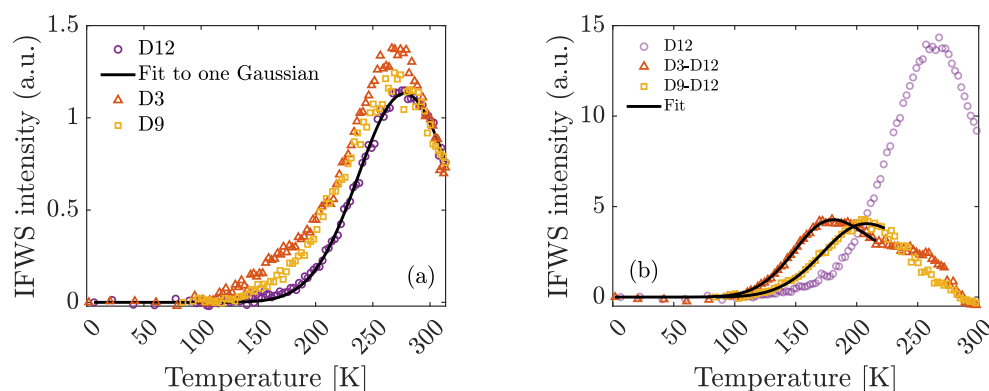


Figure 11.5: IFWS intensity of the different deuterations of Pyr14-TFSI as a function of temperature. a) Shows data from the D3, D9 and D12 liquids at $Q = 1.3 \text{ \AA}^{-1}$ as an example. The data from the D12 sample (purple) is shown together with a fit to a Gaussian function (black solid line) which illustrates that the fit can be used as interpolation of the data. b) IFWS intensity summed over Q for D12 and for D3 and D9. In order to show additional dynamics which are separated from the main mode, the interpolation from the D12 samples has been subtracted at each Q . Black solid lines in this figure are fits to the proposed model shown in equation 11.1.1.

A noticeable feature is that the local mode in D3, where only the butyl chain is visible, is faster than the mode of D9 where only the methyl group is visible. This is at first glance counter intuitively since the butyl chain should be slower than the much smaller methyl group. Furthermore, the two modes have similar intensity even though the butyl chain has three times as many hydrogen atoms than the small methyl group.

This fact leads to the conclusion that the local dynamic mode probably originates from the end methyl group of the butyl chain and that is the mode seen here. This is in line with results and discussions in another study on a RTIL with a cation similar to the pyrrolidinium from this study [144]. Here it is concluded that the part of the alkyl chain close to the aromatic ring can appear almost immobile on the time scale of the experiment.

11.1.2 Elastic fixed window scans

This section presents elastic fixed window scans (EFWS) on all four samples of Pyr14-TFSI. The EFWS of the neutron data contain information on the vibrational dynamics taking place at an even faster time scale than the IFWS. In the following it will be explained how to find the mean square displacement (MSD) from the EFWS data and subsequently analyzing this MSD data.

Finding MSD In order to find the mean square displacement (MSD) from the elastic incoherent scattering data there are several different approaches. Common

for all of them is that one fits the normalized elastic intensity as a function of Q^2 to a function that contains MSD as a free parameter. This way it comes down to the choice of the fitting function that again depends on how the system is modelled.

It is normal to use the Gaussian approximation of scattering from liquids [146]. In this model it is assumed that there is a linear relation between the logarithm of the normalized intensity and Q^2 . This means that the elastic intensity is fitted to the function

$$\ln \left(\frac{I(Q)}{I_0(Q)} \right) = \frac{\langle u^2 \rangle}{3} Q^2 \quad (11.1.3)$$

where $\langle u^2 \rangle$ is MSD. This is called the Gaussian method.

When fitting the data to equation (11.1.3) it is necessary to include a second free fitting parameter, in addition to $\langle u^2 \rangle$, which will account for multiple scattering in the sample. This will add a second term, b , to the right-hand side of equation (11.1.3), where b accounts for multiple scattering which creates an offset in the normalized intensity.

Another method is one suggested by R. Zorn [147, 148]. This model takes into account both the non-Gaussian character of the different dynamics in the liquid as well as multiple scattering. It also contains one less free parameter than the Gaussian method. R. Zorn argues [147, 148] that the Q -range, where the Gaussian approximation holds, is very limited, sometimes only 0-0.5 \AA^{-2} . This will, in the case of this work, leave only a few data points to be fitted and thus leave out important information about the system. This is also evident from figure 11.6, where the fit to the Gaussian function is shown for two different Q -ranges.

In contrast to this, the data points at higher temperatures are seen to be captured well by the fit to the R. Zorn method. The R. Zorn method also seems more robust to the fact that a coherent signal enters the signal around $Q^2 \approx 1.9 \text{\AA}^{-2}$, a signal which grows with increasing deuteration. A consequence of this coherent signal is also that the resulting MSD is somewhat dependent on the chosen Q -range in the Gaussian approximation, an effect which is more pronounced as the temperatures increases.

It should be noted that the discrepancy between the Gaussian method and the method suggested by R. Zorn is mainly present at higher temperatures. At low temperatures the elastic intensity is closer to a linear relationship with Q^2 , meaning that in this temperature range the Gaussian approximation is valid.

The analysis of EWFS data by R. Zorn is thorough but the two main points from the analysis will be mentioned here. They are that 1) the fit of the elastic data should include a multiple scattering (MS) correction and 2) another function than a Gaussian function should be used to describe the elastic scattering intensity, $I^f(Q)$. It was furthermore suggested that the chosen function to describe the elastic scattering could be a pseudo-Voigt function and therefore, in this work, this was done. All of this combined will give the total expression to

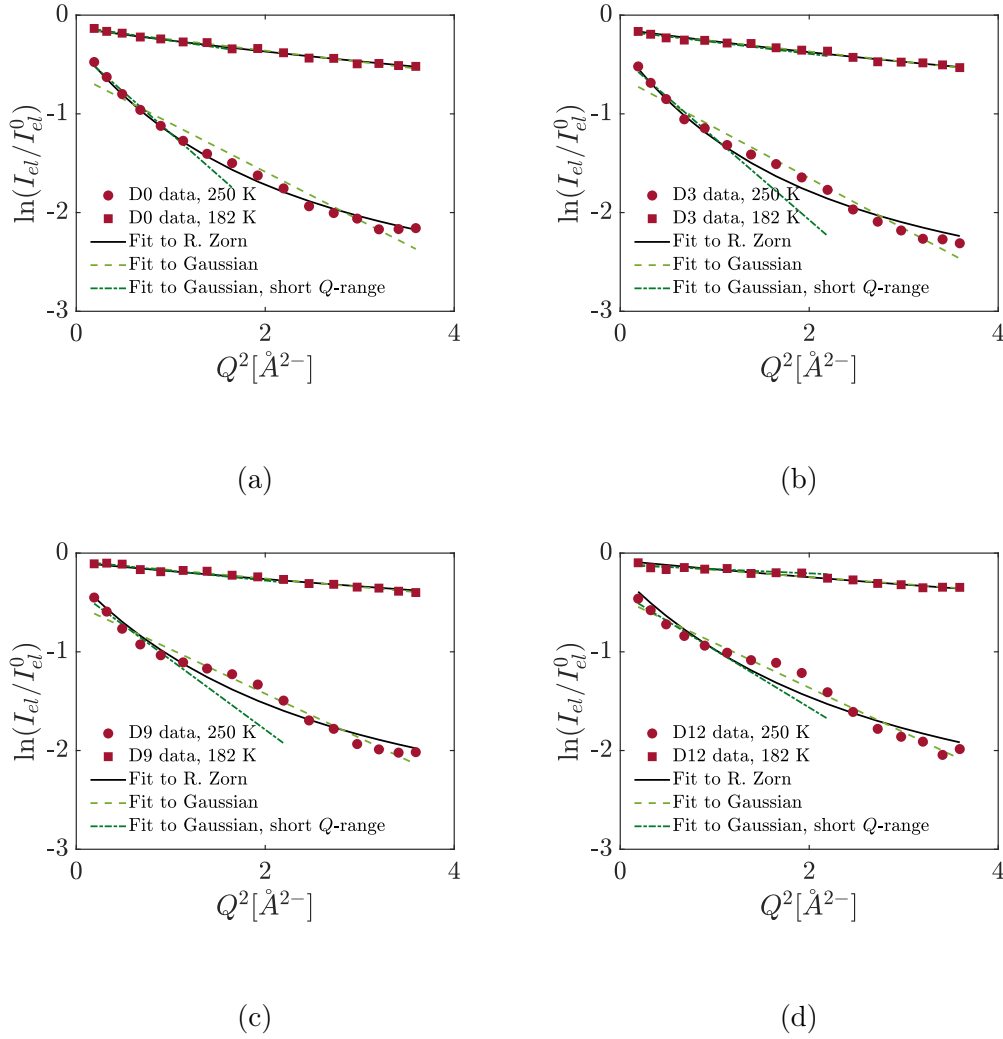


Figure 11.6: Logarithm of the normalized intensity as a function of Q^2 for Pyr14-TFSI with deuteration a) D0, b) D3, c) D9 and d) D12 at both 250 K (circles) and 182 K (squares). The qualitative difference between the fits to data with the Gaussian method (green) and the R. Zorn method (black) is clearly seen here. The four plots also show how a coherent signal starts to increase around $1.9 Q^{-2}$ with increased deuteration.

be fitted to the normalized intensity as

$$\ln \left(\frac{I(Q)}{I_0(Q)} \right) = \ln \left((1-s) \left(I^f(Q) + \frac{s\bar{I}^2}{1-s\bar{I}} \right) \right) \quad (11.1.4)$$

where

$$I^f(Q) = (1-\eta) \exp \left(-\frac{\langle u^2 \rangle}{6} Q^2 \right) + \eta \frac{1}{1 + \langle u^2 \rangle Q^2 / 6} \quad (11.1.5)$$

where s is the probability of a MS event and η is a mixing parameter.

The pseudo-Voigt is an approximation to the Voigt profile which is a convolution of the Gaussian and Lorentzian profile and a complete expression for

the mixing parameter, η , does not exist. Thompson et al. approximated this parameter with a simple formula which is accurate to about 1% [149]. \bar{I} is the elastic, single scattering intensity averaged over the solid angle given as

$$\begin{aligned}\bar{I} &= \frac{1}{2k^2} \int_0^{2k} I^f(Q) Q \, dQ \\ &= \frac{1}{2k^2} (1 - \eta) \frac{-3}{2\langle u^2 \rangle} \left(\exp \left(\frac{-4\langle u^2 \rangle k^2}{3} \right) - 1 \right) + \eta \frac{3}{2\langle u^2 \rangle} \ln \left(1 + \frac{4\langle u^2 \rangle k^2}{3} \right)\end{aligned}\tag{11.1.6}$$

where k is the wave vector of the neutrons given as $(2\pi)/\lambda$.

In figure 11.6, the fit to equation (11.1.4) is seen as the black solid line. Note that a significant improvement in the Zorn method is that it only contains one free parameter, i.e. $\langle u^2 \rangle$. s is temperature independent and is found by a fit with both $\langle u^2 \rangle$ and s as free parameters at an intermediate temperature. Then s is fixed to this best-fit value and the fit repeated at all temperatures with only $\langle u^2 \rangle$ as a free parameter. s should be found at an intermediate temperature in order to avoid overestimation.

The resulting MSD from this fitting procedure at all temperatures for D0 can be seen in figure 11.7 (black). Here is also presented results originating from fitting with the Gaussian method in order to qualitatively see the difference between the two methods. They clearly start to deviate at low temperatures and this difference increases with temperature. The difference is smaller when using the Gaussian approximation on a short Q -range, but is in both cases significant.

MSD data from different deuteration The MSD for all four deuteration calculations is shown in figure 11.8. The MSD is lowest for D12 at all measured temperatures and MSD systematically increase with decreasing deuteration. That MSD increases with decreased deuteration is interpreted as additional motion from the methyl group and the butyl chain entering the elastic signal. Note that at low temperatures it is assumed that the MSD is completely vibrational, i.e. no rotation of the alkyl groups.

When increasing the temperature, the relaxations will at some point enter the nanosecond regime and thus contribute to the calculated MSD. This is seen in figure 11.1 where the inelastic signal goes above zero. It is furthermore seen that the relaxations enter at lower temperature for the samples where the alkyl chains can contribute to the intensity. D12 is the only sample where the inelastic intensity is close to zero around the glass transition, meaning that for this sample, the calculated MSD is purely connected to the vibrational MSD.

The insert in figure 11.8 shows that for the D12 liquid there is a kink around T_g which can be understood as the MSD being affected by a simultaneous decrease in the temperature dependence of G_∞ at this temperature. Note that in this sample it is the vibrations which dominates the MSD below T_g and that the vibrational MSD is governed by the elastic moduli of the liquid.

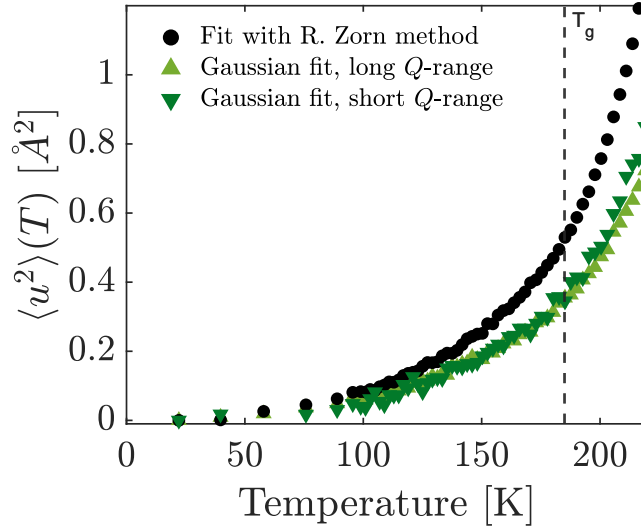


Figure 11.7: MSD for the sample D0 as a function of temperature found with the Gaussian method (green) and the R. Zorn method (black) to show the difference between the two. As expected, the difference between the two methods is small at low temperatures but becomes increasingly significant from around 150 K. The Q -range for the fit to the Gaussian function was chosen to be $0.2\text{-}3.6 \text{ \AA}^2$ (light green) and $0.2\text{-}1.9 \text{ \AA}^2$ (dark green).

Since the elastic data presented here will be used to test the shoving model in chapter 12 it is worth making some contemplations about the quality of the data in this regard. The shoving model assumes that the MSD is proportional to the temperature over the high frequency shear modulus, i.e. $\langle u^2 \rangle \propto T/G_\infty$ [11, 150]. Due to this relation, it is the MSD data of the D12 sample that is most suitable for testing the shoving model since they are the cleanest in terms of excluding relaxational dynamics from the vibrational MSD in the temperature range close to T_g .

The downside, however, of using the data from the D12 sample is that the coherent contribution to the measured elastic intensity is rather high. When calculating the MSD, it is assumed that the elastic data is purely incoherent, but as seen in table 11.1 this is not true in the D12 liquid. The coherent contribution to the signal can be seen directly in the Q -dependence of the data as seen figure 11.6 where there is a clear shoulder at $Q^2 \approx 1.9 \text{ \AA}^{-2}$. This shoulder corresponds to $Q = 1.4 \text{ \AA}^{-1}$ which is the position of the main peak in the x-ray structure factor [69, 75].

So, in conclusion, the D0 data give the cleanest result in terms of being closest to the assumption of fully incoherent scattering, but a downside is that there will also be a contribution from relaxation dynamics. In contrast to this, the D12 data gives the best result in terms of only containing vibrational MSD

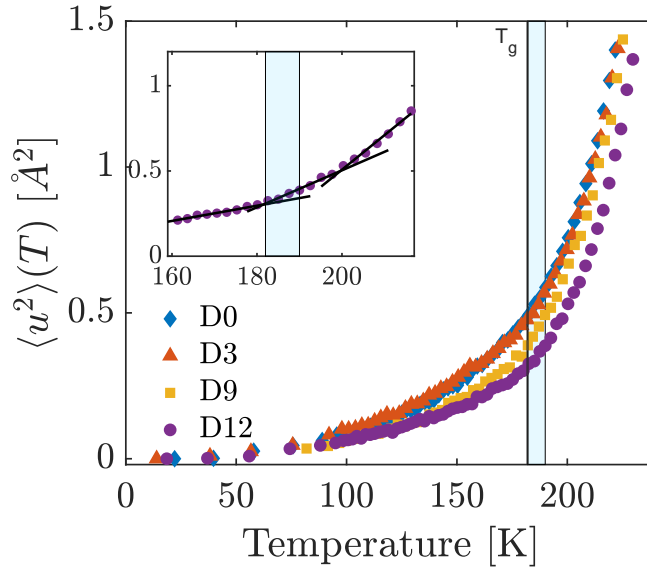


Figure 11.8: A plot showing MSD as a function of temperature for all four deuterations of Pyr14-TFSI. The blue shaded area is the temperature region where the shear modulus measurements were performed. The insert shows a zoom in of the D12 data to better show three different regions of the dynamics revealed by two distinct kinks in MSD. These regions are illustrated by solid black lines which are found from linear fits of the MSD data in the specified temperature region. The second kink is around 202 K which is close to the temperature where the inelastic signal starts to increase significantly as seen in figure 11.1.

and no contribution from relaxations, but the downside is that there will be a higher coherent scattering contribution contaminating the signal. D3 and D9 are intermediate situations of these two extremes.

11.1.3 Time scales in Pyr14-TFSI

Since several techniques were used to measure time scales in Pyr14-TFSI, this section is devoted to collect these results into a single relaxation maps or Angell plot in order to get a better overview. All shear mechanical and conductivity data are from chapter 7. The relaxation time for the alpha relaxation has in all cases been calculated as $\tau_\alpha = 1/(\nu_{max}2\pi)$ where ν_{max} is the maximum of the relaxation peak in the imaginary part of the shear modulus, and this maximum has been found with a fit to a second-degree polynomial in the range around the peak.

To get an overview of the different dynamic modes which were seen in the shear mechanical and neutron scattering data they are collected in a relaxation map or Arrhenius plot in figure 11.9, where the relaxation times of the modes are shown as a function of inverse temperature scaled to T_g , i.e. T_g/T , with $T_g = 182$

K found from shear mechanical measurements.

To compare time scales with conductivity, the relaxation map in figure 11.9 also includes an axis of the resistivity/inverse ionic conductivity. Additional data from the liquid, and not supercooled, region from literature are also shown [70, 80] together with data from this study in both the liquid and supercooled region. There is a so-called "no man's land" between the supercooled and liquid temperature region where cold-crystallization prevents one from access the liquid properties.

The inverse conductivity axis has been shifted relative to the time scale axis such that the alpha relaxation time and collapse with the inverse conductivity, both from this study at 188 K. Subsequently, the data from the two response functions follow each other closely in the supercooled regime, showing that the conductivity and the alpha relaxation time have almost the same temperature dependence as was also seen in chapter 7. A similar behavior is found in another study [151] by comparing conductivity and alpha relaxation measured by dielectric spectroscopy on 3-methyl-1-methylimidazolium bis(trifluoromethanesulfonyl)imide (Mmim-TFSI) with 1 mol Li-TFSI. This is furthermore consistent with another study showing coupling between T_g and conductivity in an ionic liquid [70].

It was not possible with the shear mechanical data do obtain an exact determination of the time scales of the small intermediate mode called τ_{wing} but it was possible to estimate its position, and then include that in the relaxation map as a gray area in the plot. Relaxation times from the beta relaxation was obtained by the shear compliance, see chapter 7 for details.

The QENS data is as mentioned a single time scale technique which provides information on dynamics on a nanosecond timescale. This has been included in the relaxation map as a dashed, horizontal line at $\tau_\alpha = 1/\omega_{IFWS} = 3.3 \cdot 10^{-10}$ s. The three dynamic modes previously identified with the IFWS method and the temperature dependence of the main mode is plotted together. This is seen as the purple triangle (average) where the error bars extend from the highest to the lowest temperature of the main mode, since there is a temperature dependence of the alpha relaxation found in the neutron signal is Q -dependent.

It is seen in figure 11.9 that this main mode fits very well with the shear mechanical alpha relaxation and the resistivity. The orange and yellow dashed-dotted lines are representing the dynamic modes originating from the butyl chain and methyl group respectively as found in the previous analysis of the IFWS data. The temperature dependence of these secondary modes is assumed to be Arrhenius in nature. Both secondary modes are faster than the main mode and the lines are seen to cross the $1/\omega_{IFWS}$ line at triangles with the same color. These triangles are calculated used the formular for T_{max} which is derived from the model in eq. (11.1.1), see B. Frick et al. [142] for details.

The relaxation map thus shows a range of different dynamic modes found from both inelastic neutron scattering, shear mechanical and dielectric measurements. With the neutron scattering data the tool of partial deuteration has made it possible to assign the secondary and low temperature dynamic modes to movement of specific parts of the cation. In the case of the shear mechanical

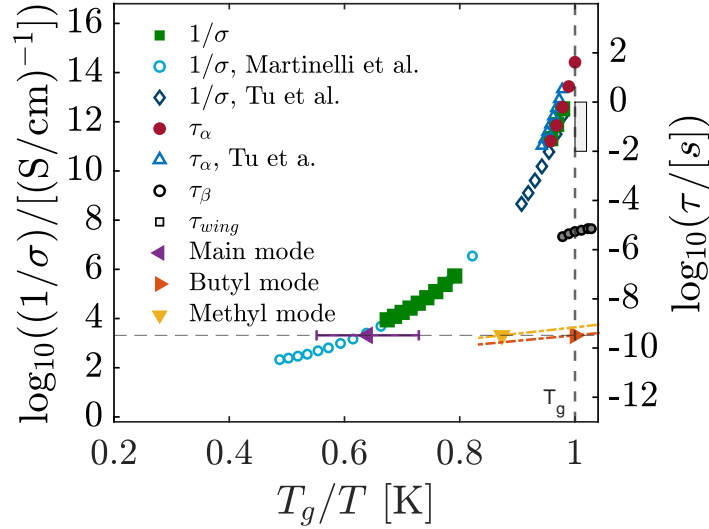


Figure 11.9: Relaxation map showing both the time scale and temperature dependence of the five different dynamic modes in the RTIL Pyr14-TFSI. The inverse conductivity is both from literature (blue) [70, 80] and from this study (green) and has been plotted in a two-axes plot together with the alpha relaxation time found from the shear modulus (red). Conductivity data from literature [70] have been scaled in absolute value so that they collapse with data from this study. The plot is scaled to T_g as found from shear measurements (182 K). The two y-axes have been shifted so that the shear modulus and conductivity measurements collapse in the supercooled temperature region and cover the same range. The purple, orange and yellow triangles are the three dynamic modes found from the neutron scattering data and are related to dynamics connected to the pyrrolidinium ring (purple), the methyl group (yellow) and the butyl chain (orange). Errorbar of the pyrrolidinium ring mode represents the Q -dependence of this. Dashed-dotted lines are the Arrhenius dependence which has been found from the model fits to the D3 and D9 data but with the D12 interpolation data subtracted. Dynamics of the pyrrolidinium ring is clearly related to the alpha relaxation (blue, green and red). Dark gray circles is the beta relaxation, τ_β , and light gray box is the intermediate relaxation, τ_{wing} , both found in the shear mechanical data of the liquid.

data it is not possible to obtain direct information of the molecular origin of the different dynamic modes. However, when combining with the dynamic modes from neutron scattering in the relaxation map it does not seem likely that the beta relaxation or the intermediate relaxation, the wing, are connected to the dynamics of the butyl chain or the methyl group.

The reason for this conclusion is that these modes are all well separated. Even if the actual temperature dependence of the two fast dynamic modes from

neutron scattering do not follow a simple, Arrhenius temperature dependence, it would require an even stronger temperature dependence than that of the alpha relaxation for them to be connected to the beta and intermediate shear mechanical relaxations. This would however be inconsistent with the fact that the alpha relaxation of a liquid is normally found to be the one with the strongest temperature dependence.

It is therefore concluded based on the relaxation map in figure 11.9 that in Pyr14-TFSI there are four different relaxational modes which are active on a shorter time scale, or equivalently at lower temperatures, than the alpha relaxation. A similar relaxation map is seen in literature [151], where four distinct relaxation modes were found by a combination of dielectric spectroscopy and neutron scattering data.

11.2 Pmim-BF4

In order to expand the conclusions from the neutron measurements on Pyr14-TFSI, the FWS experiment was repeated on three more RTIL specially selected due to a wide span in fragility. This way, it will be more justified to make more universal conclusions on ionic liquids in general, whereas the results from the different deuterated versions of Pyr14-TFSI can only lead to conclusions for this particular liquid.

The three liquids were; 1-propyl-3-methyl-imidazolium tetrafluoroborate (Pmim-BF4), 1-butylpyridinium tetrafluoroborate (Bpyr-BF4) and 1-ethyl-3-methylimidazolium tricyanomethanide (Emim-TCM) with a fragility of 73 (this study), 117 and 158 [102] respectively. See table 11.2 for the neutron scattering cross sections. All three liquids show a reasonable amount of incoherent scattering ($\sigma_{\text{inc}}/\sigma_{\text{scat}} = 87 - 91\%$) meaning that the assumption of no coherent scattering when performing the data analysis holds. Also, the anion in each of the liquids, BF4 and TCM, have very low incoherent scattering compared to the overall liquid, 8 and 2.6 barn respectively, and so can be assumed to be "invisible" in the fixed window scans.

Liquid	σ_{scat}	σ_{inc}	σ_{coh}	$\sigma_{\text{inc}}/\sigma_{\text{scat}}$ [%]
Pmim-BF4	1150	1046	103	91
Bpyr-BF4	1231	1126	105	91
Emim-TCM	1015	886	130	87

Table 11.2: The neutron scattering cross sections for the three different RTIL. All scattering cross sections are in barn.

As with Pyr14-TFSI, elastic fixed window scans (EFWS) were acquired with an energy resolution of $\Delta E \approx 0.8 \mu\text{eV}$ corresponding to a timescale of the dynamics of around 5 ns. Inelastic fixed window scans (IFWS) were measured with

two different energy off-sets of $E_{IFWS} = 3 \mu\text{eV}$ and $E_{IFWS} = 6 \mu\text{eV}$ giving a time of $1/\omega_{IFWS} = 1/(E_{IFWS}/\hbar) = 2.2 \cdot 10^{-10}$ s and $1.1 \cdot 10^{-10}$ s. The Q -range was in both cases 0.19 - 1.984 \AA^{-1} . The data were taken in continuous cooling to avoid crystallization and covered the temperature range 2 - 328 K with a cooling rate of 0.5 K/min. The elastic and inelastic scans were performed alternately.

The author of this thesis did the application for beam time, while planning the experiment was in collaboration with Kristine Niss, David Noirat and Markus Appel. The neutron scattering measurements on Pmim-BF₄, Bpyr-BF₄ and Emim-TCM were performed by David Noirat and Markus Appel during the Covid-19 pandemic lockdown.

All three liquids were purchased from IoLiTec with a purity of 98-99% and used as received. To avoid contamination from water absorption, all liquids were loaded in a glove box. The liquids showed good promise in the preliminary calorimetry measurements with the Red Box, see Section 6.3, with no visible crystallization and a clear glass transition. However, two of the liquids crystallized in this experiment leaving only liquid results from Pmim-BF₄. See figure 11.10 for a schematic of this liquid.

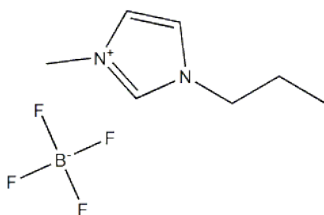


Figure 11.10: A schematic of the liquid Pmim-BF₄ with the cation Pmim at the top and the anion BF₄ at the bottom

11.2.1 Inelastic fixed window scans

Figure 11.11 shows the IFWS at all Q -values except for the first four, since the data from these Q -values were very noisy and disrupted the whole picture of the Q -dependence. Data have been normalized to the elastic scattering at the lowest measured temperature where the scattering is purely elastic since all dynamics are frozen in.

The structure of Pmim is similar to that of Pyr14, in the sense of having a ring with a methyl group and another alkyl-chain attached symmetrically to this ring. The alkyl-chain of Pmim is propyl which is even shorter than the butyl-chain of Pyr14 (3 carbon atoms versus four) which leads to the assumption that the dynamics of the Pmim cation will be mainly dominated by the imidazolium ring and thus couple to the center-of-mass motion of the cation.

Just as with Pyr14-TFSI this will then give direct information on the alpha relaxation of the liquid. Ideally, we should have used Pmim-BF₄ with the methyl and the propyl chain deuterated in order to probe the center-of-mass motion

without secondary contributions from the alkyl-chains. However, the results from deuterated Pyr14-TFSI in Chapter 12 shows that when it comes to testing the shoving model, which is the main purpose of this experiment, the fully protonated liquid shows good results when compared to the liquid with the methyl and butyl chains deuterated. Due to the before mentioned similar structure of Pyr14 and Pmim this leads to the assumption that the fully protonated Pmim will also be usable when testing the shoving model, despite the secondary dynamics from the alkyl-chains.

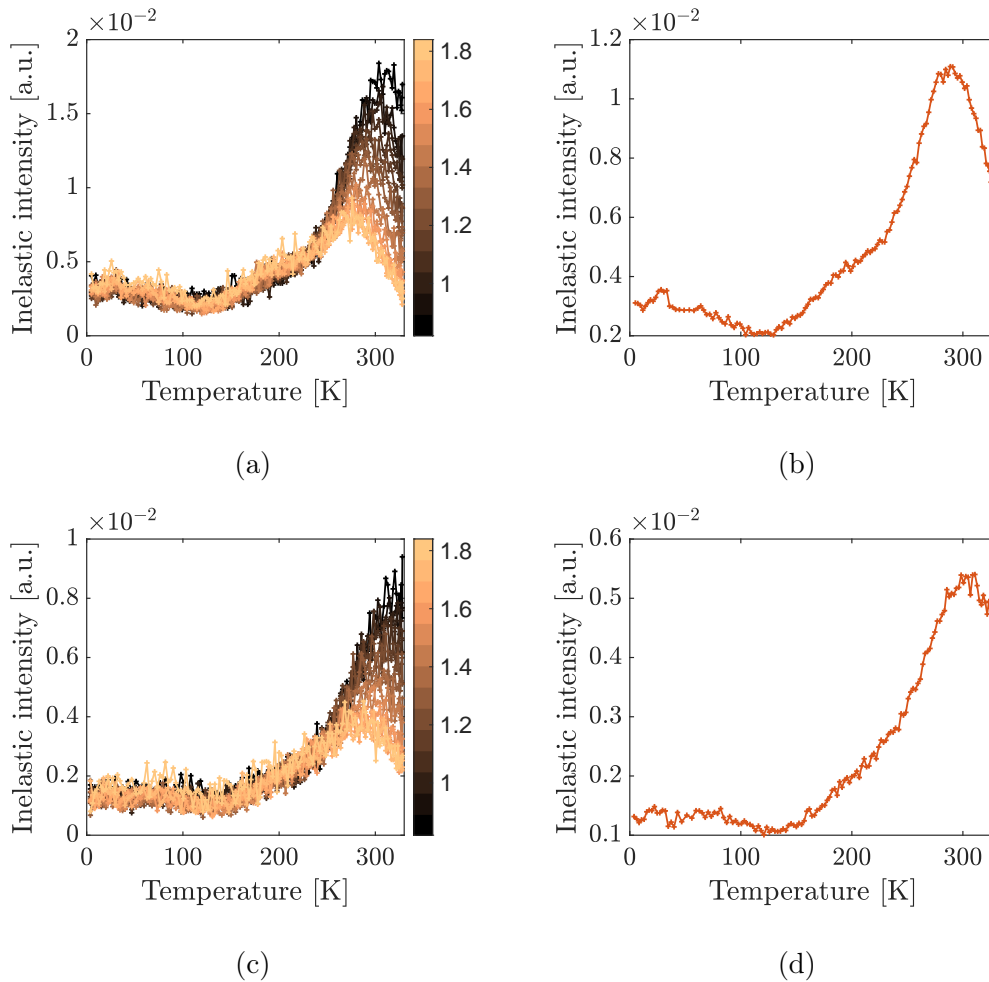


Figure 11.11: Results for the IFWS. a) and b) is for $\Delta E = 3 \mu\text{eV}$ for all Q -values and summed over all Q -values respectively and c) and d) is the same but for $\Delta E = 6 \mu\text{eV}$.

It is seen in figure 11.11 that there is indeed a dominating mode at high temperatures which is Q -dependent, shifts to lower temperatures and decreases in intensity with increasing Q -values, which suggests that the origin is diffusive [142], just like with Pyr14-TFSI. This supports the assumption that what is seen here is indeed the alpha relaxation of the liquid.

Furthermore, when comparing to Pyr14-TFSI in 11.1 it is also seen in Pmim-

BF4 what appears as small, secondary modes at lower temperatures, seen as a small shoulder on the main mode. This is present at both 3 and 6 μeV but is most prominent at 3 μeV . Following the interpretation with Pyr14-TFSI this secondary mode is due to local motions because it is Q -independent and increase in intensity with increasing Q -values and this leads to the assumption that it originates from the alkyl-chains. However, since we cannot separate these secondary motions from the main mode, not much more can be said about them.

11.2.2 Elastic fixed window scans

Figure 11.12 shows the results from the EFWS on Pmim-BF4. In the following the EFWS data will be analyzed in terms of the mean square displacement (MSD) as was also done with Pyr14-TFSI. Section 11.1.2 gives a thorough description about how to find MSD from the elastic measurements with the Zorn-method, which will be the method of choice for finding MSD in the Pmim-BF4 liquid.

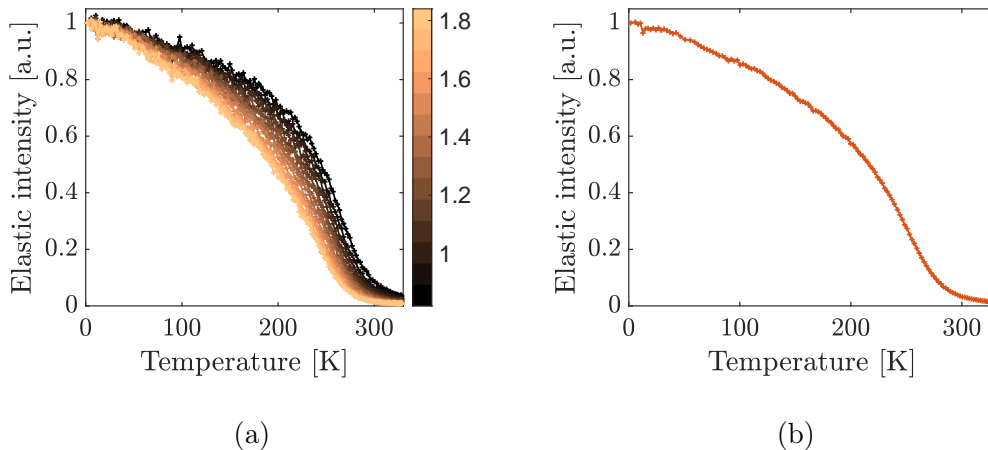


Figure 11.12: Results for the EFWS on Pmim-BF4 with the Q -dependence in a) and summed over all Q -values in b). Data have been normalized to the intensity at the lowest temperature.

The calculated MSD as a function of temperature can be seen in figure 11.13. The temperature range in which shear modulus measurements were also performed on the liquid is shown as a blue shaded area (196-174 K). This will be relevant in the following chapter where the shoving model is tested using MSD and structural relaxation times as found by the shear modulus.

There is a continuous increase in MSD from 2 K, where only molecular vibrations are assumed to contribute to the MSD, and up through the glassy state to T_g and further up in temperature. IFWS results show that below 125 K there is little activity, but above this temperature the two dynamic mode enters the window and MSD start to increase more steeply.

The shoving model assumes, as mentioned, that the MSD is proportional the temperature over the high-frequency limiting shear modulus, i.e. $\langle u^2 \rangle \propto T/G_\infty$.

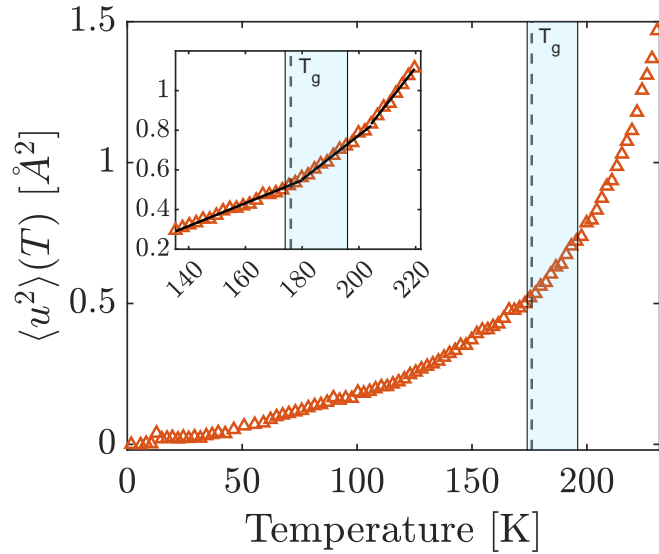


Figure 11.13: MSD for Pmim-BF4 calculated with the Zorn-method. Insert shows a zoom of the data around T_g with three linear fits (black lines) illustrating the change in dynamics. Dashed line is T_g as found from shear modulus.

A consequence of this relation is that the MSD should experience a kink around T_g where the temperature dependence of G_∞ starts to increase. The insert in figure 11.13 do show a small kink in MSD at 179 K and so it is reasonable to use the MSD data for Pmim-BF4 in the test of the shoving model, at least in this regard. That the kink enters the MSD data at 179 K gives a T_g of slightly higher temperature than with the shear mechanical measurements (174 K).

Two additional dynamic regions are also highlighted by black solid lines in the insert in figure 11.13. These lines were found by fitting the MSD in the temperature region of interest to a linear fit. The first dynamic region is just above the glass transition and lasts until 203 K where another kink in MSD marks the beginning of the final dynamic region. 203 K is also the temperature where the IFWS signal starts to increase significantly and where the structural relaxation, or main mode, is dominating.

In conclusion, the RTIL Pmim-BF4 is well suited for test of the shoving model even though it is a fully protonated liquid and thus contain dynamics from more than the center-of-mass of the cation. The intensity of these extra dynamics is however small in the region of interest, as could be seen in the inelastic scattering intensity, where there is little signal below T_g (174 K). It is also seen in the elastic intensity which is quite constant below T_g .

Chapter 12

Testing the shoving model

One of the still unsolved mysteries in condensed matter physics is the non-Arrhenius slowing down of the liquid; as the liquid is cooled down the structural relaxation time and viscosity drastically decrease. This at a rate much faster than what would be expected if the activation energy was governed by simple thermally activated transitions, i.e. the Arrhenius behavior:

$$\tau = \tau_0 e^{E/k_b T} \quad (12.0.1)$$

where τ_0 is the microscopic vibration time given by a phonon scale.

If one wants to maintain the idea of an activation energy governing the viscous slowing down it will need to be temperature dependent. This leads to a generic expression for the relaxation time as

$$\tau = \tau_0 e^{\Delta E(T)/k_B T} \quad (12.0.2)$$

To predict the structural relaxation of a liquid at a given temperature, one would need a model that encapsulates the non-Arrhenius behavior of liquids, which means finding an expression for $\Delta E(T)$. However, there is still no consensus in the scientific community as to what causes this non-Arrhenius temperature dependence of the viscosity and the relaxation time [4].

12.1 The energy landscape picture

The energy landscape picture is a way to describe the qualitative behavior of a system with many metastable states and many transitions between these states and was described by Martin Goldstein in 1969 [152]. Specifically for this chapter the energy landscape picture can be used to describe the dynamics of supercooled liquids [153].

The molecules exist in a multidimensional potential energy surface/landscape with potential maxima and minima. With N particles this landscape is $3N+1$ dimensions and is as such impossible to visualize, but a 2D representation is a good way to get an idea of the difference between the liquid, glassy and crystal state [154]. Such a representation can be seen in figure 12.1a.

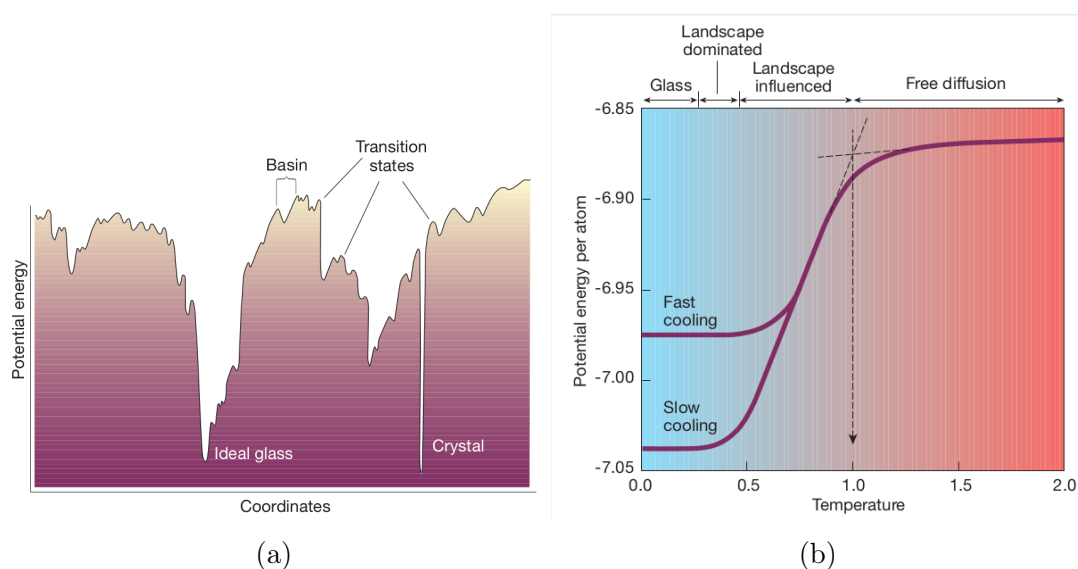


Figure 12.1: a) An illustration of the potential energy landscape in 2D with a number of potential energy minima that the molecules can sample. b) The potential energy per atom as a function of temperature showing how the potential energy decreases through different regions as temperature is lowered. First from free diffusion to landscape influenced and then into the glassy state. Both from [153].

A system like a liquid in equilibrium with a sufficiently high temperature will have a lot of energy and move in the upper part of the landscape where molecules will be able to sample many of the accessible minima - a state called free diffusion. This is also illustrated in figure 12.1b which shows the potential energy per atom as a function of temperature from a MD simulation of a binary mixture of unequal-sized Lennar-Jones atoms in a box of fixed volume.

As the temperature is lowered the molecule moves down in the energy landscape and so the more shallow minima will no longer be accessible. Instead, the molecules jump between the lower minima, and this is called the landscape influenced region, and here the potential energy decreases drastically with decreasing temperature as can be seen in figure 12.1b. In this supercooled state slow dynamics come from the rearrangement of the molecules when they overcome the potential barriers. As the liquid is cooled and the thermal energy decreases, these rearrangements will happen less and less frequently leading to the viscous slowing down of the liquid, i.e. increase in τ_α . Fast dynamics are associated with fast vibrations of the molecules around the potential minima and at low temperatures/high viscosity almost all molecular motion goes into these fast vibrations.

If the liquid crystallizes it means that the system finds its way to the crystal minimum seen in figure 12.1a. But if the system is cooled sufficiently fast it will not have time to go to this ideal minimum, ideal in the sense that this one is the one with the lowest energy, and it will get stuck in one of the lower minima

that is not the crystal. When this happens, the system goes from the landscape dominated region and into the glassy state. The lower the cooling rate, the lower the potential energy will be or in other words, the lower the minimum the system will get stuck in. It is important to note that at this state the molecules still have vibrational energy, but it will be insufficient to create jumps between minimum barriers.

12.2 Elastic models

The common goal of elastic models is to somehow connect the short-time elastic properties to the slow structural relaxation of the molecules in a liquid. At first glance it can appear impossible that a flow event taking place on a picosecond time-scale can control relaxations processes that takes a second or even more. As Jeppe Dyre puts it in his colloquium: "*Surely, one cannot predict the rate of global climate variations over millions of years from observations of the world's weather collected over a single minute*" [2]. Nevertheless, the elastic models investigate this idea. Several different elastic models explaining the viscous slowing down of supercooled liquids exist and a thorough review is given by Dyre in his colloquium [2], but a quick summary will be given here. See [2] for original references.

There is the harmonic approximation which states that the relaxation of a liquid is governed by the rate of molecules moving from one energy minimum to another. This leads to the expression, by the use of a Gaussian statistical-mechanical probability distribution, that the activation energy is

$$\Delta E(T) = \lambda_1 k_B T \frac{a^2}{\langle u^2 \rangle} \quad (12.2.1)$$

where a is the average intermolecular distance and $\langle u^2 \rangle$ is the vibrational mean-square thermal average around one minimum. This was further developed to be related to the instantaneous shear modulus, G_∞ giving the relation

$$\Delta E(T) = \lambda_2 a^3 G_\infty \quad (12.2.2)$$

with the temperature dependence of the activation energy coming from the temperature dependence of G_∞ which will always increase with decreasing temperature.

Another approach is one where it is assumed the local molecular rearrangement is caused by thermal fluctuations that will increase the local volume generating space for the molecules to move. This volume increase is generated by thermal longitudinal sound waves and thus the activation energy is directly connected to the high-frequency longitudinal sound velocity, c_∞ , giving the expression

$$\Delta E(T) = \lambda_3 m c_\infty^2 \quad (12.2.3)$$

where m is the molecular mass. Thus, the local flow event is governed by the short-time elastic properties of the liquid.

A third approach is also related to the high-frequency shear modulus, G_∞ and equation (12.2.2), with $\lambda_2 = 1$ was derived using the Maxwell relation, $\tau = \eta/G_\infty$ combined with Eyring's expressions for viscosity and Duschman's theory of relaxation time.

All three models described above have activation energies that are equivalent in their temperature variations in the simplest approximation and one have that

$$\frac{\Delta E}{k_B T} \propto \frac{m c_\infty^2}{k_B T} \propto \frac{a^3 G_\infty}{k_B T} \propto \frac{a^2}{\langle u^2 \rangle} \quad (12.2.4)$$

12.2.1 The shoving model

A fourth elastic model that aims to explain the non-Arrhenius behavior of the viscous slowing down of the structural relaxation time in liquids is the shoving model created by J. Dyre et al. in 1996 [10].

The starting point is that in a liquid the molecules or atoms will experience a strong repulsion on short distances as well as a weak attractive force on longer distances due to van der Waals forces. In other words, a molecule in a liquid will feel a weak pull from the other molecules but avoid getting too close as this will be energetically very costly. If this is the case, an obvious problem presents itself: how do the molecules then rearrange themselves in a dense liquid if they will try to avoid "squeezing" past each other?

The solution is that for a flow event to take place the molecule can shove aside the surrounding molecules and thus increasing the available volume before the flow event. This will be energetically more favorable than squeezing past the nearest neighbors at constant volume, even though it will cost some energy to move the surroundings. It is thermal fluctuations that are responsible for this increase in volume and so the phrase "shoving aside" is a little misleading, since it is not the molecules that do the work.

A further assumption in the shoving model is that the activation energy related to this flow event, and thus ΔE , will be dominated by the shoving itself. The next step is to realize that a flow event is thermally activated and will then, as any thermally activated event, take place on a very short time scale. The shoving aside of the surrounding molecules will happen so fast that the surroundings will behave like a solid leading to the core of the shoving model: that ΔE is directly related to the infinite-frequency shear and bulk modulus of the liquid, G_∞ and K_∞ respectively.

If the volume increase is spherical, elasticity theory shows that this can be simplified even further since the shoving work will then be independent of bulk modulus and the activation energy is then directly proportional to only G_∞ . The constant of proportionality is called the specific volume, V_c , leading to a final expression for the activation energy:

$$\Delta E(T) = V_c G_\infty(T) \quad (12.2.5)$$

and a full expression for the relaxation time to be

$$\tau = \tau_0 \exp\left(\frac{V_c G_\infty(T)}{k_b T}\right) \quad (12.2.6)$$

where the temperature dependence come from $G_\infty(T)$ which increases with decreasing temperature. The characteristic volume V_c is assumed to be constant.

One of the properties of the shoving model is that it can be tested relatively simply experimentally. This is shown in figure 12.2, which is from the original paper [10], where the logarithm of the viscosity is plotted as a function of $x = G_\infty(T)/T$ and $1/T$ for five different molecular liquids. Note that the relation between viscosity and relaxation time can be expressed by the Maxwell relation $\tau = \eta/G_\infty$. The black solid line is the prediction from the shoving model showing excellent agreement with data. G_∞ is in this case found from the fact that, besides from a small β -relaxation, the liquids obey time-temperature superposition, implying that $G_\infty(T) \propto G''_{max}(t)$ so that the temperature dependence is identical [155].

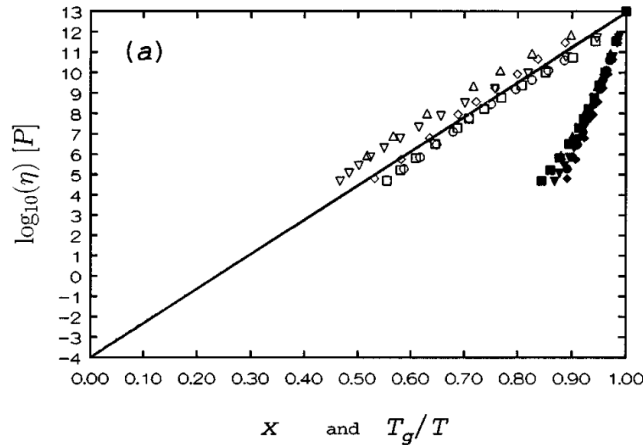


Figure 12.2: The logarithm of the viscosity as a function of both $x = G_\infty(T)/T$ (open) and $1/T$ (closed) for five molecular liquids. Black solid line is the prediction from the Shoving model showing excellent agreement with data, as opposed to the Arrhenius prediction. From [10].

12.2.2 The landscape equivalent of the shoving model

The landscape equivalent of the shoving model is an alternative way to describe the non-Arrhenius behavior for liquids as shown in equation (12.2.5). It was developed by J. Dyre and N. Boye Olsen in 2004 [150] and will be described in the following.

The starting point of this approach is, as with the first version of the shoving model, that the molecules in a highly viscous liquid almost exclusively stay in their respective potential energy minima and so almost all motion goes into vibrating around the individual minima. This means that rearrangements of

molecules by crossing a potential energy barrier between two minima happens rarely and so mostly the molecules just stay in place.

The assumption of 1) the activation energy being mainly elastic energy, 2) the elastic energy is mainly located in the surroundings of the shoving event and 3) the elastic energy is almost exclusively shear elastic energy still applies. A flow event will take place when one molecule crosses a barrier which also means that the activation energy in the flow event will depend on the height of the energy barrier between two minima.

This barrier height can be approximated by a Taylor expansion to second order around the value of the potential itself, U , in the minima.

$$U = U_0 + U'(x_{min})(x - x_{min}) + \frac{1}{2}U''(x_{min})(x - x_{min})^2 \quad (12.2.7)$$

but since the first derivative in a minimum will be equal to zero, this term cancels out and we are left with

$$U = U_0 + \frac{1}{2}U''(x_{min})(x - x_{min})^2 = U_0 + (\Lambda/2)x^2 \quad (12.2.8)$$

$$U = U_0 + (\Lambda/2)x^2 \quad (12.2.9)$$

where x is now the distance to the minimum. This shows the classic connection between a potential minimum and the harmonic oscillator, i.e. movement around the potential minimum will behave as a harmonic oscillator with potential energy U and a "spring" constant of $(\Lambda/2)$. Furthermore, statistical mechanics show that the average distance to the minimum will be

$$\langle u^2 \rangle = k_B T / \Lambda \Rightarrow \Lambda = k_B T / \langle u^2 \rangle \quad (12.2.10)$$

where $\langle u^2 \rangle$ is the mean-square fluctuation of the molecule around the minima which also corresponds to the ensemble average over all minima. A value experimentally accessible by e.g. incoherent inelastic neutron scattering as seen in chapter 11. This gives an activation energy directly related to the energy barrier height as

$$\Delta E = \frac{k_B T b^2}{\langle u^2 \rangle 2} \quad (12.2.11)$$

This gives a final expression for the relaxation time as

$$\tau = \tau_0 \exp\left(\frac{k_B T b^2}{2\langle u^2 \rangle / k_B T}\right) = \tau_0 \exp\left(\frac{b^2}{2\langle u^2 \rangle}\right) \quad (12.2.12)$$

where b is the distance between the minimum and the intersection of the two parabolas (from the expansion around the two minima). We see with eq. (12.2.12) that as with the original shoving model it is the fast elastic vibrations, here in the form of the mean square displacement, that governs the slow structural relaxation.

So how is this related to the shear and bulk modulus of the liquid? Details will not be given here, but the general idea is that the fast vibrations are related to

the phonon spectrum in a three-dimensional isotropic liquid. For each wavevector there are three degrees of freedom: two transverse related to the shear modulus and one longitudinal related to the longitudinal modulus M , which is $M = K + (4/3)G$, where K is the bulk modulus. One can then average over the two types of phonons finding that $\langle u^2 \rangle = T(2/G + 1/M)$ leading to the relation

$$\frac{1}{\Delta E(T)} = \frac{2}{G_\infty(T)} + \frac{1}{M_\infty(T)} \quad (12.2.13)$$

It is however possible to show that the instantaneous shear modulus, G_∞ contributes with 92% of the total activation energy, so it can be assumed that only the shear modulus contributes to the relaxation.

Furthermore, it should be noted that since the three basic assumptions for the original shoving model are equivalent to those of the landscape version the two will in practice be indistinguishable. This equivalence was tested on molecular liquids in a study from 2017 [11] where both G_∞ and $\langle u^2 \rangle$ were measured with shear mechanical spectroscopy and neutron scattering, respectively. It showed that both ways of testing the shoving model followed the shoving model prediction equally well.

A review of experiments testing the shoving model [155] showed that the shoving model prediction holds over a range of classes of liquids such as van der Waals bonded liquids, metal glasses oxide glasses and hydrogen bonded liquids and an obvious question is then if this shoving model prediction also holds for RTILs.

12.3 Pyr14-TFSI

The original version of the shoving model cannot be used for the test of Pyr14-TFSI, since the large beta relaxation in the shear mechanical spectra prevents the measurement of the high-frequency limiting shear modulus, G_∞ . It was attempted to fit the shear modulus spectra to a model containing an alpha and beta relaxation [109], in order to obtain a reasonable value for G_∞ . This attempt was unsuccessful due to the peak of the beta relaxation being too far out of the frequency window.

It was, therefore, necessary to use the other approach for testing the shoving model, i.e. the simplified harmonic approximation, where the vibrational mean square displacement is proportional to the temperature over the high-frequency shear modulus, $\langle u^2 \rangle \propto T/G_\infty$. The shoving model was tested for the first time on RTILs with Pyr14-TFSI in a study by the author of this thesis and co-workers [95], where the results from this paper are also presented in the following.

The shoving model prediction given in equation (12.2.12) can be normalized to the shoving model prediction at T_g given as

$$\tau_g = \tau_0 \exp\left(\frac{b^2}{2\langle u^2 \rangle_g}\right) \quad (12.3.1)$$

where τ_g is the relaxation time and $\langle u^2 \rangle_g$ is the MSD at T_g respectively.

Dividing equation (12.2.12) with equation (12.3.1) and rearrange then gives the final relation to be tested as

$$\log_{10} \tau(T) = (\log_{10} \tau_g - \log_{10} \tau_0) \frac{\langle u^2 \rangle_g}{\langle u^2 \rangle(T)} + \log_{10} \tau_0 \quad (12.3.2)$$

The shoving model has then been tested with the MSD values found for all four deuterations of Pyr14-TFSI and with shear mechanical data on the fully protonated liquid, also called D0. See chapter 11 for a detailed description of how the MSD data were obtained from quasi-elastic neutron scattering.

The reason for using all four deuterations of Pyr14-TFSI in the shoving test is that the analysis of the elastic neutron scattering data rely on two assumptions; that the scattering is completely incoherent and that there is only vibrational contributions to the MSD. None of the deuterations fulfills both assumptions fully since there is either coherent scattering or contributions from relaxation in the data. Thus, the tests of the shoving model with four different degrees of deuteration can be regarded as an estimate of the robustness of this test.

The result is shown in figure 12.3 and here the black solid line represents the shoving model prediction with $\log_{10} \tau_0 = -14$. For all four deuterations the shoving model prediction clearly works well, but it works especially well for D9 and D12.

For comparison figure 12.3 also shows the alpha relaxation time plotted as a function of T_g/T . The closeness of the shoving model test (triangles) when comparing to the Angell plot with T_g/T (crosses) shows that the shoving model does a much better job of predicting the slowing down of the alpha relaxation for all four deuterations of Pyr14-TFSI.

The shoving model test has also been performed on the same four deuterations of Pyr14-TFSI but with MSD found from the more standard Gaussian approximation method instead of the R. Zorn method used to test the shoving model in figure 12.3. This can be seen in figure 12.4. The conclusion that the shoving model predicts the viscous slowing down of the structural or alpha relaxation in the four deuterations of Pyr14-TFSI still applies, even though the resulting MSD is slightly different.

12.4 Pmim-BF4

As shown in section 11.2 successful quasi-elastic neutron scattering (QENS) measurements were performed on the RTIL Pmim-BF4, which made it possible to calculate a mean square displacement for the liquid at a large range of temperatures. Combined with shear modulus measurements at a range of temperatures in the supercooled region makes it possible to test the shoving model on Pmim-BF4 as well.

Recall that Pmim-BF4 is an imidazolium based RTIL with a fragility of approximately 73, measured in this work, which is lower than the fragility index

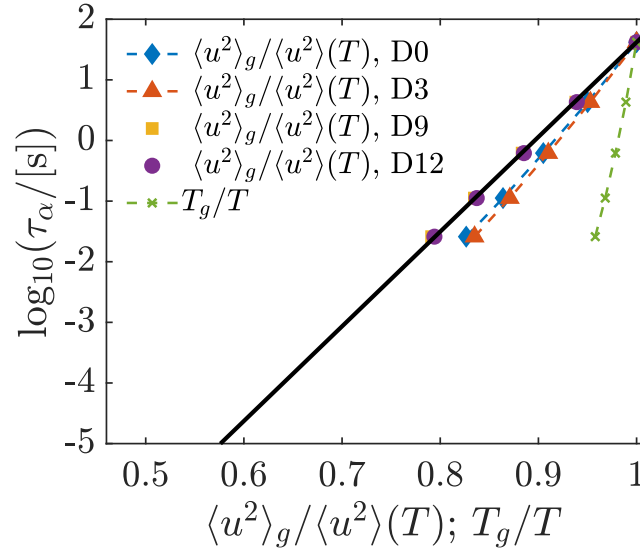


Figure 12.3: A shoving plot with MSD data found for four different deuterations of Pyr14-TFSI with the shoving model prediction as the black solid line. The relaxation time against $\langle u^2 \rangle_g / \langle u^2 \rangle(T)$ is shown as solid symbols and the standard Arrhenius plot is shown as crosses. The alpha relaxation times were found as explained in chapter 7.

for Pyr14-TFSI of 90 ± 5 . Both fragility indexes were found with a T_g defined at where $\log_{10}(\tau_\alpha) = 1.5$. The original plan was to measure on a range of RTILs with a large deviation in fragility to generate more universal conclusions. This plan was unfortunately not completed due to difficulties with crystallization in the QENS measurements. Even so, there is a difference between the fragility indices of Pmim-BF4 and Pyr14-TFSI even though they are both in the intermediate case between strong and very fragile liquids.

The result for the shoving model test for Pmim-BF4 can be seen in figure 12.5 and show that the normalized MSD follow the same trend as the shoving model prediction even though it has a higher slope and thus lie below the shoving model. A linear fit to the data show that τ_0 will be around 10^{-18} s which is not a physical meaningful time since it is simply too fast. Remember that in the shoving model prediction τ_0 was said to be equal to 10^{-14} s. Despite this discrepancy it is concluded that there is quite good agreement between the shoving model prediction and the data from Pmim-BF4. This conclusion should also be seen in the light of a shoving model test on the van der Waals liquid propylene carbonate (PC) [12], where the result matches those of Pmim-BF4 and where the conclusion was that the shoving model prediction works well.

When comparing the shoving test for Pmim-BF4 with the fully protonated Pyr14-TFSI it is seen that the two are quite close to each other, even though Pmim-BF4 lie even lower than Pyr14-TFSI when comparing to the shoving model

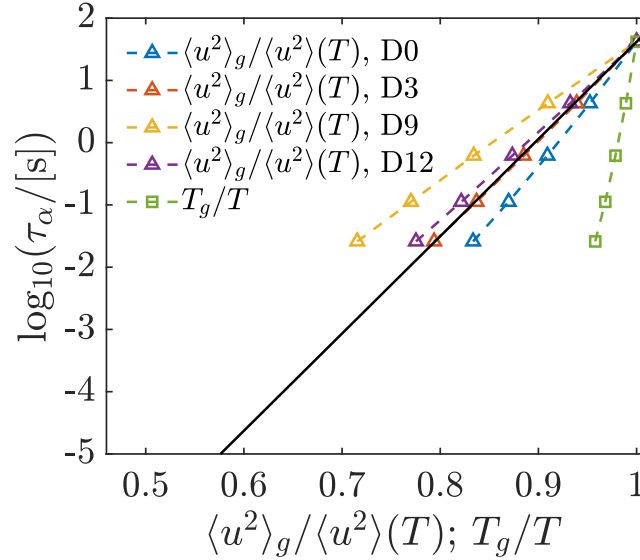


Figure 12.4: Test of the shoving model but using MSD calculated by the Gaussian method for all four deuterations where the short Q -range was used. The conclusion that the shoving model predicts the slowing down of the alpha relaxation to a high degree still applies in this case.

prediction. This is perhaps not so surprising since neutron measurements were also performed on fully protonated Pmim-BF₄ and the two liquids are quite similar in chemical composition. Even though they both follow the same trend as the shoving model prediction, the result is much better for the fully deuterated Pyr14-TFSI (D12) which follow the shoving model prediction almost exactly. This indicates that a proper shoving model test must be with a fully deuterated liquid so, that only dynamics from the ring or center-of-mass of the molecule is measured. This is despite the fully deuterated liquid having a lower incoherent scattering signal and thus, does not comply to the assumption that the QENS signal is fully incoherent.

12.5 Discussion and conclusion

The shoving test of both Pyr14-TFSI and Pmim-BF₄ shows that for these RTILs the shoving model prediction works well. This applies especially for the fully deuterated Pyr14-TFSI and Pyr14-TFSI with the butyl-arm deuterated where the results follow the shoving model prediction almost exactly. For Pyr14-TFSI with only the methyl-arm deuterated, with fully protonated Pyr14-TFSI and with Pmim-BF₄, the shoving test data show a shoving model like trend with a linear relation between the logarithm to the alpha relaxation time and the to T_g normalized MSD. However, when fitting these data to a linear relation it gives a microscopic time scale, τ_0 , in the range of 10^{-17} s which is too small to give any

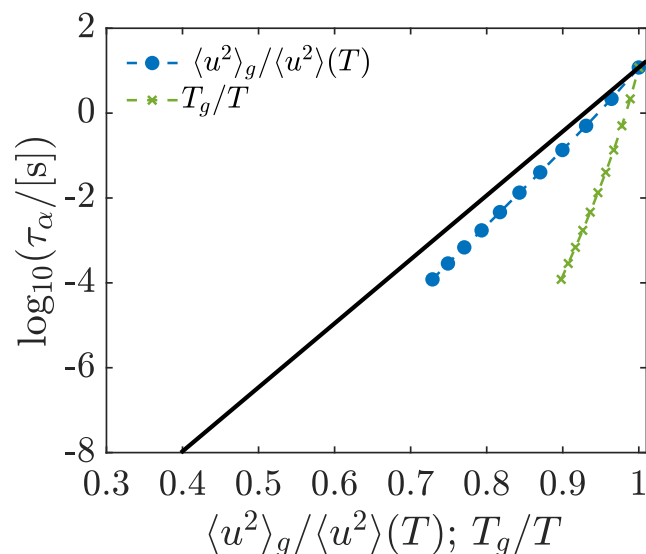


Figure 12.5: Test of the shoving model by using MSD calculated by the Zorn method. τ_α was found from the shear modulus data by a fit to a second order polynomial around the alpha relaxation peak, ν_{\max} , and $\tau_\alpha = 1/2\pi\nu_{\max}$. It shows that the shoving model prediction fits the data well.

real, physical meaning. Note that D0, D3, D9 and D12 are all the same liquid as Pyr14-TFSI, with the only difference being how much of the cation dynamics are contributing to the neutron scattering signal.

Despite this discrepancy, it is interesting to note that the shoving model prediction works so well for two RTILs, which by nature are complex systems with competing interactions and mesoscale structures. This result shows that, even though these two RTILs are not simple liquids, the viscous slowing down of the alpha relaxation follows the same trend as that of non-associated molecular liquids like cumene and 5-polyphenyl ether [11].

Chapter 13

Summary and concluding discussion

This thesis, through the last eight chapters, has presented experimental work on a handful of room temperature ionic liquids. The main aim was to answer, if this class of liquids has dynamics fundamentally different to those of non-associated molecular liquids, and if they exhibit what can be viewed as simple behavior. This is part of the basic research into viscous liquids and the glass transition, but also a part of understanding the dynamics of RTILs to help developing applications in, for example, Li-batteries. The following will summarize the main results and continue the discussion of these.

Chapter 5 investigated why ionic liquids are so viscous, by comparing the viscosity of an ionic liquid with its molecular mimic at isodense conditions. It showed that the difference in density cannot account for the factor of 200 difference in viscosity between the ionic liquids and the molecular mimic. As a consequence, ionic liquids in this regard are fundamentally different from non-associated molecular liquids.

Chapter 7 and 8 were both comparative analyses looking into the relaxation spectra in a broad frequency range of a total of five pyrrolidinium-based ionic liquids divided into two series: One with increasing alkyl chain length of the cation and one with increasing Li-salt concentration. That is Pyr1 n -TFSI with $n = 4, 6$ and 8 and Pyr18-TFSI with Li-salt molar fractions of $x = 0$, $x = 0.2$ and $x = 0.4$. Here it was shown that the ionic liquids in both series exhibit behavior resembling that of non-associated molecular liquids like squalane. There is an increased complexity in the microscopic structure of the ionic liquids, which stems from competing interactions and mesoscale structures, and which is not present in the non-associated molecular liquids. This complexity is, however, not reflected in the dynamics of the ionic liquids.

The first and third criteria for simplicity in glass-forming liquids, presented in detail in chapter 2, are time-temperature-pressure superposition and a constant time-scale index. It was shown in chapter 7 and 8 that the five pyrrolidinium-based ionic liquids most likely exhibit TTS around the alpha relaxation. This supports the idea that this is a general behavior in glass-forming liquids, and that the alpha relaxation can be viewed as simple. The beta relaxation present in all five ionic liquids has a much weaker temperature dependence and, therefore, the

entire spectrum does not obey TTS, meaning that the relaxation spectra as a whole cannot be said to have simple behavior.

The time-scale index was calculated for both series showing approximately the same degree of decoupling in the three neat liquids, i.e. across alkyl chain length. There was a slightly higher decoupling in Pyr18-TFSI mixed with Li-salt, which did not decrease when using the terminal mode. The degree of decoupling increases as T_g was approached. In all cases, the decoupling was higher than what has earlier been shown for molecular liquids like 5PPE [32], DC704 and squalane [32,33], but also for hydrogen-bonding liquids like hexanetriol [33] and glycerol-water mixtures [21]. In fact, it matches more that of squalane when using the alpha relaxation time instead of the terminal mode, where the temperature dependence seen in the time-scale index was most likely influenced by the merging of the beta relaxation.

A similar result was also seen in a study of five van der Waals bonded liquids [132], where a decoupling was observed in two of the liquids with a large beta relaxation of similar size to the ionic liquids in this work. This indicates, that it is the effect of the beta relaxation which increases the decoupling. This is even further corroborated by the fact that the beta relaxation increasingly merges with the alpha relaxation with increasing temperature. This explanation is, however, not supported by the fact that the decoupling did not decrease when using the terminal mode, except for Pyr18-TFSI, and that the decoupling was constant across increasing Li-concentration, which increased the distance between the alpha and the beta relaxations. To shed further light on this issue it could be interesting to calculate the time-scale index for RTILs with a beta relaxation of much lower intensity, e.g., Omim-BF₄ and Pmim-BF₄, to see if there is a higher degree of coupling in these liquids.

In chapter 10, the random barrier model (RBM) was tested on both the real part of the conductivity and shear fluidity for six RTILs; five pyrrolidinium-based and one imidazolium-based. The test was also performed on shear fluidity data for DC704 for comparison. The analysis showed that the RBM predicts both the real part of the conductivity and shear fluidity around 3 decades above the conductivity/alpha relaxation peak. Here, a deviation from the RBM prediction sets in and continuously increases with frequency. The onset of this deviation increased with increasing temperature and this, together with results from Omim-BF₄ and DC704, strongly indicated that the deviation from the RBM was due to the beta relaxation. This further indicated that there was spectral shape simplicity in these RTILs for the alpha relaxation, a simplicity interrupted by the presence of a beta relaxation. For future work, one could include a more quantitative determination of the spectral shape of the alpha relaxation and beta relaxation in both response functions, e.g., determination of the minimum slope of the alpha relaxation, as suggested in Ref. [156].

It is interesting to compare the degree of simplicity with results from literature. Density scaling, the fourth criterion for simplicity in glass-forming liquids, was tested on Pyr14-TFSI in a previous work by our research group and co-workers [75]. In that study, it was concluded that the conductivity, viscosity

and the alpha relaxation obey density scaling, i.e. data collapse when scaled to $\Gamma = \rho^\gamma/T$, here with $\gamma = 2.8$. Density scaling has also been found in earlier studies for viscosity and conductivity in RTILs [34, 157, 158]. This shows that the ionic liquids can be viewed as simple when looking at density scaling.

These experimental results were corroborated by simulations of a simple salt model [159], as well as a united atom model, of Pyr14-TFSI [160]. These simulations showed that several dynamic properties, such as self-intermediate scattering function, viscosity, and diffusion coefficient in reduced units show invariance and thus, simplicity along certain lines in the phase diagram.

These findings from literature add an extra dimension to the question if RTILs can be viewed as simple liquids and show that, in general, this at first seemingly complex class of liquids shows remarkable simple behavior. It also shows that the behavior of at least Pyr14-TFSI is similar to those of non-associated molecular liquids, like van der Waals liquids, even though there are some deviations from this. One deviation is that a density scaling exponent of $\gamma = 2.8$ is an intermediate case between van der Waals and hydrogen-bonding liquids.

In chapter 9, the sub-alpha dynamics of the five pyrrolidinium-based, as well as two imidazolium-based, ionic liquids were studied. It was shown that a low frequency dynamic mode, called the slow mode, was present in Pyr18-TFSI with $x = 0.2$ and $x = 0.4$ molar fraction of Li-salt, as well as in Omim-BF₄ and Pmim-BF₄. It meant that these four ionic liquids did not exhibit behavior resembling that of non-associated molecular liquids, but more that of complex liquids like monohydroxy alcohols. At least in the low-frequency region of the relaxation spectra. This was not the case for the Pyr1*n*-TFSI series where there was no slow mode present. Related to this, it would be interesting to test simplicity in RTILs even further by repeating the investigation on Pyr12-TFSI, which has no mesoscale structures, and compare the results from this thesis.

Chapter 11 presented quasi-elastic neutron scattering data on Pyr14-TFSI and Pmim-BF₄. For Pyr14-TFSI, an extensive analysis of the inelastic scattering data showed, that the liquid contains three dynamic modes at the nano-second time scale, where the slowest mode was assigned to the structural relaxation. The origin of the two faster modes could, due to the method of partial deuteration, be assigned to being motion from the methyl group and the end methyl group of the butyl chain. This supported the suggestion that the beta relaxation seen in the shear and dielectric spectra had its origin in the anion. For Pmim-BF₄ the inelastic scattering data was mainly used to assess the quality of the data in relation to its use in the test of the shoving model.

The mean square displacement was calculated for a large temperature range in both Pyr14-TFSI and Pmim-TFSI, making it possible to test the shoving model. This test is in keeping with the tradition in our research group but also serves to investigate if RTILs have dynamics similar to those of non-associated molecular liquids. It showed that the shoving model to a large extent can predict the viscous slowing down of the alpha relaxation in these two ionic liquids. This, once again, showed a behavior remarkably like that of non-associated molecular liquids, despite the presence of a slow mode in Pmim-BF₄.

Keeping in mind that it is often not possible to make general conclusions for all RTILs based on results from a few, it would be interesting to test the shoving model on more ionic liquids with, for example, large differences in fragility. If the shoving model prediction still holds, it would then be possible to at least make general assumptions independent of fragility of the ionic liquids.

Final conclusion The ionic liquids Pyr14-TFSI, Pyr16-TFSI and Pyr18-TFSI have dynamics resembling those of non-associated molecular liquids since: There is an alpha and a beta relaxation, the alpha relaxation obeys TTS, the real part of the fluidity follows the random barrier model prediction around the alpha relaxation, there is no slow mode and the temperature dependence of the alpha relaxation follows the shoving model prediction (only for Pyr14-TFSI).

For Pyr18-TFSI mixed with $x = 0.2$ and $x = 0.4$ molar fraction of Li-TFSI, these points also apply except that there is a slow mode in the shear modulus. Consequently, the addition of Li-salt in Pyr18-TFSI makes these ionic liquids resemble more that of monohydroxy alcohols and other hydrogen-bonding liquids. This is also true for Pmim-BF₄, which is shown to follow the shoving model prediction well, indicating that this test of the shoving model is robust with regards to slow modes. Furthermore, the fact that the charges in the ionic liquids account for a large part of the high viscosity, illustrates that viscosity is fundamentally different from that of non-associated molecular liquids.

It was also suggested in the introduction to investigate the degree of simplicity in the ionic liquids when increasing the complexity in the microscopic structure. The latter happens by increasing the alkyl chain length of the cation and by introducing Li-salt. It is found that the degree of simplicity in the three neat, pyrrolidinium-based ionic liquids is independent of alkyl chain length. For the ionic liquids mixed with Li-salt there is, however, a small increase in the degree of complexity.

None of the ionic liquids exhibit what is defined as simple behavior, which is seen in, for example, the molecular liquid DC704. There is, however, some degree of simplicity seen as TTS of the alpha relaxation, spectral shape simplicity around the alpha relaxation, as tested with the random barrier model, and a relatively low temperature dependence of the time-scale index. This indicates that RTILs are not fundamentally different from non-associated molecular liquids and consequently it supports the idea that it is possible to develop a simple, "zeroth-order approximation" theory. Or, in other words, an ideal gas law for supercooled liquids. This theory should be able to describe the simple behavior of the alpha relaxation as the fundamental phenomenology in the viscous slowing down of glass-forming liquids and the glass transition.

Complexities like the beta relaxation could then be added to this "zeroth-order approximation" theory as additional terms. The beta relaxation being a complication added to the alpha relaxation and thus "destroying" the simple behavior is hinted in the results of this thesis, but the hypothesis needs to be tested more extensively and quantitatively in future work.

Bibliography

- [1] G. P. JOHARI and D. PYKE, “On the glassy and supercooled liquid states of a common medicament: Aspirin,” *Physical chemistry chemical physics : PCCP*, vol. 2, no. 23, pp. 5479–5484, 2000.
- [2] J. C. Dyre, “Colloquium: The glass transition and elastic models of glass-forming liquids,” *Reviews of Modern Physics*, vol. 78, no. 3, pp. 953–972, 2006.
- [3] P. W. Anderson, “Through the glass lightly,” *Science (American Association for the Advancement of Science)*, vol. 267, no. 5204, pp. 1609–1618, 1995.
- [4] K. Niss and T. Hecksher, “Perspective: Searching for simplicity rather than universality in glass-forming liquids,” *The Journal of Chemical Physics*, vol. 149, no. 23, 2018.
- [5] L. Berthier and G. Biroli, “Theoretical perspective on the glass transition and amorphous materials,” *Reviews of modern physics*, vol. 83, no. 2, pp. 587–645, 2011.
- [6] M. D. Ediger and P. Harrowell, “Perspective: Supercooled liquids and glasses,” *The Journal of chemical physics*, vol. 137, no. 8, pp. 080901–080901, 2012.
- [7] C. A. Angell, *Strong and fragile liquids*. National Technical Information Service, U.S. Department of Commerce, Springfield, 1985.
- [8] R. Böhmer and C. A. Angell, “Correlations of the nonexponentiality and state dependence of mechanical relaxations with bond connectivity in gas-se supercooled liquids,” *Physical review. B, Condensed matter*, vol. 45, no. 17, pp. 10091–10094, 1992.
- [9] R. Böhmer, K. L. Ngai, C. A. Angell, and D. J. Plazek, “Nonexponential relaxations in strong and fragile glass formers,” *The Journal of chemical physics*, vol. 99, no. 5, pp. 4201–4209, 1993.
- [10] J. C. Dyre, N. B. Olsen, and T. Christensen, “Local elastic expansion model for viscous-flow activation energies of glass-forming molecular liquids,” *Phys. Rev. B*, vol. 53, pp. 2171–2174, Feb 1996.

-
- [11] H. W. Hansen, B. Frick, T. Hecksher, J. C. Dyre, and K. Niss, "Connection between fragility, mean-squared displacement, and shear modulus in two van der Waals bonded glass-forming liquids," *Phys. Rev. B*, vol. 95, p. 104202, 2017.
- [12] H. W. Hansen, *Dynamics of glass-forming liquids: Will theory and experiment ever meet?* PhD thesis, Roskilde University, 2018.
- [13] C. M. Roland, S. Hensel-Bielowka, M. Paluch, and R. Casalini, "Supercooled dynamics of glass-forming liquids and polymers under hydrostatic pressure," *Reports on progress in physics*, vol. 68, no. 6, pp. 1405–1478, 2005.
- [14] P. G. Wolynes and V. Lubchenko, *Dielectric Spectroscopy of Glassy Dynamics*. United States: Wiley, 2012.
- [15] G. P. Johari and M. Goldstein, "Viscous liquids and the glass transition. ii. secondary relaxations in glasses of rigid molecules," *The Journal of chemical physics*, vol. 53, no. 6, pp. 2372–2388, 1970.
- [16] B. Jakobsen, K. Niss, C. Maggi, N. B. Olsen, T. Christensen, and J. C. Dyre, "Beta relaxation in the shear mechanics of viscous liquids: Phenomenology and network modeling of the alpha-beta merging region," *J. Non-Cryst. Solids*, vol. 357, p. 267, 2011.
- [17] J. D. J. D. Ferry, *Viscoelastic properties of polymers*. New York: Wiley, 3. ed. ed., 1980.
- [18] C. Gainaru, R. Figuli, T. Hecksher, B. Jakobsen, J. C. Dyre, M. Wilhelm, and R. Böhmer, "Shear-modulus investigations of monohydroxy alcohols: Evidence for a short-chain-polymer rheological response," *Phys. Rev. Lett.*, vol. 112, p. 098301, Mar 2014.
- [19] T. Hecksher and B. Jakobsen, "Communication: Supramolecular structures in monohydroxy alcohols: insights from shear-mechanical studies of a systematic series of octanol structural isomers," *The Journal of chemical physics*, vol. 141, no. 10, pp. 101104–101104, 2014.
- [20] K. Adrjanowicz, B. Jakobsen, T. Hecksher, K. Kaminski, M. Dulski, M. Paluch, and K. Niss, "Communication: Slow supramolecular mode in amine and thiol derivatives of 2-ethyl-1-hexanol revealed by combined dielectric and shear-mechanical studies," *The Journal of Chemical Physics*, vol. 143, no. 18, p. 181102, 2015.
- [21] M. H. Jensen, C. Gainaru, C. Alba-Simionesco, T. Hecksher, and K. Niss, "Slow rheological mode in glycerol and glycerol–water mixtures," *Phys. Chem. Chem. Phys.*, vol. 20, pp. 1716–1723, 2018.

-
- [22] T. Schröder and J. C. Dyre, “Simplicity of condensed matter at its core: Generic definition of a roskilde-simple system,” *The Journal of Chemical Physics*, vol. 141, p. 204502, 2014.
- [23] U. R. Pedersen, N. Gnan, N. P. Bailey, T. B. Schröder, and J. C. Dyre, “Strongly correlating liquids and their isomorphs,” *Journal of non-crystalline solids*, vol. 357, no. 2, pp. 320–328, 2011.
- [24] S. P. Bierwirth, R. Böhmer, and C. Gainaru, “Generic primary mechanical response of viscous liquids,” *Physical review letters*, vol. 119, no. 24, pp. 248001–248001, 2017.
- [25] C. Gainaru, “Spectral shape simplicity of viscous materials,” *Physical review. E*, vol. 100, no. 2, 2019.
- [26] J. C. Dyre, “A simple model of ac hopping conductivity in disordered solids,” *Physics letters. A*, vol. 108, no. 9, pp. 457–461, 1985.
- [27] J. Dyre, “The random free-energy barrier model for ac conduction in disordered solids,” *Journal of applied physics*, vol. 64, no. 5, pp. 2456–2468, 1988.
- [28] T. Schröder and J. C. Dyre, “Ac hopping conduction at extreme disorder takes place on the percolating cluster,” 2008.
- [29] J. R. Sangoro and F. Kremer, “Charge transport and glassy dynamics in ionic liquids,” *Accounts of chemical research*, vol. 45, no. 4, pp. 525–532, 2012.
- [30] M. Paluch, *Dielectric Properties of Ionic Liquids*. Advances in Dielectrics, Cham: Springer International Publishing AG, 2016.
- [31] T. Cosby, Z. Vicars, Y. Wang, and J. Sangoro, “Dynamic-mechanical and dielectric evidence of long-lived mesoscale organization in ionic liquids,” *J. Phys. Chem. Lett.*, vol. 8, no. 15, pp. 3544–3548, 2017. PMID: 28715220.
- [32] B. Jakobsen, T. Hecksher, T. E. Christensen, N. B. Olsen, J. C. Dyre, and K. Niss, “Identical temperature dependence of the time scales of several linear-response functions of two glass-forming liquids,” *Journal of Chemical Physics*, vol. 136, p. 081102, 2012.
- [33] L. A. Roed, J. C. Dyre, K. Niss, T. Hecksher, and B. Riechers, “Time-scale ordering in hydrogen- and van der waals-bonded liquids,” *The Journal of chemical physics*, vol. 154, no. 18, pp. 184508–184508, 2021.
- [34] C. M. Roland, S. Bair, and R. Casalini, “Thermodynamic scaling of the viscosity of van der waals, h-bonded, and ionic liquids,” *The Journal of chemical physics*, vol. 125, no. 12, pp. 124508–124508–8, 2006.

- [35] F. Kremer and A. Schönhal, eds., *Broadband dielectric spectroscopy*. Berlin: Springer, 2003.
- [36] B. B. Lautrup, *Physics of continuous matter : exotic and everyday phenomena in the macroscopic world*. Boca Raton, Fla: CRC Press, 2nd ed. ed., 2011.
- [37] G. Harrison, *The Dynamic Properties of Supercooled Liquids*. Academic Press, 1976.
- [38] D. W. Davidson and R. H. Cole, “Dielectric relaxation in glycerine,” *The Journal of chemical physics*, vol. 18, no. 10, pp. 1417–1417, 1950.
- [39] C. Gainaru, M. Wikarek, S. Pawlus, M. Paluch, R. Figuli, M. Wilhelm, T. Hecksher, B. Jakobsen, J. C. Dyre, and R. Böhmer, “Oscillatory shear and high-pressure dielectric study of 5-methyl-3-heptanol,” *Colloid and polymer science*, vol. 292, no. 8, pp. 1913–1921, 2014.
- [40] T. Christensen and N. B. Olsen, “A rheometer for the measurement of a high shear modulus covering more than seven decades of frequency below 50 khz,” *Review of Scientific Instruments*, vol. 66, no. 10, pp. 5019–5031, 1995.
- [41] T. Hecksher, *Relaxation in supercooled liquids. Linear and Nonlinear, Mechanical and Dielectric Studies of Molecular Liquids*. PhD thesis, Roskilde University, 2011.
- [42] M. Mikkelsen, K. L. Eliassen, N. Lindemann, K. Moch, R. Böhmer, H. A. Karimi-Varzaneh, J. Lacayo-Pineda, B. Jakobsen, K. Niss, T. Christensen, and T. Hecksher, “Piezo-electric shear rheometry: Further developments in experimental implementation and data extraction,” *arXiv.org*, 2022.
- [43] K. F. Riley and M. P. Hobson, *Essential mathematical methods for the physical sciences*. Cambridge: Cambridge University Press, 2011.
- [44] V. S. Ryaben’kii and S. V. Tsynkov, *A Theoretical Introduction to Numerical Analysis*. Boca Raton: Chapman & Hall, 1. ed., 2007.
- [45] N. V. Pogodina, M. Nowak, J. Läger, C. O. Klein, M. Wilhelm, and C. Friedrich, “Molecular dynamics of ionic liquids as probed by rheology,” *Journal of Rheology*, vol. 55, p. 241, 2011.
- [46] M. Wübbenhorst, E. M. van Koten, J. C. Jansen, W. Mijs, and J. van Turnhout, “Dielectric relaxation spectroscopy of amorphous and liquid-crystalline side-chain polycarbonates,” *Macromolecules Rapid Communications*, vol. 18, pp. 139–147, 1997.
- [47] M. Wübbenhorst and J. van Turnhout, “Analysis of complex dielectric spectra. i. one-dimensional derivative techniques and three-dimensional modelling,” *Journal of non-crystalline solids*, vol. 305, no. 1, pp. 40–49, 2002.

- [48] B. Igarashi, T. Christensen, E. H. Larsen, N. B. Olsen, I. H. Pedersen, T. Rasmussen, and J. C. Dyre, "A cryostat and temperature control system optimized for measuring relaxations of glass-forming liquids," *Review of Scientific Instruments*, vol. 79, no. 4, p. 045105, 2008.
- [49] B. Igarashi, T. Christensen, E. H. Larsen, N. B. Olsen, I. H. Pedersen, T. Rasmussen, and J. C. Dyre, "An impedance-measurement setup optimized for measuring relaxations of glass-forming liquids," *Review of Scientific Instruments*, vol. 79, no. 4, p. 045106, 2008.
- [50] G. L. Squires, *Introduction to the Theory of Thermal Neutron Scattering*. Cambridge: Cambridge University Press, 2012.
- [51] S. W. Lovesey, *Theory of neutron scattering from condensed matter*. International series of monographs on physics ; [72]., Oxford: Clarendon, 1984.
- [52] C. Kittel, *Introduction to solid state physics*. New York: Wiley, 8. ed. ed., 2005.
- [53] K. Niss, *Fast and slow dynamics of glass-forming liquids. What can we learn from high pressure experiments?* PhD thesis, Université Paris, 2007.
- [54] A. R. Shah, R. R. C. Shutt, K. Smith, J. Hack, T. P. Neville, T. F. Headen, D. J. L. Brett, C. A. Howard, T. S. Miller, and P. L. Cullen, "Neutron studies of na-ion battery materials," *JPhys Materials*, vol. 4, no. 4, pp. 42008–, 2021.
- [55] H. Maier-Leibnitz, "Grundlagen für die beurteilung von intensitäts- und genauigkeitsfragen bei neutronenstremessungen," *Nukleonik*, vol. 8, p. 61, 1966.
- [56] B. Frick, E. Mamontov, L. v. Eijck, and T. Seydel, "Recent backscattering instrument developments at the ill and sns," *Zeitschrift für physikalische Chemie (Neue Folge)*, vol. 224, no. 1, pp. 33–60, 2010.
- [57] J. Robinson and R. A. Osteryoung, "An electrochemical and spectroscopic study of some aromatic hydrocarbons in the room temperature molten salt system aluminum chloride-n-butylpyridinium chloride," *Journal of the American Chemical Society*, vol. 101, p. 323È27, 1979.
- [58] J. S. Wilkes, J. A. Levisky, R. A. Wilson, and C. L. Hussey, "Dialkylimidazolium chloroaluminate melts: A new class of room-temperature ionic liquids for electrochemistry, spectroscopy, and synthesis," *Inorganic Chemistry*, vol. 21, pp. 1263–1264, 1982.
- [59] J. R. Sanders, E. H. Ward, , and C. L. Husse, "Aluminum bromide-1-methyl-3-ethylimidazolium bromide ionic liquids. i. densities, viscosities, electrical conductivities, and phase transitions," *Journal of The Electrochemical Society*, 1986.

- [60] D. R. MacFarlane, M. Kar, and J. M. Pringle, *Fundamentals of ionic liquids: from chemistry to applications*. Newark: Wiley-VCH, 1st ed. ed., 2017.
- [61] Y. Shimizu, Y. Ohte, Y. Yamamura, and K. Saito, “Is the liquid or the solid phase responsible for the low melting points of ionic liquids? alkyl-chain-length dependence of thermodynamic properties of [c n mim][tf 2n],” *Chemical physics letters*, vol. 470, no. 4, pp. 295–299, 2009.
- [62] C. Cruz and A. Ciach, “Phase transitions and electrochemical properties of ionic liquids and ionic liquid—solvent mixtures,” *Molecules (Basel, Switzerland)*, vol. 26, no. 12, pp. 3668–, 2021.
- [63] J. C. Araque, J. J. Hettige, and C. J. Margulis, “Modern room temperature ionic liquids, a simple guide to understanding their structure and how it may relate to dynamics,” *The journal of physical chemistry. B*, vol. 119, no. 40, pp. 12727–12740, 2015.
- [64] E. W. Castner and J. F. Wishart, “Spotlight on ionic liquids,” *The Journal of chemical physics*, vol. 132, no. 12, pp. 120901–120901–9, 2010.
- [65] A. Triolo, O. Russina, H.-J. Bleif, and E. Di Cola, “Nanoscale segregation in room temperature ionic liquids,” *The journal of physical chemistry. B*, vol. 111, no. 18, pp. 4641–4644, 2007.
- [66] A. Triolo, O. Russina, B. Fazio, G. B. Appetecchi, M. Carewska, and S. Passerini, “Nanoscale organization in piperidinium-based room temperature ionic liquids,” *The Journal of Chemical Physics*, vol. 130, no. 16, p. 164521, 2009.
- [67] O. Russina, A. Triolo, L. Gontrani, and R. Caminiti, “Mesoscopic structural heterogeneities in room-temperature ionic liquids,” *The journal of physical chemistry letters*, vol. 3, no. 1, pp. 27–33, 2012.
- [68] L. Song, B. J. Leobardo, G. Jianchang, A. Lawrence, R. Gernot, S. R. W, H. P. C, D. Sheng, B. G. A, and C. P. T, “Alkyl chain length and temperature effects on structural properties of pyrrolidinium-based ionic liquids: A combined atomistic simulation and small-angle x-ray scattering study,” *The journal of physical chemistry letters*, vol. 3, no. 1, pp. 125–130, 2012.
- [69] L. Aguilera, J. Vlkner, A. Labrador, and A. Matic, “The effect of lithium salt doping on the nanostructure of ionic liquids,” *Physical Chemistry Chemical Physics*, vol. 17, no. 40, pp. 27082–27087, 2015.
- [70] A. Martinelli, A. Matic, P. Jacobsson, L. Börjesson, A. Fericola, and B. Scrosati, “Phase behavior and ionic conductivity in lithium bis(trifluoromethanesulfonyl)imide-doped ionic liquids of the pyrrolidinium

- cation and bis(trifluoromethanesulfonyl)imide anion.," *The journal of physical chemistry. B*, vol. 113, no. 32, pp. 11247–11251, 2009.
- [71] M. Kunze, S. Jeong, E. Paillard, M. Schonhoff, M. Winter, and S. Passerini, "New insights to self-aggregation in ionic liquid electrolytes for high-energy electrochemical devices," *Advanced Energy Materials*, vol. 1, no. 2, pp. 274–281, 2011.
- [72] K. R. Harris, L. A. Woolf, M. Kanakubo, and T. R  ther, "Transport properties of N-butyl-N-methylpyrrolidinium bis(trifluoromethylsulfonyl)amide," *Journal of Chemical & Engineering Data*, vol. 56, no. 12, pp. 4672–4685, 2011.
- [73] F. M. Vitucci, D. Manzo, M. A. Navarra, O. Palumbo, F. Trequatrini, S. Panero, P. Bruni, F. Croce, and A. Paolone, "Low-temperature phase transitions of 1-butyl-1-methylpyrrolidinium bis(trifluoromethanesulfonyl)imide swelling a polyvinylidene fluoride electrospun membrane," *The Journal of Physical Chemistry C*, vol. 118, no. 11, pp. 5749–5755, 2014.
- [74] K. R. Harris and M. Kanakubo, "Self-diffusion, velocity cross-correlation, distinct diffusion and resistance coefficients of the ionic liquid [bmim][tf2n] at high pressure," *Phys. Chem. Chem. Phys.*, vol. 17, pp. 23977–23993, 2015.
- [75] H. W. Hansen, F. Lundin, K. Adrjanowicz, B. Frick, A. Matic, and K. Niss, "Density scaling of structure and dynamics of an ionic liquid," *Phys. Chem. Chem. Phys.*, vol. 22, p. 14169, 2020.
- [76] E. Zorebski, M. Zorebski, M. Dzida, P. Goodrich, and J. Jacquemin, "Iso-baric and isochoric heat capacities of imidazolium-based and pyrrolidinium-based ionic liquids as a function of temperature: Modeling of isobaric heat capacity," *Industrial & engineering chemistry research*, vol. 56, no. 9, pp. 2592–2606, 2017.
- [77] R. Ge, C. Hardacre, J. Jacquemin, P. Nancarrow, and D. W. Rooney, "Heat capacities of ionic liquids as a function of temperature at 0.1 mpa. measurement and prediction," *Journal of chemical and engineering data*, vol. 53, no. 9, pp. 2148–2153, 2008.
- [78] E. W. Castner, J. F. Wishart, and H. Shirota, "Intermolecular dynamics, interactions, and solvation in ionic liquids," *Accounts of chemical research*, vol. 40, no. 11, pp. 1217–1227, 2007.
- [79] H. Shirota, A. M. Funston, J. F. Wishart, and E. W. Castner, Jr, "Ultrafast dynamics of pyrrolidinium cation ionic liquids," *The Journal of chemical physics*, vol. 122, no. 18, pp. 184512–184512, 2005.

- [80] W. Tu, G. Szklarz, K. Adrjanowicz, K. Grzybowska, J. Knapik-Kowalczyk, and M. Paluch, "Effect of cation n-alkyl side-chain length, temperature, and pressure on the glass-transition dynamics and crystallization tendency of the [c n c1pyrr]+[tf2n]- ionic liquid family," *Journal of physical chemistry. C*, vol. 123, no. 20, pp. 12623–12637, 2019.
- [81] F. Lundin, H. W. Hansen, K. Adrjanowicz, B. Frick, D. Rauber, R. Hempelmann, O. Shebanova, K. Niss, and A. Matic, "Pressure and temperature dependence of local structure and dynamics in an ionic liquid," *Journal of Physical Chemistry B*, vol. 8, 2021.
- [82] H. Jin, B. O'Hare, J. Dong, S. Arzhantsev, G. A. Baker, J. F. Wishart, A. J. Benesi, and M. Maroncelli, "Physical properties of ionic liquids consisting of the 1-butyl-3-methylimidazolium cation with various anions and the bis(trifluoromethylsulfonyl)imide anion with various cations," *The journal of physical chemistry. B*, vol. 115, no. 5, pp. 1333–1333, 2011.
- [83] C. S. Santos, N. S. Murthy, G. A. Baker, and E. W. Castner, "Communication: X-ray scattering from ionic liquids with pyrrolidinium cations," *The Journal of chemical physics*, vol. 134, no. 12, pp. 121101–121101-4, 2011.
- [84] F. Pabst, Z. Wojnarowska, M. Paluch, and T. Blochowicz, "On the temperature and pressure dependence of dielectric relaxation processes in ionic liquids," *Physical chemistry chemical physics : PCCP*, vol. 23, no. 26, pp. 1426–14275, 2021.
- [85] T. Nishida, Y. Tashiro, and M. Yamamoto, "Physical and electrochemical properties of 1-alkyl-3-methylimidazolium tetrafluoroborate for electrolyte," *Journal of fluorine chemistry*, vol. 120, no. 2, pp. 135–141, 2003.
- [86] F. Pabst, J. Gabriel, and T. Blochowicz, "Mesoscale aggregates and dynamic asymmetry in ionic liquids: Evidence from depolarized dynamic light scattering," *The journal of physical chemistry letters*, vol. 10, no. 9, pp. 2130–2134, 2019.
- [87] J. Pitawala, J.-K. Kim, P. Jacobsson, V. Koch, F. Croce, and A. Matic, "Phase behaviour, transport properties, and interactions in li-salt doped ionic liquids," *Faraday Discuss.*, vol. 154, pp. 71–80, 2012.
- [88] F. Philippi, D. Rauber, K. L. Eliassen, N. Bouscharain, K. Niss, C. W. M. Kay, and T. Welton, "Pressing matter: why are ionic liquids so viscous?," *Chemical science (Cambridge)*, vol. 13, no. 9, pp. 2735–2743, 2022.
- [89] A. Matic and B. Scrosati, "Ionic liquids for energy applications," *MRS bulletin*, vol. 38, no. 7, pp. 533–537, 2013.
- [90] W. D. Amith, J. C. Araque, and C. J. Margulis, "A pictorial view of viscosity in ionic liquids and the link to nanostructural heterogeneity," *The journal of physical chemistry letters*, vol. 11, no. 6, pp. 2062–2066, 2020.

- [91] T. Yamaguchi, “Coupling between the mesoscopic dynamics and shear stress of a room-temperature ionic liquid,” *Physical chemistry chemical physics : PCCP*, vol. 2, no. 26, pp. 1789–17817, 2018.
- [92] W. D. Amith, J. C. Araque, and C. J. Margulis, “Relationship between the relaxation of ionic liquid structural motifs and that of the shear viscosity,” *The journal of physical chemistry. B*, vol. 125, no. 23, pp. 6264–6271, 2021.
- [93] A. F. Bouarab, J.-P. Harvey, and C. Robelin, “Viscosity models for ionic liquids and their mixtures,” *Physical chemistry chemical physics : PCCP*, vol. 23, no. 2, pp. 733–752, 2021.
- [94] S. Cheng, Z. Wojnarowska, M. Musiał, and M. Paluch, “Correlation between configurational entropy, excess entropy, and ion dynamics in imidazolium-based ionic liquids: Test of the adam–gibbs model,” *The Journal of chemical physics*, vol. 154, no. 4, pp. 044502–044502, 2021.
- [95] K. L. Eliassen, H. W. Hansen, F. Lundin, D. Rauber, R. Hempelmann, T. Christensen, T. Hecksher, A. Matic, B. Frick, and K. Niss, “High-frequency dynamics and test of the shoving model for the glass-forming ionic liquid pyr14-tfsi,” *Physical Review Materials*, vol. 5, p. 065606, 2021.
- [96] A. P. Abbott, “Application of hole theory to the viscosity of ionic and molecular liquids,” *Chemphyschem*, vol. 5, no. 8, pp. 1242–1246, 2004.
- [97] W. A. Wakeham, J. H. Dymond, J. Millat, and C. A. N. d. Castro, *Transport Properties of Fluids: Their Correlation, Prediction and Estimation*. Cambridge University Press, 2009.
- [98] S. S. Bair, *High Pressure Rheology for Quantitative Elastohydrodynamics*. San Diego: Elsevier, 2019.
- [99] P. J. Haines, *Principles of thermal analysis and calorimetry*. RSC paperbacks, Cambridge: NBN International, 2007.
- [100] G. W. H. Höhne, W. F. Hemminger, and H.-J. Flammersheim, *Differential scanning calorimetry*. New York: Springer, 2., rev. and enl. ed. ed., 2003.
- [101] B. Jakobsen, A. Sanz, K. Niss, T. Hecksher, I. H. Pedersen, T. Rasmussen, T. Christensen, N. B. Olsen, and J. C. Dyre, “Thermalization calorimetry: A simple method for investigating glass transition and crystallization of supercooled liquids,” *AIP advances*, vol. 6, no. 5, pp. 55019–055019–16, 2016.
- [102] P. Sippel, P. Lunkenheimer, S. Krohns, E. Thoms, and A. Loidl, “Importance of liquid fragility for energy applications of ionic liquids,” *Scientific reports*, vol. 5, no. 1, pp. 13922–13922, 2015.

- [103] Y. U. Paulechka, A. V. Blokhin, and G. J. Kabo, "Evaluation of thermodynamic properties for non-crystallizable ionic liquids," *Thermochimica acta*, vol. 604, pp. 122–128, 2015.
- [104] H. Tokuda, K. Hayamizu, K. Ishii, M. A. B. H. Susan, and M. Watanabe, "Physicochemical properties and structures of room temperature ionic liquids. 2. variation of alkyl chain length in imidazolium cation," *The journal of physical chemistry. B*, vol. 109, no. 13, pp. 6103–6110, 2005.
- [105] W. Zheng, A. Mohammed, L. G. Hines, D. Xiao, O. J. Martinez, R. A. Bartsch, S. L. Simon, O. Russina, A. Triolo, and E. L. Quitevis, "Effect of cation symmetry on the morphology and physicochemical properties of imidazolium ionic liquids," *The journal of physical chemistry. B*, vol. 115, no. 20, pp. 6572–6584, 2011.
- [106] M. A. A. Rocha, C. M. S. S. Neves, M. G. Freire, O. Russina, A. Triolo, J. A. P. Coutinho, and L. M. N. B. F. Santos, "Alkylimidazolium based ionic liquids: Impact of cation symmetry on their nanoscale structural organization," *The journal of physical chemistry. B*, vol. 117, no. 37, pp. 10889–10897, 2013.
- [107] Q. Zhou, P. D. Boyle, L. Malpezzi, A. Mele, J.-H. Shin, S. Passerini, and W. A. Henderson, "Phase behavior of ionic liquid–lix mixtures: Pyrrolidinium cations and tfsi⁻ anions – linking structure to transport properties," *Chemistry of materials*, vol. 23, no. 19, pp. 4331–4337, 2011.
- [108] C. D. Tran, S. H. De Paoli Lacerda, and D. Oliveira, "Absorption of water by room-temperature ionic liquids: Effect of anions on concentration and state of water," *Applied Spectroscopy*, vol. 57, no. 2, pp. 152–157, 2003.
- [109] T. Hecksher, N. B. Olsen, and J. C. Dyre, "Model for the alpha and beta shear-mechanical properties of supercooled liquids and its comparison to squalane data," *The Journal of chemical physics*, vol. 146, no. 15, pp. 154504–154504, 2017.
- [110] M. Musiał, Z. Wojnarowska, S. Cheng, K. L. Ngai, and M. Paluch, "Evidence of a fundamental mechanism governing conductivity relaxation in room-temperature ionic liquid," *Journal of physical chemistry. C*, vol. 123, no. 36, pp. 22089–22094, 2019.
- [111] M. g. Musial, S. Cheng, Z. Wojnarowska, B. Yao, K. Jurkiewicz, and M. Paluch, "Thorough studies of tricyanomethanide-based ionic liquids - the influence of alkyl chain length of the cation," *Soft matter*, vol. 16, no. 41, pp. 9479–9487, 2020.
- [112] P. Griffin, A. L. Agapov, A. Kisliuk, X.-G. Sun, S. Dai, V. N. Novikov, and A. P. Sokolov, "Decoupling charge transport from the structural dynamics in room temperature ionic liquids," *The Journal of chemical physics*, vol. 135, no. 11, pp. 114509–114509–8, 2011.

- [113] J. R. Sangoro, C. IACOB, A. SERGHEI, C. FRIEDRICH, and F. KREMER, “Universal scaling of charge transport in glass-forming ionic liquids,” *Physical chemistry chemical physics : PCCP*, vol. 11, no. 6, pp. 913–916, 2009.
- [114] R. Zorn, F. I. Mopsik, G. B. McKenna, L. Willner, and D. Richter, “Dynamics of polybutadienes with different microstructures. 2. dielectric response and comparisons with rheological behavior,” *The Journal of chemical physics*, vol. 107, no. 9, pp. 3645–3655, 1997.
- [115] A. Rivera and E. A. Roessler, “Evidence of secondary relaxations in the dielectric spectra of ionic liquids,” *arXiv.org*, 2005.
- [116] H.-J. Kwon, J.-A. Seo, T. Iwahashi, Y. Ouchi, D. Kim, H. K. Kim, and Y.-H. Hwang, “Study of alkyl chain length dependent characteristics of imidazolium based ionic liquids [nmim]+[tfsa]– by brillouin and dielectric loss spectroscopy,” *Current applied physics*, vol. 13, no. 1, pp. 271–279, 2013.
- [117] P. J. Griffin, A. P. Holt, K. Tsunashima, J. R. Sangoro, F. Kremer, and A. P. Sokolov, “Ion transport and structural dynamics in homologous ammonium and phosphonium-based room temperature ionic liquids,” *The Journal of chemical physics*, vol. 142, no. 8, pp. 084501–084501, 2015.
- [118] P. J. Griffin, Y. Wang, A. P. Holt, and A. P. Sokolov, “Communication: Influence of nanophase segregation on ion transport in room temperature ionic liquids,” *The Journal of chemical physics*, vol. 144, no. 15, pp. 151104–151104, 2016.
- [119] G. P. Johari, “Glass transition and secondary relaxations in molecular liquids and crystals,” *Annals of the New York Academy of Sciences*, vol. 279, no. 1, pp. 117–140, 1976.
- [120] L. Aguilera, J. Scheers, and A. Matic, “Enhanced low-temperature ionic conductivity via different li + solvated clusters in organic solvent/ionic liquid mixed electrolytes,” *Physical chemistry chemical physics : PCCP*, vol. 18, no. 36, pp. 25458–25464, 2016.
- [121] H. K. Kashyap, J. J. Hettige, H. V. R. Annapureddy, and C. J. Margulis, “Saxs anti-peaks reveal the length-scales of dual positive-negative and polar-apolar ordering in room-temperature ionic liquids,” *Chemical communications (Cambridge, England)*, vol. 48, no. 42, pp. 5103–5105, 2012.
- [122] K. Shimizu, C. E. S. Bernardes, and J. N. Canongia Lopes, “Structure and aggregation in the 1-alkyl-3-methylimidazolium bis(trifluoromethylsulfonyl)imide ionic liquid homologous series,” *The journal of physical chemistry. B*, vol. 118, no. 2, pp. 567–576, 2014.

- [123] D. A. Turton, J. Hunger, A. Stoppa, G. Hefter, A. Thoman, M. Walther, R. Buchner, and K. Wynne, "Dynamics of imidazolium ionic liquids from a combined dielectric relaxation and optical kerr effect study: Evidence for mesoscopic aggregation," *Journal of the American Chemical Society*, vol. 131, no. 31, pp. 11140–11146, 2009.
- [124] T. Sonnleitner, D. A. Turton, S. Waselikowski, J. Hunger, A. Stoppa, M. Walther, K. Wynne, and R. Buchner, "Dynamics of rtils: A comparative dielectric and oke study," *Journal of molecular liquids*, vol. 192, pp. 19–25, 2014.
- [125] R. Tao and S. L. Simon, "Rheology of imidazolium-based ionic liquids with aromatic functionality," *The journal of physical chemistry. B*, vol. 119, no. 35, pp. 11953–11959, 2015.
- [126] P. J. Griffin, A. P. Holt, Y. Wang, V. N. Novikov, J. R. Sangoro, F. Kremer, and A. P. Sokolov, "Interplay between hydrophobic aggregation and charge transport in the ionic liquid methyltrioctylammonium bis(trifluoromethylsulfonyl)imide," *The journal of physical chemistry. B*, vol. 118, no. 3, pp. 783–790, 2014.
- [127] T. Cosby, M. J. Schnabel, D. P. Durkin, R. A. Mantz, and P. C. Trulove, "Ion dynamics and transport properties of lewis-acidic imidazolium chloroaluminate ionic liquids," *Journal of Electrochemical Society*, vol. 168, p. 066515, 2021.
- [128] T. Cosby, Z. Vicars, M. Heres, K. Tsunashima, and J. Sangoro, "Dynamic and structural evidence of mesoscopic aggregation in phosphonium ionic liquids," *The Journal of chemical physics*, vol. 148, no. 19, pp. 193815–193815, 2018.
- [129] C. Tanford, *The hydrophobic effect : formation of micelles and biological membranes*. 'A Wiley-Interscience Publication., New York: Wiley, 2. ed. ed., 1980.
- [130] T. Cosby, U. Kapoor, J. K. Shah, and J. Sangoro, "Mesoscale organization and dynamics in binary ionic liquid mixtures," *The journal of physical chemistry letters*, vol. 10, no. 20, pp. 6274–6280, 2019.
- [131] T. Hecksher, N. B. Olsen, K. A. Nelson, J. C. Dyre, and T. Christensen, "Mechanical spectra of glass-forming liquids. i. low-frequency bulk and shear moduli of dc704 and 5-ppe measured by piezoceramic transducers," *The Journal of Chemical Physics*, vol. 138, no. 12, p. 12A543, 2013.
- [132] B. Jakobsen, K. Niss, and N. B. Olsen, "Dielectric and shear mechanical alpha and beta relaxations in seven glass-forming liquids," *J. Chem. Phys.*, vol. 123, p. 234511, 2005.

- [133] J. C. Dyre and T. B. Schrøder, “Universality of ac conduction in disordered solids,” *Reviews of modern physics*, vol. 72, no. 3, pp. 873–892, 2000.
- [134] T. Schrøder and J. Dyre, “Computer simulations of the random barrier model,” 2002.
- [135] J. C. Dyre, P. Maass, B. Roling, and D. L. Sidebottom, “Fundamental questions relating to ion conduction in disordered solids,” *Reports on progress in physics*, vol. 72, no. 4, pp. 046501–046501 (15), 2009.
- [136] T. B. Schrøder and J. C. Dyre, “Solid-like mean-square displacement in glass-forming liquids,” *The Journal of chemical physics*, vol. 152, no. 14, pp. 141101–141101, 2020.
- [137] J. R. Sangoro, A. Serghei, S. Naumov, P. Galvosas, J. Kärger, C. Wesppe, F. Bordusa, and F. Kremer, “Charge transport and mass transport in imidazolium-based ionic liquids,” *Physical review. E, Statistical, nonlinear, and soft matter physics*, vol. 77, no. 5 Pt 1, pp. 051202–051202, 2008.
- [138] C. Gainaru, E. W. Stacy, V. Bocharova, M. Gobet, A. P. Holt, T. Saito, S. Greenbaum, and A. P. Sokolov, “Mechanism of conductivity relaxation in liquid and polymeric electrolytes: Direct link between conductivity and diffusivity,” *The journal of physical chemistry. B*, vol. 120, no. 42, pp. 11074–11083, 2016.
- [139] J. R. Sangoro, C. Iacob, S. Naumov, R. Valiullin, H. Rexhausen, J. Hunger, R. Buchner, V. Strehmel, J. Kärger, and F. Kremer, “Diffusion in ionic liquids: the interplay between molecular structure and dynamics,” *Soft matter*, vol. 7, no. 5, pp. 1678–1681, 2011.
- [140] A. SANTIC, W. WROBEL, M. MUTKE, R. D. BANHATTI, and K. FUNKE, “Frequency-dependent fluidity and conductivity of an ionic liquid,” *Physical chemistry chemical physics : PCCP*, vol. 11, no. 28, pp. 5930–5934, 2009.
- [141] D. Richard, M. Ferrand, and G. J. Kearley, “Analysis and visualisation of neutron-scattering data,” *Journal of neutron research*, vol. 4, no. 1, pp. 33–39, 1996.
- [142] B. Frick, J. Combet, and L. van Eijck, “New possibilities with inelastic fixed window scans and linear motor doppler drives on high resolution neutron backscattering spectrometers,” *Nuclear instruments & methods in physics research. Section A, Accelerators, spectrometers, detectors and associated equipment*, vol. 669, pp. 7–13, 2012.
- [143] M. Busch, T. Hofmann, B. Frick, J. P. Embs, B. Dyatkin, and P. Huber, “Ionic liquid dynamics in nanoporous carbon: A pore-size- and temperature-dependent neutron spectroscopy study on supercapacitor materials,” 2020.

- [144] T. Burankova, G. Simeoni, R. Hempelmann, J. F. Mora Cardozo, and J. P. Embs, “Dynamic heterogeneity and flexibility of the alkyl chain in pyridinium-based ionic liquids,” *The journal of physical chemistry. B*, vol. 121, no. 1, pp. 240–249, 2017.
- [145] T. Burankova, E. Reichert, V. Fossog, R. Hempelmann, and J. P. Embs, “The dynamics of cations in pyridinium-based ionic liquids by means of quasielastic- and inelastic neutron scattering,” *Journal of molecular liquids*, vol. 192, pp. 199–207, 2014.
- [146] A. Rahman, K. S. Singwi, and A. Sjölander, “Theory of slow neutron scattering by liquids. i,” *Physical Review*, vol. 126, no. 3, pp. 986–996, 1962.
- [147] R. Zorn, “Multiple scattering correction of neutron scattering elastic scans,” *Nuclear Inst. and Methods in Physics Research, A*, vol. 572, no. 2, pp. 874,881, 2007.
- [148] R. Zorn, “On the evaluation of neutron scattering elastic scan data,” *Nuclear Inst. and Methods in Physics Research, A*, vol. 603, no. 3, pp. 439,445, 2009.
- [149] P. Thompson, D. E. Cox, and J. B. Hastings, “Rietveld refinement of debye-scherrer synchrotron x-ray data from al₂o₃,” *Journal of Applied Crystallography*, vol. 20, pp. 79–83, 1987.
- [150] J. C. Dyre and N. B. Olsen, “Landscape equivalent of the shoving model,” *Phys. Rev. E*, vol. 69, p. 042501, Apr 2004.
- [151] C. J. Jafta, C. Bridges, L. Haupt, C. Do, P. Sippel, M. J. Cochran, S. Krohns, M. Ohl, A. Loidl, E. Mamontov, P. Lunkenheimer, S. Dai, and X.-G. Sun, “Ion dynamics in ionic-liquid-based li-ion electrolytes investigated by neutron scattering and dielectric spectroscopy,” *ChemSusChem*, vol. 11, no. 19, pp. 3512–3523, 2018.
- [152] M. Goldstein, “Viscous liquids and the glass transition: A potential energy barrier picture,” *The Journal of Chemical Physics*, vol. 51, no. 9, pp. 3728–3739, 1969.
- [153] P. G. Debenedetti and F. H. Stillinger, “Supercooled liquids and the glass transition,” *Nature (London)*, vol. 410, no. 6825, pp. 259–267, 2001.
- [154] A. Angell, “Liquid landscape,” *Nature (London)*, vol. 393, no. 6685, pp. 521–523, 1998.
- [155] T. Hecksher and J. C. Dyre, “A review of experiments testing the shoving model,” *Journal of Non-Crystalline Solids*, vol. 407, pp. 14 – 22, 2015. 7th IDMRCS: Relaxation in Complex Systems.

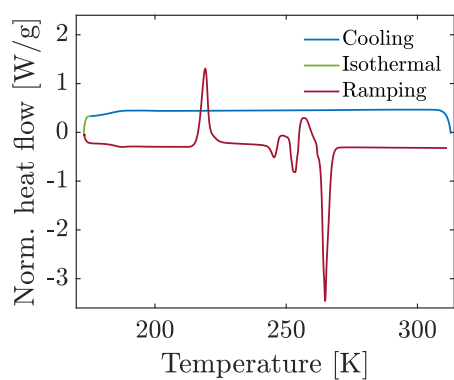
-
- [156] N. B. Olsen, T. Christensen, and J. C. Dyre, “Time-temperature superposition in viscous liquids,” *Physical review letters*, vol. 86, no. 7, pp. 1271–1274, 2001.
- [157] A. S. Pensado, A. A. H. Pádua, M. J. P. Comuñas, and J. Fernández, “Relationship between viscosity coefficients and volumetric properties using a scaling concept for molecular and ionic liquids,” *The journal of physical chemistry. B*, vol. 112, no. 18, pp. 5563–5574, 2008.
- [158] M. Paluch, S. Haracz, A. Grzybowski, M. Mierzwa, J. Pionteck, A. Rivera-Calzada, and C. Leon, “A relationship between intermolecular potential, thermodynamics, and dynamic scaling for a supercooled ionic liquid,” *The journal of physical chemistry letters*, vol. 1, no. 6, pp. 987–992, 2010.
- [159] P. A. Knudsen, K. Niss, and N. P. Bailey, “Quantifying dynamical and structural invariance in a simple molten salt model,” *The Journal of chemical physics*, vol. 155, no. 5, pp. 54506–054506, 2021.
- [160] P. Knudsen, *An Investigation of Isodynes in Coarse Grained Ionic Liquid Models*. PhD thesis, Roskilde University, 2022.
- [161] M. F. Atitar, H. Belhadj, R. Dillert, and D. W. Bahnemann, “The relevance of atr-ftir spectroscopy in semiconductor photocatalysis,” *Emerging Pollutants in the Environment*, 2015.
- [162] S. ichi Amma, J. Luo, C. G. Pantano, and S. H. Kim, “Specular reflectance (sr) and attenuated total reflectance (atr) infrared (ir) spectroscopy of transparent flat glass surfaces: A case study for soda lime float glass,” *Journal of Non-Crystalline Solids*, vol. 428, pp. 189 – 196, 2015.

Appendices

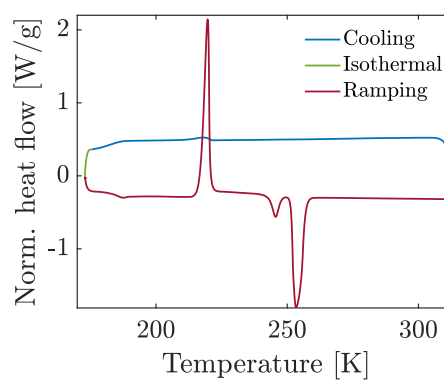
Appendix A

Calorimetric measurements

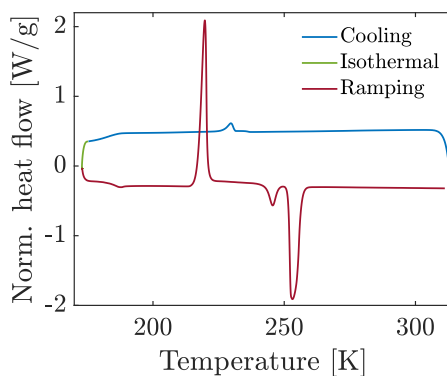
A.1 Extra results



(a)

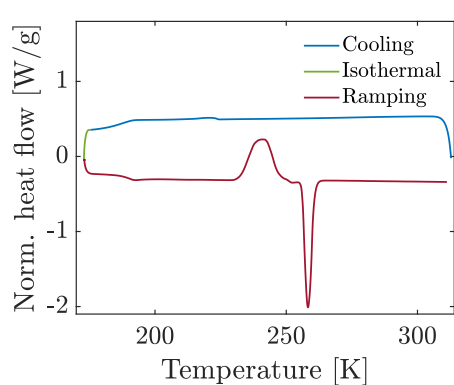


(b)

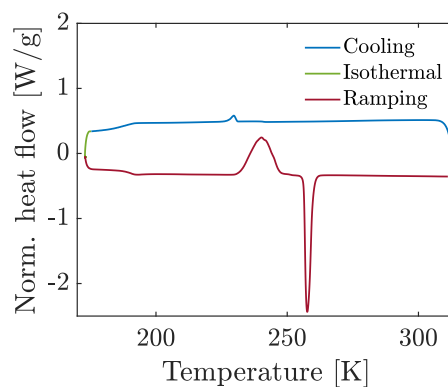


(c)

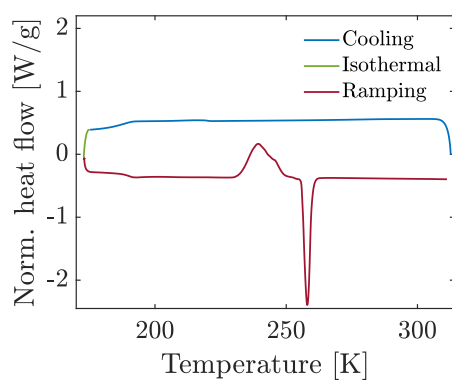
Figure A.1: DSC results for Pyr14-TFSI exposed to air for a) 1 minutes, b) 1 hour and c) 18 hours.



(a)



(b)



(c)

Figure A.2: DSC results for Pyr18-TFSI exposed to air for a) 1 minutes, b) 1 hour and c) 18 hours.

Appendix B

Water contamination

B.0.1 Water contamination

Pyr14-TFSI and Pyr18-TFSI are hydrofobic and are known to absorb water when exposed to air. This was tested to see the effect in the dynamic properties, since performing rheological experiments in sealed, inert atmosphere is not possible with the rheometer.

DSC The effect of water absorption on the mechanical properties cannot be measured directly. However, these are closely connected to the glass transition and even small changes in T_g can give large changes in dynamics. So in order to get a sense of the water content's effect on the mechanical properties, Differential Scanning Calorimetry (DSC) experiments were performed on both Pyr14-TFSI and Pyr18-TFSI.

The samples were exposed to air for 0, 5 and 60 minutes as well as 18 hours (not including time to prepare and run the experiments). However, all experiments were prepared and run the same way in order to ensure consistency. T_g was found as the midpoint in the glass transition curve (W/g as a function of T). The TA-instrument software connected to the DSC instrument automatically calculates T_g , and the calculation was repeated five times with the final T_g as an average. The result can be seen in tabel B.1 and figure B.1.

Both tabel B.1 and figure B.1 show that the change in T_g for Pyr14-TFSI is very small with a decrease of only 0.2 K from 0 to 18 hours. Furthermore, there is no clear tendency in the change, since T_g decreases 0.6 K after 5 minutes and then again increases with 0.5 K after an additional 55 minutes. For Pyr18-TFSI the change is more significant with a decrease in T_g of 1.1 K from 0 to 18 hours.

	0 min	5 min	60 min	18 hours
T_g Pyr14-TFSI	184.9 K	184.3 K	184.8 K	184.7 K
T_g Pyr18-TFSI	191.1 K	189.4 K	189.9 K	190 K

Table B.1: T_g measured with DSC and calculated as the midpoint in the glass transition.

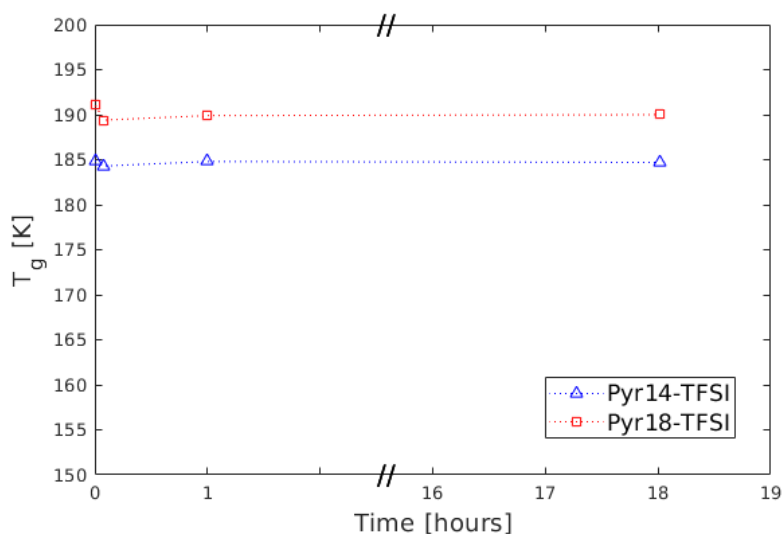


Figure B.1: A graph showing T_g for Pyr14-TFSI and Pyr18-TFSI measured with DSC after being exposed to air for 0, 0.08, 1 and 18 hours. The change in T_g is for Pyr14-TFSI very small, only 0.2 K from 0 to 18 hours. For Pyr18-TFSI the change is more significant with a change in T_g of 1.1 K from 0 to 18 hours.

However, in between we see the same effect as with Pyr14-TFSI, where T_g first decreases 1.7 K after 5 minutes and then increases 0.5 K after an additional 55 minutes. In any case, the change in T_g is still very small and within experimental uncertainties.

IR spectroscopy Infrared (IR) spectroscopy is a common method for identifying both organic and inorganic chemicals in solids, liquids and gaseous samples. The method can be used for both quantitative and qualitative analysis in order to identify molecules as well as chemical reactions in the sample. The concept behind the method is the absorption of IR light through molecular vibrational modes. This absorption due to an excitation from the ground molecular vibration to a vibration of higher energy will result in a spectra revealing information about the molecular composition of the sample [161].

Attenuated Total Reflection (ATR) spectroscopy is based upon the phenomenon of total internal reflection. A suitable internal reflection element (IRE), in this case diamond, is chosen in order to get the desired wavenumber range. For diamond that is $45000\text{-}2500\text{ cm}^{-1}$. The sample is in contact with the surface of the IRE and the IR beam is focused on the IRE with an incident angle, that ensures complete internal reflection. As the IR beam reflects one or more times on the internal surface of the IRE that is in contact with the sample, an evanescent wave with a penetration depth, d_p , is created in the sample [161]. Due to absorption of the IR light inside the sample, the final, transmitted beam will be attenuated, which is registered by the detector. The final result is a spectrum showing the absorbance, I_t/I_0 , as a function of wavenumber, where I_t and I_0 are

the transmitted and incident intensity of the IR beam [162].

The results from the ATR IR spectroscopy experiments can be seen in figure B.2 and B.3. In order to test qualitatively if water is present in the samples, a measurement with pure water was performed as a reference.

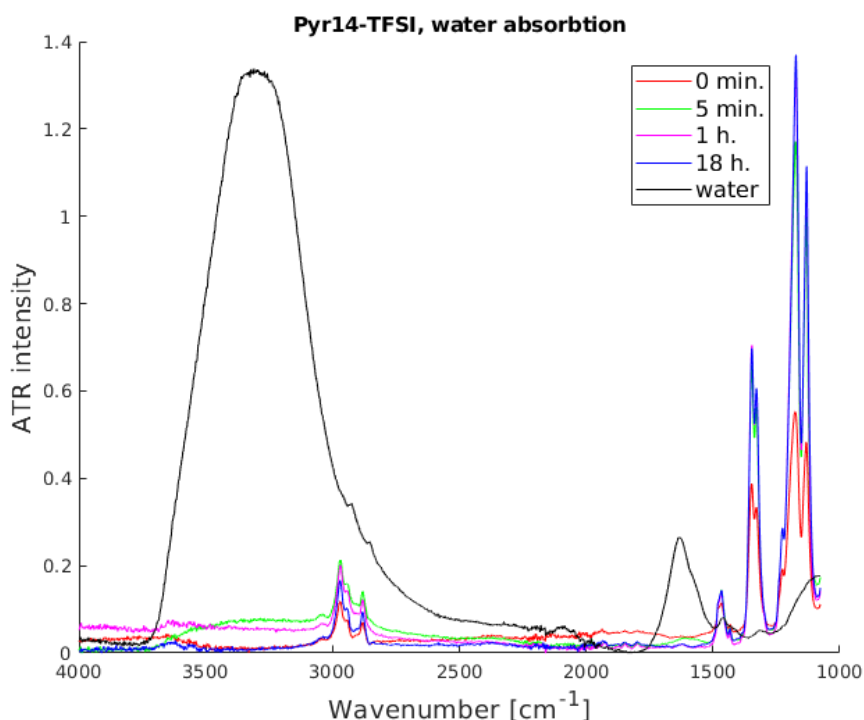


Figure B.2: A graph showing the results from ATR IR spectroscopy measurements, where ATR intensity is related to absorbance of light at a given wavenumber. The different colors correspond to the sample being exposed to air for different amounts of time. The black spectrum is for pure water, in order to compare with the spectra from Pyr14-TFSI. It is seen that the spectra from Pyr14-TFSI do not seem to be affected by the peaks from pure water, qualitatively indicating that water is not being absorbed over time.

For Pyr14-TFSI, it looks like the Pyr14-TFSI measurements are not influenced by water, since the water-peaks are not present here. There is a difference between 0 min., 5 min., 1 h. and 18 h., especially between 3500 and 3000 cm^{-1} , but this is most likely due to differences in the loading of the sample. This is confirmed since the 5 min. result has a higher absorbance than the 18 h. result at the position of the large water peak.

A clear contrast to this are the Pyr18-TFSI measurements. Here it seems like the water spectrum is increasingly present in the Pyr18-TFSI spectra. Both the large absorption peak around 3250 cm^{-1} and the smaller peak around 1600 cm^{-1} . This is the case with the 1 h. and 18 h. sample where as the 5 min. sample does not seem to contain water.

That the Pyr14-TFSI does not seem to absorb water, even after 18 hours, is consistent with the DSC measurements which showed no significant change

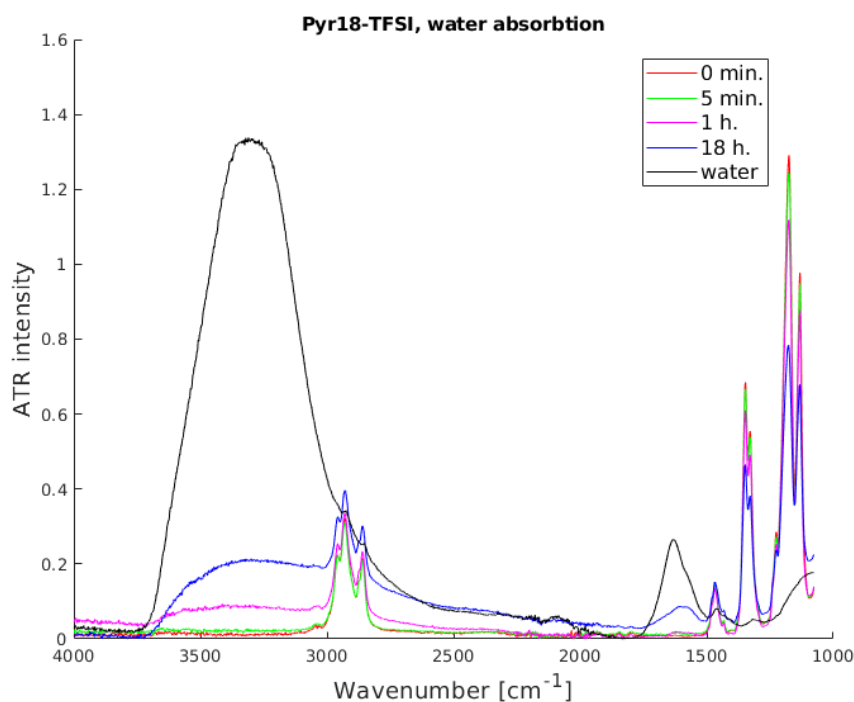


Figure B.3: A graph showing the results from ATR IR spectroscopy measurements, where ATR intensity is related to absorbance of light at a given wavenumber. The different colors correspond to the sample being exposed to air for different amounts of time. The black spectrum is for pure water, in order to compare with the spectra from Pyr18-TFSI. It is seen how the peaks from pure water get introduced in the spectra for Pyr18-TFSI as the liquid is exposed to air for longer periods of time. This indicates qualitatively that water is indeed being absorbed.

in T_g over time exposed to air. This comparison between the DSC and the IR spectroscopy measurements is not so clear with the Py18-TFSI samples. Here the IR results show no water in the sample after 5 min., but with DSC, T_g drops 1.7 K in the sample that was exposed to air for 5 min. The afterwards increase in T_g of 0.6 K is also not consistent with the IR results, which show an increase of water in the sample after 18 hours. That is, if a decrease in T_g is connected with an increase of water in the sample. However, the error on the resulting T_g calculated by the TA-instrument software is not known, and so it is possible that a change of $\pm 0.5 K$ is within errors.

Appendix C

Fit to model

Fit to model The data was fitted to a model proposed by Hecksher et al. [109] which includes both the alpha and the beta process. The final function of the shear compliance comes from modelling the viscoelastic system with electrical circuits and it tries to capture the merging of the alpha and beta relaxations. The total expression for the compliance is

$$J(\omega) = J_\alpha \left(1 + \frac{1}{i\omega\tau_\alpha} + \frac{k_1}{1 + k_2(i\omega\tau_\alpha)^{1/2}} \right) + \frac{J_\beta}{1 + (i\omega\tau_\beta)^b} \quad (\text{C.0.1})$$

where $G(\omega) = 1/J(\omega)$. Due to the fact that the beta relaxation peak was not visible in the experimental window, the fitting procedure implemented was as follows

- Find the top point of the beta relaxation peak from a second degree polynomial and use this value as a starting point for the parameter guess for τ_β
- Fit the model to the data at 184 K to find the shape parameters k_1 , k_2 and b
- Fit the data for all temperatures with the three parameters k_1 , k_2 and b fixed.

The resulting fit together with data is shown in figure C.1 and shows that the fit was not able to capture all the features of the relaxation spectra. Note that several different fitting procedures was tested, i.e. finding the shape parameters at different temperatures and fixing different parameters when fitting to all temperatures, but non of this improved the fit.

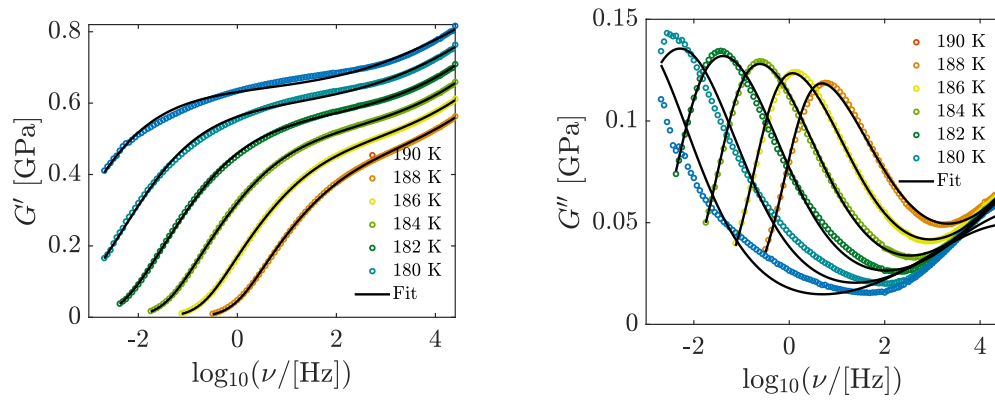
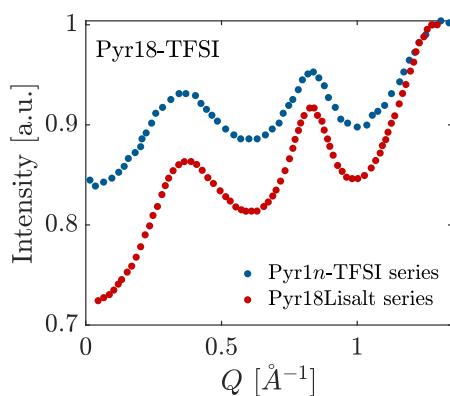


Figure C.1: The a) real and b) imaginary part of the shear modulus of Pyr14-TFSI from at 180-190 K plotted together with a fit to the model seen in eq. (C.0.1). It shows that the fit could not find the beta relaxation or the alpha relaxation at lower temperatures.

Appendix D

X-ray structure factor on RTIL

The following shows the comparison between two different measurements of the x-ray structure factor of neat Pyr18-TFSI. The reason behind is to show that the two datasets are quite similar with regards to peak position, even though the backgrounds are different.



(a)





Figure D.1: X-ray scattering structure factor for neat Pyr18-TFSI measured in two different studies. One by Augilera et al. (red) [69] and one by Li et al. (blue) [68].

Appendix E

Reprint of publications

- E.1 High frequency dynamics and test of the showing model for the glass-forming ionic liquid Pyr14-TFSI

High-frequency dynamics and test of the shoving model for the glass-forming ionic liquid Pyr14-TFSI

Kira L. Eliassen ¹, Henriette W. Hansen,^{1,2,4} Filippa Lundin ², Daniel Rauber ³, Rolf Hempelmann,³ Tage Christensen,¹ Tina Hecksher,¹ Aleksandar Matic,² Bernhard Frick,⁴ and Kristine Niss ^{1,*}

¹“Glass and Time”, IMFUFA, Department of Science and Environment, Roskilde University, P.O. Box 260, DK-4000 Roskilde, Denmark

²Department of Physics, Chalmers University of Technology, Göteborg, Sweden

³Department of Chemistry, Saarland University, 66123, Saarbrücken, Germany

⁴Institut Laue-Langevin, 71 Avenue des Martyrs, F-38042 Grenoble, France



(Received 9 March 2021; revised 17 May 2021; accepted 1 June 2021; published 25 June 2021)

In studies of glass-forming liquids, one of the important questions is to understand to which degree chemically different classes of liquids have the same type of dynamics. In this context, room-temperature ionic liquids are interesting because they exhibit both van der Waals and Coulomb interactions. In this work we study the α relaxation and faster relaxation dynamics in the room-temperature ionic liquid 1-butyl-1-methylpyrrolidinium bis(trifluoromethanesulfonyl)imide (Pyr14-TFSI). The paper presents quasielastic neutron and shear mechanical spectroscopy data measured over seven decades in frequency (10^{-3} – 10^4 Hz). The use of these two methods in combination reveal the α relaxation and four separate, faster modes. Two of these faster modes, based on the partial deuterations, can be assigned to the methyl group and the methyl end of the butyl chain of the cation. The neutron data are also used to determine the mean-square displacement (MSD) on the nanosecond timescale. It is shown that the temperature dependence of the MSD can account for the super-Arrhenius behavior of the α relaxation as predicted by the shoving model [Dyre, *Rev. Mod. Phys.* **78**, 953 (2006)], similarly to what is seen in simpler glass-forming liquids.

DOI: [10.1103/PhysRevMaterials.5.065606](https://doi.org/10.1103/PhysRevMaterials.5.065606)

I. INTRODUCTION

Room-temperature ionic liquids (RTILs) are salts with melting points below 100 °C [1], typically composed of a large organic cation and an inorganic anion. Ionic liquids have attracted attention over the last decades due to their potential applications, e.g., as candidates for highly stable electrolytes in the next generation of energy-storage systems [2,3]. RTILs are also interesting from a fundamental point of view because they constitute an interesting class of liquids: due to the competition of Coulomb interactions and van der Waals interactions they exhibit structural correlations on nanometer length scales with a clear signal in small-angle x-ray scattering (SAXS). Two peaks in addition to the nearest-neighbor correlation peak are found in the range of momentum transfers of $Q = 0.1$ – 0.5 \AA^{-1} for the nonpolar domains and $Q = 0.6$ – 1 \AA^{-1} for the charge ordering, which is not found in ordinary liquids [4–10]. Ionic liquids are therefore ideal systems to test how changes in chemical interactions and structure influence the dynamics of liquids. Like many other liquids, ionic liquids can be supercooled and brought into the glassy state. Viscosity and conductivity of the supercooled ionic liquids have a marked super-Arrhenius temperature dependence which puts ionic liquids in the category of so-called fragile liquids [11,12].

The main relaxation in liquids is the α relaxation which, like the viscosity, has a super-Arrhenius temperature depen-

dence. In addition to this, it has been found that complex systems like mono-alcohols and recently also other hydrogen bonding systems have a mode slower than the α relaxation believed to be associated with the dynamics of the hydrogen bonding network [13–16]. Inspired by this, several studies have investigated whether the nanoscale structures in ionic liquids give rise to similar slow modes, and in fact, a mode slower than the α relaxation has been demonstrated in 1-octyl-3-methylimidazolium tetrafluoroborate [17]. However, little attention has been paid to dynamics faster than the α relaxation. The fast (high-frequency) part of the relaxational dynamics is the focus of the current paper. Moreover, we look into the connection between fast vibrational dynamics and the temperature dependence of the α relaxation, which has been investigated in many other classes of liquids [18] but rarely in ionic liquids.

Dielectric spectroscopy is the standard technique for studying the frequency and temperature dependence of the relaxational dynamics in organic glass-forming liquids, but the relaxation signal is masked by ionic conductivity in the case of ionic liquids. For ionic liquids the dielectric modulus, which reveals translational ionic motions as peaks in the imaginary part of the modulus [19], is often studied [12,20–23]. To get direct information on the α relaxation of ionic liquids other techniques like light scattering, neutron scattering, or shear mechanical spectroscopy must be applied. In this work, the two latter techniques are employed with focus on dynamics in the supercooled liquid. We find from frequency-dependent shear modulus data and incoherent neutron scattering that the RTIL 1-butyl-

*kniss@ruc.dk

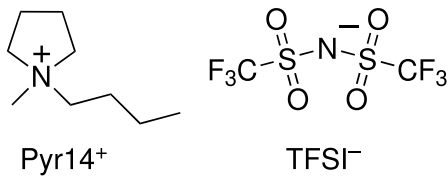


FIG. 1. A schematic of the sample Pyr14-TFSI with the cation to the left and the anion to the right.

1-methylpyrrolidinium bis(trifluoromethanesulfonyl)imide (Pyr14-TFSI) has as many as four different dynamic modes at higher frequencies than the α relaxation. Yet the temperature dependence of the α relaxation is connected to the vibrational mean-square displacement, as found in other classes of liquids and as predicted by the shoving model [18,24–26]. Moreover, earlier works have shown that Pyr14-TFSI obeys density scaling of both α relaxation and viscosity and conductivity [27–29]. The overall picture is that while ionic liquids have additional structural features and rich dynamics, the α relaxation which governs the transport properties and the glass transition has a behavior remarkably similar to that of other glass-forming liquids.

The paper is structured as follows. Section II presents the samples and the experimental techniques. The shear mechanical data and neutron inelastic fixed window scan data are presented in Secs. III and IV. The timescales of the modes found in the two techniques are compared to each other and to conductivity in Sec. V. In Sec. VI, the mean-square displacement is determined based on elastic fixed window scans, and these results are used in combination with the shear mechanical α -relaxation times to test the shoving model in Sec. VII. The final section, Sec. VIII, contains a discussion of the results and conclusions.

II. EXPERIMENTAL DETAILS

A. The sample

The ionic liquid studied in this work is Pyr14-TFSI, which is well studied with various other techniques [6,27,28,30–37]. T_m found from literature is 260 K [33], and $T_g = 185$ K was measured in this work by differential scanning calorimetry (DSC), see Supplemental Material for details [38]. It has only a small degree of nanoscale structures due to the alkyl-chain lengths, which are visible in NMR measurements [31] but not in x-ray scattering experiments [6,10]; moreover the x-ray signal clearly shows a charge ordering peak [6]. It was found in this study that the supercooled sample is prone to cold crystallization at around 192 K in the shear measurements and 215 K in the DSC measurements.

The sample used in the shear mechanical study was of 99.9% purity, purchased from Solvionic and used as received. See Fig. 1 for an illustration of the sample. Previous studies [39] show that the liquid is highly hygroscopic and quickly absorbs water when exposed to atmospheric moisture; therefore all preparation and storage of the samples took place inside a glove box with inert nitrogen atmosphere.

For the neutron experiment the sample was synthesized with different degrees of deuteration in order to separate the dynamics of three parts of the cation: the pyrrolidinium ring,

the methyl group, and the butyl chain. The first, called D12, has both the butyl chain and the methyl group deuterated; D9 has the butyl chain deuterated, while D3 has merely the methyl group deuterated. The sample without deuteration was called D0 and is the same as the sample used in the shear measurements.

The deuterated samples were synthesized at the Department of Chemistry, Saarland University, Germany. The 1,1-dialkylated pyrrolidinium halide precursors used for the synthesis of the bis(trifluoromethanesulfonyl)imide ionic liquids were obtained by quaternization reactions of the corresponding 1-alkyl-pyrrolidines in acetonitrile under argon at ambient temperature for several days. 1-(d9-butyl)-pyrrolidine was synthesized by nucleophilic substitution of d9-butylbromide with fivefold excess of pyrrolidine in acetonitrile at ambient temperature for five days, followed by purification via distillation. The methyl-deuterated precursor 1-butyl-1-(d3-methyl)-pyrrolidinium iodide was obtained by reaction of butylpyrrolidine with slight excess of d3-methyl iodide. 1-(d9-butyl)-1-methyl-pyrrolidinium bromide was obtained by reaction of slight excess of 1-methyl-pyrrolidine with d9-butylbromide. 1-(d9-butyl)-1-(d3-methyl)-pyrrolidinium iodide was obtained by the reaction of 1-(d9-butyl)-pyrrolidine with slight excess of d3-methyl iodide. All halide salts were dried in high vacuum to remove the solvent and excess reagents, and their purity and identity was checked by multinuclear NMR spectroscopy. The halide precursors obtained this way were dissolved in water, and a slight excess of lithium bis(trifluoromethanesulfonyl)imide was added. After stirring for 18 hours the hydrophobic ionic liquids were extracted with dichloromethane, followed by washing the organic phase with water several times. The pure ionic liquids were obtained after removal of the solvent and drying in high vacuum for several days. Their purity was checked by multinuclear NMR spectroscopy, and the absence of residual halides was confirmed by testing with AgNO_3 solution. See Supplemental Material for more detailed information about the synthesis of the three deuterated samples [38].

B. Shear measurements

Frequency-dependent shear measurements were performed at Department of Science and Environment, Roskilde University, Denmark, using the piezoelectric shear modulus gauge (PSG) [40]. A version of the PSG with just one piezoelectric disk was used for these measurements. The PSG works by filling liquid in two gaps between two sapphire and a single piezoelectric (PZ) disk. An oscillating voltage is applied to the electrodes, causing the PZ disk to expand or contract radially due to the piezoelectric effect. The frequency-dependent capacitance of the PZ disk is measured and the shear modulus of the sample extracted therefrom [40]. The method works in the 1-mHz range up to as much as 40 kHz, and the capacitance of the disk was measured using the setup described in Ref. [41]; measurements were performed in a closed-cycle cryostat [42].

The sample is prone to cold crystallization and was therefore cooled rapidly down to 190 K, because previous tests showed no crystallization below this temperature. Subsequently, the spectra of the supercooled state were measured in cooling with 2-K steps from 190 to 180 K. Two frequency

TABLE I. The neutron cross sections for the four different samples D0 (fully protonated), D3 (methyl group deuterated), D9 (butyl group deuterated), and D12 (both methyl and butyl group deuterated). All scattering cross sections are in barn.

Sample	σ_{scat}	σ_{inc}	σ_{coh}	$\sigma_{\text{inc}}/\sigma_{\text{scat}}$ [%]
D0	1768	1606	161.3	91
D3	1545	1372	172.8	89
D9	1098	902.4	195.8	82
D12	875.1	667.8	207.3	76
TFSI	65.7	0.522	65.2	0.8

sweeps were made at each temperature, with a 10-min waiting time in between. Each spectrum takes 1 h if going to 10 mHz and roughly 10 h if going to 1 mHz. No change was observed between these two spectra, indicating that no crystallization is taking place. At 182 K, $\log_{10}(\tau_{\alpha}/[\text{s}]) = 1.62$. To avoid extrapolation we define this as the dynamic T_g for the shear measurements, since it is close to a relaxation time of 100 s.

Spectra in the glassy state (i.e., below 182 K) were measured on a new sample by cooling to 188 K, measuring a spectrum which collapsed with the previous 188-K data. Subsequently, the sample was cooled to 178 and 177 K for two additional spectra. The waiting time was 24 h before initiating measurements at 178 and 177 K. Two spectra were again measured at each temperature with each spectrum taking approximately 10 h, and no aging in the modulus was observed between the two spectra.

In addition to shear mechanical data, conductivity data were measured in the same cryostat as the shear measurements and with more data in the supercooled range than previously reported [30]. Details on the conductivity measurements can be found in the Supplemental Material [38].

C. Neutron measurements

Quasielastic neutron scattering was performed on the backscattering instrument IN16B Institute Laue-Langevin (ILL), Grenoble. Elastic fixed window scans (EFWSs) were acquired with an energy resolution of $\Delta E \approx 0.8 \mu\text{eV}$, corresponding to a timescale of the dynamics of around 5 ns. Inelastic fixed window scans (IFWS) [43] were measured with an energy offset of $E_{\text{IFWS}} = 2 \mu\text{eV}$, giving a time of $1/\omega_{\text{IFWS}} = 1/(E_{\text{IFWS}}/\hbar) = 3.3 \times 10^{-10}$ s. The Q range in both cases was $0.19\text{--}1.90 \text{ \AA}^{-1}$. The data were taken in cooling to avoid crystallization and covered the temperature range 10–310 K with a cooling rate of 0.5 K/min.

When using incoherent neutron scattering, it is often assumed in the analysis that no coherent scattering is present. This is a reasonable assumption for liquids containing a large fraction of hydrogen, since this element has a very high incoherent cross section. Deuterium, however, scatters only coherently, so an increased value of deuterium will decrease the incoherent cross section per molecular unit. Specifically, this will reduce the percentage of incoherent scattering from 91% in D0 to 76% in D12; see Table I for an overview of the incoherent contribution from each sample. The table also shows that the incoherent scattering from the TFSI anion can be neglected. Consequently, it is mainly the dynamics of the cation that is probed with inelastic neutron scattering in this

study. The type of dynamics expected from the cation will be a combination of (1) the global diffusion of the center of mass of the cation and (2) local motions due to ring wagging and segmental rotation of the butyl chain and the methyl arm [44].

The raw neutron-scattering data were reduced using the LAMP software package [45]. All EFWS and IFWS intensities were normalized to the elastic intensity at the lowest measured temperature.

III. SHEAR MODULUS

Figure 2 shows the real and imaginary part of the shear modulus for Pyr14-TFSI in the temperature range 177–190 K plotted on a log-linear scale (a, b) as well as a log-log scale (c, d). Shear mechanical data on ionic liquids have been reported before, e.g., in [17,46], and for Pyr14-TFSI in particular by Palumbo *et al.* (2015) [47] and Tu *et al.* (2019) [23]. The main difference from these studies is that the frequency range in the isothermal spectra in this work is much larger, which makes it possible to also detect higher frequency relaxation modes in the ionic liquid.

The α relaxation is seen as a rapid increase in the real part of the modulus and a prominent peak in the imaginary part. As expected, these features move to lower frequencies upon cooling.

The spectra, moreover, reveal a large β relaxation at high frequency near 10 kHz, a feature which is commonly seen in other liquids [48,49] but not earlier reported for ionic liquids due to lack of data in the relevant frequency range. The observed β relaxation is intense and appears to be temperature independent in position and amplitude in the liquid state, whereas it has a slight change in behavior in the glassy state. The low-frequency wing of the β relaxation is clearly resolved. However, different combinations of the high-frequency shear modulus, G_{∞} , and the relaxation time of the β relaxation, τ_{β} , gave fits of the same quality, which means that τ_{β} and G_{∞} cannot be well determined from these data.

In addition to the β relaxation, another feature located at around 0.1 Hz is also seen in the data. It has a low amplitude and only appears as a small shoulder around 182 K, becoming more evident in the glass at around 178 K. The mode appears to have weak or no temperature dependence but is merged with the α relaxation, which makes it hard to judge.

In the time-temperature superposition (TTS) plot [inset of Fig. 2(c)], our data is compared to the data of Tu *et al.* [23]. There is good agreement between the spectral shapes of the two sets of data, but it is also clear that the two high-frequency modes, τ_{β} and τ_{wing} , are not resolved in data from Tu *et al.* and that our data are more precise/less noisy, especially at frequencies above the α -relaxation peak.

At frequencies below the α relaxation, the signal corresponds to viscous flow with the characteristic power-law behaviors in the real and imaginary parts [13]. This means that there is no slow mode, which is not surprising since x-ray scattering and simulation does not show a prepeak in this liquid [6,8].

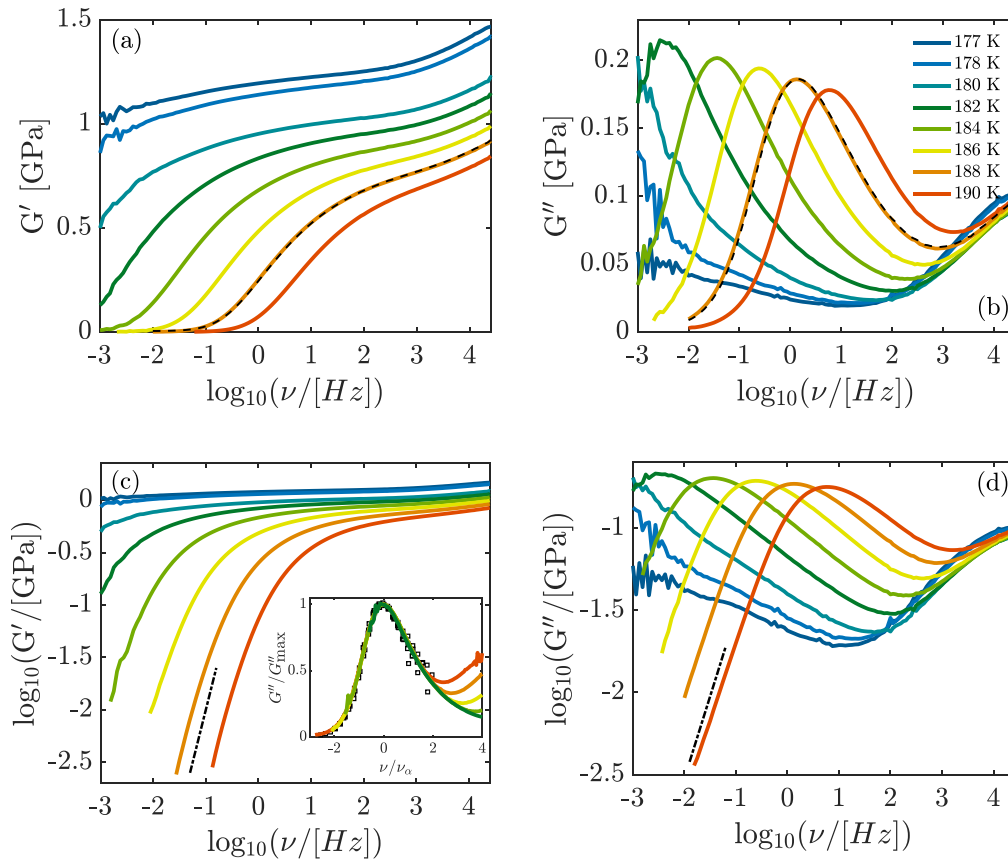


FIG. 2. The complex shear modulus of neat Pyr14-TFSI plotted as the (a) real part, (b) imaginary part, (c) logarithm of the real part, and (d) logarithm of the imaginary part. Data were taken at temperatures ranging from 177 to 190 K. The black dashed-dotted line illustrates the terminal, fully viscous behavior of a liquid at low frequencies. Black dashed line on top of the 188-K curve is from the second measurement at 188 K, which was followed by measuring in the glass at 178 and 177 K. Insert in (c) is a TTS plot of G'' with data from literature (black squares) [23].

IV. QUASIELASTIC NEUTRON SCATTERING—FIXED WINDOW SCANS

Figure 3 shows temperature-dependent inelastic fixed window scans for the four different deuterations of the sample at different Q values. The incoherent scattering is in all cases well above 70%, and most of the signal can be assumed to come from hydrogen. This means that data on the D12 sample, which has both the butyl chain and the methyl group deuterated, mainly is sensitive to the pyrrolidinium ring dynamics, which we assume to couple to the center-of-mass motion of the cation and thus give direct information on the α relaxation of the liquid. This main mode, around 300 K, is present in all four samples, whereas in D0, D3, and D9 the presence of other, additional modes, assumed to be connected to the butyl and methyl arm, appear at lower temperatures.

The high-temperature peak seen in all samples is clearly Q dependent, shifts to lower temperature, and decreases in intensity with increasing Q value, suggesting that the origin is diffusive [43]. This corroborates the interpretation that it is the α relaxation of the liquid. The position of the low-temperature shoulders seen in the D9, D3, and D0 samples appears to be Q independent but increase in intensity with increasing Q values. This can be interpreted as the low-temperature mode being

due to local motions, consistent with the assumption that it originates from the butyl and methyl groups [43].

Thus our interpretation is that three different modes can be seen in the IFWS data of the nondeuterated sample. D0: The pyrrolidinium ring that is assumed to be coupled to the center of mass of the cation molecule, the methyl group motion, and the motion of the butyl group. This is also consistent with a recent interpretation of IFWS by Busch *et al.* [44]. In order to separate the different spectral contributions from each other, the data from the D12 sample have been fitted to a single Gaussian function at each Q value. The Gaussian is purely phenomenological but fits the data very well and can therefore be used to interpolate between data points. An example of the result can be seen in Fig. 4(a). The interpolation of the D12 data makes it possible to subtract the D12 intensity from the D3 and D9 intensity. Figure 4(b) shows the D3 and D9 data obtained through the following procedure: Fit the D12 data at each Q with a Gaussian function to establish the interpolation, subtract this from the D3 and D9 data at each Q , and then finally sum over all Q (see Supplemental for the result at individual Q). This procedure makes it evident that the samples D3 and D9 indeed have dynamics separated from the main mode of the pyrrolidinium ring, visible as a peak in intensity at around 184 and 208 K, respectively.

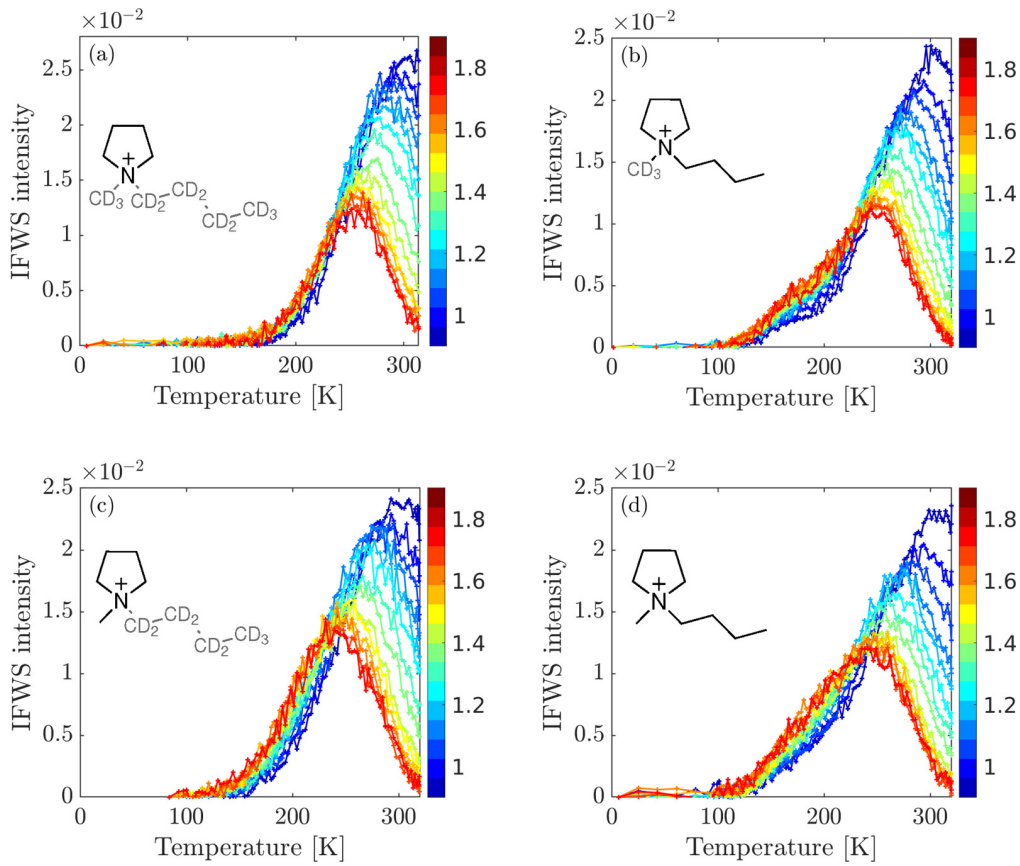


FIG. 3. IFWS intensity for the whole Q range (red to blue, see the color bar in units of \AA^{-1}) and for all four Pyr14-TFSI samples: (a) D12, (b) D3, (c) D9, and (d) D0. Intensity was normalized (after subtracting background) to the lowest temperature elastic signal, and the four lowest Q values were excluded since the data here are very noisy and disrupted the whole picture of the Q dependence. The main peak present in all samples is Q dependent and decreases in intensity with higher Q values. Two additional, Q -independent modes appear to be present in the D3 and D9 sample, respectively, as shoulders at lower temperatures.

The simplest assumption is that these localized motions have a Lorentzian spectral shape which leads to the following

functional form of the IFWS signal [43,44]:

$$I(T) = e^{-aT} \left[I_0 \frac{1}{\pi} \frac{\tau(T)}{1 + \tau(T)^2 \omega_{\text{IFWS}}^2} \right], \quad (1)$$

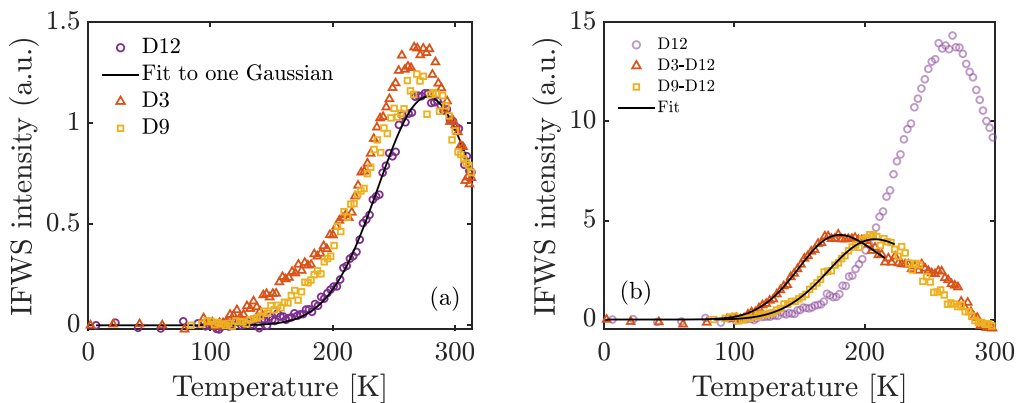


FIG. 4. IFWS intensity of Pyr14-TFSI as a function of temperature. (a) Data from the D3, D9, and D12 samples at $Q = 1.3 \text{ \AA}^{-1}$ as an example. The data from the D12 sample (purple) is shown together with a fit to a Gaussian function (black solid line), showing excellent agreement between the two, meaning that the fit can be used as interpolation of the data. (b) IFWS intensity summed over Q for D12 and for D3 and D9, where the interpolation from the D12 sample has been subtracted at each Q in order to show additional dynamics that are separated from the main mode. Black solid lines are fit to the proposed model shown in Eq. (1).

where $\tau(T)$ is the temperature-dependent relaxation time, and ω_{IFWS} is the angular frequency given by the energy offset at which the data is acquired, $\omega_{\text{IFWS}} = \Delta E/\hbar$. The exponential prefactor is the temperature-dependent Debye-Waller factor and a is found from a fit to the low-temperature region of the EFWS intensity (see Supplemental Material [38]).

Assuming that the temperature dependence is Arrhenius in nature gives

$$\tau(T) = \tau_0 e^{E_a/RT}, \quad (2)$$

where R is the universal gas constant, τ_0 is the high-temperature limit of the relaxation time, and E_a the activation energy of the local dynamics. Combining Eqs. (1) and (2) gives a model with τ_0 , E_a , and I_0 as free parameters (in addition to a , which is found from the EFWS data). This approach for fitting IFWS data was proposed by Frick *et al.* [43] and has recently been used by Busch *et al.* to analyze IFWS data on a RTIL [44].

Figure 4(b) shows the fit (black solid lines) to the D3-D12 and D9-D12 data. The fit is only performed in a temperature range where the residual is at least 50% of the total signal, i.e., $(D3-D12)/D12 > 50\%$). The model gives a convincing fit, and with a τ_0 in the picosecond range which is physically reasonable. The activation energies for the localized motions are found to be $E_a = 7.8$ kJ/mol for the D3 sample and $E_a = 9.1$ kJ/mol for the D9 sample. These activation energies show good correspondence with previous studies [44,50,51] on the fully protonated RTIL N-butylpyridinium bis(trifluoromethanesulfonyl)imide, which is a sample very similar to the one in this study, except that the cation ring only has the alkyl chain and not the methyl group.

It is worth noting that the local mode in D3 where the butyl is the visible alkyl group is faster than the mode of D9 where the methyl is visible. In addition, the two modes have similar intensity, even though the butyl has three times as many hydrogen atoms than the methyl. This leads to the conclusion that it is probably mainly the end methyl group that is active in the butyl mode seen here. This is in line with results and discussions in Ref. [50], where the part of the alkyl chain close to the aromatic ring in a similar cation can appear to be almost immobile on the timescale of the experiment. In Ref. [29] where the focus is on the pressure dependence and on the geometry of the dynamics of Pyr14-TFSI, it is found that there is also active dynamics in the picosecond timescale at room temperature. This is assigned to the conformational dynamics of the butyl chain and libration of the pyrrolidinium ring.

V. TIMESCALES

To get an overview of the different dynamic modes which were seen in the shear mechanical and neutron scattering data, we collect them in a relaxation map/Angell plot in Fig. 5, where the relaxation time of the modes is shown as a function of normalized inverse temperature T_g/T , with $T_g = 182$ K found from shear measurements.

The measurement of shear mechanical spectra over 7 decades in frequency per temperature makes it possible to track the α -relaxation time, τ_α , with decreasing temperatures all the way down to the glass transition. The α -relaxation

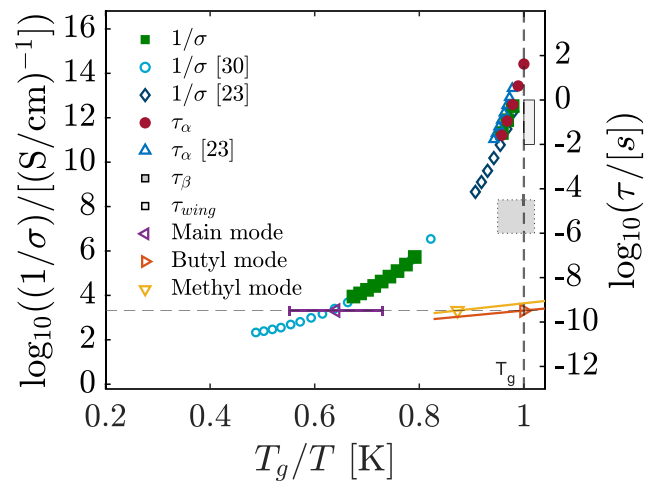


FIG. 5. Relaxation map showing the timescale and temperature dependence of the five different dynamic modes found in this study of Pyr14-TFSI. The inverse conductivity is a combination of data from literature (blue, open circles and diamonds) [23,30] and from this study (green, filled squares), plotted here together with the structural relaxation time from this study (red, filled circle) and from literature (blue, open triangles) [23]. Conductivity data from Martinelli *et al.* [30] have been scaled in absolute value in order to collapse with data from this study. Temperature is normalized to T_g as found from shear measurements (182 K). Note that the two different y axes have been shifted so that the shear modulus and conductivity measurements collapse in the supercooled regime and cover the same range (16 decades). The purple, orange, and yellow triangles show the three dynamic modes found from the IFWS intensity and are related to dynamics connected to the pyrrolidinium ring, the butyl group, and the methyl group, respectively (see details in Sec. IV). The error bar of the main mode represents the Q dependence of this. Solid lines are the Arrhenius dependence found from the model fits to the D3 and D9 data with the D12 interpolation subtracted. Dynamics of the pyrrolidinium ring, and thus the center-of-mass motion of the cation, is seen to be related to the α relaxation (blue, green, and red). The dark gray square box is the β relaxation, τ_β , and light gray box is the third relaxation, τ_{wing} , found as a wing at low temperatures, both from the shear modulus.

time was found from the shear modulus data by a fit to a second-order polynomial around the α -relaxation peak, f_{max} , and $\tau_\alpha = 1/(2\pi f_{\text{max}})$.

This gives information to calculate the isobaric Angell fragility index, m_p , from shear modulus measurements. The fragility index is given by [52,53].

$$m_p = \left. \frac{d \log_{10} \tau_\alpha}{d T_g/T} \right|_{T=T_g}. \quad (3)$$

For Pyr14-TFSI we find that $m_p = 85$, which is consistent with fragility found for other RTILs [12]. This value is also reasonably close to what Tu *et al.* found in their study of Pyr14-TFSI [23], $m_p = 82$ with T_g defined as $\log_{10}(\tau_\alpha/[s]) = 1$.

In addition to the timescale axis, the relaxation map in Fig. 5 also includes an axis of the resistivity/inverse ionic conductivity. Conductivity data from this work are shown both in the supercooled region and in the liquid above the

melting point. Additional liquid data from literature are also shown. The pronounced cold-crystallization tendency leads to a “no-man’s land” just below the melting point where the liquid properties cannot be accessed.

The position of the inverse conductivity axis relative to the timescale axis is chosen such that the α -relaxation time and inverse conductivity, from this study, collapse at 188 K. Subsequently, the two data sets at the other temperatures in the supercooled range follow each other closely, showing that the conductivity and the α -relaxation time have the same temperature dependence. This behavior is qualitatively consistent when including conductivity and α -relaxation data from literature [23]. A similar behavior is found by Jafta *et al.* [54] by comparing conductivity and α relaxation measured by dielectric spectroscopy on 3-methyl-1-methylimidazolium bis(trifluoromethanesulfonyl)imide (DMIM-TFSI) with 1 mol Li-TFSI. This implies that ion translation and structural relaxation are directly coupled or governed by the same parameters. This is consistent with a study by Martinelli *et al.* showing coupling between T_g and conductivity in an ionic liquid [30]. At higher temperatures above the “no-man’s land,” the conductivity data from this study and from literature [30] have the same temperature dependence. Another way to represent the data is by comparing inverse conductivity and viscosity; see Supplemental Material [38] for a discussion of this.

The shear mechanical data do not allow for an exact determination of the timescales of the β relaxation nor of the additional mode seen between the α and β relaxation in the shear data of the glassy sample. However, it is possible to estimate their position, and these are indicated with two gray areas in the plot and are denoted τ_{wing} (light gray) and τ_β (dark gray) for the middle and fast relaxation, respectively.

The neutron-scattering fixed window scan is a “single timescale” technique giving information on nanosecond dynamics, which is illustrated in the relaxation map as a dashed, horizontal line at $\tau_\alpha = 1/\omega_{\text{IFWS}} = 3.3 \times 10^{-10}$ s. Three dynamic modes were identified with the IFWS method, and the temperature dependence of the main mode, which is directly related to the translational motion of the center of mass of the cation, was found by fitting the D12 data with a Gaussian function at Q values of 0.44–1.9 \AA^{-1} and then assuming the peak position of the fit to be equal to the temperature of the main mode. This is seen as the purple triangle (average), with the error bars extending from the highest to the lowest temperature of the main mode, since the temperature dependence of the neutron signal is Q -dependent for the α relaxation. This main mode of the cation fits very well with the shear mechanical α relaxation and the resistivity. The orange and yellow lines, representing the dynamic mode from the butyl and methyl group, respectively, are calculated from the best-fit parameters found Sec. IV, assuming Arrhenius behavior. Both of these secondary modes are faster than the main mode and are assumed to have a Q -independent temperature dependence. The lines are seen to cross the $1/\omega_{\text{IFWS}}$ line at triangles with the same color. These triangles are found from the T_{max} formula derived from the model in Eq. (1), see Frick *et al.* [43] for details.

In case of the neutron data the tool of partial deuteration has made it possible to assign the modes at low temperatures to movements in a particular part of the cation. In case of

the shear data there is no direct information on what part of the molecule(s) the modes are related to. However, based on the relaxation map (Fig. 5), it does not seem likely that the β relaxation nor the wing are connected to butyl or methyl dynamics, since the temperature dependence of the butyl and methyl modes is very low, and thus these modes are well separated from the β relaxation and the wing of the shear mechanical data. Even if the actual temperature dependence does not follow a simple Arrhenius behavior, it would require a stronger temperature dependence than that of the α relaxation for the butyl and methyl mode to be connected to the β relaxation and the wing. This is inconsistent with the fact that the α relaxation of a liquid is normally found to be the mode with the strongest temperature dependence. Moreover, the wing and the β relaxation in the Pyr14-TFSI spectra also appear to have very weak temperature dependencies in the range where they are detected. Therefore we conclude based on the relaxation map that four different relaxational modes are active at shorter timescales or equivalently, at lower temperatures than the α relaxation. The origin of the β relaxation and the wing are open to speculation, but it could be related to anion dynamics or be so-called genuine Johari-Goldstein β relaxation [49,55]. A similar relaxation map is also seen in the study by Jafta *et al.* [54], where four distinct relaxation modes were detected by a combination of dielectric spectroscopy and neutron-scattering data.

VI. MEAN-SQUARE DISPLACEMENT

So far the focus of the paper has been on relaxational dynamics. However, the elastic fixed window scans (EFWS) of the neutron data also contain information on the vibrational dynamics taking place at faster timescales than the nanosecond. In the following the EFWS data will be analyzed in terms of the mean-square displacement (MSD), and the extracted results will be connected to the temperature dependence of the α relaxation in terms of the shoving model in Sec. VII.

A. Finding the mean-square displacement from neutron data

A number of different approaches may be employed to determine MSD from the elastic incoherent scattering data. Common for all of them is that one fits the Q^2 dependence of the logarithm of the normalized elastic intensity to a function that contains the MSD as a free parameter. The traditional way is to use the Gaussian approximation of scattering from liquids [56], where a linear relation between the logarithm of the normalized intensity and Q^2 is assumed. Another method is one suggested by Zorn [57,58], which takes into account multiple scattering and the non-Gaussian character of the dynamics and has one less free parameter than the Gaussian approximation.

Figure 6 shows the normalized intensity as a function of Q^2 at two different temperatures and deuteration. Fits to the Gaussian approximation are shown for two different Q ranges and it is seen that the Gaussian approximation breaks down as temperature is increased. In contrast to this, the data points at higher temperatures are well captured by the fit to the Zorn method. Furthermore, this method also seems more robust to the fact that a coherent signal enters as a shoulder at around

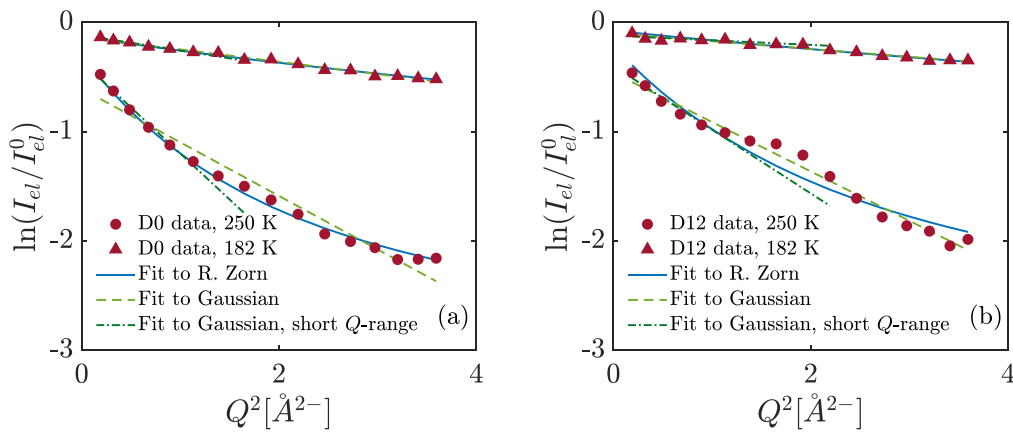


FIG. 6. Logarithm of the normalized intensity as a function of Q^2 for Pyr14-TFSI with deuteration (a) D0 and (b) D12 at both 250 K (circles) and 182 K (triangles) in order to show the qualitative difference between the fits to data with the Gaussian method (green) and the Zorn method (blue). This plot also illustrates how a coherent signal slowly starts to increase at around 1.9 \AA^{-2} with increased deuteration.

$Q^2 \approx 1.9 \text{ \AA}^{-2}$ and grows with increasing deuteration (see next section). This coherent signal is also a reason for the resulting MSD being somewhat dependent on the chosen Q range in the Gaussian approximation, an effect that is most pronounced at higher temperatures. This leads to the conclusion that the Zorn method will be used to calculate MSD from the elastic incoherent scattering data in this study. See Supplemental Material for details [38].

B. MSD data from different deuteration

The MSD for all four deuteration is shown in Fig. 7. The MSD values are lowest for D12 at all temperatures

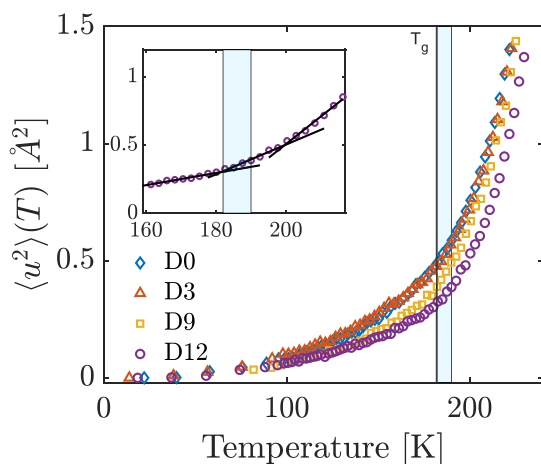


FIG. 7. Mean-square displacement (MSD) as a function of temperature for all four samples of Pyr14-TFSI. The blue shaded area illustrates the temperature region where the shear modulus measurements were performed. The inset is the data for D12 zoomed in around T_g in order to more clearly show three different regions with different dynamics revealed by two kinks in the MSD. This is illustrated by the solid black lines that are linear fits to the MSD in the specified region. The second kink is around 202 K, close to the temperature where the inelastic signal starts to increase significantly, see Fig. 3.

and increase with a decrease in deuteration. This is interpreted as additional motion from the methyl and butyl arms on the cation. The calculated MSD is connected to a motion faster than a nanosecond, and at low temperatures we assume that the MSD is completely vibrational. When relaxations enter the nanosecond regime, these also contribute to the calculated MSD. It is seen from the IFWS data in Fig. 3 that the relaxations enter at lower temperature for samples with nondeuterated alkyl groups. But the D12 is the only sample where the inelastic intensity is still low at the glass transition temperature $T_g = 182 \text{ K}$, meaning that the calculated MSD is connected to the vibrational MSD.

In the D12 sample where vibrations dominate the MSD there is a kink at T_g which can be understood in terms of the decrease in G_∞ at this temperature. The vibrational MSD is governed by the elastic moduli of the sample. In the simplest approximation it is proportional to temperature over the high-frequency shear modulus, $\langle u^2 \rangle \propto T/G_\infty$ [26,59]. It is this temperature dependence of the elastic and vibrational properties above T_g that is related to the shoving model, and from this point of view it is the MSD data of the D12 sample that is most suitable for the purpose of testing the model.

While the D12 data are the cleanest in terms of excluding relaxational components from the vibrational MSD in the temperature range close to T_g , these data are hampered by the fact that the coherent contribution to the measured elastic intensity is rather high. The calculations of the MSD rely on the assumption that the data is purely incoherent, but as seen in Table I, this is far from true in D12. The coherent contribution can be seen directly in the Q dependence of the data in especially Fig. 6(b) where there is a clear shoulder at $Q^2 \approx 1.9 \text{ \AA}^{-2}$ corresponding to $Q = 1.4 \text{ \AA}^{-1}$, which is the position of the main structure factor peak measured with the (coherent) x-ray scattering technique [6,28].

In conclusion, the D0 data give the cleanest signal in terms of being closest to the assumption of fully incoherent scattering, which is also visible in Fig. 6(a) where the coherent signal is close to zero, but there will be a contribution from relaxations. In contrast to this, the D12 data is the cleanest in terms of only containing vibrational MSD and no contribution

from relaxations, but there will be a higher coherent scattering contaminating the signal. D3 and D9 are intermediate situations. Thus data from all four samples are used in the MSD analysis.

VII. TESTING THE SHOVING MODEL

From Fig. 5 it is seen that Pyr14-TFSI is a rather fragile liquid, similar to many van der Waals bonded liquids. This means that the α -relaxation time depends more on temperature than a simple Arrhenius dependence. There is no consensus on what leads to this super-Arrhenius behavior, but one class of models suggests that it is due to the increase in the elastic moduli as the liquid approaches the glassy state. The shoving model assumes that the activation energy of the α relaxation is proportional to the high-frequency shear modulus [60]. For liquids without a β relaxation, this high-frequency plateau can be measured with the PSG (see Refs. [18,26,61]); however, as we have shown, Pyr14-TFSI has a strong β relaxation and the high-frequency plateau lies beyond the frequency window of the technique. Another approach for testing the shoving model is to use the simplified harmonic approximation, which states that the vibrational MSD is proportional to temperature over high-frequency shear modulus, $\langle u^2 \rangle \propto T/G_\infty$. Both MSD data and high-frequency shear moduli have previously been used in tests of the shoving model [18], and it has been shown that the two methods were equivalent for van der Waals liquids with weak or no β relaxations [26]. The shoving model has been tested on a wide range of glass-forming liquids of different classes [18,26], but it has never before been tested on room-temperature ionic liquids.

The prediction of the shoving model is that the α -relaxation time, τ , is given by the following expression:

$$\log_{10} \tau(T) = (\log_{10} \tau_g - \log_{10} \tau_0) \frac{\langle u^2 \rangle_g}{\langle u^2 \rangle(T)} + \log_{10} \tau_0, \quad (4)$$

where τ_0 is the microscopic vibration time given by a phonon scale, and τ_g is defined as the relaxation time at the glass transition.

The shoving model has been tested with MSD values from all four samples and α -relaxation times from the shear mechanical spectra on the D0 sample. The reason we use four different data sets for finding the MSD values is that all of these methods rely on different assumptions and none of the methods are ideal; there is either coherent scattering or contributions from relaxation in the data. The different curves can in this sense be regarded as an estimate of the robustness of the shoving model test. The result is shown in Fig. 8, where the black solid line represents the shoving model prediction setting $\log_{10} \tau_0 = -14$. For all four MSD calculations the shoving model prediction works rather well. Figure 8 also shows the α -relaxation time as an Angell plot, i.e., as a function of T_g/T . The black line corresponds to Arrhenius behavior when regarded with respect to the T_g/T x axis. The closeness of the shoving model test compared to the Angell plot shows how much better the shoving model is compared to assuming an Arrhenius behavior. It is clear that the shoving model does a much better job in all the representations tested.

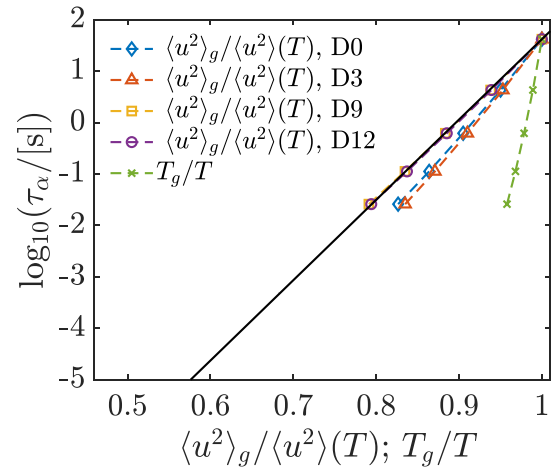


FIG. 8. A shoving plot with MSD data from for all four deuterations of Pyr14-TFSI with the shoving model prediction (black solid line). Relaxation time against $\langle u^2 \rangle_g / \langle u^2 \rangle(T)$ and temperature for the standard Angell plot (crosses). The α relaxation was found from the peak position of the shear mechanical α -relaxation peak in Fig. 2(b), with $\tau_\alpha = 1/(2\pi f_{\max})$.

VIII. CONCLUSION

In this work we have presented shear mechanical spectroscopy data, inverse ionic conductivity data found by dielectric spectroscopy, and quasielastic neutron fixed window scans on the room-temperature ionic liquid Pyr14-TFSI. From this we reveal features consistent with results on other RTILs, as well as additional features.

From the shear mechanical data we determine the temperature dependence of the α -relaxation time in the supercooled region just above the glass transition temperature and find that Pyr14-TFSI has an Angell fragility of $m_p = 85$, which is consistent with previous results. The shear data also reveal a strong and temperature-independent β relaxation as well as a relaxation mode, seen as a wing in the spectrum, appearing between the α relaxation and the β relaxation as the α relaxation moves out of the frequency window of the PSG technique. Because our study is not limited to the somewhat small frequency ranges covered by conventional rheometers we are able to report these high-frequency modes in the ionic liquids.

Elastic and inelastic fixed window scans have been measured with the backscattering instrument IN16B on samples with different degrees of deuteration of the cation. It is demonstrated that the methyl group and the end methyl group on the butyl chain, both placed on the cation, give rise to dynamics which are faster than, and clearly separated from, the α relaxation. By comparing the modes detected with the shear mechanical and neutron-backscattering techniques in a relaxation map it is found that the α relaxation from both techniques have consistent behavior, as expected. It is, on the other hand, clear that the β relaxation and the wing seen in the shear spectra are unrelated to the methyl and butyl group dynamics observed with the neutron data. Consequently, a total of four distinct relaxational modes faster than the α relaxation have been identified for Pyr14-TFSI. This rich dynamical picture is

maybe not surprising, given that an ionic liquid intrinsically is a binary system and that both van der Waals and Coulomb interactions play a role. Ionic liquids are also known to have structure on different length scales. The structure factor of Pyr14-TFSI reported in literature has a characteristic main structure factor peak as well as a peak at lower Q values which is believed to be associated with the charge ordering.

From the α -relaxation and transport properties, we find that Pyr14-TFSI has a behavior similar to that of other simpler glass-forming liquids, since the temperature dependence of the shear mechanical α relaxation is proportional to the resistivity (inverse ionic conductivity), showing that the viscous slowing down and the ionic conductivity are coupled, which is also shown in other studies on RTIL [30,54].

This picture of simple behavior in a structurally and dynamically complex ionic liquid is further strengthened by Pyr14-TFSI's compliance to the shoving model, which predicts that the temperature dependence of the α -relaxation time is governed by the vibrational mean-square displacement, i.e.,

high-frequency rigidity. This is also the case in other, more simple classes of liquids [26]. Moreover, earlier work has shown that Pyr14-TFSI obeys density scaling of both α relaxation and viscosity and resistivity [27–29].

The overall picture of this study is that while Pyr14-TFSI has complex structural features and rich dynamics, the α relaxation has a behavior remarkably similar to that of other glass-forming liquids in that (1) ionic transport and structural relaxation is coupled as also proposed earlier, and (2) the temperature dependence of the α relaxation is governed by high-frequency rigidity, through vibrational MSD, as predicted by the shoving model.

ACKNOWLEDGMENT

This work is part of the project RiDILiq, which is funded by the Independent Research Fund, Denmark.

-
- [1] Z. Lei, B. Chen, Y.-M. Koo, and D. R. MacFarlane, Introduction: Ionic liquids, *Chem. Rev.* **117**, 6633 (2017).
- [2] A. Matic and B. Scrosati, Ionic liquids for energy applications, *MRS Bull.* **38**, 533 (2013).
- [3] E. Jónsson, Ionic liquids as electrolytes for energy storage applications—A modelling perspective, *Energy Storage Mater.* **25**, 827 (2020).
- [4] A. Triolo, O. Russina, H.-J. Bleif, and E. Di Cola, Nanoscale segregation in room temperature ionic liquids, *J. Phys. Chem. B* **111**, 4641 (2007).
- [5] A. Triolo, O. Russina, B. Fazio, G. B. Appetecchi, M. Carewska, and S. Passerini, Nanoscale organization in piperidinium-based room temperature ionic liquids, *J. Chem. Phys.* **130**, 164521 (2009).
- [6] L. Aguilera, J. Vlkner, A. Labrador, and A. Matic, The effect of lithium salt doping on the nanostructure of ionic liquids, *Phys. Chem. Chem. Phys.* **17**, 27082 (2015).
- [7] A. M. Flesham and N. A. Mauro, Temperature-dependent structure and transport of ionic liquids with short-and intermediate-chain length pyrrolidinium cations, *J. Mol. Liq.* **279**, 23 (2019).
- [8] S. Li, J. L. Bañuelos, J. Guo, L. Anovitz, G. Rother, R. W. Shaw, P. C. Hillesheim, S. Dai, G. A. Baker, and P. T. Cummings, Alkyl chain length and temperature effects on structural properties of pyrrolidinium-based ionic liquids: A combined atomistic simulation and small-angle x-ray scattering study, *J. Phys. Chem. Lett.* **3**, 125 (2012).
- [9] T. Mackoy, N. A. Mauro, and R. A. Wheeler, Temperature dependence of static structure factor peak intensities for a pyrrolidinium-based ionic liquid, *J. Phys. Chem. B* **123**, 1672 (2019).
- [10] C. S. Santos, N. S. Murthy, G. A. Baker, and E. W. Castner, Communication: X-ray scattering from ionic liquids with pyrrolidinium cations, *J. Chem. Phys.* **134**, 121101 (2011).
- [11] C. A. Angell, Relaxation in liquids, polymers and plastic crystals—Strong fragile patterns and problems, *J. Non-Cryst. Solids* **131-133**, 13 (1991).
- [12] P. Sippel, P. Lunkenheimer, S. Krohns, E. Thoms, and A. Loidl, Importance of liquid fragility for energy applications of ionic liquids, *Sci. Rep.* **5**, 13922 (2015).
- [13] C. Gainaru, R. Figuli, T. Hecksher, B. Jakobsen, J. C. Dyre, M. Wilhelm, and R. Böhmer, Shear-Modulus Investigations of Monohydroxy Alcohols: Evidence for a Short-Chain-Polymer Rheological Response, *Phys. Rev. Lett.* **112**, 098301 (2014).
- [14] K. Adrjanowicz, B. Jakobsen, T. Hecksher, K. Kaminski, M. Dulski, M. Paluch, and K. Niss, Communication: Slow supramolecular mode in amine and thiol derivatives of 2-ethyl-1-hexanol revealed by combined dielectric and shear-mechanical studies, *J. Chem. Phys.* **143**, 181102 (2015).
- [15] M. H. Jensen, C. Gainaru, C. Alba-Simionesco, T. Hecksher, and K. Niss, Slow rheological mode in glycerol and glycerol-water mixtures, *Phys. Chem. Chem. Phys.* **20**, 1716 (2018).
- [16] S. Arrese-Igor, A. Alegría, and J. Colmenero, Multimodal character of shear viscosity response in hydrogen bonded liquids, *Phys. Chem. Chem. Phys.* **20**, 27758 (2018).
- [17] T. Cosby, Z. Vicars, Y. Wang, and J. Sangoro, Dynamic-mechanical and dielectric evidence of long-lived mesoscale organization in ionic liquids, *J. Phys. Chem. Lett.* **8**, 3544 (2017).
- [18] T. Hecksher and J. C. Dyre, A review of experiments testing the shoving model, *J. Non-Cryst. Solids* **407**, 14 (2015).
- [19] F. S. Howell, R. A. Bose, P. B. Macedo, and C. T. Moynihan, Electrical relaxation in a glass-forming molten salt, *J. Phys. Chem.* **78**, 639 (1974).
- [20] A. Rivera, A. Brodin, A. Pugachev, and E. A. Rössler, Orientational and translational dynamics in room temperature ionic liquids, *J. Chem. Phys.* **126**, 114503 (2007).
- [21] J. R. Sangoro, A. Serghei, S. Naumov, P. Galvosas, J. Kärger, C. Wespe, F. Bordusa, and F. Kremer, Charge transport and mass transport in imidazolium-based ionic liquids, *Phys. Rev. E* **77**, 051202 (2008).
- [22] Z. Wojnarowska and M. Paluch, Recent progress on dielectric properties of protic ionic liquids, *J. Phys.: Condens. Matter* **27**, 073202 (2015).

- [23] W. Tu, G. Szklarz, K. Adrjanowicz, K. Grzybowska, J. Knapik-Kowalczyk, and M. Paluch, Effect of cation *n*-alkyl side-chain length, temperature, and pressure on the glass-transition dynamics and crystallization tendency of the [c n c1pyrr]+[tf2n]- ionic liquid family, *J. Phys. Chem. C* **123**, 12623 (2019).
- [24] J. C. Dyre, Colloquium: The glass transition and elastic models of glass-forming liquids, *Rev. Mod. Phys.* **78**, 953 (2006).
- [25] J. C. Dyre, T. Christensen, and N. B. Olsen, Elastic models for the non-Arrhenius viscosity of glass-forming liquids, *J. Non-Cryst. Solids* **352**, 4635 (2006).
- [26] H. W. Hansen, B. Frick, T. Hecksher, J. C. Dyre, and K. Niss, Connection between fragility, mean-squared displacement and shear modulus in two van der Waals bonded glass-forming liquids, *Phys. Rev. B* **95**, 104202 (2017).
- [27] K. R. Harris and M. Kanakubo, Self-diffusion, velocity cross-correlation, distinct diffusion and resistance coefficients of the ionic liquid [BMIM][Tf₂N] at high pressure, *Phys. Chem. Chem. Phys.* **17**, 23977 (2015).
- [28] H. W. Hansen, F. Lundin, K. Adrjanowicz, B. Frick, A. Matic, and K. Niss, Density scaling of structure and dynamics of an ionic liquid, *Phys. Chem. Chem. Phys.* **22**, 14169 (2020).
- [29] F. Lundin, H. W. Hansen, K. Adrjanowicz, B. Frick, D. Rauber, R. Hempelmann, O. Shebanova, K. Niss, and A. Matic, Pressure and temperature dependence of local structure and dynamics in an ionic liquid, *J. Phys. Chem. B* **125**, 2719 (2021).
- [30] A. Martinelli, A. Matic, P. Jacobsson, L. Börjesson, A. Fernicola, and B. Scrosati, Phase behavior and ionic conductivity in lithium bis(trifluoromethanesulfonyl)imide-doped ionic liquids of the pyrrolidinium cation and bis(trifluoromethanesulfonyl)imide anion, *J. Phys. Chem. B* **113**, 11247 (2009).
- [31] M. Kunze, S. Jeong, E. Paillard, M. Schonhoff, M. Winter, and S. Passerini, New insights to self-aggregation in ionic liquid electrolytes for high-energy electrochemical devices, *Adv. Energy Mater.* **1**, 274 (2011).
- [32] K. R. Harris, L. A. Woolf, M. Kanakubo, and T. Rütger, Transport properties of N-butyl-N-methylpyrrolidinium bis(trifluoromethylsulfonyl)amide, *J. Chem. Eng. Data* **56**, 4672 (2011).
- [33] F. M. Vitucci, D. Manzo, M. A. Navarra, O. Palumbo, F. Trequattrini, S. Panero, P. Bruni, F. Croce, and A. Paolone, Low-temperature phase transitions of 1-butyl-1-methylpyrrolidinium bis(trifluoromethanesulfonyl)imide swelling a polyvinylidene fluoride electrospun membrane, *J. Phys. Chem. C* **118**, 5749 (2014).
- [34] E. Zorebski, M. Zorebski, M. Dzida, P. Goodrich, and J. Jacquemin, Isobaric and isochoric heat capacities of imidazolium-based and pyrrolidinium-based ionic liquids as a function of temperature: Modeling of isobaric heat capacity, *Ind. Eng. Chem. Res.* **56**, 2592 (2017).
- [35] R. Ge, C. Hardacre, J. Jacquemin, P. Nancarrow, and D. W. Rooney, Heat capacities of ionic liquids as a function of temperature at 0.1 mPa. measurement and prediction, *J. Chem. Eng. Data* **53**, 2148 (2008).
- [36] E. W. Castner, J. F. Wishart, and H. Shirota, Intermolecular dynamics, interactions, and solvation in ionic liquids, *Acc. Chem. Res.* **40**, 1217 (2007).
- [37] H. Shirota, A. M. Funston, J. F. Wishart, and E. W. Castner, Jr., Ultrafast dynamics of pyrrolidinium cation ionic liquids, *J. Chem. Phys.* **122**, 184512 (2005).
- [38] See Supplemental Material at <http://link.aps.org/supplemental/10.1103/PhysRevMaterials.5.065606> for detailed description of the data analysis used in this study [[62,63]].
- [39] C. D. Tran, S. H. De Paoli Lacerda, and D. Oliveira, Absorption of water by room-temperature ionic liquids: Effect of anions on concentration and state of water, *Appl. Spectrosc.* **57**, 152 (2003).
- [40] T. Christensen and N. B. Olsen, A rheometer for the measurement of a high shear modulus covering more than seven decades of frequency below 50 kHz, *Rev. Sci. Instrum.* **66**, 5019 (1995).
- [41] B. Igarashi, T. Christensen, E. H. Larsen, N. B. Olsen, I. H. Pedersen, T. Rasmussen, and J. C. Dyre, An impedance-measurement setup optimized for measuring relaxations of glass-forming liquids, *Rev. Sci. Instrum.* **79**, 045106 (2008).
- [42] B. Igarashi, T. Christensen, E. H. Larsen, N. B. Olsen, I. H. Pedersen, T. Rasmussen, and J. C. Dyre, A cryostat and temperature control system optimized for measuring relaxations of glass-forming liquids, *Rev. Sci. Instrum.* **79**, 045105 (2008).
- [43] B. Frick, J. Combet, and L. van Eijck, New possibilities with inelastic fixed window scans and linear motor Doppler drives on high resolution neutron backscattering spectrometers, *Nucl. Instrum. Methods Phys. Res., Sect. A* **669**, 7 (2012).
- [44] M. Busch, T. Hofmann, B. Frick, J. P. Embs, B. Dyatkin, and P. Huber, Ionic liquid dynamics in nanoporous carbon: A pore-size- and temperature-dependent neutron spectroscopy study on supercapacitor materials (2020).
- [45] D. Richard, M. Ferrand, and G. J. Kearley, Analysis and visualisation of neutron-scattering data, *J. Neutron Res.* **4**, 33 (1996).
- [46] T. Cosby, Z. Vicars, M. Heres, K. Tsunashima, and J. Sangoro, Dynamic and structural evidence of mesoscopic aggregation in phosphonium ionic liquids, *J. Chem. Phys.* **148**, 193815 (2018).
- [47] O. Palumbo, F. Trequattrini, F. M. Vitucci, and A. Paolone, Relaxation dynamics and phase transitions in ionic liquids: Viscoelastic properties from the liquid to the solid state, *J. Phys. Chem. B* **119**, 12905 (2015).
- [48] T. Hecksher, N. B. Olsen, and J. C. Dyre, Model for the alpha and beta shear-mechanical properties of supercooled liquids and its comparison to squalane data, *J. Chem. Phys.* **146**, 154504 (2017).
- [49] B. Jakobsen, K. Niss, C. Maggi, N. B. Olsen, T. Christensen, and J. C. Dyre, Beta relaxation in the shear mechanics of viscous liquids: Phenomenology and network modeling of the alpha-beta merging region, *J. Non-Cryst. Solids* **357**, 267 (2011).
- [50] T. Burankova, G. Simeoni, R. Hempelmann, J. F. Mora Cardozo, and J. P. Embs, Dynamic heterogeneity and flexibility of the alkyl chain in pyridinium-based ionic liquids, *J. Phys. Chem. B* **121**, 240 (2017).
- [51] T. Burankova, E. Reichert, V. Fossog, R. Hempelmann, and J. P. Embs, The dynamics of cations in pyridinium-based ionic liquids by means of quasielastic- and inelastic neutron scattering, *J. Mol. Liq.* **192**, 199 (2014).
- [52] R. Böhmer and C. A. Angell, Correlations of the nonexponentiality and state dependence of mechanical relaxations with bond connectivity in Ge-As-Se supercooled liquids, *Phys. Rev. B* **45**, 10091 (1992).
- [53] R. Böhmer, K. L. Ngai, C. A. Angell, and D. J. Plazek, Non-exponential relaxations in strong and fragile glass formers, *J. Chem. Phys.* **99**, 4201 (1993).

- [54] C. J. Jafra, C. Bridges, L. Haupt, C. Do, P. Sippel, M. J. Cochran, S. Krohns, M. Ohl, A. Loidl, E. Mamontov, P. Lunkenheimer, S. Dai, and X.-G. Sun, Ion dynamics in ionic-liquid-based li-ion electrolytes investigated by neutron scattering and dielectric spectroscopy, *ChemSusChem* **11**, 3512 (2018).
- [55] G. P. Johari, Glass transition and secondary relaxations in molecular liquids and crystals, *Ann. N.Y. Acad. Sci.* **279**, 117 (1976).
- [56] A. Rahman, K. S. Singwi, and A. Sjölander, Theory of slow neutron scattering by liquids. I, *Phys. Rev.* **126**, 986 (1962).
- [57] R. Zorn, Multiple scattering correction of neutron scattering elastic scans, *Nucl. Instrum. Methods Phys. Res., Sect. A* **572**, 874 (2007).
- [58] R. Zorn, On the evaluation of neutron scattering elastic scan data, *Nucl. Instrum. Methods Phys. Res., Sect. A* **603**, 439 (2009).
- [59] J. C. Dyre and N. B. Olsen, Landscape equivalent of the shoving model, *Phys. Rev. E* **69**, 042501 (2004).
- [60] J. C. Dyre, N. B. Olsen, and T. Christensen, Local elastic expansion model for viscous-flow activation energies of glass-forming molecular liquids, *Phys. Rev. B* **53**, 2171 (1996).
- [61] B. Jakobsen, K. Niss, and N. B. Olsen, Dielectric and shear mechanical alpha and beta relaxations in seven glass-forming liquids, *J. Chem. Phys.* **123**, 234511 (2005).
- [62] F. Kremer and A. Schönhalz (editors), *Broadband Dielectric Spectroscopy* (Springer, Berlin, 2003).
- [63] P. Thompson, D. E. Cox, and J. B. Hastings, Rietveld refinement of Debye–Scherrer synchrotron x-ray data from Al_2O_3 , *J. Appl. Crystallogr.* **20**, 79 (1987).

E.2 Pressing matter: why are ionic liquids so viscous?

Cite this: *Chem. Sci.*, 2022, 13, 2735

All publication charges for this article have been paid for by the Royal Society of Chemistry

Received 8th December 2021
Accepted 6th February 2022

DOI: 10.1039/d1sc06857a

rsc.li/chemical-science

Pressing matter: why are ionic liquids so viscous?†

Frederik Philippi,^a Daniel Rauber,^b Kira Lieberkind Eliassen,^c
Nathalie Bouscharain,^d Kristine Niss,^c Christopher W. M. Kay^{be}
and Tom Welton^{id}*^a

Room temperature ionic liquids are considered to have huge potential for practical applications such as batteries. However, their high viscosity presents a significant challenge to their use changing from niche to ubiquitous. The modelling and prediction of viscosity in ionic liquids is the subject of an ongoing debate involving two competing hypotheses: molecular and local mechanisms *versus* collective and long-range mechanisms. To distinguish between these two theories, we compared an ionic liquid with its uncharged, isoelectronic, isostructural molecular mimic. We measured the viscosity of the molecular mimic at high pressure to emulate the high densities in ionic liquids, which result from the Coulomb interactions in the latter. We were thus able to reveal that the relative contributions of coulombic compaction and the charge network interactions are of similar magnitude. We therefore suggest that the optimisation of the viscosity in room temperature ionic liquids must follow a dual approach.

Introduction

In recent years, ionic liquids have transformed from a scientific curiosity to extensively used functional fluids, both in academia and industry.^{1–5} However, the practical applicability of most ionic liquids is limited by their high viscosity compared with conventional molecular solvents. This is a key aspect for applications such as batteries, gas separation or biomass processing. In order to optimise the viscosity, it is necessary to develop a mechanistic understanding of the difference between how viscosity arises in ionic liquids and conventional molecular solvents.

A fair, unbiased comparison between ionic liquids and conventional molecular solvents necessitates two systems which are as similar as possible; one charged, and one neutral. The neutral system has been called the ‘molecular mimic’^{6,7} and is a mixture of neutral analogues of the anionic and cationic molecular constituents.^{6–8} To ensure similarity, the molecular

mimic and the corresponding ionic liquid should ideally be isoelectronic and isostructural to each other. Fig. 1 shows the molecular mimic used by Shirota and Castner, together with the viscosity and density values at room temperature and ambient pressure.⁹ Crucially, the viscosity of the ionic liquid is almost 30 times that of the molecular mimic, despite the similar molecular structures. One might interpret this factor of 30 as the difference between conventional molecular solvent and ionic liquid, *i.e.* the isolated effect of the added charge. However, the ionic liquid also has a higher density than the molecular mimic, which still constitutes a bias. The higher density is the result of coulombic compaction, *i.e.* strong (attractive) coulombic interactions which reduce the volume of the liquid phase.⁹

The differences in density and viscosity lead to an important question: what is the degree to which coulombic compaction causes the high viscosity of ionic liquids? It is well known that an increase in density (*i.e.* pressure) generally leads to an increase in viscosity.^{10,11} Indeed, the viscosity of both molecular and ionic liquids can often be expressed as a function of ρ^γ/T , where ρ is the density, T the temperature and γ a material

^aDepartment of Chemistry, Molecular Sciences Research Hub, Imperial College London, White City Campus, London W12 0BZ, UK. E-mail: t.welton@imperial.ac.uk

^bDepartment of Chemistry, Saarland University, Campus B2.2, Saarbrücken, Germany
^c“Glass and Time”, IMFUFA, Department of Science and Environment, Roskilde University, P.O. Box 260, DK-4000 Roskilde, Denmark

^dUniversity of Lyon, INSA Lyon, CNRS, LaMCoS, UMR 5259, 69621 Villeurbanne, France

^eLondon Centre for Nanotechnology, University College London, 17-19 Gordon Street, London WC1H 0AH, UK

† Electronic supplementary information (ESI) available: Experimental selection of the Molecular Mimic, isodensity conditions from the literature, *P*–*V*–*T* measurements at ambient and elevated pressure, viscosity measurements at ambient and elevated pressure, diffusion coefficients and syntheses. See DOI: 10.1039/d1sc06857a

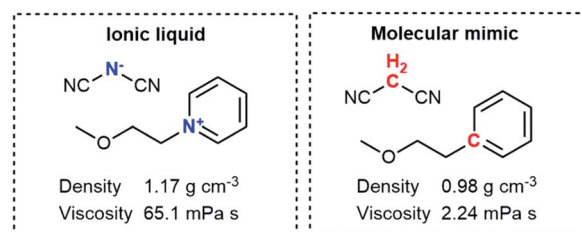


Fig. 1 The ionic liquid (left) and molecular mimic (right) investigated by Shirota and Castner.⁹



parameter.^{12–15} Consequently, the comparison between a molecular mimic and an ionic liquid should be made under isodensity conditions. In other words, the molecular mimic must be subjected to pressure high enough so that its density becomes equal to that of the ionic liquid under ambient pressure at the same temperature. It is conceivable that the two systems would then also have similar viscosities.¹⁶ If this were the case, it would imply that the high density itself was the cause of the high viscosity.

A wide variety of models with considerable conceptual overlap have been developed to describe viscous flow of ionic liquids.^{17–33} Some models aim to further our understanding of the underlying physics from a basic scientific viewpoint with often limited predictive value. Other models aim to provide predictive tools – which are numerically accurate but often without physical basis – for engineering purposes. At present, there is considerable dispute about which of the approaches is preferable for ionic liquids, but clearly the ultimate goal is to develop physically sound models which also provide reliable quantitative predictions.

In order to resolve these difficulties, we separate the change in viscosity into two steps. First from the molecular mimic under ambient conditions to the molecular mimic when isodense with the ionic liquid, and second from the isodense molecular mimic to the ionic liquid. The viscosity models can then be separated into two groups accordingly.

Some researchers favour models describing the indirect effects of coulombic compaction, for example hole theory, free volume theory or the shoving model.^{24,28–32,34} These models are not unique to ionic liquids, but gain significance due to the apparent ‘high pressure’ conditions. Mechanistically, the processes are dominated by molecular level relaxation. Related concepts such as the ion cage or activation volumes are commonly used in the ionic liquids community.^{35–38}

Others prefer models which approach the problem on a collective rather than molecular level. In contrast to molecular liquids, ionic liquids are subject to intermolecular electro-neutrality conditions, leading to the formation of a charge network.^{39,40} Viscous flow was found to be coupled to the structural relaxation of this charge network.^{19–21} Shelepova *et al.* recently compared the structure of an ionic liquid and its isodense molecular mimic by means of molecular dynamics simulations.⁴¹ The authors observed rather similar total radial distribution functions for the charged and uncharged systems, despite the additional screening conditions for the charged system which lead to the formation of a charge network, *i.e.* a shell structure of oppositely charged ions around each reference ion.^{41–43}

The concept of experimentally measuring molecular mimics under isodensity conditions was explored in 1968 by Morrison and Lind,⁴⁴ however only at elevated temperatures.^{45,46} For tetrabutylammonium tetrabutylborate $[\text{NBu}_4][\text{BBu}_4]$, a viscosity of 18.7 mPa s at 114 °C was reported. The viscosity of the corresponding molecular mimic, tetrabutylmethane $[\text{CBu}_4][\text{CBu}_4]$, was about 2.5 mPa s at isodensity conditions and 0.92 mPa s at ambient pressure (see ESI, Section 1†).⁴⁴ Hence, the two factors by which viscosity increases were 2.7 (from the molecular mimic

to the isodense molecular mimic) and 7.5 (from the isodense molecular mimic to the ionic liquid).⁴⁴ Data at lower temperatures are not available due to the high melting point of $[\text{NBu}_4][\text{BBu}_4]$ of about 110 °C.⁴⁵ However, comparison with the viscosity ratios at higher temperatures shows that the relative difference in viscosity between the ionic liquid and the isodense molecular mimic increases significantly at lower temperatures. At 163 °C, the viscosity ratios were 2.4 (from the molecular mimic to the isodense molecular mimic) and 5.1 (from the isodense molecular mimic to the ionic liquid).

Molecular dynamics simulations can also be employed to directly compare ionic liquids and their molecular mimics. Roy *et al.* performed molecular dynamics simulations on a coarse grained model of 1-butyl-3-methylimidazolium hexafluorophosphate.⁴⁷ In order to realise the molecular mimic, the authors simply removed electrostatic interactions. At a simulation temperature of 450 K, the viscosity increases by a factor of 75 from the isodense molecular mimic (1.1 mPa s) to the ionic liquid (83 mPa s).⁴⁷ Unfortunately a comparison between the molecular mimic under ambient pressure and the isodense molecular mimic is not feasible since at this temperature the molecular mimic is a gas (under ambient pressure).

The large difference between isodense molecular mimics and ionic liquids is surprising, given that Shirota *et al.* observed only a factor of 30 between their molecular mimic under ambient conditions and the ionic liquid. Critically, if the experimental results from Morrison and Lind were universally transferable, then the relative viscosity increases observed by Roy *et al.* should be smaller than those observed by Shirota *et al.* since the latter are (a) at a lower temperature and (b) additionally include the change from the molecular mimic under ambient pressure to the molecular mimic under isodensity conditions. Importantly, Roy *et al.* revised their model to more closely match experimental values.⁴⁸ In the revised model, the viscosity of the ionic liquid is only 3.4 mPa s at 450 K,⁴⁸ compared to 83 mPa s in the original model.⁴⁷ A direct comparison at 450 K across the two models would not be meaningful due to various changes to simulation conditions and the force field itself. However, the authors provide the required data at 350 K: here, the viscosity changes by a factor of 22 from the isodense molecular mimic (1.2 mPa s) to the ionic liquid (26 mPa s).⁴⁸ In addition, the authors provide viscosity data under ambient pressure and temperature. At 298 K, the molecular mimic has a viscosity of 0.42 mPa s, compared to the ionic liquid with a viscosity of 330 mPa s (with a reported uncertainty of ± 100 mPa s).⁴⁸ This corresponds to a change in viscosity by a factor of 785, however there is no information regarding the relative contributions of charge network and coulombic compaction.

A similar approach has been followed by Park *et al.* who performed MD simulations on a generalised coarse grained model based on ionic liquids such as 1-butyl-3-methylimidazolium hexafluorophosphate.⁴⁹ The authors provide diffusion coefficients, from which the viscosity ratios can be estimated (see ESI Section 1†). The relative increases in viscosity from the isodense molecular mimic to the ionic liquid are 12 (at 370 K) and ≈ 370 (at 250 K). These results clearly show



the pronounced temperature dependence of the viscosity difference between ionic liquids and their molecular mimics, even if the numerical values are not quantitatively transferable to realistic ionic liquids.

Due to recent advances in the field of (room temperature) ionic liquids, a study at ambient temperatures is now possible. Here, we demonstrate a proof of concept for the entire approach, from the selection of an experimental system to the characterisation under high pressure. Our results have far-reaching implications for the development of viscosity models, which must account for the diverse nature of ionic liquids.

Choice of experimental system

The selection of an appropriate experimental system is non-trivial, since a multitude of requirements have to be simultaneously fulfilled:

- (1) The molecular mimic should be structurally similar to the ionic liquid.
- (2) Both molecular mimic and ionic liquid must be experimentally accessible.
- (3) The two components of the molecular mimic must not react with each other, even under pressure.
- (4) The components must be miscible, and the molecular mimic must remain homogeneous and liquid under isodensity conditions.
- (5) The equipment must be resistant to the involved compounds.

The similarity of the ionic liquid and the molecular mimic is an obvious requirement, but some cases require compromises. For example, the malononitrile chosen by Shirota and Castner as a neutral analogue to the dicyanamide anion may introduce hydrogen bonding to the ether group present in the cation's neutral analogue.⁹ Hydrogen bonds between ether groups and the C–H acidic malononitrile have been reported in the literature using both experimental and theoretical methods.^{50–53} An alternative would be cyanogen oxide $O(CN)_2$, but this violates at least the second and third requirements. Similarly, one trivial neutral analogue of the acetate anion is the rather hazardous and volatile acetyl fluoride. For our preliminary studies, therefore, we considered acetyl chloride, acetic acid and nitromethane as neutral analogues.

The second point applies for compounds such as Ar, CF_4 and SF_6 , which are the trivial neutral analogues for Cl^- , $[BF_4]^-$ and $[PF_6]^-$. These neutral analogues are, while stable, all gaseous under ambient conditions, presenting a significant obstacle for experimental investigations. In contrast, neutral analogues of this type are predestined for computer simulation. Even if the experimental setup can be prepared with an equimolar mixture of, say, propane and tetrafluoromethane, it would be preferable to have an estimate for required pressures and liquid–liquid critical points beforehand.

We initially considered the commonly used ionic liquid $[C_4C_{1im}][NTf_2]$. To this end, the imidazolium cation could be replaced with a furan or pyrrole based neutral analogue, and the anion could be replaced with triflic anhydride OTf_2 , the free

acid $HNTf_2$ or methylene ditriflone CH_2Tf_2 . However, as these compounds are rather reactive, they are not compatible with each other and indeed many other neutral analogues. Phosphonium and ammonium ionic liquids are much more benign in this respect, as they may be mimicked by thermodynamically stable silanes and hydrocarbons.

The fourth point must be kept in mind for the measurements under high pressure. For example, we considered nitromethane as a neutral analogue for the acetate anion. At ambient temperature, pure nitromethane solidifies at 400 MPa, even if the decomposition pressure itself is too high (around 30 GPa) to be of relevance for the measurements in this work.^{54,55} Similar issues arise for the actual molecular mimic, *i.e.* the mixture of two neutral analogues. High pressure might effectively raise the critical temperature of this mixture to above ambient temperatures, leading to undesirable phase separation.⁵⁶ Our solution to this problem was to optimise towards molecular mimics with low critical temperatures. To this end, promising molecular mimics were subjected to progressively lower temperatures (ambient temperature 20 °C, fridge 5 °C, freezer –20 °C, dry ice –78 °C). For example, the molecular mimic composed of triethyl pentyl silane and 1-nitropropane was miscible at 20 °C, but not at 5 °C. A similar molecular mimic with 1-nitrohexane instead of 1-nitropropane remained homogeneous and liquid at –20 °C, but solidified at –78 °C.

Finally, the equipment itself puts restrictions on the scope of molecular mimics that can be investigated. Many instruments for high-pressure rheology and densitometry are built for engineering fluids, without consideration of resistance to aggressive compounds.

Considering all these points, we identified the experimental system shown in Fig. 2. The ionic liquid is triethyl(3-methoxypropyl)phosphonium butyrate, the corresponding molecular mimic is an equimolar mixture of triethyl(3-methoxypropyl)silane and 1-nitropropane. The presence of an ether group helped achieve miscibility over a wide temperature range. For the sake of simplicity, we will henceforth use “the ionic liquid” and “the molecular mimic” for this system. Details on the exploratory experiments leading to this choice can be found in the ESI, Section 2.†

Results

The densities of the ionic liquid and the molecular mimic were measured at ambient pressure as a function of temperature (see ESI, Section 3†). The experimental densities at room temperature and ambient pressure were 0.874(1) $g\ cm^{-3}$ for the molecular mimic and 1.032(1) $g\ cm^{-3}$ for the ionic liquid.

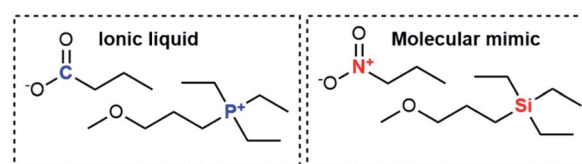


Fig. 2 The ionic liquid/molecular mimic combination used in this work.



Furthermore, we have measured the viscosity of the ionic liquid and the molecular mimic at ambient pressure (see ESI, Section 4†). The experimental viscosities at room temperature and ambient pressure were 0.86 mPa s for the molecular mimic and 217 mPa s for the ionic liquid. These values were obtained from Arrhenius and Vogel–Fulcher–Tammann fits, respectively, see ESI, Section 4.† However, our cone-plate setup was optimised for (relatively viscous) ionic liquids and does not perform well with low viscosity fluids. Hence, we repeated the measurement at ambient pressure and room temperature using a setup with coaxial geometry, and obtained a viscosity of 0.99(4) mPa s for the molecular mimic. While not significantly different from the cone-plate setup, this value is in quantitative agreement with the viscosity value obtained from the falling body experiment and will be used henceforth.

Pressure–volume measurements were then performed to identify the pressure required for isodensity conditions, *i.e.* the pressure at which the density of the molecular mimic reaches 1.032 g cm^{-3} . The density was extrapolated from the highest attainable pressure with our equipment ($\approx 340 \text{ MPa}$) using the Tait equation.^{57,58} The results are presented in Fig. 3, details can be found in the ESI, Section 3.† We thus identified $\approx 460 \text{ MPa}$ as the pressure for isodensity conditions. Subsequently, the viscosity of the molecular mimic was measured as a function of pressure up to 500 MPa using a falling body viscometer. The viscosity of the molecular mimic at a pressure of 460 MPa, *i.e.* at a density of 1.032 g cm^{-3} , was approximately 14 mPa s, Fig. 4. Details of the high-pressure rheology and the interpolation can be found in the ESI, Section 4.†

In contrast to viscosity, diffusion coefficients can be determined separately for cation and anion. Diffusion coefficients were measured at ambient pressure and $25 \text{ }^\circ\text{C}$, Table 1.

Discussion

The key findings of this work are summarised schematically in Fig. 5. The viscosity of the ionic liquid at ambient temperature

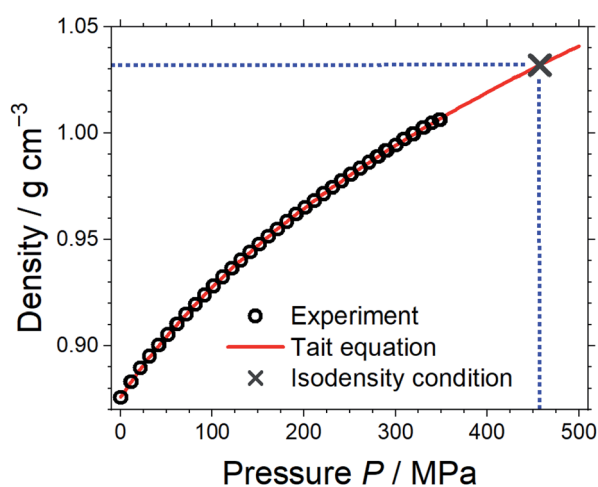


Fig. 3 Density of the molecular mimic as a function of pressure. The Tait equation was used to extrapolate to the density of the corresponding ionic liquid, and the blue dashed lines indicate how the pressure required for isodensity conditions was obtained.

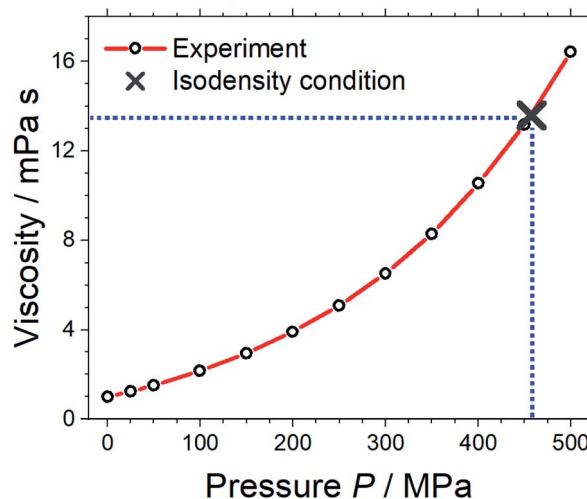


Fig. 4 Viscosity of the molecular mimic as a function of density. The blue dashed lines indicate the viscosity under isodensity conditions.

and pressure is higher by a factor of 219 than the viscosity of the isostructural, isoelectronic molecular mimic. This significant increase in viscosity can be separated into two contributions using pressure-dependent densitometry and rheology. First, the higher density of the ionic liquid – or, equivalently, the high pressure isodensity conditions for the molecular mimic – leads to an increase in viscosity. This can be understood in terms of viscosity models established for molecular liquids. Second, the charged nature of the ionic liquids leads to an additional increase in viscosity due to additional electrostatic restrictions on the motion of molecular ions.

Importantly, the relative contribution to the bulk viscosity was of equal magnitude in this case, with the viscosity increasing by a factor of 14 and 16. Hence, the indirect effects of coulombic compaction (factor of 14) and the direct effects of the charge network (factor of 16) are equally important. It appears that viscous flow in ionic liquids at room temperature enters a regime where a balance of different relaxation mechanisms becomes important, rather than just one dominating mechanism. This finding is interesting in light of the viscosity models discussed in the literature, many of which are reported to be applicable to ionic liquids.^{17–23,25–33} Indeed, the debate mentioned above is resolved insofar as different approaches to model the viscosity of ionic liquids seem to be not only justified, but necessary.

The two major contributions to ionic liquid viscosity are also important from a practical point of view. The results shown in

Table 1 Diffusion coefficients obtained from PFGSTE NMR diffusometry

System	Constituent	Diffusion coefficient
Molecular mimic	Si222(3O1)	$8.46 \times 10^{-10} \text{ m}^2 \text{ s}^{-1}$
	Nitropropane	$1.39 \times 10^{-9} \text{ m}^2 \text{ s}^{-1}$
Ionic liquid	$[\text{P222(3O1)}]^+$	$5.39 \times 10^{-12} \text{ m}^2 \text{ s}^{-1}$
	$[\text{C}_3\text{H}_7\text{COO}]^-$	$5.90 \times 10^{-12} \text{ m}^2 \text{ s}^{-1}$

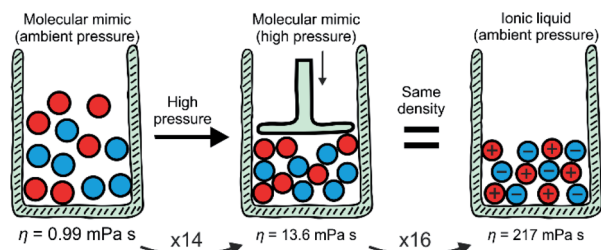


Fig. 5 Summary of the results. Scheme adapted from ref. 8 – published by The Royal Society of Chemistry.

Fig. 5 demonstrate that the optimisation of viscosity at room temperature must follow a dual approach. Different design concepts have been proposed to adjust the viscosity of ionic liquids, such as hydrogen bonding or conformational flexibility. For example, Fumino *et al.* proposed directional hydrogen bonding as a way to disrupt the charge network.⁵⁹ This hypothesis could be tested using the approach we presented in this work. To name an example regarding the second contribution, *i.e.* Coulombic compaction, several groups have proposed conformational flexibility as a means to facilitate dynamics such as viscous flow and diffusion.^{35,60}

The two major contributions observed for the ionic liquid in this work can be expected to be relevant for other ionic liquids as well, since coulombic compaction and the formation of a charge network will be present in any case. The central question for future work is how ionic liquids can be designed to shift the balance in one or the other direction.

Design concepts tend to mechanistically exploit one of the two major contributions. Hence, there is a limit to what can be achieved with, say, conformational flexibility. Lowering the viscosity of an ionic liquid below this limit will require additional leverage from complementary design concepts, for example the addition of molecular solvent to facilitate momentum transport without violating electroneutrality conditions. Both components must be considered during the design process; for example focusing on directional bonding will not give the best possible result if conformational flexibility is disregarded, and *vice versa*.

It is worth comparing the results of this work with an overview of the literature data. To this end, Table 2 provides a summary of the prior work presented in the Introduction.

The viscosity ratios from MD simulations cover a wide range, however unfortunately no comparison is possible between the three relevant viscosity ratios due to a lack of data. A comparison of relative values based on one type of simulation would be preferable since MD simulations rarely provide quantitative predictions.

The results from MD simulations are furthermore very sensitive to the simulation setup. For example, the viscosity of the ionic liquid in the refined model by Roy *et al.* is 3.4 mPa s at 450 K, compared to 83 mPa s in the original model.^{47,48} The refined model includes charge scaling, *i.e.* a mean-field version of polarisability and charge transfer.⁴⁸ Phenomena such as polarisability are key for accurate simulations of ionic

liquids.^{61,62} Error cancellation, otherwise a strength of relative comparisons from MD simulations, is less helpful if results are to be compared between charged and uncharged systems.

Our data and the data from Morrison and Lind both show a balance of the two contributions to viscosity, especially at room temperature. The overall viscosity increase reported by Shirota *et al.* is much lower than what we observed. This might be due to hydrogen bonding induced by the malononitrile.^{50–53} It would be desirable to have high pressure data for the molecular mimic proposed by Shirota *et al.* at hand. However, the molecular mimic is likely to solidify under high pressure since the melting point of malononitrile is near room temperature.

Diffusion coefficients, unlike the viscosity, can be measured separately for each constituent and thus give access to additional information. The diffusion coefficients can be compared by analogy to the viscosity values, *cf.* the Stokes–Einstein relation in the ESI, Section 1.† We were unable to access the high pressures required for isodensity conditions, however we have measured diffusion coefficients under ambient pressure and at 25 °C. The corresponding diffusion coefficient ratios between the molecular mimic and ionic liquid diffusion are 157 for the cation (analogue) and 236 for the anion (analogue). Thus, the overall increase in viscosity from the molecular mimic to the ionic liquid translates to a comparable decrease in the translational diffusion. Interestingly, the ratio of diffusion between anion and cation (analogues) decreases from $D(\text{nitropropane})/D(\text{Si222(3O1)}) = 1.64$ in the molecular mimic to $D([\text{C}_3\text{H}_7\text{COO}]^-)/D([\text{P222(3O1)}]^+) = 1.09$ in the ionic liquid. Hence, the diffusion coefficients of the two constituents are much more similar in the ionic liquid than in the molecular mimic, which can be rationalised by the electrostatic interactions coupling the motion of cations and anions. The degree to which this coupling of motion already occurs under isodensity conditions, if at all, would be an interesting topic for future experimental and theoretical studies.

Overall, this study clearly shows how valuable insight can be gained from a comparison of ionic liquids and their molecular mimics. Without doubt, the practical importance of understanding the transport properties in ionic liquids justifies the considerable effort of performing experiments at such high pressures. It would be intriguing to study more types of ionic liquids in the future to probe the generality of the conclusions drawn from the phosphonium butyrate in this work.

Furthermore, during the selection process, we observed incompatibilities which in themselves are interesting. For example, in several cases, the cation and anion neutral analogues were not miscible. Naturally, in the ionic liquid, the two constituents must mix due to electroneutrality conditions. We hypothesise that this effect – known as nanosegregation – to some degree counteracts the effects of the charge network. The use of molecular mimics can help to identify such cases, using the mixing behaviour of the cation and anion neutral analogues as design element.

The future development of physically sound models should consider both coulombic compaction and the charge network as the two main contributors to ionic liquid viscosity. For



Table 2 Summary of viscosity ratios comparing ionic liquids (IL), molecular mimics (MM) and molecular mimics under isodensity conditions (MM*)

Setup	Temperature	MM → MM*	MM* → IL	Overall (MM → IL)	References
Coarse grained MD simulation	450 K	—	75	—	47
Coarse grained MD simulation after refinement	350 K	—	22	—	48
	298 K	—	—	785 ^a	48
Coarse grained MD simulation	370 K	—	12 ^b	—	49
	250 K	—	Approx. 370 ^b	—	49
Experimental, see Fig. 1	295 K	—	—	30 ^c	9
Experimental	436 K	2.4	5.1	12	44
	387 K	2.7	7.5	20	44
Experimental	298 K	14	16	219	This work

^a The factor is approximately 550 to 1000 within the viscosity uncertainty. ^b Obtained *via* diffusion coefficients, see ESI Section 1. ^c Likely too low due to additional hydrogen bonding in the molecular mimic.

example, mode coupling is a good approach to study and describe the connection between viscous flow and the charge network.^{19,63,64} Here, future work could explore the evolution of the dynamic structure factor of molecular mimics at wavenumbers corresponding to the charge network in the corresponding ionic liquid with the help of molecular dynamics simulations. The use of molecular dynamics has the added advantage that high pressures and even intermediates between molecular mimic and ionic liquid – with fractional charges on the molecules – are possible. *Vice versa*, approaches such as hole theory should factor in the presence of a charge network. In other words, a good model for any transport property in ionic liquids must be able to predict the difference between the isodense molecular mimic and the ionic liquid.

From an engineering point of view, the results from this work can be used to select appropriate models. Good examples are machine learning approaches, which are becoming more and more popular recently for quantitative predictions of ionic liquid properties.^{65,66} Machine learning algorithms use a number of input properties to produce an estimate of an output property. Easily accessible input properties, such as molecular weight or connectivity, are advantageous. Based on our observations, both coulombic compaction and charge network formation should be present in the input properties. Furthermore, it might be beneficial to introduce feature extraction with coulombic compaction and charge network formation as intermediate features to improve the performance of machine learning algorithms.

For future studies, it could also be worth expanding the measurements to several isotherms, which in combination with density scaling would allow the use of a ‘density–temperature superposition principle’, in analogy to the time–temperature superposition principle.^{67,68} This might enable the experimental comparison of those pairs of ionic liquid and molecular mimic where isodensity conditions are not attainable, but where common points of ρ^*/T can be found (see ESI, Section 1†). For example, it might not be possible to measure the experimental system shown in Fig. 1 under isodensity conditions due to pressure-induced crystallisation. In this case, common points of ρ^*/T could still be accessible by recording additional

isotherms for the ionic liquid (at higher temperature) and molecular mimic (at lower temperature).

Finally, experimentally challenging systems such as CF₃/[BF₄][−] may still be studied *in silico* by means of molecular dynamics simulation. Here, one of the key issues remains consistency of the parameterisation across charged and uncharged systems, for example with regards to polarisability. Our experimental results at room temperature could be used to benchmark force fields and simulation setups. Once a reliable (classical simulation) model has been identified it can be used to generate further valuable data points at different temperatures or pressures, with considerably lower expense and hazards compared to the experimental high pressure studies.

Methods

Samples were prepared under Schlenk conditions or in a glovebox, ionic liquids were dried in high vacuum before use. AgNO₃ solution was used to confirm the absence of halides in the carboxylate ionic liquids. Syntheses and (additional) physico-chemical characterisation are described in detail in the ESI.†

Densities as a function of temperature under ambient pressure were measured with a 5 mL (nominal) Reischauer pycnometer (Neubert Glas, Geschwenda, Germany) calibrated with octane and confirmed with water.⁶⁹ The pycnometer was dried in vacuum before use, weighed, and filled with sample to above the mark in a glovebox. The pycnometer was then sealed, placed in a thermostat bath (thermostatted to ±0.01 K), equilibrated for 20 min, the liquid level adjusted to the mark with a Pasteur pipette, cooled to room temperature, and weighed again.

The density of the molecular mimic under high pressure was measured to find the isodensity conditions using a U111 high pressure pump and an MV1-30 pressure chamber, both provided by Unipress in Poland. The sample is loaded into a cylindrical container with a movable piston at one end and the container is then submerged into enclosed pressure fluid which is connected to a high-pressure pump. The increasing pressure moves the piston inwards, compressing the liquid sample, during which the displacement of the piston is recorded. The density change is then calculated using the absolute mass and the change in



volume of the sample due to the increase in pressure. Measurements were performed from 0–350 MPa at 25 °C.

The viscosity under ambient pressure was measured with a cone-plate setup as well as with a coaxial setup. The cone-plate setup was used on a stress-controlled MCR 301 rheometer (Anton Paar, Graz, Austria) with a CP50-1 cone (diameter 49.95 mm, cone angle 1°) and a gap size of 0.101 mm. The measurements were performed under nitrogen atmosphere with shear rates varying from 5 to 150 s⁻¹ in 30 linear steps. Newtonian behaviour was observed, and the viscosity obtained as an average over the shear rates. The temperature was allowed to equilibrate for 15 min before the measurements. The coaxial setup was used only for the molecular mimic with outer radius 14.4600 mm, inner radius 13.3292 mm, gap 1.1308 mm. The temperature was set to 25 °C with a Peltier heater.

Viscosity measurements under high pressure up to 500 MPa were performed at LaMCoS – INSA de Lyon using a falling body viscometer as described by Scott Bair.⁷⁰ To this end, the sample is filled in a cartridge containing falling body (=sinker). One end of the cartridge is sealed with a plug, the other with a moveable piston to allow for pressure transfer. The cartridge is placed in a high pressure vessel surrounding by a pressurising medium. The high pressure vessel containing the cartridge is then rotated, causing the sinker to fall, the position of the latter is detected *via* a linear variable differential transformer. The viscosity is obtained from the falling time.

Diffusion coefficients were measured on an Avance Neo 500 MHz NMR spectrometer (Bruker, Billerica, USA) with Prodigy TCI CryoProbe (maximum gradient strength 65.7 G cm⁻¹) using the pulsed field-gradient stimulated echo sequence with bipolar gradients and longitudinal eddy current delay ('ledbpgp2s' in the Bruker library) and smoothed rectangular gradient pulses similar to previous work.⁷¹ The individual self-diffusion coefficients of the constituents could be determined using resolved signals of the two species. The uncertainty of the measurement with this setup is approximately 2% of the absolute value (from our own repeat measurements on this setup and comparing different pulse sequences).

Author contributions

Frederik Philippi: conceptualisation, methodology, investigation (syntheses of molecular mimics, mixing experiments), writing (original draft, revision), visualization, project administration. Daniel Rauber: investigation (synthesis of the ionic liquid, physicochemical characterisation). Kira Lieberkind Eliassen: validation, formal analysis (density fitting), investigation (pressure-dependent densitometry). Nathalie Bouscharain: validation, formal analysis (viscosity fitting), investigation (pressure-dependent rheology). Kristine Niss: resources (high pressure laboratory). Christopher W. M. Kay: resources (physicochemical characterisation equipment). Tom Welton: supervision, funding acquisition, resources (facilities for syntheses).

Conflicts of interest

There are no conflicts to declare.

Acknowledgements

This work is funded by the Imperial President's PhD Scholarship. We thank Julian Becker, Imperial College London, for help with the preliminary mixing experiments. Instrumentation and technical assistance for this work were provided by the Service Center NMR at UdS, with financial support from Saarland University and German Research Foundation DFG (project number 447298507). We are grateful to Park *et al.* for providing us with their numerical data.⁴⁹

References

- M. B. Shiflett, *Commercial Applications of Ionic Liquids*, Springer International Publishing, 2020, DOI: 10.1007/978-3-030-35245-5.
- A. J. Greer, J. Jacquemin and C. Hardacre, *Industrial Applications of Ionic Liquids*, *Molecules*, 2020, **25**, 5207.
- K. E. Gutowski, *Industrial uses and applications of ionic liquids*, *Phys. Sci. Rev.*, 2018, **3**, 1–10.
- T. Welton, *Ionic liquids: a brief history*, *Biophys. Rev.*, 2018, **10**, 691–706.
- N. V. Plechkova and K. R. Seddon, *Applications of ionic liquids in the chemical industry*, *Chem. Soc. Rev.*, 2008, **37**, 123–150.
- D. H. Zaitsau, V. N. Emel'yanenko, P. Stange, S. P. Verevkin and R. Ludwig, *Dissecting the Vaporization Enthalpies of Ionic Liquids by Exclusively Experimental Methods: Coulomb Interaction, Hydrogen Bonding, and Dispersion Forces*, *Angew. Chem., Int. Ed.*, 2019, **58**, 8589–8592.
- T. Niemann, *et al.*, *Cooperatively enhanced hydrogen bonds in ionic liquids: closing the loop with molecular mimics of hydroxy-functionalized cations*, *Phys. Chem. Chem. Phys.*, 2019, **21**, 18092–18098.
- F. Philippi and T. Welton, *Targeted modifications in ionic liquids – from understanding to design*, *Phys. Chem. Chem. Phys.*, 2021, **23**, 6993–7021.
- H. Shirota and E. W. Castner, *Physical Properties and Intermolecular Dynamics of an Ionic Liquid Compared with Its Isoelectronic Neutral Binary Solution*, *J. Phys. Chem. A*, 2005, **109**, 9388–9392.
- J. W. P. Schmelzer, E. D. Zanutto and V. M. Fokin, *Pressure dependence of viscosity*, *J. Chem. Phys.*, 2005, **122**, 074511.
- I. Avramov, *Pressure dependence of viscosity of glassforming melts*, *J. Non-Cryst. Solids*, 2000, **262**, 258–263.
- E. R. López, *et al.*, *Density scaling of the transport properties of molecular and ionic liquids*, *J. Chem. Phys.*, 2011, **134**, 144507.
- R. Casalini and C. M. Roland, *Thermodynamical scaling of the glass transition dynamics*, *Phys. Rev. E: Stat., Nonlinear, Soft Matter Phys.*, 2004, **69**, 062501.
- H. W. Hansen, *et al.*, *Density scaling of structure and dynamics of an ionic liquid*, *Phys. Chem. Chem. Phys.*, 2020, **22**, 14169–14176.
- S. Cheng, *et al.*, *Structurally Related Scaling Behavior in Ionic Systems*, *J. Phys. Chem. B*, 2020, **124**, 1240–1244.



- 16 S. A. Rice, Kinetic theory of ideal ionic melts, *Trans. Faraday Soc.*, 1962, **58**, 499.
- 17 S. Glasstone, K. J. Laidler and H. Eyring, *The Theory of Rate Processes*, McGraw-Hill Book Company, 1941.
- 18 M. Goldstein, Viscous Liquids and the Glass Transition: A Potential Energy Barrier Picture, *J. Chem. Phys.*, 1969, **51**, 3728–3739.
- 19 W. D. Amith, J. C. Araque and C. J. Margulis, A Pictorial View of Viscosity in Ionic Liquids and the Link to Nanostructural Heterogeneity, *J. Phys. Chem. Lett.*, 2020, **11**, 2062–2066.
- 20 T. Yamaguchi, Coupling between the mesoscopic dynamics and shear stress of a room-temperature ionic liquid, *Phys. Chem. Chem. Phys.*, 2018, **20**, 17809–17817.
- 21 W. D. Amith, J. C. Araque and C. J. Margulis, Relationship between the Relaxation of Ionic Liquid Structural Motifs and That of the Shear Viscosity, *J. Phys. Chem. B*, 2021, **125**, 6264–6271.
- 22 A. F. Bouarab, J.-P. Harvey and C. Robelin, Viscosity models for ionic liquids and their mixtures, *Phys. Chem. Chem. Phys.*, 2021, **23**, 733–752.
- 23 S. Cheng, Z. Wojnarowska, M. Musiał and M. Paluch, Correlation between configurational entropy, excess entropy, and ion dynamics in imidazolium-based ionic liquids: test of the Adam–Gibbs model, *J. Chem. Phys.*, 2021, **154**, 044502.
- 24 K. L. Eliassen, *et al.*, High-frequency dynamics and test of the shoving model for the glass-forming ionic liquid Pyr14-TFSI, *Phys. Rev. Mater.*, 2021, **5**, 065606.
- 25 I. H. Bell, J. C. Dyre and T. S. Ingebrigtsen, Excess-entropy scaling in supercooled binary mixtures, *Nat. Commun.*, 2020, **11**, 4300.
- 26 M. Goldstein, The past, present, and future of the Johari–Goldstein relaxation, *J. Non-Cryst. Solids*, 2011, **357**, 249–250.
- 27 R. E. Powell, W. E. Roseveare and H. Eyring, Diffusion, Thermal Conductivity, and Viscous Flow of Liquids, *Ind. Eng. Chem.*, 1941, **33**, 430–435.
- 28 H. D. Weymann, On the hole theory of viscosity, compressibility, and expansivity of liquids, *Kolloid Z. Z. Polym.*, 1962, **181**, 131–137.
- 29 A. P. Abbott, Application of Hole Theory to the Viscosity of Ionic and Molecular Liquids, *ChemPhysChem*, 2004, **5**, 1242–1246.
- 30 C. Maggi, B. Jakobsen, T. Christensen, N. B. Olsen and J. C. Dyre, Supercooled Liquid Dynamics Studied via Shear-Mechanical Spectroscopy, *J. Phys. Chem. B*, 2008, **112**, 16320–16325.
- 31 J. C. Dyre and N. B. Olsen, Landscape equivalent of the shoving model, *Phys. Rev. E: Stat., Nonlinear, Soft Matter Phys.*, 2004, **69**, 042501.
- 32 J. C. Dyre, N. B. Olsen and T. Christensen, Local elastic expansion model for viscous-flow activation energies of glass-forming molecular liquids, *Phys. Rev. B: Condens. Matter Mater. Phys.*, 1996, **53**, 2171–2174.
- 33 J. C. Dyre, Perspective: Excess-entropy scaling, *J. Chem. Phys.*, 2018, **149**, 210901.
- 34 S. Yasutomi, S. Bair and W. O. Winer, An Application of a Free Volume Model to Lubricant Rheology I—Dependence of Viscosity on Temperature and Pressure, *J. Tribol.*, 1984, **106**, 291–302.
- 35 S. N. Suarez, *et al.*, Do TFSA Anions Slither? Pressure Exposes the Role of TFSA Conformational Exchange in Self-Diffusion, *J. Phys. Chem. B*, 2015, **119**, 14756–14765.
- 36 K. Pilar, *et al.*, Investigation of Dynamics in BMIM TFSA Ionic Liquid through Variable Temperature and Pressure NMR Relaxometry and Diffusometry, *J. Electrochem. Soc.*, 2017, **164**, H5189–H5196.
- 37 R. Shi and Y. Wang, Dual Ionic and Organic Nature of Ionic Liquids, *Sci. Rep.*, 2016, **6**, 1–12.
- 38 Q. Berrod, *et al.*, Ionic Liquids: evidence of the viscosity scale-dependence, *Sci. Rep.*, 2017, **7**, 2241.
- 39 J. G. McDaniel and A. Yethiraj, Understanding the Properties of Ionic Liquids: Electrostatics, Structure Factors, and Their Sum Rules, *J. Phys. Chem. B*, 2019, **123**, 3499–3512.
- 40 H. K. Kashyap, H. V. R. Annapureddy, F. O. Raineri and C. J. Margulis, How Is Charge Transport Different in Ionic Liquids and Electrolyte Solutions?, *J. Phys. Chem. B*, 2011, **115**, 13212–13221.
- 41 E. A. Shelepova, R. Ludwig, D. Paschek and N. N. Medvedev, Structural similarity of an ionic liquid and the mixture of the neutral molecules, *J. Mol. Liq.*, 2021, **329**, 115589.
- 42 E. A. Shelepova, D. Paschek, R. Ludwig and N. N. Medvedev, Comparing the void space and long-range structure of an ionic liquid with a neutral mixture of similar sized molecules, *J. Mol. Liq.*, 2020, **299**, 112121.
- 43 J. C. Araque, J. J. Hettige and C. J. Margulis, Ionic liquids—Conventional solvent mixtures, structurally different but dynamically similar, *J. Chem. Phys.*, 2015, **143**, 134505.
- 44 G. Morrison and J. E. Lind, Effect of the Internal Coulomb Field upon the Viscosity of a Fused Salt, *J. Chem. Phys.*, 1968, **49**, 5310–5316.
- 45 T. Grindley and J. E. Lind, Thermodynamics of Molten Salts, *J. Chem. Phys.*, 1972, **56**, 3602–3607.
- 46 N. Weiden, B. Wittekopf and K. G. Weil, Viscosities, Electric Conductivities and Self Diffusion Coefficients of Tetraalkylammonium-tetraalkylborides, *Ber. Bunsen-Ges. Phys. Chem.*, 1990, **94**, 353–358.
- 47 D. Roy, N. Patel, S. Conte and M. Maroncelli, Dynamics in an Idealized Ionic Liquid Model, *J. Phys. Chem. B*, 2010, **114**, 8410–8424.
- 48 D. Roy and M. Maroncelli, An Improved Four-Site Ionic Liquid Model, *J. Phys. Chem. B*, 2010, **114**, 12629–12631.
- 49 S.-W. Park, S. Kim and Y. Jung, Time scale of dynamic heterogeneity in model ionic liquids and its relation to static length scale and charge distribution, *Phys. Chem. Chem. Phys.*, 2015, **17**, 29281–29292.
- 50 A. El Basyony, J. Klimes, A. Knöchel, J. Oehler and G. Rudolph, Anionenaktivierung, III. Zur Bedeutung von Wasserstoffbrückenbindungen für das reaktive Verhalten von Kronenäthern und Aminopolyäthern/Anionactivation, III. Anionactivation, III 1 Concerning the Significance of Hydrogen-Bonding for the Reactivity of Cro, *Z. Naturforsch., B: J. Chem. Sci.*, 1976, **31**, 1192–1200.
- 51 J. A. A. De Boer, D. N. Reinhoudt, S. Harkema, G. J. Van Hummel and F. De Jong, Thermodynamic constants of



- complexes of crown ethers and uncharged molecules and X-ray structure of the 18-crown-6 (MeNO₂)₂ complex, *J. Am. Chem. Soc.*, 1982, **104**, 4073–4076.
- 52 R. A. Kumpf and J. R. Damewood, Do nitromethane and malononitrile form C–H···O hydrogen bonds? Implications for molecular recognition by crown ethers, *J. Chem. Soc., Chem. Commun.*, 1988, 621–622, DOI: 10.1039/C39880000621.
- 53 J. R. Damewood, J. J. Urban, T. C. Williamson and A. L. Rheingold, Isomer-dependent complexation of malononitrile by dicyclohexano-18-crown-6, *J. Org. Chem.*, 1988, **53**, 167–171.
- 54 S. Courtecuisse, F. Cansell, D. Fabre and J. Petitet, Phase transitions and chemical transformations of nitromethane up to 350 °C and 35 GPa, *J. Chem. Phys.*, 1995, **102**, 968–974.
- 55 M. Citroni, *et al.*, Crystal Structure of Nitromethane up to the Reaction Threshold Pressure, *J. Phys. Chem. B*, 2008, **112**, 1095–1103.
- 56 A. Drozd-Rzoska, S. J. Rzoska and J. Kalabiński, Impact of Pressure on Low-Molecular Weight Near-Critical Mixtures of Limited Miscibility, *ACS Omega*, 2020, **5**, 20141–20152.
- 57 K. M. Reuck, R. J. B. Craven and A. E. El Hassan, Equations of State, in *Transport Properties of Fluids Their Correlation, Prediction and Estimation*, ed. J. Millat, J. H. Dymond and C. A. Nieto de Castro, Cambridge University Press, 1996.
- 58 S. Bair, Compressibility and the Equation of State, in *High Pressure Rheology for Quantitative Elastohydrodynamics*, Elsevier, 2019, pp. 73–95, DOI: 10.1016/B978-0-444-64156-4.00004-0.
- 59 K. Fumino, A. Wulf and R. Ludwig, Strong, Localized, and Directional Hydrogen Bonds Fluidize Ionic Liquids, *Angew. Chem., Int. Ed.*, 2008, **47**, 8731–8734.
- 60 S. Tsuzuki, H. Matsumoto, W. Shinoda and M. Mikami, Effects of conformational flexibility of alkyl chains of cations on diffusion of ions in ionic liquids, *Phys. Chem. Chem. Phys.*, 2011, **13**, 5987.
- 61 D. Bedrov, *et al.*, Molecular Dynamics Simulations of Ionic Liquids and Electrolytes Using Polarizable Force Fields, *Chem. Rev.*, 2019, **119**, 7940–7995.
- 62 J. G. McDaniel, Polarization Effects in Binary [BMIM⁺][BF₄[−]]/1,2-Dichloroethane, Acetone, Acetonitrile, and Water Electrolytes, *J. Phys. Chem. B*, 2018, **122**, 4345–4355.
- 63 T. Yamaguchi, Mode-coupling theoretical study on the roles of heterogeneous structure in rheology of ionic liquids, *J. Chem. Phys.*, 2016, **144**, 124514.
- 64 T. Yamaguchi, Experimental study on the relationship between the frequency-dependent shear viscosity and the intermediate scattering function of representative viscous liquids, *J. Chem. Phys.*, 2016, **145**, 194505.
- 65 F. Yusuf, T. Olayiwola and C. Afagwu, Application of Artificial Intelligence-based predictive methods in Ionic liquid studies: a review, *Fluid Phase Equilib.*, 2021, **531**, 112898.
- 66 S. Koutsoukos, F. Philippi, F. Malaret and T. Welton, A review on machine learning algorithms for the ionic liquid chemical space, *Chem. Sci.*, 2021, **12**, 6820–6843.
- 67 N. B. Olsen, T. Christensen and J. C. Dyre, Time-Temperature Superposition in Viscous Liquids, *Phys. Rev. Lett.*, 2001, **86**, 1271–1274.
- 68 K. S. Cho, Time-Temperature Superposition, *Viscoelasticity of Polymers*, 2016, pp. 437–457, DOI: 10.1007/978-94-017-7564-9_8.
- 69 *CRC Handbook of Chemistry and Physics*, CRC Press, 2014.
- 70 S. A. Bair, Routine High-Pressure Viscometer for Accurate Measurements to 1 GPa, *Tribol. Trans.*, 2004, **47**, 356–360.
- 71 F. Philippi, D. Rauber, J. Zapp and R. Hempelmann, Transport properties and ionicity of phosphonium ionic liquids, *Phys. Chem. Chem. Phys.*, 2017, **19**, 23015–23023.



E.3 Piezoelectric shear rheometry: Further developments in experimental implementation and data extraction



Piezoelectric shear rheometry: Further developments in experimental implementation and data extraction

Mathias Mikkelsen,^{1,2,a)} Kira L. Eliassen,¹ Niclas Lindemann,^{2,3} Kevin Moch,⁴ Roland Böhmer,⁴ Hossein Ali Karimi-Varzaneh,² Jorge Lacayo-Pineda,^{2,5} Bo Jakobsen,¹ Kristine Niss,¹ Tage Christensen,¹ and Tina Hecksher^{1,b)}

¹*Glass and Time, IMFUFA, Department of Science and Environment, Roskilde University, Roskilde, Denmark*

²*Research and Development, Continental Reifen Deutschland GmbH, Hannover, Germany*

³*Institut für Physikalische Chemie und Elektrochemie, Leibniz Universität Hannover, Hannover, Germany*

⁴*Fakultät Physik, Technische Universität Dortmund, 44221 Dortmund, Germany*

⁵*Institut für Anorganische Chemie, Leibniz Universität Hannover, Hannover, Germany*

(Received 28 September 2021; final revision received 25 June 2022; published 26 August 2022)

Abstract

The piezoelectric shear gauge (PSG) [Christensen and Olsen, *Rev. Sci. Instrum.* **66**, 5019 (1995)] is a rheometric technique developed to measure the complex shear modulus of viscous liquids near their glass transition temperature. We report recent advances to the PSG technique: (1) The data extraction procedure is optimized, which extends the upper limit of the frequency range of the method to between 50 and 70 kHz. (2) The measuring cell is simplified to use only one piezoelectric ceramic disk instead of three. We present an implementation of this design intended for liquid samples. Data obtained with this design revealed that a soft extra spacer is necessary to allow for thermal contraction of the sample in the axial direction. Model calculations show that flow in the radial direction is hindered by the confined geometry of the cell when the liquid becomes viscous upon cooling. The method is especially well-suited for—but not limited to—glassy materials. © 2022 The Society of Rheology. <https://doi.org/10.1122/8.0000379>

I. INTRODUCTION

Mechanical properties, e.g., stiffness and viscosity, of complex materials are important for many applications [1,2] as well as for the fundamental understanding of matter [3,4]. A number of rheometric techniques that map these properties as a function of frequency, temperature, and, in some cases, stress or strain amplitude are in use in research labs and industry [5,6]. These techniques can roughly be divided into three categories: quasistatic methods, resonant methods, and (sound) propagation methods.

Quasistatic methods are techniques that deform the entire sample. These techniques include most standard commercial rheometers, but also sliding plate rheometers using piezoceramic disks, e.g., [7]. This entails that the deformation rate must be relatively slow and the sample size must be small compared to the sound velocity wavelength. The upper frequency limit of standard rheometers is determined by the resonance frequency of the driving device (in most cases a rotating shaft), which typically lies around 100 Hz. The limitation in frequency range leads to the need for the construction of master curves if one wants to obtain the entire relaxation function. This procedure assumes time-temperature superposition (TTS), i.e., that the shape of the relaxation spectrum is conserved so that each measured temperature

gives a different part of the full function that may be shifted with respect to the others to form the master curve.

Standard rheometers are sensitive to low moduli/viscosities but less optimal for harder samples due to the instrument compliance being comparable to the sample compliance [8,9], i.e., instead of deforming the sample the instrument itself deforms. Corrections are routinely applied to account for this effect, but the method remains more accurate for soft materials.

Resonant methods function by monitoring the resonance of the measuring device while it shifts due to the effect of the viscoelastic sample compared to a freely oscillating device. Traditional examples of implementations include torsional resonators and cantilever devices [10]. Recent developments for resonant methods go in the direction of microrheology, e.g., using atomic force microscopy [11,12] and MEMS based devices [13,14]. These techniques work mainly for low-viscosity (the Pa s range) liquids. Resonance methods typically operate at discrete frequencies in the kHz region and are rather precise.

Propagation methods generate deformations that travel through the sample and get detected after some propagation length. Delay time and wave amplitude changes are then recorded and translated into sound velocity and attenuation coefficient. These methods include classical ultrasonic techniques in the 1–10 MHz region [15] and laser techniques such as impulsive stimulated scattering [16,17] in the 100 MHz–1000 GHz region, time domain Brillouin scattering [18] in the 1–10 GHz region and Picosecond Ultrasonics, exciting longitudinal acoustic waves [19] or shear acoustic

^{a)}Electronic mail: mathiasm@ruc.dk

^{b)}Author to whom correspondence should be addressed; electronic mail: tihe@ruc.dk

waves [20] up to several hundred GHz. These high-frequency techniques are limited to rather high moduli and low loss as the sample must be able to support a sound wave at the given frequency.

The piezoelectric shear gauge (PSG) [21] is a rheometric method originally developed with a focus on measuring shear mechanical properties of supercooled liquids. It is an electro-mechanical transducer that utilizes the coupling of strain and electric field in a piezoelectric material using piezoelectric ceramic (PZ) disks. A sample attached to the PZ disk will experience a tangential force on its surface as the PZ disk deforms when a field is applied through electrodes on its surface. If the sample is stiff, it will partially clamp the motion of the PZ disk, thus lowering its capacitance. The shear modulus of the sample can be calculated based on the capacitance of the PZ disks. This makes the PSG ideal for relatively hard samples (moduli from MPa to tens of GPa) exactly because the deformation of the measuring device (the PZ disks) is the essence of the method. This, however, also makes it less suitable for soft materials and low-viscosity liquids.

The PSG is a quasistatic method and has a uniquely broad frequency range (1 mHz–10 kHz) due to the high resonance frequency of the device (~ 100 kHz). The method has been in use for more than two decades and has been pivotal in several scientific achievements: the development of a theoretical model for the non-Arrhenius temperature dependence of viscosity of supercooled liquids [22] and subsequent tests of that model [23], testing a prediction of the isomorph theory connecting the empirically found density scaling exponent to linear response measurements [24], the first evidence of short-chain polymerlike rheological signatures in monoalcohols [25,26] and a polyalcohol [27], compiling the first true broadband mechanical spectrum in conjunction with high frequency propagation methods spanning 14 decades in frequency [28], testing rheological models for the shear relaxation in supercooled liquids [29,30], showing that time scales from different response functions (including rheological) have the same temperature dependence [31,32] and showing that the local and global shear moduli are identical [33].

The original PSG of Christensen and Olsen [21] consists of three PZ disks between which two layers of a liquid sample are suspended. We will refer to this as the “3-PZ PSG.” In this work, we present a new version of the PSG where the two outer PZ disks have been replaced by rigid disks (made from sapphire or steel) such that the PSG consists of a single PZ disk mounted between two rigid supports. This assembly will be referred to as the “1-PZ PSG.” Figure 1 shows a schematic illustration of the 3-PZ and the 1-PZ PSG.

The 1-PZ PSG allows for use on sample types that the 3-PZ PSG design is not well-suited for. Liquid samples are loaded into the 3-PZ PSG from the side assisted by capillary forces that pull the liquid into the sample space and ensure a homogeneously distributed liquid layer. To mount solid samples, e.g., polymers and rubbers, a design is needed that can easily be disassembled so that disks of the sample material with matching radii can be sandwiched between the PZ disks/rigid support. Solid samples need to be glued to the disks to ensure the no-slip condition that is essential for the method to work. Because the PZ disks are quite brittle, they break easily when solid samples are removed after a measurement, and thus a 1-PZ PSG design reduces the potential waste of disks. Another advantage of using one instead of three PZ disks is to avoid the tedious and time consuming task of matching three disks carefully among a batch of commercial ceramic disks. The matching is necessary because the method ideally requires the three disks to be identical (same size, weight, capacitance, etc.). In addition, in the 3-PZ assembly, it is necessary to drill holes in the two outer disks, which again entails the risk of breaking the disks.

Another use case for the 1-PZ PSG is given by measurements on conductive samples, e.g., ionic liquids as was done by Eliassen *et al.* [23], where the risk of excess liquid at the edge of the PZ disks (which could short the electrodes) is greatly reduced in the 1-PZ design compared to the 3-PZ PSG.

Furthermore, we report on recent developments in the data extraction procedure that yield more precise results and

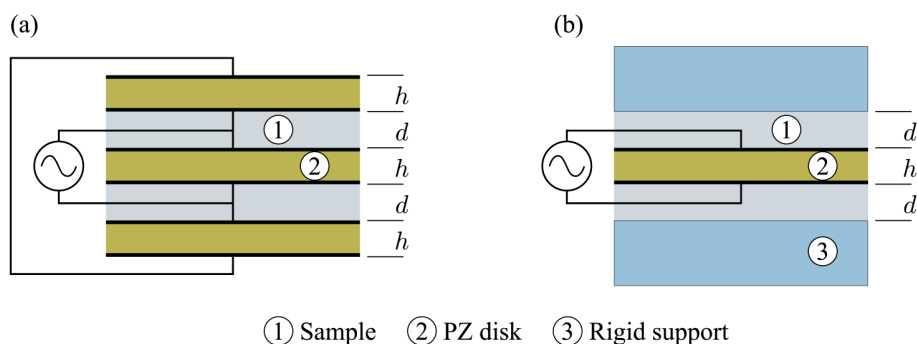


FIG. 1. Schematic of the piezoelectric shear modulus gauge (PSG). (a) 3-PZ version. Two layers of the sample of thickness d , are sandwiched between three PZ disks of thickness h . Silvering on the surfaces of the PZ disks forms the electrodes of capacitors. The three capacitors are connected to an AC voltage source. The two outer PZ disks are connected in series, and the middle PZ disk is in parallel with the others. (b) 1-PZ version. A layer of sample on either side of the PZ disk is sandwiched between the PZ and a rigid disk. In the 3-PZ PSG, the electrodes on the sides facing each other of two neighboring PZ disks are at the same potential and thus there is no electrical field across the sample. In the 1-PZ PSG, the field outside the capacitor formed by the silvered surface electrodes of the PZ disk is also zero everywhere except for a small field at the edge, which will be negligible due to the high dielectric permittivity of the PZ ceramic material. Thus, in neither case do the dielectric properties of the sample contribute to the signal.

extend the frequencies that can be resolved with this technique.

In this paper, we present the needed background and construction details for the 1-PZ PSG and show the application for glassy materials. The paper starts with a brief review of the mathematical modeling of the PSG from Christensen and Olsen [21] in Sec. II to give the background for the new data extraction algorithm described in Sec. III. In Sec. IV, we validate the 1-PZ PSG against 3-PZ PSG measurements with a liquid sample in a fixed assembly with sapphire supports. Interestingly, measurements with this cell initially gave slightly different results when compared to 3-PZ PSG results. The slight deviations in the measured time scales are fully explained by taking into account the flow of a highly viscous liquid in geometrical confinement imposed by the PSG plates, and the problem was solved by introducing soft spacers in the 1-PZ PSG, allowing for thermal contraction of the liquid when cooled to temperatures near the glass transition.

II. THE PIEZOELECTRIC SHEAR MODULUS GAUGE

The PSG works by measuring the capacitance of the PZ disks as a function of frequency. When an AC voltage is applied across the disks, they expand and contract in an oscillatory motion, thus shearing the sample sandwiched between the disks. In the low-modulus limit (either at high temperatures or at low frequencies), the measured capacitance of the disks is the same as that of the freely moving disks because the liquid is able to follow the imposed deformation without resistance. If the sample is viscous, it resists the deformation and will partially clamp the disks, leading to a lower measured capacitance. With a viscoelastic sample, the sample might flow at low frequencies and behave as an elastic solid at high frequencies, which shows up in the PSG as a transition between the free and partially clamped capacitance. Figure 2 illustrates how the capacitance of the liquid filled PSG matches that of the empty device at low frequencies and decreases with frequency to the partially clamped level. This difference in capacitance between the freely moving PZ disk and the partially clamped PZ disk is directly related to the shear modulus of the sample. Through analysis of the equations of motion for the disks (briefly sketched in the following, for more details consult Christensen and Olsen [21]), the frequency dependence of the sample shear modulus can then be found by inversion of a function that maps sample modulus to capacitance of the PZ disks.

A. Mapping of the PSG to “one-one” configuration

In this section, we show how both the 3-PZ PSG and the 1-PZ PSG can be mapped to a mathematically equivalent configuration that consists of one liquid layer between a PZ disk and an infinitely rigid support, which we will refer to as the “one-one configuration.” The mathematical model derived by Christensen and Olsen [34] assumes this mapping, but the argument given here (and in Appendix A) is more detailed. We establish that the model used for the 3-PZ PSG also applies for the 1-PZ PSG, only with a different effective sample layer thickness.

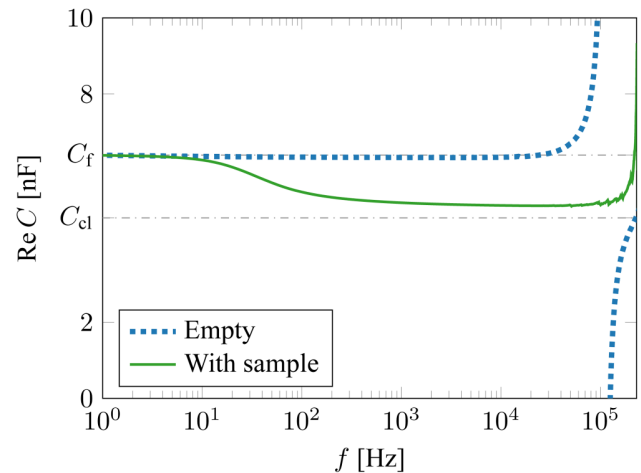


FIG. 2. Real part of the capacitance of a 1-PZ PSG transducer as a function of frequency. The dotted line is data from an empty PSG, and the full line is data with a liquid sample. The PSG (without sample) has one capacitance, C_f , in the mechanically free state and another, lower, capacitance C_{cl} in the mechanically clamped state. The dashdotted lines represent the calculated values. If a liquid sample is mounted, the PZ still moves freely at low frequencies, where the sample modulus vanishes. At frequencies between this limit and the resonance, the sample modulus becomes significant. The sample then partially clamps the PZ disks, and the capacitance drops to a level between C_f and C_{cl} . It is this partial clamping—and the associated change in capacitance—that enables us to measure the shear modulus using the PSG.

In the 3-PZ PSG, the middle disk moves opposite the two outer disks and always moves twice as much; both in the freely moving case and when there is a mechanical load of the sample; see Fig. 3(a) for an illustration. This can be understood by considering an axial liquid filament reaching from the top plate to the middle plate. If the filaments are noninteracting, then—due to Newton’s third law—the stress one filament exerts on the top plate is equal and opposite to the stress it exerts on the middle plate. This argument assumes the liquid inertia is negligible, which is reasonable in the quasistatic limit where the displacement accelerations are small. As the frequencies approach the resonance, this assumption becomes worse. However, liquid inertia is accounted for by including a correction to the apparent modulus obtained by assuming negligible inertia (more details given below in Sec. II A and Appendix E).

Since the bottom plate exerts an equal stress on the middle plate, the total stress on the middle plate is twice the magnitude of, and opposite in direction to, each of the stresses on the outer plates (see also Fig. 10, Appendix A). By the electric wiring (see Fig. 1), the voltage across the middle plate is also twice those across the outer plates, and thus the displacement of the middle plate is twice that of the outer plates, but in the opposite direction. This means that there is a neutral plane $2/3$ of the distance from the middle plate both above and below the middle plate (see Fig. 3). This assumes that the sample displacement profile is linear, i.e., the considered axial sample filaments are straight and not curved. The assumption is reasonable because, in our case, the strain is small (10^{-5} to 10^{-6}) and as is the ratio of sample thickness d and radius R ($d/R = 0.05$).

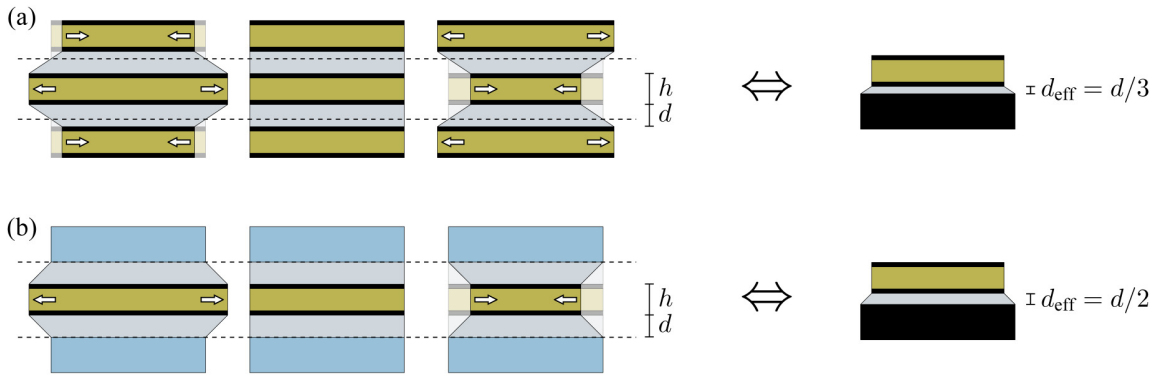


FIG. 3. Schematic illustration of the shearing motion of the two PSG implementations and their mapping to a one-one configuration. Arrows illustrate the direction of expansion/contraction of the disks. Note that these sketches highly exaggerate the disk displacement for illustrative purposes. The actual strain is on the order of 10^{-5} to 10^{-6} . The ratio of radius and sample/disk thickness is also not to scale: in the measuring cells used in this work radius of the PZ disk is 10 mm while $h \approx 0.5$ mm and $d \approx 0.5$ mm (see the photo in Fig. 6). (a) The 3-PZ PSG. This device, with a central PZ disk that moves in opposition to, and twice as far as, the outer PZ disks, has a sample thickness of d and neutral planes (shown as dashed lines) that lie at one third of the distance from the outer disks to the central one. The 3-PZ PSG is, therefore, equivalent to a device with a single PZ disk, a sample thickness of $d/3$, and an infinitely rigid support below the sample. This equivalent device is shown on the right. (b) The 1-PZ PSG. This has the neutral plane lying at the surfaces of the rigid disks. It, therefore, maps to a device with a sample thickness of $d/2$.

Thus, the outer plates “see” one rigid support at a distance of $(1/3)d$, illustrated by the dashed line in Fig. 3(a). The middle plate “sees” two rigid supports at a distance of $(2/3)d$, but this is equal to seeing only one rigid surface $(1/3)d$ away. The three disks thus have exactly the same change in capacitance due to the sample shear modulus. (A detailed mathematical derivation of this argument is given in Appendix A.) This means that the mathematical problem of relating the electrical capacitance of the 3-PZ PSG to the shear modulus of the sample can be mapped to the one-one configuration, consisting of a sample layer placed between a single PZ disk (with the full capacitance of the PSG) and an infinitely rigid support, the effective sample thickness being $1/3$ of the actual sample thickness.

The 1-PZ PSG has actual physical rigid supports instead of a mathematically neutral plane, but the argument still holds if the support can be considered “infinitely” rigid, i.e., that the stiffness of the support is much larger than the stiffness of the sample. The mathematical models of the 3-PZ and the 1-PZ PSG are, therefore, the same, only with different effective sample thickness of $d/3$, respectively $d/2$, see Fig. 3.

For this mapping to hold, a proper centering and parallelism of plate(s), sample, and supports in the implementation in the measuring cells is crucial. Details on how this is done practically in the two cells presented here are given in Sec. IV and Appendix D.

B. Mathematical model of one-one configuration

Having established the mapping to the one-one configuration, we now proceed to give the essential steps of the derivation of the mathematical model of that configuration. Equations (1)–(10) are taken directly from Christensen and Olsen [21]. They are included here to give the complete background for the new inversion algorithm that determines the shear modulus.

The PSG (without sample) has one capacitance, C_f , in the mechanically free state and another, lower, capacitance C_{cl} in the mechanically clamped state. The free capacitance is equal to the low-frequency limiting capacitance, C_0 , i.e., $C_0 = C_f$. These levels, C_f and C_{cl} , are illustrated in Fig. 2, that shows the measured capacitance as a function of frequency for an empty (blue dotted line) as well as a filled PSG (green full line). The clamped and the free capacitances are related by the planar coupling constant, k_p ,

$$\frac{C_{cl}}{C_f} = 1 - k_p^2. \quad (1)$$

The ceramic material used in our experiment is a lead zirconate titanate compound known as Pz26. The coupling constant, k_p , for this material is nominally 0.56,¹ and thus one expects $C_{cl}/C_f = 0.69$. The actual value varies as a function of temperature and thermal history, and thus it is calibrated for each measurement. Other characteristics of the Pz26 material include a density of 7.70 g cm^{-3} and a relative dielectric permittivity of 1300 at 1 kHz.¹

In the piezoelectric material, the stress, σ_{ij} , and strain, ϵ_{ij} , couple with each other as well as to the electric field, E_i , and the displacement field, D_i . For an axially polarized and cylindrically symmetric PZ disk, these couplings can be reduced to [21]

$$\begin{pmatrix} \sigma_{rr} \\ \sigma_{\phi\phi} \\ D_z \end{pmatrix} = \begin{pmatrix} c_{11} & c_{12} & -e_{13} \\ c_{12} & c_{11} & -e_{13} \\ e_{13} & e_{13} & \epsilon_{33}^S \end{pmatrix} \begin{pmatrix} \epsilon_{rr} \\ \epsilon_{\phi\phi} \\ E_z \end{pmatrix}, \quad (2)$$

where c_{11} and c_{12} are elastic constants, ϵ_{33}^S is a dielectric constant, and e_{13} is a piezoelectric constant. r denotes a

¹Meggitt A/S, Data Sheet: Hard relaxor type PZT Type Pz26 (Navy I) (2019), <https://www.meggittferroperm.com/resources/data-sheets>.

radial component, z a component in the axial direction, and ϕ an azimuthal component.

The measured capacitance of the PZ disk, C_m , can be found as the ratio of charge, Q , to voltage, U , with the charge found from the surface integral of the displacement field, D_z , and the voltage found from the electric field and the thickness, h , of the PZ disk,

$$C_m = \frac{Q}{U} = \frac{\int_0^R 2\pi r D_z(r) dr}{h E_z}. \quad (3)$$

This leads to the capacitance only being a function of the radial displacement at the edge of the PZ disk, $u_r(r = R)$,

$$C_m = \frac{2\pi e_{13} R}{h E_z} u_r(R) + C_{cl}. \quad (4)$$

The pivotal function describing the shear transducer response is thus the normalized capacitance

$$F = \frac{C_m - C_{cl}}{C_f - C_{cl}}, \quad (5)$$

which is directly proportional to the displacement, $u_r(R)$.

The displacement may be found by solving the equation of motion of the PZ disk, which in cylindrical coordinates becomes

$$c_{11}(r^2 u_r'' + u_r' r - u_r) - \frac{\sigma_l}{h} r^2 = -\omega^2 r^2 \rho u_r, \quad (6)$$

where a prime denotes a derivative in r , ω is the frequency of the electrical field and ρ is the density of the ceramic. σ_l denotes the tangential stress exerted by the sample on the PZ disk and is proportional to the complex shear modulus, $G^* = G' + iG''$, of the sample, $\sigma_l = G^* u_r(r)/d_{\text{eff}}$. At high frequencies and low moduli, one has to take liquid inertia into account [35]. This can be done by substituting G^* by the apparent modulus $G^*_{\text{app}} = G^* \frac{x}{\tan(x)}$, where $x = \sqrt{\rho_l/G^*} \omega d$ (see Appendix E for more details). Rewriting the equation of motion Eq. (6) in terms of the dimensionless variable $x = r/R$, we obtain

$$x^2 e'' + x e' + \left(\left[\frac{\omega^2 \rho R^2}{c_{11}} - \frac{G^* R^2}{c_{11} d_{\text{eff}} h} \right] x^2 - 1 \right) e = 0, \quad (7)$$

where e is now the normalized displacement (see Appendix B).

Defining the characteristic frequency, ω_c , and modulus, G_c , of the PSG as

$$\omega_c^2 = \frac{c_{11}}{\rho R^2}, \quad G_c = \frac{c_{11} d_{\text{eff}} h}{R^2}, \quad (8)$$

it becomes clear that F depends on the frequency and the

shear modulus G^* via the wave vector, k ,

$$k^2 = \left(\frac{\omega}{\omega_c} \right)^2 - \frac{G^*}{G_c}. \quad (9)$$

Solving the equation of motion Eq. (7) with the appropriate set of boundary conditions, we obtain for the normalized capacitance (for more details, see Christensen and Olsen [21]),

$$F(k) = (1 + \nu) \frac{J_1(k)}{kJ_0(k) + (\nu - 1)J_1(k)}, \quad (10)$$

where J_0 and J_1 are Bessel functions and $\nu \approx 0.31$ is the Poisson ratio of the Pz26 material [36].

The above model of the PSG has not involved any dissipation, and thus, the imaginary part of the capacitance is zero. In practice, a peak is seen in the imaginary part at resonances due to a small dissipation. This is included simply by adding a quality factor Q_{pz} into the expressions for k^2 , i.e.,

$$k^2 = \left(\frac{\omega}{\omega_c} \right)^2 - i \left(\frac{\omega}{\omega_c} \right) \frac{1}{Q_{\text{pz}}} - \frac{G^*}{G_c}. \quad (11)$$

Other adjustments to the model include (1) a correction for thermal contraction of the sample (see Appendix B) resulting in F also being a function of the actual sample radius, x_l , $F = F(k, x_l)$; (2) a correction for the hub in the center of the PSG (see Appendix C); and (3) an assumption to handle the weak dispersion of the ceramic material, i.e., that C_f and C_{cl} are not constants, but have a weak frequency dependence. To account for this frequency dependence, we assume that their ratio, C_{cl}/C_f ,—and thus the coupling constant [Eq. (1)]—is frequency independent. In that case, the effect of dispersion can be scaled out by a reference measurement of the empty transducer, C_r . Taking the ratio of the reference and sample spectra then scales out the dispersion. The ratio becomes

$$\frac{C_m}{C_r} = \frac{F(S, V, x_l) \frac{k_p^2}{1 - k_p^2} + 1}{F(S, 0, 1) \frac{k_p^2}{1 - k_p^2} + 1}, \quad (12)$$

where we have introduced the notation

$$S = \left(\frac{\omega}{\omega_c} \right)^2 - i \left(\frac{\omega}{\omega_c} \right) \frac{1}{Q_{\text{pz}}}, \quad V = \frac{G^*}{G_c}, \quad (13)$$

replacing the previous expression for k^2 , Eq. (11), by $k^2 = S - V$.

Thus, the normalized capacitance for the sample measurement may be written as

$$F(S, V, x_l) = \frac{C_m}{C_r} \left(F(S, 0, 1) + \frac{1 - k_p^2}{k_p^2} \right) - \frac{1 - k_p^2}{k_p^2}, \quad (14)$$

where the right-hand side is calculated from the

experimentally determined C_m and C_r , while V is found by inversion of $F(S, V, x_l)$.

III. NEW INVERSION ALGORITHM

The model gives the ingredients to determine the frequency-dependent shear modulus of the sample from a measurement of the capacitance of the PZ disks. The characteristic properties of the PSG (C_{cl} , k_p , and ω_c) can, in principle, be determined by the reference measurement of the capacitance, C_r .

However, it is not possible to isolate G^* in the expression for $F(k)$ Eq. (10) [or more generally Eq. (C21), see Appendix C] in a simple way. The strategy in Christensen and Olsen [21] involved approximating the function

$$\Phi(S, V, x_l) = \frac{F(S, V, x_l)}{F(S, 0, 1)}, \quad (15)$$

with a rational function with a numerator of degree one and a denominator of degree two in G^*/G_c . The inversion to isolate G^* was based on this expression.

$F(S, V, x_l)$ may also be directly inverted by fitting G^* for each frequency in Eq. (14). This method is accurate, but time consuming when implemented with a nonlinear, least squares brute-force algorithm, since a minimization is executed for each measured frequency (~ 150) in the spectrum.

In the following, we present an implementation of the inversion using the Newton–Raphson algorithm [37], which yields results identical to those obtained with the brute-force algorithm, but is much faster.

Specifically, we use the Newton–Raphson algorithm to determine the zero-points of the difference between the measured normalized capacitance, F_m , and the theoretical expression for F in Eq. (10) [or more generally Eq. (C21)] with the sample shear modulus, G^* , as the variable. The Newton–Raphson inversion algorithm should thus converge to the solution, G^* , of the equation

$$F_m = F(G^*), \quad (16)$$

where G^* is the limit of the iterations of trial functions $G_t^{(n)}$ and

$$G_t^{(n+1)} = G_t^{(n)} \left(1 + \delta \frac{F_m - F(G_t^{(n)})}{F((1 + \delta)G_t^{(n)}) - F(G_t^{(n)})} \right). \quad (17)$$

Here, δ is a small number (typically 0.01) that sets the step size of the numerical differentiation of F .

For the method to work, we need a good starting trial function, $G_t^{(1)}(\omega)$. To obtain this, the normalized capacitance of the shear transducer, $F(k)$, will be approximated by a rational fraction that matches the measured F_m up to a frequency a little above the first resonance frequency. F has its first resonance, $\omega_1 = k_1\omega_c$, for $k_1 = 2.054$ when $\nu = 0.31$ (see Christensen and Olsen [21]). Thus, by measuring ω_1 , we can

find ω_c and G_c of Eq. (8). The function

$$F_1(k) = \frac{1}{1 - \left(\frac{k}{k_1}\right)^2}, \quad (18)$$

matches $F(k)$ both for $k \rightarrow 0$ and at the resonance frequency. Inverting F_1 using the nondissipative definition of k [Eq. (9)] gives

$$G_t^{(1)} = G_c \left[\left(\frac{\omega}{\omega_c}\right)^2 + k_1^2 \frac{1 - F_1}{F_1} \right], \quad (19)$$

which may then be used as an initial trial function for the Newton–Raphson inversion algorithm with F_m inserted for F_1 .

Figure 4 shows model examples of F and F_1 for cases where the sample modulus is set to values of $G = (10 + 0.1i)G_c \sim 0.7$ GPa and $G = (50 + 0.1i)G_c \sim 3.5$ GPa, corresponding to “soft” and “hard” liquids, respectively. The shear modulus of a hard liquid like glycerol is ~ 4 GPa [38–40], which is a little more than 50 times the characteristic modulus, $G_c = 0.07$ GPa, of the PSG.

Figure 5 presents a comparison between the previous inversion algorithm [21] for determining G^* of the sample and the Newton–Raphson implementation. Figures 5(a) and 5(b) show data on squalane, a “soft” liquid, which in addition to the main (alpha) relaxation feature a secondary (beta) contribution ($G_\infty < 1$ GPa [28]). Figures 5(c) and 5(d) show the same comparison for glycerol, which has a high plateau modulus ($G_\infty \sim 4$ GPa [27]). The results from the

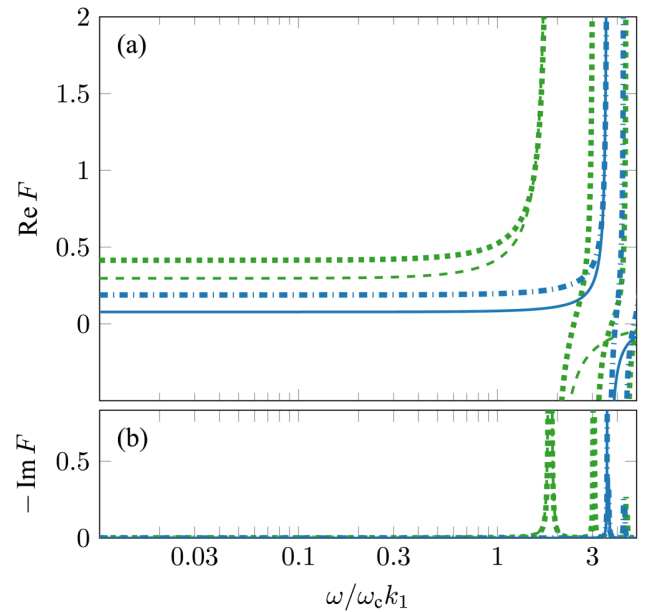


FIG. 4. The normalized capacitance, F (dotted and dashed lines), of the PSG transducer as a function of frequency along with the trial function, F_1 (dashed and solid lines), for two values of G^* : $G^* = (10 + 0.1i)G_c$ (dotted and dashed lines) and $G^* = (50 + 0.1i)G_c$ (dashdotted and solid lines). The frequencies are scaled relative to the resonance frequency of the empty transducer, $\omega_c k_1$, where ω_c is the characteristic frequency of the PSG and $k_1 = 2.054$.

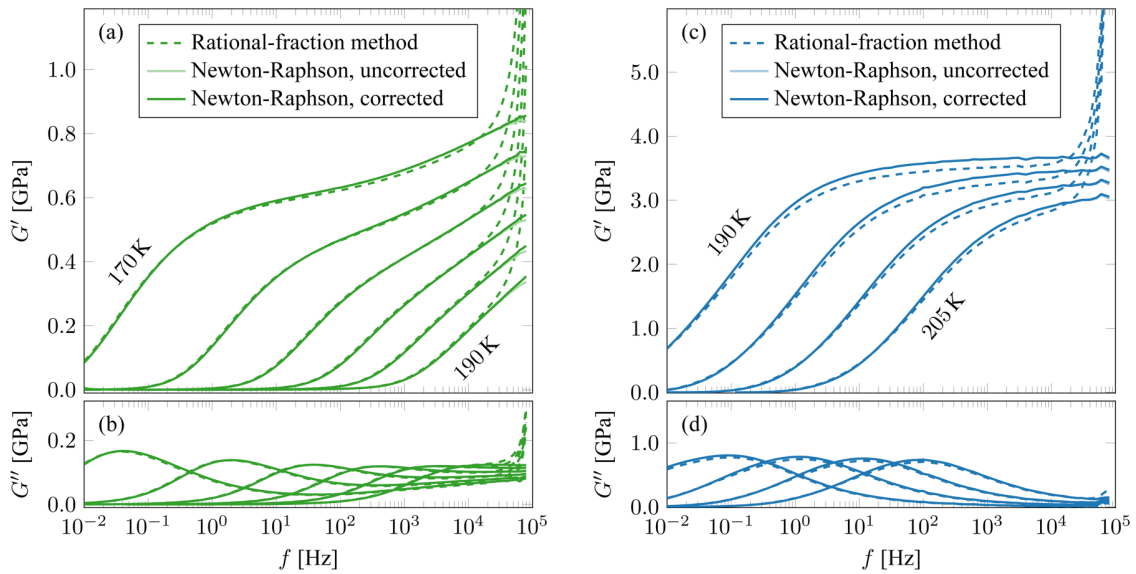


FIG. 5. Comparison of inversion methods used on data from squalane (left) and glycerol (right). These data are obtained with the 3-PZ PSG. To compare the two different inversion algorithms, we have used raw data (i.e., measured capacitance of the PSG with and without liquid) and inverted them using the two algorithms. Shear moduli extracted from these data have previously been published by Roed *et al.* [32] (squalane) and Jensen *et al.* [27] (glycerol). Dashed lines are data inverted using the algorithm described in Christensen and Olsen [21]. Lighter colored solid lines are inverted using the Newton–Raphson algorithm, and the darker solid lines have subsequently been corrected for sample inertia. The difference between corrected and uncorrected data is only visible at frequencies above 30 kHz and only in the storage modulus for squalane. The glycerol moduli are so high that the correction is almost not visible. Note how data inverted by the rational fraction algorithm diverges as the frequency approaches the resonance frequency of the PSG (at 100 kHz), while data inverted by the new algorithm levels off to approach G_∞ , thus extending the frequency range up to 50–70 kHz.

previous procedure and the Newton–Raphson algorithm yield comparable results in the low-frequency region. At higher frequencies, though, the Newton–Raphson method clearly gives better results. The rational-fraction algorithm introduces an artefact where both real and imaginary parts of the modulus rise sharply as the frequency approaches the resonance, which is located around 100 kHz. Moduli computed with the Newton–Raphson method approach a plateau, G_∞ at high frequencies. As expected, the inversion cannot go above the first resonance frequency of the empty transducer.

IV. RESULTS AND DISCUSSION

In this section, we present measurements carried out with the 1-PZ PSG. All measurements are carried out using cryostats and measurement equipment constructed at Roskilde University [41,42].

Figure 6 shows a photo and a schematic drawing of the 1-PZ PSG implementation designed for liquid measurements (for a different implementation intended for solid samples, see Appendix D). The rigid outer disks are made from sapphire glass. When assembling the cell, the two sapphire disks are self-centered in the cell casing by the electrode pins that go through a small hole drilled in the center of the thick sapphire disks. The PZ disk in the middle is then clamped between the ends of the two electrode pins, which have flat heads ensuring electrical contact, but also acting as spacers. These spacers ensure parallelism of the plates. The horizontal alignment of the middle PZ disk is done by hand when assembling and later inspected in a microscope.

The sample is loaded into the cell from the side at room temperature where the liquid has a low viscosity and is

drawn into the gaps by capillary forces. It is subsequently cooled to temperatures close to the glass transition temperature covering viscosities from 1 kPa s to 100 GPa s.

As argued above, the 1-PZ PSG should yield results identical to those of the 3-PZ PSG if the assumption holds that the rigid disks replacing the outer PZ disks can be considered “infinitely” rigid. We test this assumption by comparing two consecutive measurements in the same experimental setup

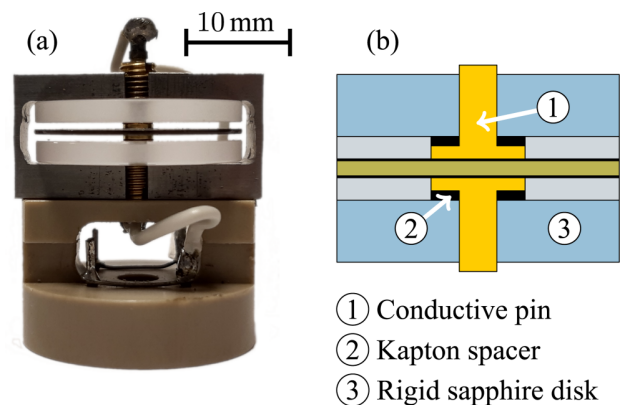


FIG. 6. (a) Photo of 1-PZ PSG for liquid samples. The rigid supports are made from sapphire glass and are held in place by an aluminum casing. Conductive pins leading through the sapphire glass hold the PZ disk in place and provide electrical connection to the electrodes. These electrode pins also define the thickness of the sample space and their presence means that this PSG has a rigid hub in the center. Wires lead from the pins to connecting points for measurement equipment. (b) Schematic drawing of the center of the device. Kapton spacers were placed between the flat head of the electrode pin and the sapphire glass to allow the liquid sample to contract axially.

(same cryostat, same electronics): one with a 3-PZ PSG and the other with a 1-PZ PSG. Results obtained with the 3-PZ PSG have previously been found to be in agreement with other mechanical measurements: Gainaru *et al.* [25] used master curves obtained by standard rheological measurements and spectra from a 3-PZ PSG to evidence a low-frequency rheological signal in monoalcohols like that of a short chain polymer, and Hecksher *et al.* [28] combined PSG spectra with ultrahigh-frequency propagation methods form true broadband mechanical spectra spanning 14 decades in frequency.

The sample chosen for these measurements is tetramethyl-tetraphenyl-trisiloxane (DC704), a diffusion-pump oil used as a model glass-former [43]. DC704 is chemically stable, it does not absorb water, and it has been

measured numerous times [44–47] showing that it obeys time-temperature superposition and that its mechanical and electrical properties do not change over time. Thus, DC704 is ideal for this test because any discrepancy between data obtained by 3- and by 1-PZ measurements must originate from the cell and not the sample.

The result of the initial measurements is shown in Figs. 7(a) and 7(b). The spectra from the 1-PZ (full lines) have a slightly different overall vertical scaling than the 3-PZ measurement (dashed lines). This is a well-known uncertainty of the measurement of 5%–10% [46]. However, a vertical scaling does not correct or explain the general shift of the spectra obtained with 1-PZ PSG to higher frequencies.

To explain this discrepancy, we look into the details of the thermal contraction of the sample in the two different

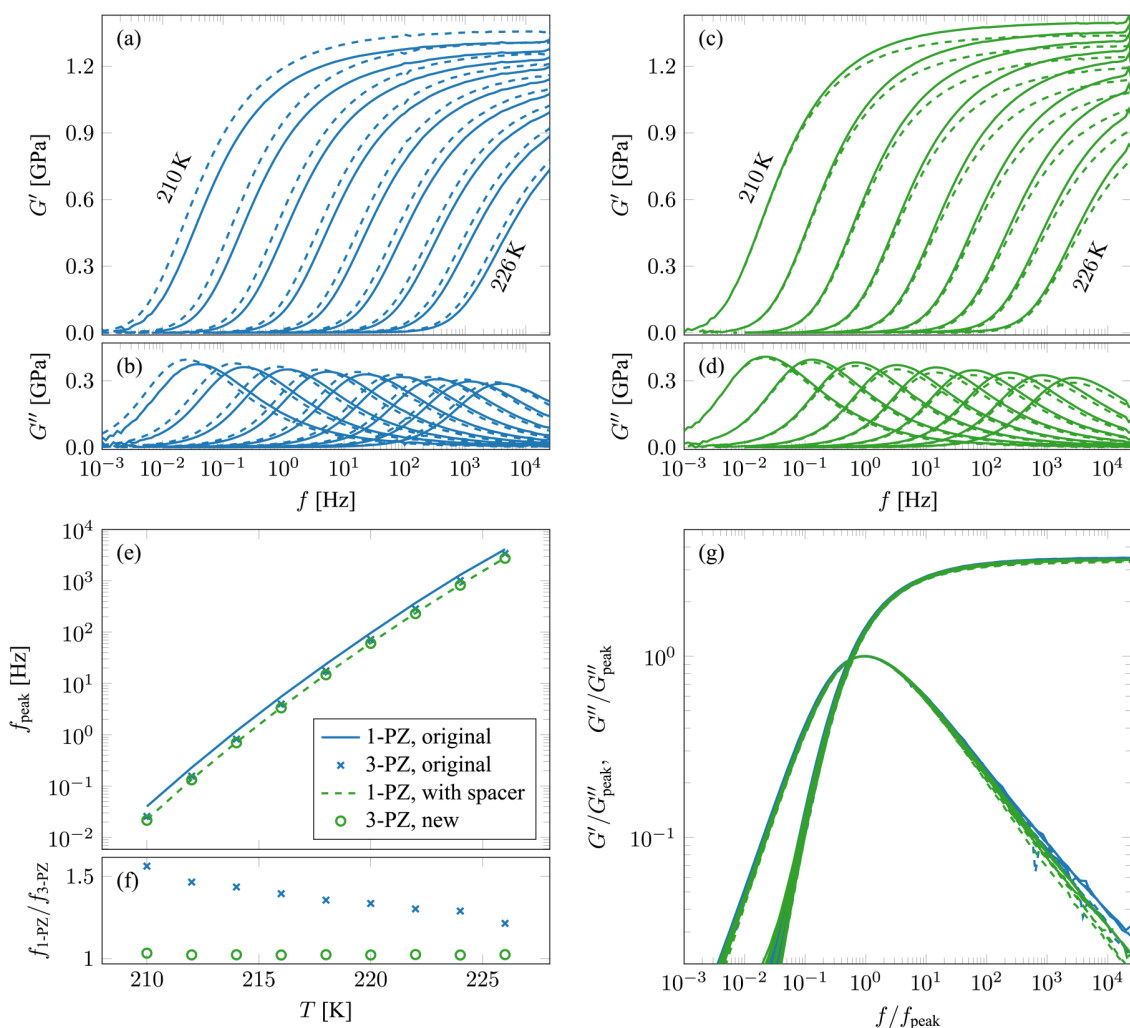


FIG. 7. Shear modulus of DC704, comparing two sets of measurements made using a 3-PZ and a 1-PZ PSG (a total of four measurements: both 3-PZ and 1-PZ PSG measurements were repeated, since the two sets were carried out in different cryostats with slightly different absolute temperature calibration). Measurements were made at temperatures from 210 to 226 K in steps of 2 K. (a) and (b) show the storage modulus, G' , and loss modulus, G'' , respectively, measured using a 3-PZ and a 1-PZ PSG (without a soft spacer). (c) and (d) show G' and G'' , measured using a 3-PZ and a 1-PZ PSG with kapton spacers that allow the sample to contract axially. (e) shows the loss peak position as a function of temperature for all four measurements. (f) shows the ratio of loss peak position, f_{peak} , of the 3-PZ and the 1-PZ PSG measurements, respectively. Clearly, the time scales obtained with the 1-PZ PSG are different than those obtained with the 3-PZ PSG in the original measurements, and the ratio is increasing as the temperature is lowered. Identity of the time scales is restored, when a soft spacer is added in the 1-PZ PSG. (g) shows all spectra scaled on the frequency axis with the loss peak frequency and modulus (both real and imaginary part) scaled by the value of G'' at the loss peak, G''_{peak} . Plotted this way, all four data sets collapse within the experimental uncertainty, showing that the sample obeys time-temperature superposition (TTS), i.e., the spectral shape is unchanged between the different measurements. The deviations seen at the flanks of the loss peak are on the order of a few percent and reflect the uncertainty of the measurement.

cells upon cooling. The liquid is filled into the cell at room temperature and thus it contracts when cooled towards its glass transition temperature. For DC704, the isobaric thermal expansion coefficient is roughly $\alpha_p = 7 \times 10^{-4} \text{K}^{-1}$, and the glass transition temperature is $T_g = 210 \text{ K}$. This gives an estimated relative change in sample volume of $\sim 5\%$ at the measurement temperatures.

One would guess that this contraction happens primarily in the radial direction, where the surface is free. However, as the liquid cools, its viscosity increases enormously. Consequently, the radial flow of the contracting liquid is severely hampered due to the confined geometry, where the sample thickness is much smaller than the radius, $d \ll R$. This was discussed by Niss *et al.* [48], where the radial flow time, i.e., the characteristic time for flow in the radial direction, was estimated to be $\tau_{\text{flow}} \propto \tau_M (R/d)^2$, where $\tau_M = \eta/G_\infty$ is the Maxwell relaxation time. This estimate is based on a situation, where the liquid is not able to contract/flow in the axial direction, which can be assumed to be the case for the 1-PZ PSG with thick sapphire supports. Thus, at some finite temperature, the radial flow time exceeds the experimental time scale and flow ceases. Upon continued cooling, the liquid volume will then no longer change and the thermodynamic boundary condition ends up being closer to isochoric than isobaric.

However, in the 3-PZ PSG the outer PZ disks are relatively thin and flexible, so the contraction/flow might progress slightly differently due to bending of the outer plates. In Subsections IV A and IV B, we show model calculations of the bending of a flexible disk in contact with liquid that is radially clamped and how that leads to a flow time that scales as $(R/d)^6$, indeed confirming that a liquid sample in the 3-PZ PSG is able to bend the outer disks during thermal contraction and that this is the main mechanism for volume change.

A. Plate bending after stopped radial flow

Consider a sample between two cylindrical disks of equal radii, R . The lower disk is thick and rigid, whereas the upper disk, of thickness h , is considered thin ($h \ll R$) and flexible with flexural rigidity D . The two disks are connected by a central hub of radius r_h . The gap between the disks is filled with liquid to the edge at ambient temperature.

We start out by analyzing what happens if we assume that radial flow has stopped to find the characteristic length scale of bending.

Plate bending, $\zeta(r)$, due to a normal force per area, $p(r)$, is governed by the fourth-order differential equation [49]

$$D\Delta^2\zeta - p = 0, \quad (20)$$

where D is the flexural rigidity given by the Young's modulus, E , the Poisson ratio, ν , and the thickness, h , of the plate,

$$D = \frac{Eh^3}{12(1-\nu^2)}. \quad (21)$$

Δ is the Laplace operator which in the cylindrically symmetric situation we consider here is given by

$$\Delta = \frac{1}{r} \frac{d}{dr} r \frac{d}{dr}. \quad (22)$$

The radius variable, r , ranges between the fixed hub, at r_h , and the rim, at R . The boundary conditions at r_h are no displacement and no bending,

$$\zeta = 0, \quad (23)$$

$$\frac{d\zeta}{dr} = 0, \quad (24)$$

and at R the boundary conditions are

$$\frac{d}{dr} \Delta\zeta = 0, \quad (25)$$

$$\Delta\zeta - \frac{1-\nu}{r} \frac{d\zeta}{dr} = 0. \quad (26)$$

The situation is depicted in Fig. 8. The plate is in contact with an elastic medium with longitudinal modulus M_T . The medium has an equilibrium thickness a , which before contraction of the liquid is equal to d . d is the distance between the rigid support and the flexible plate in the unbent state. Upon cooling, the medium contracts by flow in the radial direction while a stays equal to d . However, at some temperature flow becomes hindered by the increasing viscosity and the medium starts to contract in the z direction. Then, $a < d$ and the medium exerts an elastic force on the plate proportional to u_z , the displacement of the medium surface from the equilibrium position. The force per area on the plate due to

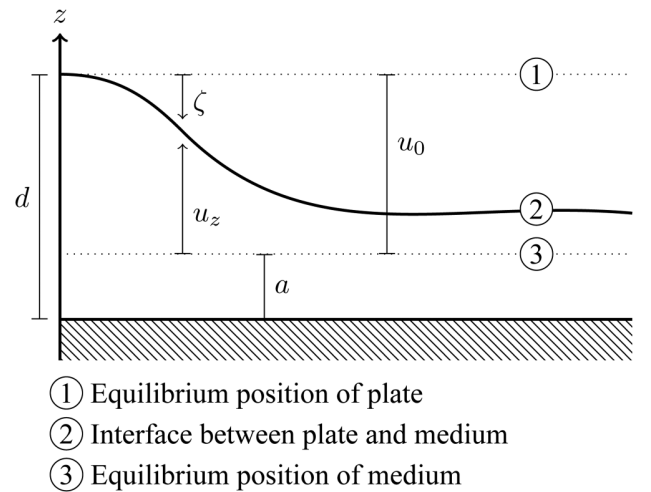


FIG. 8. Plate bending by thermal contraction of a liquid in the axial direction. ζ is the deviation of plate position from equilibrium, d is the distance between plate and rigid support, and u_0 is the distance from plate equilibrium to elastic medium equilibrium.

the elastic medium thus becomes

$$p = -\frac{u_z}{a}M_T, \quad (27)$$

where M_T is the longitudinal modulus. Since $u_z = \zeta + u_0$ and $a \approx d$, we have

$$\Delta^2 \zeta + (\zeta + u_0) \frac{M_T}{Dd} = 0. \quad (28)$$

Now, we define a characteristic length

$$l = \left(\frac{dD}{M_T}\right)^{1/4} = \left(\frac{dh^3E}{12(1-\nu^2)M_T}\right)^{1/4}. \quad (29)$$

If $d \approx h$ and $E \approx M_T$, then $l \approx d$. We now use l as the unit of length. Then, the differential Eq. (28) becomes

$$\Delta^2 \zeta + \zeta + u_0 = 0, \quad (30)$$

which is an inhomogeneous differential equation. If we, however, look at u_z instead, we get the corresponding homogeneous equation which is more convenient to solve

$$\Delta^2 u_z + u_z = 0. \quad (31)$$

Only the first boundary condition for u_z differs from those of ζ , becoming

$$u_z(r_h) = u_0. \quad (32)$$

The solution to Eq. (31) is a linear combination of the four Kelvin functions, Ber, Bei, Ker, and Kei,

$$u_z(r) = A_1 \text{Ber}(r) + A_2 \text{Bei}(r) + A_3 \text{Ker}(r) + A_4 \text{Kei}(r), \quad (33)$$

and the values of the four constants may be found by applying the boundary conditions (see Appendix F). Figure 9 shows an example of such a solution for the profile of the bending.

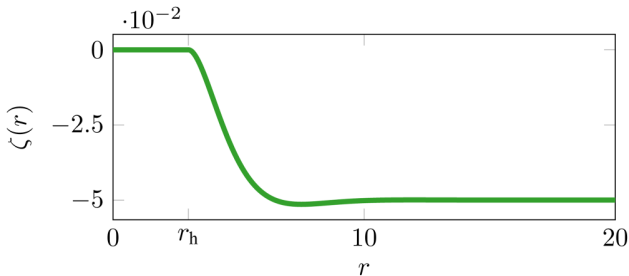


FIG. 9. Solution to the differential Eq. (31) governing bending of a thin disk, showing the radial profile of the disk, where r_h is the radius of the hub (the head of the conductive pin in Fig. 6). Both axes are in units of the characteristic elastic length l [see Eq. (29)]. Since $l \sim d$, a bending of $\zeta = -0.05$ corresponds to the liquid contracting 5% in the axial direction. The radius of $20d$ thus corresponds to ~ 10 mm, which is the radius of the PZ disks used in the measurements. The profile is rather flat except close to the hub.

B. Flow time

We proceed to derive the characteristic flow time for the process where the radial pressure gradient exerted on the liquid by the bending plate makes the liquid flow. Let $V(r)$ be the volume of the liquid inside radius r and $\dot{V}(r)$ its time derivative. In order to simplify the modeling of the flow, we assume that different parts of the liquid flow *either* in the radial direction *or* in the axial direction. The gain in volume between r and $r + dr$ due to flow in the radial direction in time dt is $\dot{V}(r + dr)dt - \dot{V}(r)dt$. This must equal the loss in volume due to flow in the axial direction which is $-2\pi r dr \dot{\zeta} dt$. The volume continuity equation thus becomes

$$\dot{\zeta}(z) = -\frac{1}{2\pi r} \frac{d\dot{V}}{dr}. \quad (34)$$

The flow in the r direction is considered to be planar Poiseuille flow, implying that the one-dimensional volume flow per length orthogonal to the flow direction is $-\frac{dp}{dr} d^3 / 12\eta$. If for the radial flow we take the length as $2\pi r$, we get

$$\dot{V} = -\frac{dp}{dr} \frac{r\pi d^3}{6\eta}. \quad (35)$$

Applying the Laplacian, Δ , to the equation of quasistatic equilibrium of the circular plate, Eq. (20), we get

$$D\Delta^3 \zeta - \Delta p = 0. \quad (36)$$

From Eqs. (34) and (35), we have

$$\begin{aligned} \Delta p &= \frac{1}{r} \frac{d}{dr} r \frac{d}{dr} p \\ &= -\frac{1}{r} \frac{d}{dr} \frac{6\eta}{\pi d^3} \dot{V} \\ &= \frac{12\eta}{d^3} \dot{\zeta}. \end{aligned} \quad (37)$$

When inserting this into the differential equation (36), we get the following 6th order partial differential equation describing the time evolution of ζ ,

$$\Delta^3 \zeta - \frac{12\eta}{Dd^3} \dot{\zeta} = 0. \quad (38)$$

We can estimate the time scale for the relaxation of the plate by fluid flow through dimensional analysis. The parameter $12\eta/Dd^3$ has the dimension time divided by length to the power of 6. If we take the characteristic length as the radius, R , of the disk, the characteristic flow time must be

$$\begin{aligned} \tau_{\text{flow}} &= \frac{12\eta}{Dd^3} R^6 \\ &= 144(1-\nu^2) \frac{G}{E} \left(\frac{R^6}{h^3 d^3}\right) \tau_M. \end{aligned} \quad (39)$$

Here, G is the shear modulus of the liquid and $\tau_M = \eta/G$ the Maxwell relaxation time. The factor $(1 - \nu^2)G/E$ is of the order of 1, whereas

$$144 \left(\frac{R^6}{h^3 d^3} \right) = 144(20^6) \approx 10^{10}. \quad (40)$$

According to these calculations, at room temperature, where $\tau_M \sim 1$ Pas/1 GPa is on the order of 1 ns, the flow time will be on the order of 10 s ($\tau_{\text{flow}} \sim 10^{10} \tau_M$). Even if this is just an estimate, it shows that when the liquid is cooled and its viscosity increases orders of magnitude, it will start contracting axially and bend the outer disks in the 3-PZ PSG, when the radial flow time exceeds the experimental time scale.

Consequently, the liquid is allowed to continue adjusting its volume (albeit mainly in the axial rather than the radial direction) in the 3-PZ PSG, whereas in the 1-PZ PSG the liquid volume freezes in at some temperature (above T_g during cooling). This would explain why the typical relaxation times measured in the 1-PZ PSG are faster than those measured in the 3-PZ PSG since the isochoric relaxation times are lower than the isobaric.

To test this conjecture, we added a soft kapton spacer with a thickness of 50 μm between the hub and the sapphire disks to allow for axial contraction of the sample [see Fig. 6(b)]. Both the 1-PZ (with soft spacers) and the 3-PZ measurement were repeated to ensure identical experimental conditions. The results are shown in Figs. 7(c) and 7(d). Again, we see a slight difference in the overall scaling between 1-PZ and 3-PZ measurement, but here the time scales of the spectra are identical. This is illustrated more clearly in Fig. 7(e) which shows the loss peak frequencies of all four measurements, as well as in Fig. 7(f) showing that the ratio of 1-PZ and 3-PZ loss peak frequencies increases as temperature decreases in the original set of measurements. This is consistent with the interpretation that the thermodynamic boundary condition moves further away from the isobaric case as the temperature is lowered. Ratio of the time scales obtained by 1-PZ and 3-PZ PSG is identically one in the new set of measurements.

Figure 7(g) shows all spectra from the four measurements scaled on the frequency axis to the loss peak frequency, f_{peak} , and scaled to the maximum value, $G''_{\text{peak}} = G''(f_{\text{peak}})$ on the modulus axis. The plot demonstrates that all spectra have the same shape, irrespective of the thermodynamic boundary conditions. This is consistent with DC704 obeying not only TTS but also time-temperature-pressure superposition (TTPS) [50,51].

We conclude that the 1-PZ PSG principle is validated as long as the sample is allowed to contract axially. The outer sapphire disks can for this purpose be considered “infinitely” rigid.

Appendix D contains an implementation of the 1-PZ PSG with steel support that can easily be disassembled to mount solid samples. Pilot measurements on synthetic isoprene rubber (IR) with carbon black N121 filler with this device look promising, but still lack full quantitative agreement with

other methods. Further work is ongoing to bring the 1-PZ PSG in better quantitative agreement with other techniques for solid samples.

V. SUMMARY

The PSG technique works by measuring the capacitance of PZ disk(s) in a sandwich assembly with thin sample layers. A mathematical model connects the measured capacitance to the shear modulus of the sample, but isolating G^* from this is not straightforward. We implemented the Newton–Raphson method for extracting the shear modulus from the measured capacitance spectra and validated our implementation. The new data analysis approach gives results that are in agreement with results obtained with the previously published method [21] at low frequencies and performs even better at higher frequencies which approach the resonance of the PSG. The new method is thus both more precise and extends the frequency range of measurements. In addition, a correction for sample inertia has been implemented.

We proposed a simplification of the PSG measurement principle using only a single PZ disk instead of three and demonstrated that it is equivalent to the 3-PZ design and showed data for two implementations of the 1-PZ PSG.

Measurements on liquid were performed with silicone oil and initially showed a discrepancy in measured time scales between the 1-PZ and 3-PZ PSG, which lead to an analysis of the flow behavior in the two different cells. This shows that one needs to be careful to control the boundary conditions. Liquid samples become very viscous near their glass transition temperature and consequently, their flow is extremely slow and depending on the exact details of the measurement cell that can lead to different consequences: in the first implementation of the 1-PZ PSG with thick sapphire supports, the radial flow—and thus the thermal contraction—stops when the flow time exceeds the experimental time scale, while for the 3-PZ PSG thermal contraction continues in the axial direction. The two implementations were brought in quantitative agreement with respect to the material time scales by introducing a soft spacer between the sapphire supports and the hub that allowed the liquid to contract axially. The absolute levels of the shear moduli measured by the two implementations agree to within 10%, which is equivalent to measurement-to-measurement variations found in 3-PZ PSG measurements. We thus consider the 1-PZ PSG technique to be fully validated for liquid samples and ready to deploy as a routine measurement.

The new 1-PZ design has several advantages over the 3-PZ PSG: (1) it is simpler (no need for matching of PZ disks); (2) it reduces the waste of disks when PZ disks break either due to gluing, drilling, or simply because they are brittle; (3) it is more versatile, i.e., it can be implemented in different ways and for different sample types. Here, we exemplified this by two different implementations, one with sapphire supports for liquid samples and one with steel supports for solid samples (Appendix D). In general, it is easier to design a 1-PZ PSG cell for different sample environments, e.g., an oven or a different cryostat system, when there is no

requirement of three PZ disks in a stacked configuration electrically isolated from surroundings. Furthermore, the 1-PZ PSG with sapphire windows allows for simultaneous optical investigations.

The limitations on the modulus resolution remain the same in the 1-PZ PSG as in the 3-PZ PSG, i.e., the range from 1 MPa to ~ 10 GPa, so the method is best suited for relatively stiff samples.

ACKNOWLEDGMENTS

This work was supported by the VILLUM Foundation's *Matter* Grant (No. 16515) and by Innovation Fund Denmark (Case No. 9065-00002B). Work at TU Dortmund was supported by the Deutsche Forschungsgemeinschaft (Grant No. 461147152).

AUTHOR DECLARATIONS

Conflict of Interest

The authors have no conflicts to disclose.

APPENDIX A: MATHEMATICAL DERIVATION OF THE MAPPING FROM 3-PZ PSG TO THE ONE-ONE CONFIGURATION

For the 3-PZ PSG, numerate the top piezodisk by 1, the middle one by 2, and the bottom one by 3. The equations of motion for 1 and 3 are identical. By f_1 , we denote the stress from the liquid layer on the upper disk. h is the thickness of the disk, ρ is its density, and u_1 is the radial displacement. Newton's second law for a volume element becomes

$$(r + dr)d\phi h\sigma_{r+dr,r+dr}^{(1)} - rd\phi h\sigma_{rr}^{(1)} - drhd\phi\sigma_{\phi,\phi}^{(1)} + f_1 drrd\phi = \rho h drrd\phi \ddot{u}_1 \quad (\text{A1})$$

and dividing by $drrd\phi h$ gives for plate 1

$$\frac{\partial}{\partial r} r\sigma_{rr}^{(1)} - \sigma_{\phi,\phi}^{(1)} + f_1 \frac{r}{h} = \rho r \ddot{u}_1, \quad (\text{A2})$$

which is Eq. (18) of Christensen and Olsen [21] (with $\sigma_l = -f_1$). The stresses can be expressed in terms of the displacement fields using the constitutive equations and expressions of strains [Eqs. (2) and (8) of Christensen and Olsen [21]]. Using the fact that E_z is independent of r , this leads to the substitution rule

$$\frac{\partial}{\partial r} (r\sigma_{rr}) - \sigma_{\phi,\phi} \rightarrow c_{11} \left(ru'' + u' - \frac{u}{r} \right) \quad (\text{A3})$$

by which Eq. (A2) becomes

$$c_{11} \left(ru_1'' + u_1' - \frac{u_1}{r} \right) + f_1 \frac{r}{h} = \rho r \ddot{u}_1. \quad (\text{A4})$$

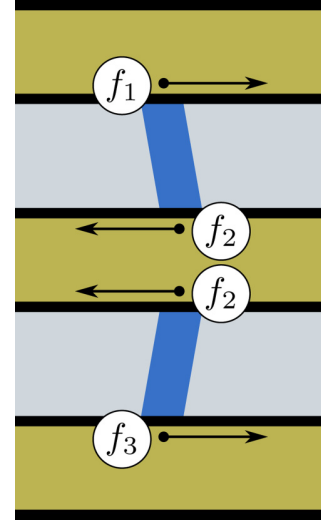


FIG. 10. Stresses from sample on disks in the 3-PZ PSG. This figure shows a section of the disks with the sample between the disks (cf. Fig. 1). One liquid filament (shaded darker) exerts stress on two disks. The top liquid filament exerts stress f_1 on the upper disk and stress f_2 on the middle disk. The bottom liquid filament exerts f_2 on the middle disk and f_3 on the bottom disk. The middle disk is thus under a shear stress of $2f_2$.

Correspondingly, we have for plate 2

$$c_{11} \left(ru_2'' + u_2' - \frac{u_2}{r} \right) + 2f_2 \frac{r}{h} = \rho r \ddot{u}_2, \quad (\text{A5})$$

where f_2 is the stress from one of the liquid layers. For plate 3, we get the same equation as for plate 1,

$$c_{11} \left(ru_3'' + u_3' - \frac{u_3}{r} \right) + f_3 \frac{r}{h} = \rho r \ddot{u}_3. \quad (\text{A6})$$

Assuming a (radially dependent) shear deformation of the two liquid layers, we have by symmetry and Newton's third law that

$$f_2 = -f_1 = -f_3 = -G^* \frac{u_2 - u_1}{d} = -G^* \frac{u_2 - u_3}{d}. \quad (\text{A7})$$

We assume that the time dependence of the fields is proportional to $e^{-i\omega t}$ and redefine u to be the complex amplitude. This corresponds to the substitution $\ddot{u} \rightarrow -\omega^2 u$. When inserting Eq. (A7) into Eqs. (A4) and (A5), we get

$$c_{11} \left(ru_1'' + u_1' - \frac{u_1}{r} \right) + G^* \frac{u_2 - u_1}{dh} r = -\omega^2 \rho r u_1, \quad (\text{A8})$$

$$c_{11} \left(ru_2'' + u_2' - \frac{u_2}{r} \right) - 2G^* \frac{u_2 - u_1}{dh} r = -\omega^2 \rho r u_2. \quad (\text{A9})$$

We do not continue writing up the differential equation and boundary conditions of plate 3 since they are completely identical to those of plate 1.

Now, introduce the variable

$$u \equiv u_2 - u_1 = u_2 - (u_1 + u_3)/2. \quad (\text{A10})$$

Subtracting Eq. (A8) from Eq. (A9), we get

$$c_{11} \left(ru'' + u' - \frac{u}{r} \right) - 3G^* \frac{u}{dh} r = -\omega^2 \rho ru \quad (\text{A11})$$

or

$$r^2 u'' + ru' + \left[\left(\frac{\omega^2 \rho}{c_{11}} - \frac{3G^*}{c_{11} dh} \right) r^2 - 1 \right] u = 0. \quad (\text{A12})$$

Comparing to Eq. (20) in Christensen and Olsen [21], we see that d has been replaced by $d/3$. However, we also have to see what happens to the boundary conditions and the expression for the normalized capacitance F . The boundary conditions become zero displacement at the centers,

$$u_1(0) = 0, \quad u_2(0) = 0, \quad (\text{A13})$$

and zero stress at the boundaries

$$\begin{aligned} u_1'(R) + \frac{\nu}{R} u_1(R) &= (1 + \nu) d_{13} E_z^{(1)}, \\ u_2'(R) + \frac{\nu}{R} u_2(R) &= (1 + \nu) d_{13} E_z^{(2)}. \end{aligned} \quad (\text{A14})$$

The two outer disks are electrically coupled in series, and this couple is then connected in parallel with the middle disk. Furthermore, the polarity of the middle disk is reversed compared to that of the outer disks to reverse the motion of the middle disk. That means that

$$E_z \equiv E_z^{(2)} = -2E_z^{(1)}, \quad (\text{A15})$$

and thus the boundary conditions for u become

$$u(0) = 0 \quad (\text{A16})$$

and

$$u'(R) + \frac{\nu}{R} u(R) = (1 + \nu) d_{13} \frac{3}{2} E_z. \quad (\text{A17})$$

If we normalize a little differently than for the one-one configuration [21] and include the factor of $3/2$ in front of E_z ,

$$x \equiv \frac{r}{R}, \quad e(x) \equiv \frac{2}{3(1 + \nu) d_{13} E_z R} u(Rx), \quad (\text{A18})$$

we get exactly the same differential equation and boundary conditions for $e(x)$ as in Christensen and Olsen [21],

$$x^2 e'' + x e' + (k^2 - 1) e = 0, \quad (\text{A19})$$

$$e(0) = 0, \quad e'(1) + \nu e(1) = 1, \quad (\text{A20})$$

with k given as in Eq. (9).

This means that the solution in terms of $e(x)$ is exactly the same. Only the scaling factor of the modulus G_c is changed by $1/3$. The normalized modulus $V = G^*/G_c$ is the same for

the 3-PZ PSG and the one-one configuration, but G_c is changed.

Finally, let us discuss the measured capacitance C_m . For each of the three disks, Eq. (14) of Christensen and Olsen [21] is valid. It can be written for disk 1 (and 3) as

$$\begin{aligned} C_m^{(1)} &= (C_f - C_{cl}) \frac{u_1(R)}{E_z^{(1)} R d_{13}} + C_{cl} \\ &= (C_f - C_{cl}) \frac{-2u_1(R)}{E_z R d_{13}} + C_{cl} \end{aligned} \quad (\text{A21})$$

and for disk 2 as

$$\begin{aligned} C_m^{(2)} &= (C_f - C_{cl}) \frac{u_2(R)}{E_z^{(2)} R d_{13}} + C_{cl} \\ &= (C_f - C_{cl}) \frac{u_2(R)}{E_z R d_{13}} + C_{cl}. \end{aligned} \quad (\text{A22})$$

The total capacitance of the configuration becomes

$$\begin{aligned} C_m &= \frac{1}{2} C_m^{(1)} + C_m^{(2)} \\ &= (C_f - C_{cl}) \frac{u_2(R) - u_1(R)}{E_z R d_{13}} + \frac{3}{2} C_{cl} \\ &= (C_f - C_{cl}) \frac{3}{2} (1 + \nu) e(1) + \frac{3}{2} C_{cl}. \end{aligned} \quad (\text{A23})$$

Thus, the normalized capacitance of the 3-PZ PSG,

$$F = \frac{C_m - \frac{3}{2} C_{cl}}{\frac{3}{2} (C_f - C_{cl})} = (1 + \nu) e(1), \quad (\text{A24})$$

is exactly identical to that of the one-one configuration. The only difference is that the effective liquid layer thickness is one third of the real layer in the 3-PZ PSG.

APPENDIX B: INCLUDING EFFECTS OF PARTIAL LIQUID FILLING

The liquid sample is filled into the PSG at room temperature such that the sample diameter exactly matches the diameter of the disks. But, because of thermal contraction, when the PSG and sample are cooled down, the radius, r , of the liquid layer will be smaller than the disk radius, R . This partial filling leads to the sample clamping the disks to a lesser extent. Therefore, a lower modulus than the true value would be determined if the contraction was not taken into account in the inversion procedure. In Christensen and Olsen [21], an expression for the normalized capacitance, F [defined by Eq. (5)], was given, making $F = F(S, V, x_l)$ also a function of the scaled liquid radius, $x_l = r/R$.

First, we review the analytic solution to the problem of partial filling including some more details on the derivations. The differential equations shown as Eq. (46) of Christensen

and Olsen [21] were

$$\begin{aligned} x^2 e_1'' + x e_1' + [(k_1 x)^2 - 1] e_1 &= 0, \\ k_1^2 &= \left(\frac{\omega}{\omega_c}\right)^2 - \frac{G^*}{G_c}, \\ x^2 e_2'' + x e_2' + [(k_2 x)^2 - 1] e_2 &= 0, \\ k_2^2 &= \left(\frac{\omega}{\omega_c}\right)^2 \end{aligned} \tag{B1}$$

and the boundary conditions were

$$e_1(0) = 0, \tag{B2}$$

$$e_1(x_l) = e_2(x_l), \tag{B3}$$

$$e_1'(x_l) + \frac{\nu}{x_l} e_1(x_l) = e_2'(x_l) + \frac{\nu}{x_l} e_2(x_l), \tag{B4}$$

$$e_2'(1) + \nu e_2(1) = 1. \tag{B5}$$

By using the second boundary condition, the third can be simplified to

$$e_1'(x_l) = e_2'(x_l). \tag{B6}$$

The solutions are, in terms of Bessel functions J_1 and Y_1 ,

$$e_1(x) = A J_1(k_1 x) + B Y_1(k_1 x), \tag{B7}$$

$$e_2(x) = C J_1(k_2 x) + D Y_1(k_2 x). \tag{B8}$$

Now, $J_1(0) = 0$ and $Y_1(0) = -\infty$. Thus, Eq. (B2) implies $B = 0$ and Eq. (B3) becomes

$$A J_1(k_1 x_l) = C J_1(k_2 x_l) + D Y_1(k_2 x_l). \tag{B9}$$

The derivative of the Bessel function J_1 (and likewise Y_1) fulfills

$$\frac{d}{dx} J_1(kx) = k J_0(kx) - \frac{1}{x} J_1(kx). \tag{B10}$$

When inserting the solutions of Eqs. (B7) and (B8) into Eq. (B6) using Eq. (B10), a number of terms with zeroth and first order Bessel functions appear. The first order terms cancel due to Eq. (B9), and we are left with

$$A k_1 J_0(k_1 x_l) = C k_2 J_0(k_2 x_l) + D k_2 Y_0(k_2 x_l). \tag{B11}$$

Multiplying this equation with $J_1(k_1 x_l)$ and inserting Eq. (B9), we get rid of the constant A ,

$$\begin{aligned} C k_1 J_0(k_1 x_l) J_1(k_2 x_l) + D k_1 J_0(k_1 x_l) Y_1(k_2 x_l) \\ = C k_2 J_0(k_2 x_l) J_1(k_1 x_l) + D k_2 Y_0(k_2 x_l) J_1(k_1 x_l), \end{aligned} \tag{B12}$$

or, collecting terms,

$$RC + TD = 0, \tag{B13}$$

where

$$\begin{aligned} R &= k_1 x_l J_0(k_1 x_l) J_1(k_2 x_l) - k_2 x_l J_0(k_2 x_l) J_1(k_1 x_l), \\ T &= k_1 x_l J_0(k_1 x_l) Y_1(k_2 x_l) - k_2 x_l Y_0(k_2 x_l) J_1(k_1 x_l). \end{aligned} \tag{B14}$$

(Note: The R and T terms could have been defined without the superfluous x_l factors outside the Bessel functions. However, we comply with the original definitions in Christensen and Olsen [21].)

Finally, the fourth boundary condition, Eq. (B5), yields

$$PC + QD = 1, \tag{B15}$$

where

$$\begin{aligned} P &= k_2 J_0(k_2) + (\nu - 1) J_1(k_2), \\ Q &= k_2 Y_0(k_2) + (\nu - 1) Y_1(k_2), \end{aligned} \tag{B16}$$

once again using Eq. (B10). Define the determinant

$$\Delta = PT - RQ \tag{B17}$$

and the solution of Eqs. (B13) and (B15) with respect to C and D is

$$C = T/\Delta, \quad D = -R/\Delta. \tag{B18}$$

APPENDIX C: INCLUDING THE INELASTIC HUB

Including an inelastic hub essentially just moves the first boundary condition to the relative radius $x_h = r_h/R$ of the hub. Thus, Eq. (B2) is replaced by

$$e_1(x_h) = 0. \tag{C1}$$

The solutions are still of the form Eqs. (B7) and (B8), but now $B \neq 0$. For the sake of readability, let

$$a = J_1(k_1 x_h), \quad b = Y_1(k_1 x_h), \tag{C2}$$

$$c = J_1(k_1 x_l), \quad d = Y_1(k_1 x_l), \tag{C3}$$

$$e = J_1(k_2 x_l), \quad f = Y_1(k_2 x_l), \tag{C4}$$

$$g = k_1 x_l J_0(k_1 x_l), \quad h = k_1 x_l Y_0(k_1 x_l), \tag{C5}$$

$$i = k_2 x_l J_0(k_2 x_l), \quad j = k_2 x_l Y_0(k_2 x_l), \tag{C6}$$

and the three first boundary conditions become

$$Aa + Bb = 0, \tag{C7}$$

$$Ac + Bd = Ce + Df, \quad (C8)$$

$$Ag + Bh = Ci + Dj, \quad (C9)$$

while the fourth is still

$$PC + QD = 1. \quad (C10)$$

The last equation is the unaltered Eq. (B15) with P and Q still defined by Eq. (B16).

Multiplying Eqs. (C8) and (C9) with b and using Eq. (C7) to eliminate B , the second and third boundary conditions become

$$A(bc - ad) = Cbe + Dbf, \quad (C11)$$

$$A(bg - ah) = Cbi + Dbj. \quad (C12)$$

Multiplying Eq. (C12) with $bc - ad$ and using Eq. (C11), the third boundary condition becomes

$$(Cbe + Dbf)(bg - ah) = (Cbi + Dbj)(bc - ad) \quad (C13)$$

or (cancelling a common b factor and collecting terms)

$$[b(ge - ci) + a(di - he)]C + [b(fg - cj) + a(dj - fh)]D = 0. \quad (C14)$$

We recognize that

$$R = ge - ci, \quad T = fg - cj \quad (C15)$$

as defined in Eq. (B14) for the problem without a hub. Define

$$U = di - he, \quad W = dj - fh \quad (C16)$$

and

$$R' = bR + aU, \quad T' = bT + aW. \quad (C17)$$

Then, the third boundary condition of the problem with the hub becomes

$$R'C + T'D = 0, \quad (C18)$$

which resembles that of the problem without hub. The solution likewise becomes

$$C = T'/\Delta', \quad D = -R'/\Delta' \quad (C19)$$

with

$$\Delta' = PT' - R'Q. \quad (C20)$$

Written in this form, it is easy to see that the solutions for

the two problems coincide when $x_h \rightarrow 0$. Then, $a \rightarrow 0$, since $J_1(0) = 0$. On the other hand, $b \rightarrow -\infty$. However, since $R' \rightarrow bR$ and $T' \rightarrow bT$, it follows that $\Delta' \rightarrow b\Delta$. Thus, the common diverging b factors of the denominator and the numerator in Eq. (C19) cancel, giving the right limiting behavior.

Now, $V = G^*/G_c$ can be found by inversion of

$$F(S, V, x_l) = (1 + \nu)(CJ_1(k_2) + DY_1(k_2)), \quad (C21)$$

recalling that the left-hand side can be measured and C and D depend on V via k_1 . When including the hub, we can still determine ω_c by a fit to the resonance spectrum of the empty transducer, but the relation to the first resonance is changed. Now, $\omega_1 \neq 2.054\omega_c$.

APPENDIX D: MEASUREMENTS ON A SOLID SAMPLE (RUBBER)

Figure 11(a) shows a photo of the 1-PZ PSG implementations for solid samples. Here, the rigid supports are steel disks and the assembly is encased in a PEEK housing. This assembly can easily be taken apart so that solid samples can be mounted in the cell. A solid sample needs to be glued to the supports as well as the PZ disk to ensure a no-slip boundary condition in the measurement. The centering of the disk, sample and rigid supports is ensured in the gluing process: the “sample sandwich” [outer plate—sample disk—PZ disk—sample disk—outer plate, see Fig. 11(b)] is glued inside a Teflon mold that ensures all layers are perfectly aligned. Parallelism is ensured if all layers have a uniform thickness.

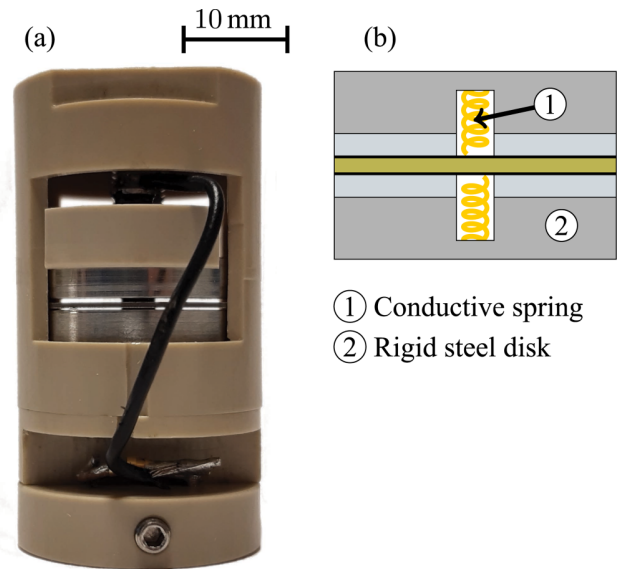


FIG. 11. (a) Photo of 1-PZ PSG for solid samples. The assembly of PZ disk and rigid supports is encased in a plastic housing, which may be opened to take the disks apart for sample mounting. The rigid supports are made from steel and form part of the electrical connection to the PZ disk. (b) Schematic drawing of the center of the device. Metal springs placed in recesses in the steel plates make electrical connection to the PZ disk, when a sample is mounted.

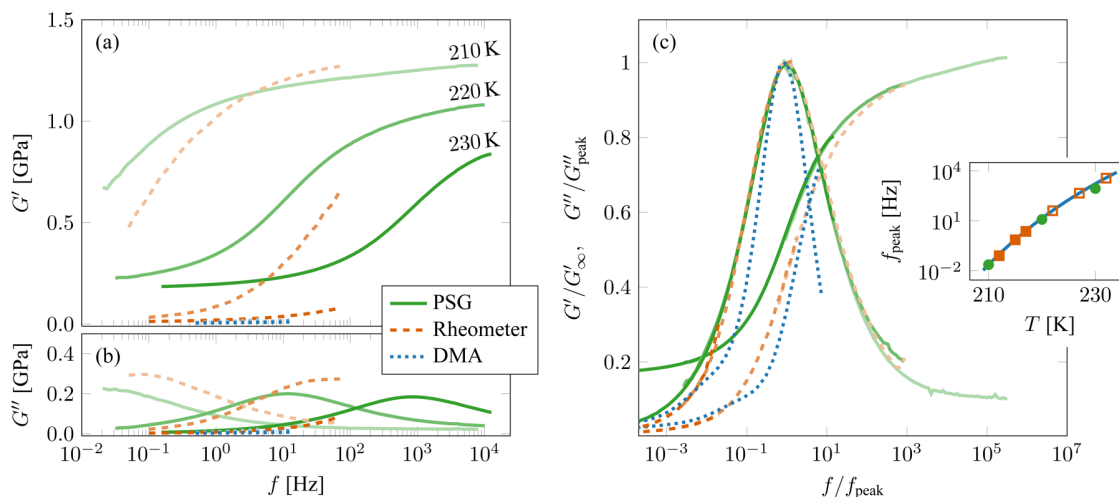


FIG. 12. Shear modulus of filled rubber, measured by PSG, standard rheometer, and dynamic mechanical analysis (DMA). Solid lines are measurements made by PSG at 210, 220, and 230 K. Dashed lines are standard rheometer measurements made at the same temperatures. Dotted lines are DMA measurements carried out at 223, 228, and 233 K. (a) and (b) show storage and loss moduli, while (c) shows both, scaled by the high-frequency limit of G' , denoted G_∞ , and the value of G'' at the loss peak, G''_{peak} , respectively. The inset in (c) shows the temperature dependence of the loss-peak position for the three measurement series. For the PSG measurements (filled circles), as well as the lowest-temperature rheometer measurements (unfilled squares), the peak positions were determined directly from the loss modulus spectra. For higher-temperature rheometer measurements (unfilled squares) and all DMA measurements (full line), the positions were found by mastering and shifted to match the value of the PSG measurement at 210 K (see main text for more details).

A schematic drawing of the inner part is shown in Fig. 11(b). The electrical connection to the PZ disk is secured through the steel supports by small springs in the center going through a small hole in the sample to make contact with the electrodes on the PZ disk. In this case, the sample itself acts as a spacer between the steel support and the PZ disk.

As a proof of concept, measurements on a rubber sample are shown in Fig. 12. The sample used is a synthetic isoprene rubber (IR) with carbon black N121 filler. The recipe (see Table I) was defined in analogy to ASTM D3191,² but using synthetic polyisoprene instead of styrene-butadiene rubber and adding antiaging additives [wax, TMQ; oligomers of 1,2-dihydro-2,2,4-trimethylquinoline 6PPD; *N*-(1,3-dimethyl butyl)-*N'*-phenyl-*p*-phenylenediamine]. The specification of N121 can be found in ASTM D1765.³

The shear modulus was measured by the 1-PZ PSG at temperatures from 210 to 230 K in steps of 10 K. At these temperatures, the shear loss peak is in the frequency window of the PSG. At the peaks, the frequency, f_{peak} , and loss modulus, G''_{peak} , were determined, and along with the high-frequency storage modulus, G_∞ , these values were used to construct the normalized master curve, shown in Fig. 12(c).

For comparison, the shear modulus was also measured with a commercial rheometer (Modular Compact Rheometer MCR 502, Anton Paar, Graz, Austria) as well as by dynamic mechanical analysis (DMA Gabo Eplexor[®] 2000N, Netzsch, Alhden, Germany).

The rheometer measurements were conducted in the oscillatory mode with a deformation of 0.02% in a temperature range from 210 to 230 K. A frequency sweep was performed (from 0.1 to 70 Hz) at each temperature and the complex shear modulus was recorded. For the lowest temperatures, the loss peak frequency and modulus could be determined, and this was used as the basis for a master curve, along with shift factors determined by matching $\tan \delta$ at higher temperatures.

The DMA measurements were conducted in compression with a deformation of up to 2% in a temperature range from -55 to 80 °C (218–353 K). A frequency sweep was performed (from 0.5 to 50 Hz) every 5 K and the complex Young's modulus, E , was determined. Young's modulus was converted [49] into shear modulus using $G = E/(2(1 + \nu))$. For rubber where the Poisson ratio is $\nu = 1/2$, this becomes $G = (1/3)E$. A master curve was then produced using Williams–Landel–Ferry shift factors [52]. From these shift factors, we also obtain the temperature dependence of the material times.

The frequency window of the DMA measurement is rather narrow and measurements were only carried out in the soft region around 1–20 MPa, whereas the PSG and rheometer measurements resolve moduli from around 1 MPa up to several GPa.

Figures 12(a) and 12(b) show real and imaginary parts of all three measurements and Fig. 12(c) shows the corresponding master curves. The real part of PSG and rheometer measurements agree within 10% on a high-frequency plateau,

²ASTM International, ASTM D3191-10(2020), standard test methods for carbon black in SBR (styrene-butadiene rubber)—Recipe and evaluation procedures, in *Annual Book of ASTM Standards* Vol. 09.01 (ASTM International, West Conshohocken, 2021), <https://www.astm.org/d3191-10r20.html>.

³ASTM International, ASTM D1765-21 standard classification system for carbon blacks used in rubber products, in *Annual Book of ASTM Standards* Vol. 09.01 (ASTM International, West Conshohocken, 2021), <https://www.astm.org/d1765-21.html>.

TABLE I. Components of the IR+N121 rubber compound. All amounts are given by weight relative to 100 units of weight of the rubber polymer (*per hundred rubber* or phr). TBBS is *N-tert-butyl-2-benzothiazolesulfenamide*.

Substance	Amount (phr)
Polyisoprene ^a	100
N121 ^b	50
Additives ^c	6
Zink oxide ^d	3
Stearic acid ^d	2
Sulfur ^e	1.4
TBBS ^e	0.75

^aPolymer.

^bFiller.

^cE.g., antiaging.

^dVulcanization activator.

^eVulcanization package.

G_∞ , of about 1.2 GPa [Fig. 12(a)], while the spectral shape of the imaginary parts are nearly identical [Fig. 12(c)]. DMA and rheometer measurements agree in the low-frequency region in their estimation of the rubber plateau. In this region, the PSG measurements gives a value that is 20 times higher. This could be due to the relatively low sensitivity at low moduli of the PSG measurement or it could be an artifact introduced by, for instance, the glue. Work is ongoing to pinpoint the origin of this discrepancy.

The inset of Fig. 12(c) shows the temperature dependence of the characteristic time scales for relaxation derived from the three measurements. Using the PSG loss peak frequencies (full circles) as a reference, time scales from the rheometer (squares) and DMA (full line) measurements are shifted to ensure agreement with the PSG loss peak frequency at 210 K. The shift for the rheometer measurement was 2 K on the temperature axis and reflects a difference in absolute temperature calibration between the setups. For the DMA measurements the Williams–Landel–Ferry curve for the shift factors was converted into frequencies and shifted on the y-axis to match the PSG measurements at 210 K. Note that only for the PSG measurements can the loss peaks be directly determined in the full temperature range. Nevertheless, the temperature dependence of the time scales for all three measurements match remarkably well.

APPENDIX E: INCLUDING LIQUID INERTIA

In the derivation of the equation of motion of the piezoelectric disk, it was assumed that the inertia of the liquid could be ignored in the liquid stress response to the disk displacement. In order to take the inertia into account, we consider the wave-equation for shear waves in the z -direction

$$-\omega^2 u_x(z) = \frac{G^*}{\rho_l} \frac{d^2 u_x(z)}{dz^2}, \quad (\text{E1})$$

with boundary conditions

$$u_z(0) = 0, \quad \sigma_l = G^* \left(\frac{du_x(z)}{dz} \right)_{z=d}. \quad (\text{E2})$$

Solving these equations one finds that the modulus determined by neglecting inertial effects—the apparent modulus G_{app}^* —is a function of actual modulus G^* ,

$$G_{\text{app}}^* \equiv d \frac{\sigma_l}{u_x(d)} = G^* \frac{kd}{\tan(kd)} \quad (\text{E3})$$

with

$$k = \sqrt{\frac{\rho_l}{G^*}} \omega, \quad (\text{E4})$$

where ρ_l is the sample density. Note that in the general case where the modulus G is complex, k is also complex, $k = k' + ik''$, with k' representing the wavenumber of the transverse sound wave and k'' the damping coefficient.

In order to correct for the effect of liquid inertia, one has to invert G_{app}^* (as determined by the method described in Secs. II and III) by Eq. (E3). This is done by introducing

$$a = \frac{\rho_l \omega^2 d^2}{G_{\text{app}}^*} \quad \text{and} \quad x = kd \quad (\text{E5})$$

whereby Eq. (E3) becomes

$$a = x \tan(x), \quad (\text{E6})$$

which is solved for x from which G^* is found.

Figure 13 shows the ratio of $|G_{\text{app}}^*/G^*|$ as a function of $k'd$ for a $G' = 1$ MPa and a range of $\tan \delta$ from 0 (the purely elastic case) to 100 (a very viscous case). The plot illustrates that the correction factor starts to matter when $k'd \approx 1/4$. Two values for $k'd$ are marked by dashed lines: (1) where the correction becomes sizeable (corresponding to a transverse sound wavelength of $\lambda = 8\pi d$) and (2) the theoretical limit for the correction in the purely elastic case, where $|G_{\text{app}}^*/G^*| = 0$. This corresponds to a transverse sound wavelength of $\lambda = 4d$. When the modulus is complex there is no theoretical limit to the correction; $|G_{\text{app}}^*/G^*|$ never vanishes and thus the correction factor never diverges. However, we still consider $\lambda = 4d$ (equivalent to $k'd = \pi/2$ in the purely elastic case) to be the practical limit for the PSG method.

Figure 14 shows where the practical limit of the method lies in the frequency-versus-modulus plane. The limit is determined by $\lambda = 4d$ as well as where the effect of inertia becomes significant. The elastic case ($G'' = 0$) is shown in Fig. 14(a). The limits on the frequency and modulus axes correspond to the range of the PSG measurement. The red area in the lower right corner marks the practical limit of the PSG measurement, i.e., where $\lambda = 4d$, below which the method cannot measure meaningfully. The dashed line marks where the inertia correction is 2% and the hatched area thus

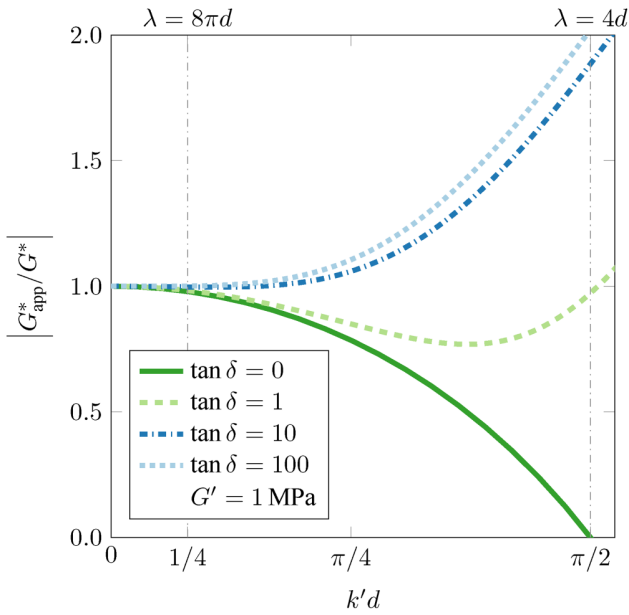


FIG. 13. $|G_{\text{app}}^*/G^*|$ as a function of $k'd$ for the real modulus of $G' = 1$ GPa for four values of $\tan \delta$: 0 (the elastic case), 1, 10, and 100 (the very viscous case). Two values of $\lambda = 2\pi/k'$ are highlighted: $\lambda = 8\pi d$ ($k'd = 1/4$), where for a purely real G , $|G_{\text{app}}^*/G^*| = 0.98$ and $\lambda = 4d$ ($k'd = \pi/2$), where for a purely real G , $|G_{\text{app}}^*/G^*| = 0$, and the correction factor diverges. For a finite imaginary part, the correction factor is always finite (i.e., the curves for $\tan \delta \neq 0$ never vanish), meaning that a correction is always possible. In the region between the two vertical lines, a correction for sample inertia is necessary. For $\tan \delta \neq 0$, it is, in principle, possible to correct also above $k'd = \pi/2$, but the PSG method is not meaningful when the transverse sound wavelength becomes comparable to the sample thickness. This thus marks the lower limit for the method for all moduli. See also Fig. 14.

shows where a correction is necessary. The viscoelastic case is illustrated in Fig. 14(b) in a plot similar to Fig. 14(a), except here $\tan \delta$ is varied (equivalent to adding an imaginary part) for a fixed $G' = 1$ MPa. In this plot, the practical limit of the measurement is again the solid line in the lower right corner. The dashed and dotted lines mark where the absolute value, respectively the phase, of the correction factor G_{app}^*/G^* are 2%. In Fig. 14(c), G' is varied for different fixed values of $\tan \delta$. The color shows the wavelength of the transverse sound wave and the white area where $\lambda \leq 4d$. Clearly, this area shrinks as the imaginary part grows. Note that the locations of “forbidden” areas depend on the sample thickness. All illustrations used here are for $d = 0.5$ mm. The limit of the method ($\lambda \leq 4d$) goes as $\propto d^2$, so a smaller sample thickness would lower the limit.

Finally, in Fig. 15, we show a zoom on the high frequency region of the real and imaginary part of uncorrected (G'_{app} and G''_{app} in light green) and corrected (G' and G'' in dark green) data for squalane (same data as in Fig. 5) to demonstrate the effect on our data. The corrected real part is slightly higher than the uncorrected, while the correction shifts the imaginary part to a very slightly lower value.

The correction for inertial effects derived here is identical to that of Schrag [35]. The only difference is that we keep

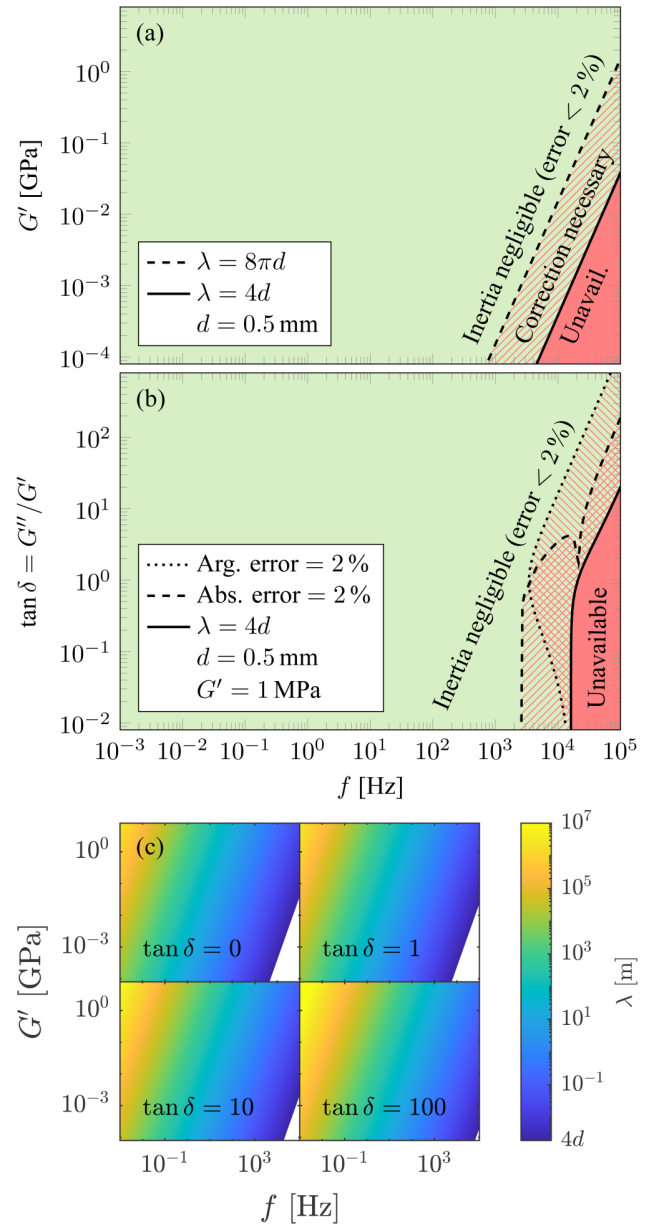


FIG. 14. Illustration of the necessity of correcting for inertial effects for a sample thickness $d = 0.5$ mm. (a) The elastic case, i.e., $G'' = 0$. In most of the plane, inertial effects are negligible, but at a combination of high frequency and low modulus, the wavelength of the shear wave in the sample becomes comparable to the sample thickness. For $\lambda = 8\pi d$ (shown as a dashed line), we have $G_{\text{app}}^*/G^* \approx 0.98$. Hence, the correction is less than 2% for the area to the left of this line. The solid line, where $\lambda = 4d$, marks the limit of the correction where $G_{\text{app}}^*/G^* = 0$ and the correction factor diverges. (b) Like (a), but showing the situation for a fixed $G' = 1$ MPa when varying $\tan \delta$. In this case, the dashed line marks a 2% error in the absolute correction factor $|G_{\text{app}}^*/G^*|$ and the dotted line marks the 2% error in the phase, $\arg(G_{\text{app}}^*/G^*)$. Inertia is negligible in the area to the left of the union of these two areas. (c) The wavelength of the shear wave for four values of $\tan \delta$. The areas where $\lambda < 4d$ are shown in white. Note how the white area shrinks for higher $\tan \delta$.

the complex notation instead of splitting the calculations in absolute modulus and phase, which makes the equations simpler and more operational for our experimental realization.

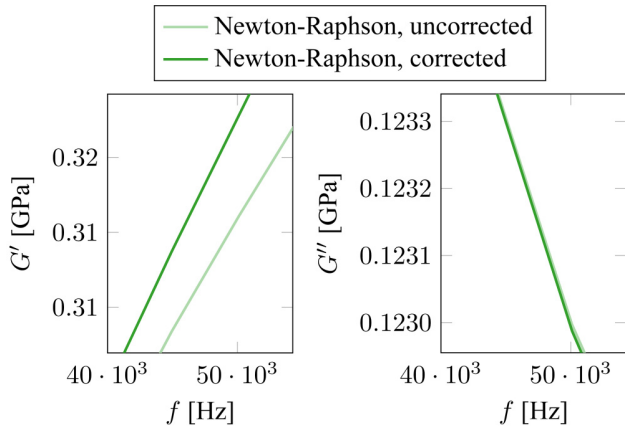


FIG. 15. Comparison of uncorrected and corrected data, G_{app}^* and G^* , for squalane measured at 190 K. These data are also shown in Fig. 5. The correction on the loss modulus is relatively much smaller than that on the storage modulus. Note how the correction raises the storage modulus from the measured value, while it lowers the loss modulus.

APPENDIX F: PLATE BENDING CALCULATIONS

The Kelvin functions are defined as

$$\begin{aligned} \text{Ber}_n(r) + i\text{Bei}_n(r) &= J_n(re^{3\pi i/4}), \\ \text{Ker}_n(r) + i\text{Kei}_n(r) &= e^{-\pi ni/2} K_n(re^{\pi i/4}), \end{aligned} \quad (\text{F1})$$

where J_n are the Bessel functions and K_n are the modified Bessel functions of the first kind. The following recursion formulas hold for the derivatives:

$$\begin{aligned} \text{Ber}' &= \frac{1}{\sqrt{2}}(\text{Ber}_1 + \text{Bei}_1), \\ \text{Bei}' &= \frac{1}{\sqrt{2}}(\text{Bei}_1 - \text{Ber}_1), \\ \text{Ber}'_1 &= -\frac{1}{\sqrt{2}}(\text{Ber} + \text{Bei}) - \frac{1}{r}\text{Ber}_1, \\ \text{Bei}'_1 &= -\frac{1}{\sqrt{2}}(\text{Bei} - \text{Ber}) - \frac{1}{r}\text{Bei}_1 \end{aligned} \quad (\text{F2})$$

and identical relations for the Ke-functions.

Define the Laplacian $\Delta = \frac{1}{r}\frac{\partial}{\partial r}r\frac{\partial}{\partial r}$. The recursion formulas lead to

$$\begin{aligned} \Delta \text{Ber} &= -\text{Bei}, \\ \Delta \text{Bei} &= \text{Ber}, \\ \Delta \text{Ker} &= -\text{Kei}, \\ \Delta \text{Kei} &= \text{Ker} \end{aligned} \quad (\text{F3})$$

and thus all four Kelvin functions fulfill

$$\Delta^2 u = -u. \quad (\text{F4})$$

The solution to Eq. (31) of the main text is Eq. (33), which we repeat here

$$u(r) = A_1 \text{Ber}(r) + A_2 \text{Bei}(r) + A_3 \text{Ker}(r) + A_4 \text{Kei}(r). \quad (\text{F5})$$

The four boundary conditions of Eqs. (32) and (23)–(25)

then become

$$u_0 = A_1 \text{Ber}(r_h) + A_2 \text{Bei}(r_h) + A_3 \text{Ker}(r_h) + A_4 \text{Kei}(r_h), \quad (\text{F6})$$

$$\begin{aligned} 0 &= A_1(\text{Ber}_1(r_h) + \text{Bei}_1(r_h)) \\ &\quad + A_2(\text{Bei}_1(r_h) - \text{Ber}_1(r_h)) \\ &\quad + A_3(\text{Ker}_1(r_h) + \text{Kei}_1(r_h)) \\ &\quad + A_4(\text{Kei}_1(r_h) - \text{Ker}_1(r_h)), \end{aligned} \quad (\text{F7})$$

$$\begin{aligned} 0 &= A_1(\text{Ber}_1(R) - \text{Bei}_1(R)) \\ &\quad + A_2(\text{Ber}_1(R) + \text{Bei}_1(R)) \\ &\quad + A_3(\text{Ker}_1(R) - \text{Kei}_1(R)) \\ &\quad + A_4(\text{Ker}_1(R) + \text{Kei}_1(R)), \end{aligned} \quad (\text{F8})$$

and

$$\begin{aligned} 0 &= A_1[-\text{Bei}(R) - g(\text{Ber}_1(R) + \text{Bei}_1(R))] \\ &\quad + A_2[\text{Ber}(R) - g(\text{Bei}_1(R) - \text{Ber}_1(R))] \\ &\quad + A_3[-\text{Kei}(R) - g(\text{Ker}_1(R) + \text{Kei}_1(R))] \\ &\quad + A_4[\text{Ker}(R) - g(\text{Kei}_1(R) - \text{Ker}_1(R))], \end{aligned} \quad (\text{F9})$$

where $g = (1 - \nu)/(\sqrt{2}R)$.

REFERENCES

- [1] Ashby, M. F., and A. L. Greer, "Metallic glasses as structural materials," *Scr. Mater.* **54**, 321–326 (2006).
- [2] Fischer, P., and E. J. Windhab, "Rheology of food materials," *Curr. Opin. Colloid Interface Sci.* **16**, 36–40 (2011).
- [3] Angell, C., "Perspective on the glass transition," *J. Phys. Chem. Solids* **49**, 863–871 (1988).
- [4] Mauro, J. C., Y. Yue, A. J. Ellison, P. K. Gupta, and D. G. Allan, "Viscosity of glass-forming liquids," *Proc. Natl. Acad. Sci. U.S.A.* **106**, 19780–19784 (2009).
- [5] Hou, Y. Y., and H. O. Kassim, "Instrument techniques for rheometry," *Rev. Sci. Instrum.* **76**, 101101 (2005).
- [6] Schroyen, B., D. Vlassopoulos, P. Van Puyvelde, and J. Vermant, "Bulk rheometry at high frequencies: A review of experimental approaches," *Rheol. Acta* **59**, 1–22 (2020).
- [7] Athanasiou, T., G. K. Auernhammer, D. Vlassopoulos, and G. Petekidis, "A high-frequency piezoelectric rheometer with validation of the loss angle measuring loop: Application to polymer melts and colloidal glasses," *Rheol. Acta* **58**, 619–637 (2019).
- [8] Schröter, K., S. A. Hutcheson, X. Shi, A. Mandanici, and G. B. McKenna, "Dynamic shear modulus of glycerol: Corrections due to instrument compliance," *J. Chem. Phys.* **125**, 214507 (2006).
- [9] Laukkanen, O.-V., "Small-diameter parallel plate rheometry: A simple technique for measuring rheological properties of glass-forming liquids in shear," *Rheol. Acta* **56**, 661–671 (2017).
- [10] Ferry, J. D., *Viscoelastic Properties of Polymers*, 3rd ed. (Wiley, New York, 1980).
- [11] Sader, J. E., "Frequency response of cantilever beams immersed in viscous fluids with applications to the atomic force microscope," *J. Appl. Phys.* **84**, 64–76 (1998).

- [12] Ahmed, N., D. F. Nino, and V. T. Moy, "Measurement of solution viscosity by atomic force microscopy," *Rev. Sci. Instrum.* **72**, 2731–2734 (2001).
- [13] Christopher, G. F., J. M. Yoo, N. Dagalakis, S. D. Hudson, and K. B. Migler, "Development of a MEMS based dynamic rheometer," *Lab Chip* **10**, 2749–2757 (2010).
- [14] Mather, M. L., M. Rides, C. R. G. Allen, and P. E. Tomlins, "Liquid viscoelasticity probed by a mesoscale piezoelectric bimorph cantilever," *J. Rheol.* **56**, 99–112 (2012).
- [15] McSkimin, H. J., Ultrasonic methods for measuring the mechanical properties of liquids and solids, in *Physical Acoustics: Principles and Methods*, edited by W. P. Mason (Academic, New York, 1964), Vol. IA, pp. 271–334.
- [16] Yan, Y., and K. A. Nelson, "Impulsive stimulated light scattering. I. General theory," *J. Chem. Phys.* **87**, 6240–6256 (1987).
- [17] Pick, R. M., C. Dreyfus, A. Azzimani, A. Taschin, M. Ricci, R. Torre, and T. Franosch, "Frequency and time resolved light scattering on longitudinal phonons in molecular supercooled liquids," *J. Phys.: Condens. Matter* **15**, S825–S834 (2003).
- [18] Klieber, C., T. Pezeril, S. Andrieu, and K. A. Nelson, "Optical generation and detection of gigahertz-frequency longitudinal and shear acoustic waves in liquids: Theory and experiment," *J. Appl. Phys.* **112**, 013502 (2012).
- [19] Morath, C. J., and H. J. Maris, "Phonon attenuation in amorphous solids studied by picosecond ultrasonics," *Phys. Rev. B* **54**, 203–213 (1996).
- [20] Pezeril, T., C. Klieber, S. Andrieu, and K. A. Nelson, "Optical generation of gigahertz-frequency shear acoustic waves in liquid glycerol," *Phys. Rev. Lett.* **102**, 107402 (2009).
- [21] Christensen, T., and N. B. Olsen, "A rheometer for the measurement of a high shear modulus covering more than seven decades of frequency below 50 kHz," *Rev. Sci. Instrum.* **66**, 5019–5031 (1995).
- [22] Dyre, J. C., N. B. Olsen, and T. Christensen, "Local elastic expansion model for viscous-flow activation energies of glass-forming molecular liquids," *Phys. Rev. B* **53**, 2171–2174 (1996).
- [23] Eliassen, K. L., H. W. Hansen, F. Lundin, D. Rauber, R. Hempelmann, T. Christensen, T. Hecksher, A. Matic, B. Frick, and K. Niss, "High-frequency dynamics and test of the shoving model for the glass-forming ionic liquid Pyr14-TFSI," *Phys. Rev. Mater.* **5**, 065606 (2021).
- [24] Gundermann, D., U. R. Pedersen, T. Hecksher, N. P. Bailey, B. Jakobsen, T. Christensen, N. B. Olsen, T. B. Schröder, D. Fragiadakis, R. Casalini, C. Michael Roland, J. C. Dyre, and K. Niss, "Predicting the density-scaling exponent of a glass-forming liquid from Prigogine–Defay ratio measurements," *Nat. Phys.* **7**, 816–821 (2011).
- [25] Gainaru, C., R. Figuli, T. Hecksher, B. Jakobsen, J. C. Dyre, M. Wilhelm, and R. Böhm, "Shear-modulus investigations of monohydroxy alcohols: Evidence for a short-chain-polymer rheological response," *Phys. Rev. Lett.* **112**, 098301 (2014).
- [26] Hecksher, T., and B. Jakobsen, "Communication: Supramolecular structures in monohydroxy alcohols: Insights from shear-mechanical studies of a systematic series of octanol structural isomers," *J. Chem. Phys.* **141**, 101104 (2014).
- [27] Jensen, M. H., C. Gainaru, C. Alba-Simionesco, T. Hecksher, and K. Niss, "Slow rheological mode in glycerol and glycerol–water mixtures," *Phys. Chem. Chem. Phys.* **20**, 1716–1723 (2018).
- [28] Hecksher, T., D. H. Torchinsky, C. Klieber, J. A. Johnson, J. C. Dyre, and K. A. Nelson, "Toward broadband mechanical spectroscopy," *Proc. Natl. Acad. Sci. U.S.A.* **114**, 8710–8715 (2017).
- [29] Hecksher, T., N. B. Olsen, and J. C. Dyre, "Model for the alpha and beta shear-mechanical properties of supercooled liquids and its comparison to squalane data," *J. Chem. Phys.* **146**, 154504 (2017).
- [30] Hecksher, T., N. B. Olsen, and J. C. Dyre, "Model for the alpha and beta shear-mechanical properties of supercooled liquids and its comparison to squalane data," *J. Chem. Phys.* **146**, 154504 (2017).
- [31] Jakobsen, B., T. Hecksher, T. Christensen, N. B. Olsen, J. C. Dyre, and K. Niss, "Communication: Identical temperature dependence of the time scales of several linear-response functions of two glass-forming liquids," *J. Chem. Phys.* **136**, 081102 (2012).
- [32] Roed, L. A., J. C. Dyre, K. Niss, T. Hecksher, and B. Riechers, "Time-scale ordering in hydrogen- and van der waals-bonded liquids," *J. Chem. Phys.* **154**, 184508 (2021).
- [33] Weigl, P., T. Hecksher, J. C. Dyre, T. Walther, and T. Blochowicz, "Identity of the local and macroscopic dynamic elastic responses in supercooled 1-propanol," *Phys. Chem. Chem. Phys.* **23**, 16537–16541 (2021).
- [34] Christensen, T., and N. B. Olsen, "Determination of the frequency-dependent bulk modulus of glycerol using a piezoelectric spherical shell," *Phys. Rev. B* **49**, 15396–15399 (1994).
- [35] Schrag, J. L., "Deviation of velocity gradient profiles from the 'gap loading' and 'surface loading' limits in dynamic simple shear experiments," *Trans. Soc. Rheol.* **21**, 399–413 (1977).
- [36] In Christensen and Olsen, the symbol p was used instead of v . We change it here to be consistent throughout the current paper.
- [37] Ryaben'kii, V. S., and S. V. Tsynkov, *A Theoretical Introduction to Numerical Analysis* (Taylor & Francis, London, 2006).
- [38] Schröter, K., and E. Donth, "Viscosity and shear response at the dynamic glass transition of glycerol," *J. Chem. Phys.* **113**, 9101–9108 (2000).
- [39] Scarponi, F., L. Comez, D. Fioretto, and L. Palmieri, "Brillouin light scattering from transverse and longitudinal acoustic waves in glycerol," *Phys. Rev. B* **70**, 054203 (2004).
- [40] Klieber, C., T. Hecksher, T. Pezeril, D. H. Torchinsky, J. C. Dyre, and K. A. Nelson, "Mechanical spectra of glass-forming liquids. II. Gigahertz-frequency longitudinal and shear acoustic dynamics in glycerol and DC704 studied by time-domain Brillouin scattering," *J. Chem. Phys.* **138**, 12A544 (2013).
- [41] Igarashi, B., T. Christensen, E. H. Larsen, N. B. Olsen, I. H. Pedersen, T. Rasmussen, and J. C. Dyre, "A cryostat and temperature control system optimized for measuring relaxations of glass-forming liquids," *Rev. Sci. Instrum.* **79**, 045105 (2008).
- [42] Igarashi, B., T. Christensen, E. H. Larsen, N. B. Olsen, I. H. Pedersen, T. Rasmussen, and J. C. Dyre, "An impedance-measurement setup optimized for measuring relaxations of glass-forming liquids," *Rev. Sci. Instrum.* **79**, 045106 (2008).
- [43] Niss, K., and T. Hecksher, "Perspective: Searching for simplicity rather than universality in glass-forming liquids," *J. Chem. Phys.* **149**, 230901 (2018).
- [44] Niss, K., B. Jakobsen, and N. B. Olsen, "Dielectric and shear mechanical relaxations in glass-forming liquids: A test of the Gemant-DiMarzio-Bishop model," *J. Chem. Phys.* **123**, 234510 (2005).
- [45] Jakobsen, B., K. Niss, and N. B. Olsen, "Dielectric and shear mechanical alpha and beta relaxations in seven glass-forming liquids," *J. Chem. Phys.* **123**, 234511 (2005).
- [46] Hecksher, T., "Relaxation in supercooled liquids," Ph.D. thesis, Roskilde University, Roskilde, 2011.

- [47] Hecksher, T., N. B. Olsen, K. A. Nelson, J. C. Dyre, and T. Christensen, "Mechanical spectra of glass-forming liquids. I. Low-frequency bulk and shear moduli of DC704 and 5-PPE measured by piezoceramic transducers," *J. Chem. Phys.* **138**, 12A543 (2013).
- [48] Niss, K., D. Gundermann, T. Christensen, and J. C. Dyre, "Dynamic thermal expansivity of liquids near the glass transition," *Phys. Rev. E* **85**, 041501 (2012).
- [49] Landau, L. D., and E. M. Lifshitz, *Theory of Elasticity* (Elsevier, New York, 1986).
- [50] Nielsen, A. I., S. Pawlus, M. Paluch, and J. C. Dyre, "Pressure dependence of the dielectric loss minimum slope for ten molecular liquids," *Philos. Mag.* **88**, 4101–4108 (2008).
- [51] Roed, L. A., D. Gundermann, J. C. Dyre, and K. Niss, "Communication: Two measures of isochronal superposition," *J. Chem. Phys.* **139**, 101101 (2013).
- [52] Williams, M. L., R. F. Landel, and J. D. Ferry, "The temperature dependence of relaxation mechanisms in amorphous polymers and other glass-forming liquids," *J. Am. Chem. Soc.* **77**, 3701–3707 (1955).